Cooling Performance of Storable Propellants for a micro rocket engine

by

Carole Joppin

Submitted to the Department of Aeronautics and Astronautics
in partial fulfillment of the requirements for the degree of

MASTER OF SCIENCE

at the

MASSACHUSETTS INSTITUTE OF TECHNOLOGY

June 2002

Author .....
Department of Aeronautics and Astronautics
May 24, 2002

Certified by .....
Professor Alan H. Epstein
R.C. Maclaurin Professor of Aeronautics and Astronautics
Thesis Supervisor

Accepted by .....
Professor Wallace E. Vander Velde
Professor of Aeronautics and Astronautics
Chair, Committee on Graduate Students

Cooling Performance of Storable Propellants for a Micro Rocket Engine

by

Carole Joppin

Submitted to the Department of Aeronautics and Astronautics
on May 24, 2002, in partial fulfillment of the
requirements for the degree of
MASTER OF SCIENCE

Abstract

This thesis studies the selection of propellants for a liquid regeneratively cooled micro rocket engine focusing on the characterization of their cooling performance. Propellants will be at high pressures and under high heat fluxes in the cooling passages and will be supercritical. A summary of the propellant combination selection process and a brief evaluation of potential propellants are presented.

A series of heat transfer tests in electrically heated stainless steel micro tubes 95 microns inner diameter has been conducted with two hydrocarbons JP7 and JP10 at subcritical, critical and supercritical conditions and under high heat fluxes. JP7 and JP10 have been evaluated on the basis of their heat transfer capabilities, their stability and the formation of deposits in micro channels. JP7 offers a high heat capacity. An increase in the heat transfer coefficient at the end of the tube, combined with an increase in the Stanton number, seems to indicate that JP7 undergoes an endothermic decomposition which causes a significant enhancement in heat transfer capacity. JP10 offers lower heat transfer coefficients. Both hydrocarbons show a good stability and no evidence of deposits has been seen.

Previous results with supercritical ethanol were compared to the results with JP7 and JP10. JP7 seems to provide the highest heat transfer coefficients at high pressures and seems to be the most promising coolant for the regeneratively cooled rocket engine.

Compatibility issues associated with the use of hydrogen peroxide as oxidizer for the liquid rocket engine have been addressed. Materials used in MEMS devices show good compatibility with 98 % hydrogen peroxide after passivation in 30 % hydrogen peroxide except for platinum.

Thesis Supervisor: Professor Alan H. Epstein
Title: R.C. Maclaurin Professor of Aeronautics and Astronautics

Acknowledgments

I would like first to thank my thesis advisor Professor Alan Epstein for offering me the opportunity to be part of such an exciting project as the micro rocket engine program. Working under his supervision has been an invaluable experience. I also wish to extend my gratitude to Professor Kerrebrock for his precious guidance, his constant support and his encouragements. My graduate experience and my understanding of my project would not be what they are without their help and I thank them for their dedication to my research work and to furthering my education.

I had the privilege to work with an exceptional group of people in the Gas Turbine Laboratory and the microengine program. I am grateful to Dr. Gerald Guenette for his help to improve the test rig and the experimental protocol; Dr. Yoav Peles for giving me the right contacts; James Letendre for his invaluable advice and help with my numerous technical problems to improve and fix my test rig; Paul Warren for his patience and advice with all the problems I would come to him with; Jack Costa and Viktor Dubrowski for their contribution to the test rig; Bill Ames, Marie Mc Davitt, Holly Anderson, Susan Parker and Diana Park for dealing with my questions. A special attention to Lori Martinez not only for her support but also for her constant good mood and for establishing such a good social atmosphere in the laboratory.

I am grateful to Chris Protz for his patience with my numerous questions, for his assistance in my project, for introducing me with the micro rocket engine and for letting me steal his mass flow meter so often. Special thanks to Laurent Jamonet for his advice on technical issues and for keeping me company during the late nights of work. I am also grateful to the remainder of the micro rocket engine team Sumita Pennathur, Antoine Deux, Erin Noonan, Shana Diez, Dr. Sun, Nori Miki and Jin-Wook Lee.

I would like to thank all the students in the Gas Turbine Laboratory with whom I had a great time, especially my office mates, Chris Spadaccini and Chiang-Juay Teo.

My experience at MIT would not have been as unforgettable as it is without the friendship

of so many people and the love and support of my family. I am particularly grateful to Yann for his advice, his constant support and for agreeing to read every single page of my thesis.

This research was sponsored by NASA. This support is gratefully acknowledged.

Contents

List of Figures

List of Tables

Nomenclature

Roman

A_e	Cross-section area
A_i	Inside wall surface
BV	Ball valve
C	Influence coefficient
Cp	Specific heat
D	Passage size
DC	Direct current
E	Electrical field
G	Mass velocity
H	Enthalpy
I	Current
Id	Density specific impulse
IR	Infra-red
Isp	Specific impulse
$JP7$	Jet Fuel 7
$JP10$	Jet Fuel 10
$JPTS$	Jet Fuel Thermally Stable
MF	Mass flowmeter
Nu	Nusselt number
NV	Needle valve
P	Pressure (also pressure transducer)
P_1	Pressure before the test section

P_2 Pressure after the test section

P_c Critical pressure

Pr Prandtl number

Q Power

R Resistance

S Fractional uncertainty

SR Relieve valve

St Stanton number

SV Solenoid valve

T Temperature (also tank)

Th Thermocouple

V Voltage (also valve)

X Position (also fluid component in the enthalpy model)

f Friction factor

h Heat transfer coefficient

l Micro tube length

$\dot{m}$ Mass flow

q Heat flux

r Radial distance from the center radius

r_i Inner radius

r_o Outer radius

t Time

u Fluid velocity

x Fractional distance

Greek

α	Oxidizer to fuel mass ratio
β	Scale factor on the pressure measurements
ΔP	Pressure drop across the pump
κ	Conductivity
μ	Viscosity
ρ	Density
σ	Dielectric constant of the 304 stainless steel

Subscripts

av	Average
b	Bulk
$bulk$	Bulk
c	Critical (also calibration)
C_p	Constant temperature properties
f	Film
$fluid$	Fluid
$fuel$	Fuel
i	Inside wall conditions
o	Outside wall conditions
ox	Oxidizer
pc	pseudo critical
ss	Stainless steel
w	Wall

Acronyms

3D	Three-dimensional
CEA	Computer Program Calculation of Complex Chemical Equilibrium Compositions and Applications
MEMS	Micro electro mechanical systems
rpm	Rotations per minute

Chapter 1

Introduction

Micro-electromechanical systems (MEMS) refer to small systems produced using the same methods as for computer chips. They can be made by bonding together several planar silicon wafers to create a 3D device. First appearing two decades ago in the high-tech community, they are considered to offer great promise for applications in various fields from automobile airbags to aircraft engines. MEMS devices offer high performance to mass ratios and potentially a substantial cost advantage due to their manufacturing techniques of production, which allow large scale production.

At MIT, a large effort is dedicated to the study of power-MEMS, especially for propulsion and electric applications. In 1994, Epstein et al. [19] proposed the concept of micro engines using the MEMS technology. Two programs are on-going at MIT: a micro-gas engine and a micro rocket engine [17].

Micro engine program The micro-gas engine device is a gas turbine engine regrouping in a cm-scale device turbine, compressor and combustor. Many potential applications are considered from the propulsion of micro air vehicles to power generation. A demonstration engine has been designed by Protz [28] for a 10 g thrust level. The baseline design of the current device is shown in Figure 1-1.

Micro rocket program The concept of a micro rocket engine has been first introduced by Adam London [23]. Designed to produce 15 N of thrust, this bipropellant engine

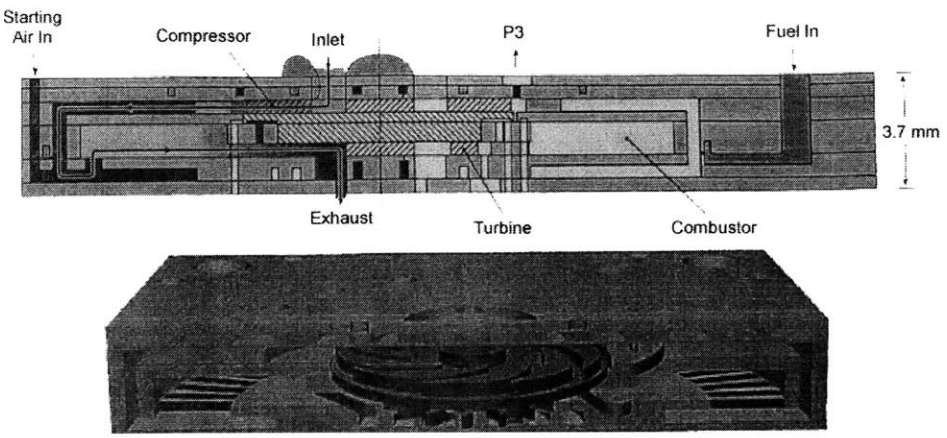

Figure 1-1: Baseline design of the micro engine. Cross section of the demo engine at two different locations and 3D section of the demo engine device [14].

uses gaseous propellants and a liquid coolant. On-going tests have demonstrated a maximum thrust of 2 N and a maximum chamber pressure of 90 atm.

As part of the micro rocket engine program, this work is a study of the cooling properties of potential storable propellants for a liquid regeneratively cooled micro rocket engine. This chapter gives an overview of the micro rocket project and the objectives of the present propellant study within the general framework of the micro rocket engine application.

1.1 MEMS fabricated micro rocket engine

1.1.1 Justification for a micro rocket engine

The thrust of an engine scales with the area of the nozzle whereas the weight of the engine scales with the volume. As the size of the engine decreases, the mass decreases faster than the thrust. Therefore, micro engines offer good thrust to weight ratios. The micro rocket engine can produce thrust to weight ratios higher by an order of magnitude than macro scale rocket engines. The thrust to weight ratio is directly related to the mass of payload that can be delivered to orbit.

Moreover, the silicon fabrication technique allows large scale production, therefore potentially decreasing production costs. This can lead to significant cost reductions in satellite systems or launch vehicles.

Many applications have been envisioned for such micro rocket engines giving a thrust in the 15 N range. A first potential use would be for attitude control or as propulsion system for manoeuvering satellite systems. Their light weight would give them a great advantage over current macro scale propulsion systems in small thrust applications. The option of using them as main propulsion devices was also investigated. Associated in parallel, a group of micro rocket engines would be able to power a 2 m high launch vehicle that could be used to deliver a micro satellite in low Earth orbit.

1.1.2 Description of the concept of the micro rocket engine

The objective of the micro rocket engine program is to design a liquid motor regeneratively cooled, in which the propellants are pressurized using micro turbopumps in an expander cycle. The use of turbopumps to pressurize the propellants eliminates the need for pressurized tanks, which are a main contribution to weight in current satellite systems. The overall propulsion system will therefore be lighter allowing more payload to be carried.

Propellants are fed to the rocket through valves at low pressures before being pressurized up to the required inlet pressure of the cooling passages. The propellants are heated while cooling the rocket chamber and reach supercritical conditions. Part of the propellants enter the turbine to drive the turbopumps. Propellants are then injected in the chamber for combustion. The products of the reaction expand in the nozzle and produce thrust.

1.1.3 Different components of the micro rocket engine

1.1.3.1 Turbopump

The micro rocket engine design requires the propellants to be pressurized up to 300 atm at the inlet of the cooling passages. The turbopump must provide a 300 atm pressure rise. Moreover, the propellants entering the turbine are under supercritical conditions. Therefore, the turbine is driven by gaseous like propellants whereas the propellants in the pump are in a liquid like state.

It was decided to first design a demonstration turbopump device that would provide a

30 atm pressure rise using water as the pumped liquid and gas as the driving fluid for the turbine. This smaller pressure rise was chosen as a demonstration of the feasibility of the concept but also because it corresponds to the pressure rise that would be required for a boost pump to prevent cavitation from occurring in the main pump. The demo pump, designed by Deux [14], proposes a new concept in which turbine and pump blades are on the same side of a single wafer rotor. The turbopump concept is presented in Figure 1-2. A hydrostatic thrust bearing provides a seal between the two. This design simplifies the fabrication process but adds issues mainly about the behavior of the seal between the liquid circuit in the pump and the gas circuit in the turbine. Tests to date have demonstrated a rotation speed of 100,000 rpm with air in the pump and rotation speeds between 25,000 rpm and 65,000 rpm with water [21]. Figure 1-3 presents a layout of the turbopump device. Separate experimental studies on cavitation [26] have shown that cavitation at micro scale

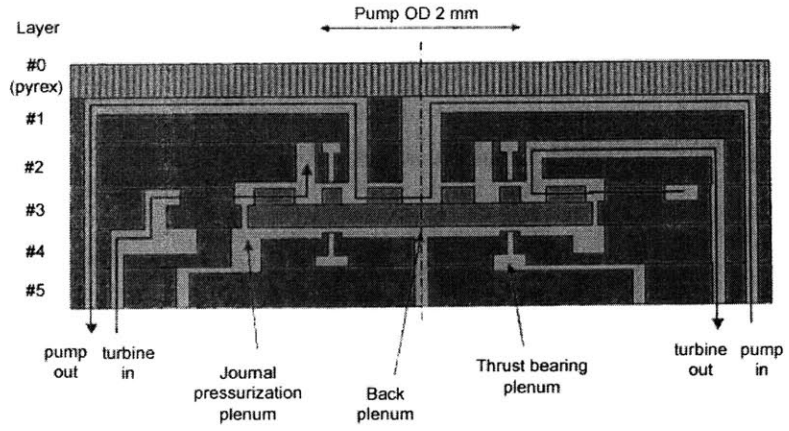

Figure 1-2: Concept of the turbopump. Cross section of the device [14].

can occur and must be taken into account in the design of the micro turbopump. Micro scale cavitation follows the same theory as at macro scale. However, the performance loss (decrease in ΔP across the pump) appears to be lower and the erosion less damaging than for macro scale cavitation.

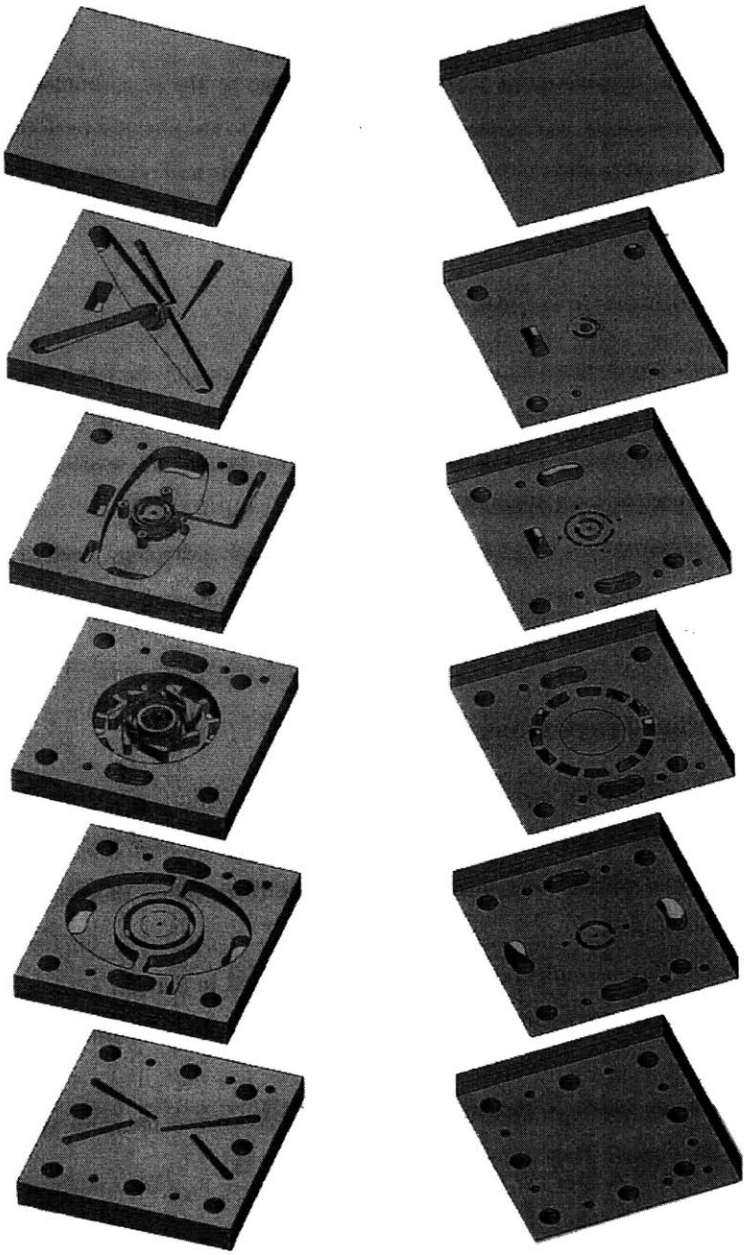

Figure 1-3: Exploded top and bottom views of the turbopump device. The horizontal separation appearing on each layer is not representative of the design and only comes from the rendering[14].

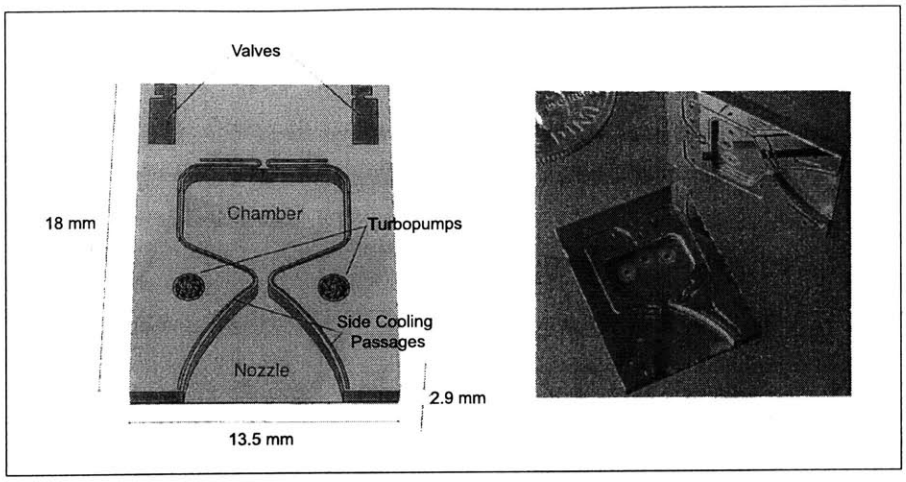

Figure 1-4: Micro rocket engine developed and tested in the Gas Turbine Laboratory at MIT [14].

1.1.3.2 Micro rocket chamber

The first micro rocket engine, designed and tested by London [23], includes injectors, rocket chamber, nozzle and cooling passages in a 6-wafer - 18 mm long - 13.5 mm wide - 3 mm high device. The engine is designed to produce 15 N of thrust at a chamber pressure of 125 atm and a total mass flow of 5 g/s. The specific impulse, which is a characteristic of the performance of the engine, is estimated around 290 s.

Gaseous oxygen and gaseous methane were chosen as oxidizer and fuel respectively. To demonstrate the feasibility of the concept of a micro rocket engine, the micro rocket engine uses separate propellant and coolant circuits. Propellants are directly injected in the chamber and do not participate in the cooling of the device. Cooling is performed by a separate fluid, liquid ethanol. The different design parameters of London's micro rocket engine are summarized in Table 1.1.

The integrity of the chamber and packaging at high pressures and temperatures are the current major issues.

1.1.4 From a gaseous rocket engine to a liquid regeneratively cooled micro rocket engine

Going from the current design to a liquid regeneratively cooled rocket engine requires several modifications. First, the injectors must be modified for liquid rather than gaseous propellants. However, the main modification comes from the fact that the liquid propellants are also used as coolants, circulating in the cooling passages before entering the combustion

Characteristics of the micro rocket engine summary

Thrust	15 N
Thrust to weight ratio	1320:1
Isp	307 s
Total mass flow	5 g/s
Fuel	Gaseous methane
Oxidizer	Gaseous oxygen
Coolant	Liquid ethanol
Total coolant flow rate	5 g/s
Chamber pressure	125 atm
Number of wafers	6
Number of injectors per fluid	242

Table 1.1: Summary of the main characteristics of the micro rocket engine [23].

Heat fluxes in the rocket $[W/mm^2]$

Chamber	20
Throat	200
Expansion nozzle	10

Table 1.2: Heat fluxes at different points in the rocket engine [23, p. 97].

chamber. This implies that there is now a link between performance in the combustion chamber and cooling of the device: a trade must be done between high performance and suitability of the propellants as coolants.

Heat loads are critical in the rocket engine design. They have been estimated between 4 kW and 6.5 kW. Table 1.2 summarizes some estimations of the heat fluxes at different points in the rocket engine. In the regeneratively cooled micro rocket engine, the propellants will be under very high heat fluxes and at very high pressures. They will reach supercritical conditions. Their behavior can be quite different under such extreme conditions. Since there is little knowledge of the characteristics of fuels and oxidizers at micro scale under such conditions, experiments must be conducted to characterize their properties under an environment close to what they would experience in the micro rocket engine.

Selection of the propellants for the liquid regeneratively cooled rocket engine requires:

- study of the performance of different combinations of propellants
- study of the cooling capacity of the propellants
- estimation of the characteristics of the propellants (density, viscosity, specific heat, heat transfer coefficient, etc) at conditions near to those experienced in the rocket engine

1.2 Background

A study of the performance of different combinations of currently used propellants was done by Protz [27]. The Computer Program for Calculation of Complex Chemical Equilibrium Compositions and Applications (CEA) was used to compare the specific impulse (Isp), the density specific impulse (Id), which is the Isp weighted by the average density of the propellants, and the temperature reached in the chamber for the different pairs of propellants. Heat transfer experiments were carried out by Lopata [24] on ethanol and by Faust [18] on water and ethanol at supercritical conditions. Dang [13] and Chen [5] have conducted a preliminary study of the behavior of JP7 under high heat fluxes and pressures.

1.3 Objectives

The work presented in this thesis aims at the characterization of the behavior of two hydrocarbons, JP7 and JP10, as potential fuels for the micro rocket engine. Compatibility issues associated with the use of hydrogen peroxide as oxidizer are also addressed.

1.4 Thesis organization

The first chapter has presented the micro rocket engine program and motivated a study of propellants in supercritical conditions for a future selection of the best combination of propellants for the liquid regeneratively cooled micro rocket engine.
Chapter 2 introduces the issues of the selection of a best combination of propellants for the liquid regeneratively cooled micro rocket engine.
Chapter 3 presents the principles of the heat transfer experiments carried out with JP7 and

JP10 and gives an overview of the experimental apparatus.

Chapter 4 is dedicated to the study of the behavior of JP7 under high heat fluxes and at high pressures.

Chapter 5 presents the results of the experiments carried out with JP10 and a comparison with JP7 is given.

Chapter 6 presents the study of the compatibility issues associated with hydrogen peroxide.

Chapter 7 analyzes the results for future application in the micro rocket engine and gives recommendations for the selection of the final set of propellants.

Chapter 8 summarizes the work presented in this thesis and gives some recommendations for future work.

Chapter 2

Selection process and potential propellants

2.1 Criteria for selection

Different criteria have to be taken into account for the selection of the best candidate propellants to be used in the liquid regeneratively cooled micro rocket engine.

2.1.1 Performance [27]

The combination of propellants impacts the performance of the rocket. Three parameters are important to study:

- The vacuum specific impulse (Isp) is a common performance measure, a measure of the fuel efficiency.
- The density specific impulse (Id) is defined as the ratio of the specific impulse to the average density of the propellants, defined as:

$$I_d = \rho_{av} Isp \tag{2.1}$$

$$\rho_{av} = \frac{\rho_{ox}\,\rho_{fuel}\,(1+\alpha)}{\alpha\,\rho_{fuel} + \rho_{ox}} \tag{2.2}$$

where Isp is the specific impulse, Id the density specific impulse, ρ_{av} the average density of the propellants, ρ_{ox} the oxidizer density, ρ_{fuel} the fuel density, α the oxidizer

to fuel mass ratio. Id takes into account the density of the propellants, the higher the propellant density, the lower the tank volume required and therefore the lighter the tank mass.

- The chamber temperature is also an important factor as it influences the heat load on the rocket and therefore the cooling of the device.

It must be noted in the evaluation of the performance of the propellants that they will enter the chamber in a supercritical state after having circulated in the cooling passages. The characteristics of the fluid may not be perfectly known in such conditions and the fluid may have experienced decomposition or chemical modifications which may alter the performance.

2.1.2 Capacity as a coolant

Since the engine is regeneratively cooled, the capacity of the propellants to cool the device is a major issue, as important as their performance.
Several parameters are important to characterize the suitability of a propellant as coolant for the micro rocket engine.

- **Heat capacity of the fluid**: Silicon starts softening around 950 K and a maximum wall temperature of 900 K has been chosen for the design of the engine. Therefore, depending on the heat capacity of the coolant, cooling passages are designed and sized to keep the wall temperature below 900 K. The design of the cooling passages deals mainly with tailoring the local mass flux (ρu) and the cooling surface to maintain an allowable wall temperature. The liquid propellants must have enough cooling capacity to manage to keep the wall temperature below 900 K with the allowable sizes of the passages.

- **Stability of the fluid**: There are two different types of stability that need to be considered.

  Oscillations in the fluid

  Mass flow, temperature and pressure can oscillate in the cooling passages with supercritical fluids. Oscillations are reported to appear at pressures below twice the critical

pressure, for a wall temperature above the critical temperature and a bulk temperature below the critical temperature [9]. The oscillations result from the mixing of the gas-like layer at the wall and the liquid-like bulk fluid in the viscous layer at the wall. Two types of oscillations have been observed in heat transfer experiments with supercritical fuels in macro tubes [9] [8]:

* low frequency Helmholtz oscillations in the range of 1 Hz to 2 Hz; this movement of the fluid is similar to a classical mass-spring-damper model
* high frequency acoustic oscillations in the range of 75 Hz to 450 Hz

The oscillations had higher amplitudes near the critical point and were almost not apparent at critical pressure ratios above 2. Amplitudes of 50 psi and 100°C have been obtained. The onset of the oscillations seems to correspond to an increase in the heat transfer coefficient. Even if they provide a small increase in cooling performance, oscillations are undesirable in a rocket engine. They introduce variations in temperature and may imply hot spots and therefore thermal stress concentrations that may form single points of failure. Moreover, oscillations may lead to unstable operation of the engine and therefore a loss of performance. At the pressures experienced in the micro rocket engine, oscillations should not be an issue.

Deposits and decomposition

At high heat fluxes and pressures, the propellants may decompose and form solid deposits. This is a concern especially for hydrocarbons that have a tendency to crack and form non negligible amounts of carbon deposits. First, deposits may clog the cooling passages or injectors. Second, deposits on the walls decrease the heat transfer causing the wall temperature to increase.

2.1.3 Prediction for rocket design

Sufficient knowledge of the characteristics of the propellants is required for the future design of the micro rocket engine. The main characteristics required for the design are the physical properties of the fluid (density, viscosity, and the heat capacity), which characterize the heat transfer performance of the fluid. The *level of uncertainty* in the estimation of those parameters is an important parameter in the design of the engine.

2.1.4 Other criteria

Other criteria which must be taken into account include:

- **Material compatibility with the materials used in the engine system:** Compatibility between rocket propellants and MEMS materials has never been an issue before. Propellants must be compatible with silicon and all the materials that will be used in the components of the final liquid regeneratively cooled turbopump-fed engine.
- **Toxicity:** Toxic propellants require special facilities for handling and storage and therefore increase operational costs and the complexity of the system.
- **Storable vs. cryogenic propellants:** Storable propellants are preferred to cryogenic propellants. Cryogenic propellants require specific facilities increasing engine operation costs.
- **Availability:** Availability must be sufficient so that the engines can be readily used.

2.2 Introduction to supercritical fluids behavior

Under the very high heat fluxes and pressures experienced in the micro rocket engine, most propellants will be supercritical.

The critical point is defined by a critical pressure and temperature, which depend on the fluid. Critical conditions for some typical fluids are shown in Table 2.1. The critical pressure is the pressure that is needed to condense the fluid to a liquid at the critical temperature. Above the critical temperature the gas cannot be condensed into a liquid regardless of the pressure applied to the substance. Below this temperature, the gas is a condensable vapor. The critical point is illustrated in a (P,T) diagram in Figure 2-1.

A supercritical fluid is a fluid above its critical point, meaning above its critical pressure and temperature. In a supercritical state, there is no more phase transition between liquid and vapor. The supercritical fluid has physicochemical properties intermediate between those of liquids and gases. Its density, diffusivity and viscosity are closer to those of gases

Fluid	Pc [atm]	Tc [°C]
Water	220.9	374.14
Ethanol	62.55	242.85
JP7	17.7	400
JP10	36.8	
H_2O_2	214	457

Table 2.1: Critical point for different fluids [18] [15] [29].

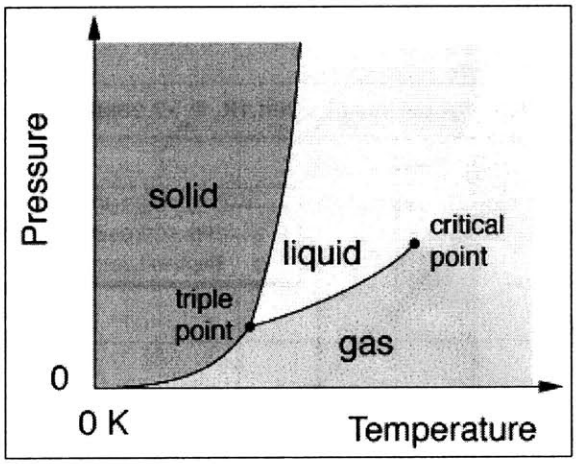

Figure 2-1: P-T diagram showing the critical point for a typical fluid [22].

whereas its solubility is closer to that of a liquid.

Supercritical fluids are characterized by rapid changes in fluid properties in the region of the critical point. Small variations in temperature can correspond to large changes in fluid properties. Density, viscosity and conductivity sharply decrease when reaching critical conditions as shown in Figures 2-2, 2-3 and 2-4. The specific heat peaks near the critical point. The temperature at which the maximum Cp is found is called the pseudo critical temperature and is usually slightly above the critical temperature.

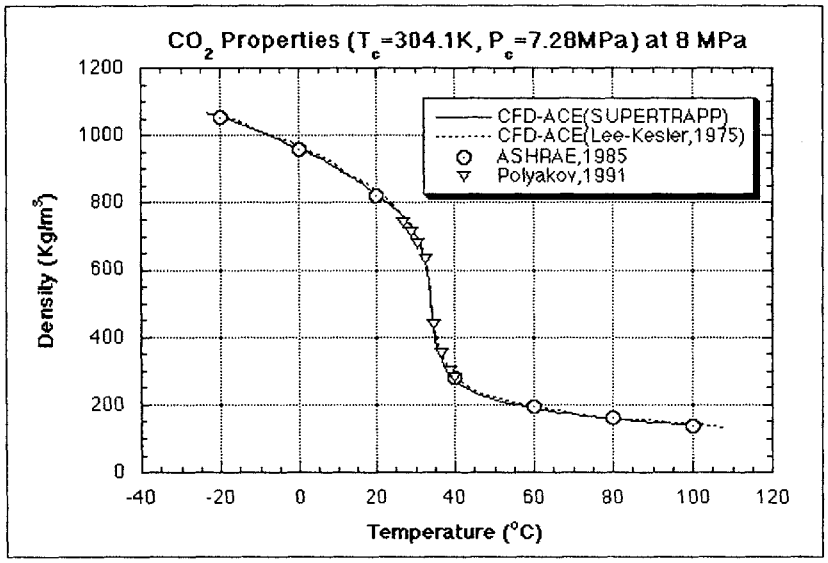

Figure 2-2: Density variation for CO_2 as a function of temperature near the critical point [11].

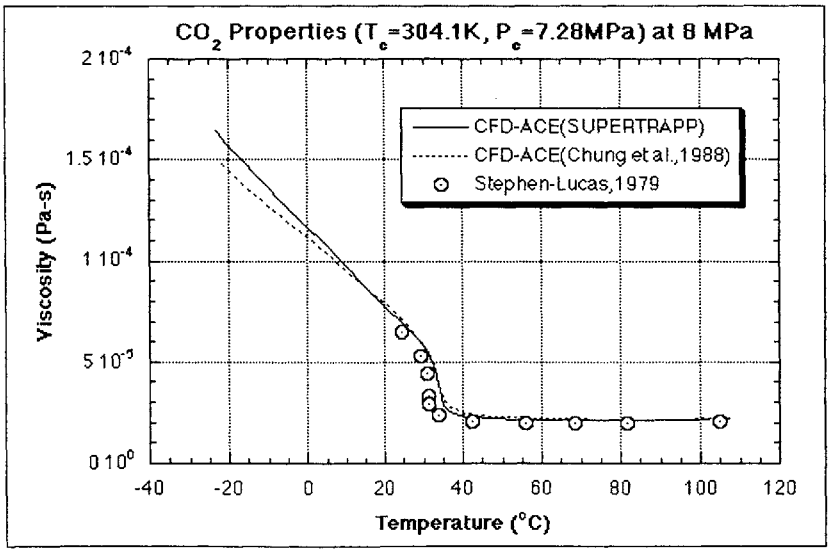

Figure 2-3: Viscosity variation for CO_2 as a function of temperature near the critical point [11].

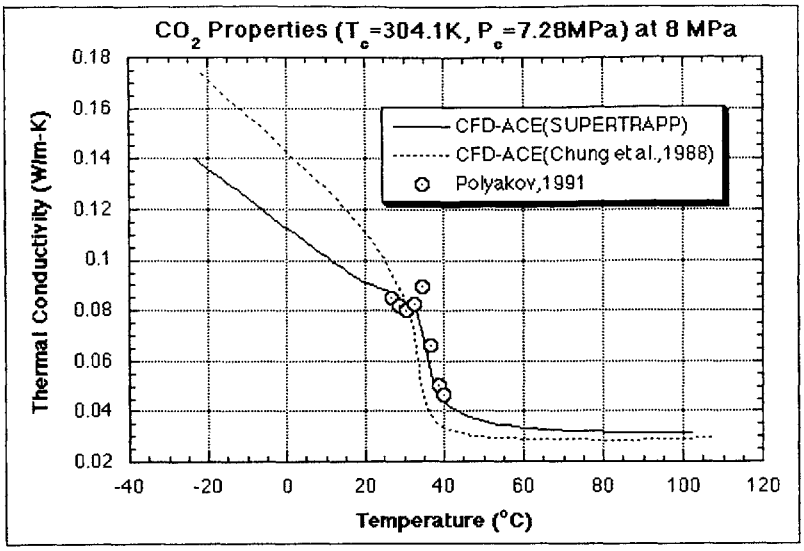

Figure 2-4: Thermal conductivity variation for CO_2 as a function of temperature near the critical point [11].

Fluids near the critical point offer an increased cooling capacity. At the pseudo temperature, Cp increases and reaches a maximum resulting in an increased fluid enthalpy and therefore an increased heat capacity. Moreover, as viscosity is decreased at supercritical conditions, turbulence is increased, which results in an increase of the heat transfer coefficient of the fluid.

All these variations in fluid properties are temperature and pressure dependent. Variations in fluid properties are less drastic as pressure increases above the critical pressure as shown in Figure 2-5 and Figure 2-6 for respectively the density and the viscosity. As pressure increases above the critical pressure, the amplitude of the peak of Cp decreases while the pseudo temperature increases and the peak widens. Figure 2-7 shows a 3D representation of the specific heat as a function of pressure and temperature. The evolution of the Cp profile as pressure and temperature are increased is illustrated in the two graphics on the upper part of Figure 2-7. As pressure increases above the critical pressure, the supercritical enhancement of heat transfer is less apparent and appears at a higher temperature.

A deterioration of the heat capacity has been seen in supercritical fluids at high heat fluxes. The heat transfer coefficient enhancement due to the supercritical phenomenon is less and less apparent as the heat flux increases above a critical heat flux. Eventually at very high

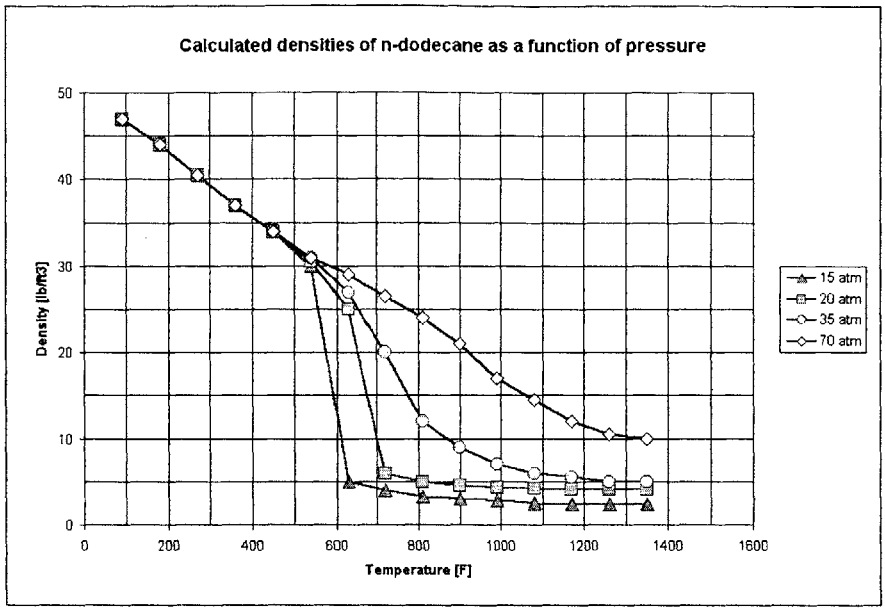

Figure 2-5: n-dodecane density as a function of temperature for subcritical, critical and supercritical pressures [11].

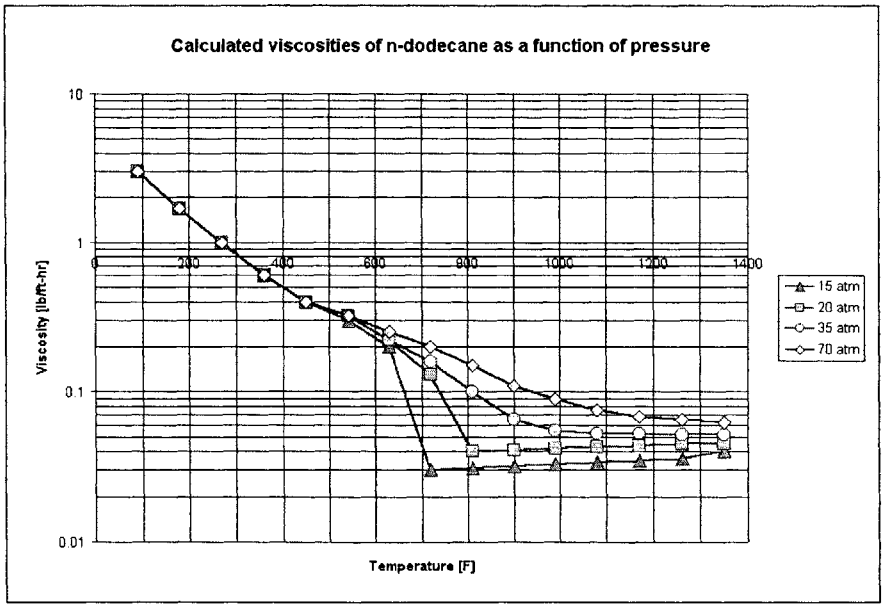

Figure 2-6: n-dodecane viscosity as a function of temperature for subcritical, critical and supercritical pressures [11].

heat fluxes, the enhancement in heat transfer coefficient is not apparent anymore and a decrease in the heat transfer coefficient is seen. For more details refer to Section 5.3.4.1.2. Supercritical fluids are sensitive to buoyancy forces. Tests in vertical macro tubes have shown a serious deterioration of the heat transfer coefficient due to buoyancy forces [9]. High mass flows seem to reduce this deterioration.

Some instabilities have been shown to appear at supercritical conditions in macro and micro scale experiments [18] [9] [8] because of the appearance of low density fluid in the flow. Even if these oscillations offer an increased heat transfer coefficient, they could be an issue in the micro rocket engine and are undesirable. They disappear at high pressure ratios.

2.3 Candidate propellants

This section lists propellants that have been considered as candidates for the micro rocket engine. A first order evaluation of their respective advantages and disadvantages is presented.

2.3.1 List of potential candidates

A first evaluation was done by Protz [27]. Cryogenic propellants were not considered since they imply a great increase in complexity, in particular for the storage and tank systems. The following propellants were selected for further study:

Fuel

- Ethanol (C_2H_6O)
- Hydrazine (N_2H_4)
- Hydrocarbons: JP7, JP10

Oxidizer

- Nitrogen tetroxide (N_2O_4)
- Hydrogen peroxide (H_2O_2)

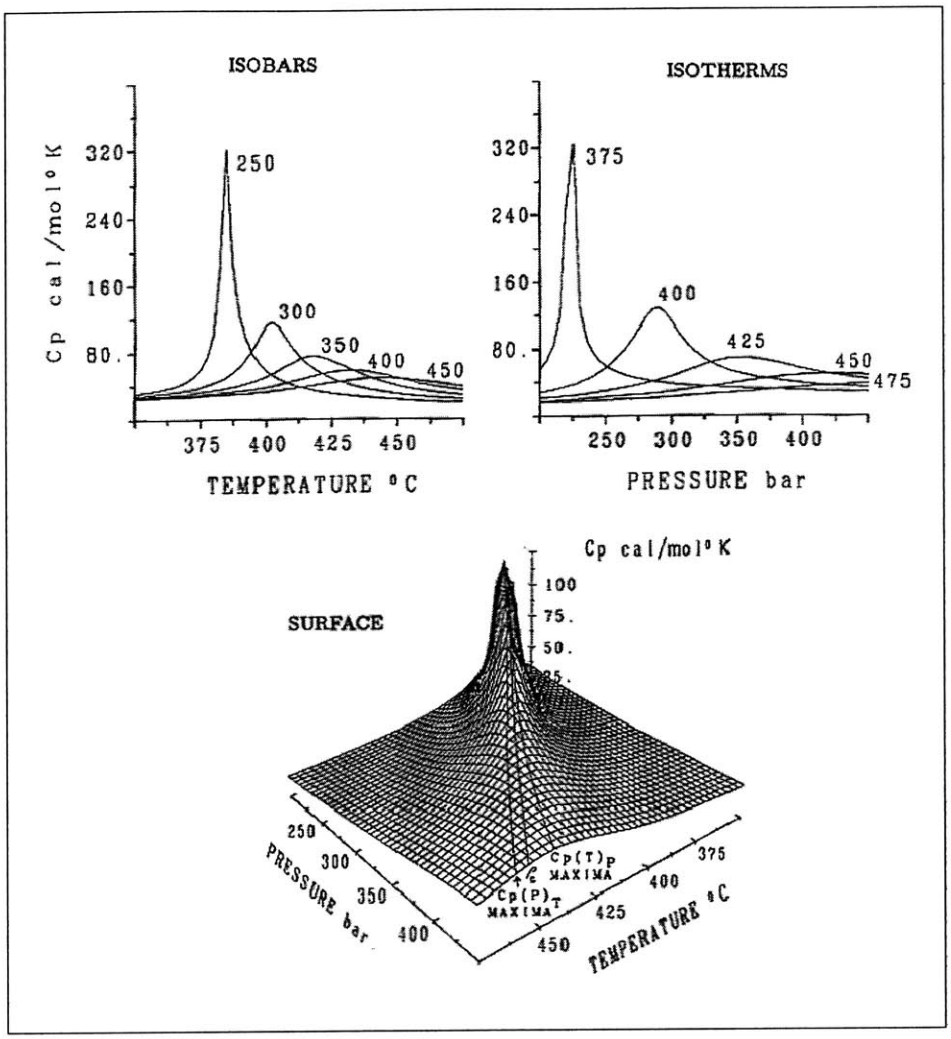

Figure 2-7: Effects of temperature and pressure on the specific heat of CO2 near the critical point [10]. *ISOBARS*: Cp as a function of temperature for different pressures. *ISOTHERMS*: Cp as a function of pressure for different temperatures. *SURFACE*: Cp as a function of temperature and pressure.

2.3.2 Performance as propellants

Combinations of the selected propellants were studied for their performance based on the specific impulse of the combination, the density specific impulse and the temperature reached in the chamber [27].

Figures 2-8 and 2-9 present the specific impulse and density specific impulse of different combinations of propellants as a function of chamber temperature. The expected Isp and

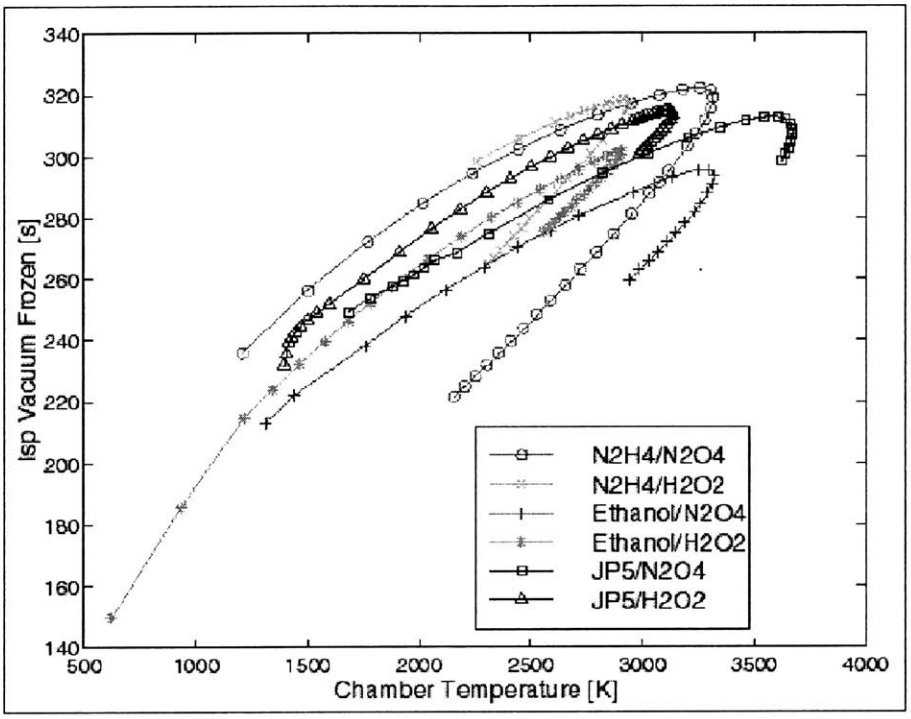

Figure 2-8: Vacuum specific impulse (Isp) as a function of chamber temperature for different combinations of propellants assuming flow chemically frozen from the throat to the nozzle exit [27].

Id obtained for different combinations of propellants for the same chamber temperature can be compared.

The combination N_2H_4/N_2O_4 offers the maximum specific impulse. Hydrazine gives the highest specific impulse closely followed by hydrocarbons. Ethanol offers lower Isp. Combinations using N_2O_4 usually offer higher Isp than those using H_2O_2 as oxidizer but the differences are small, on the order of 1 second to 5 seconds.

Hydrocarbon/H_2O_2 gives the best density specific impulse at high oxidizer to fuel ratios due to the relatively high density of H_2O_2. More generally, H_2O_2 allows higher maximum Id than N_2O_4. Id reached with ethanol are again lower than for other fuels. A more detailed

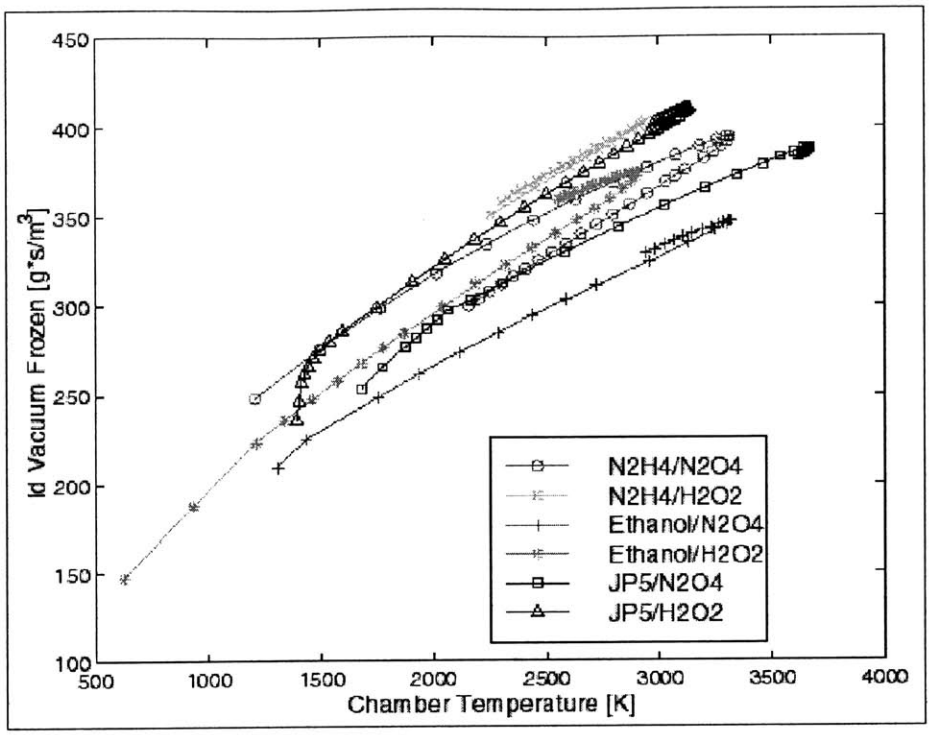

Figure 2-9: Vacuum density specific impulse (Id) as a function of chamber temperature for different combinations of propellants assuming flow chemically frozen from the throat to the nozzle exit [27].

analysis can be found in [27].

2.3.3 Capacity as a coolant

Ethanol has been tested at supercritical pressures and temperatures [24] [18]. It is currently used as a coolant in the micro rocket engine and therefore has demonstrated its suitability as a coolant for the gaseous engine. It shows a good stability and it can support the high heat loads of the chamber, its heat capacity being in the middle range of the propellants considered.

Hydrazine is commonly used as rocket engine propellant and has one of the highest heat capacities of the potential propellants. The main concern is that hydrazine may decompose at the temperatures and pressures experienced in the rocket engine. At 1 atm and 540 K, hydrazine is said to decompose when in contact with most materials [20]. If hydrazine decomposes, the oxidizer must have enough heat capacity to absorb the heat that cannot be absorbed by the hydrazine.

One of the major issues with **hydrocarbons** is their chemical stability. They tend to decompose and coke, forming undesirable carbon deposits. Hydrocarbons have a heat capacity among the smallest of the propellants considered.
JP7 is a deoxygenated hydrocarbon and therefore forms fewer carbon deposits than other hydrocarbons such as JP10. JP7 also offers the important advantage of having a higher heat capacity than fluids with similar properties, since in a certain temperature range, JP7 undergoes an endothermic decomposition which increases significantly its heat capacity. Little is known about this reaction and its study at micro scale is one of the objectives of the work presented in this thesis. It can offer great advantages for cooling. However, this reaction may cause deposits to form, may make it difficult to predict the fluid properties for the design of the engine, or may induce instabilities in the fluid which would prohibit its use in the micro rocket engine.

Nitrogen tetroxide has a high heat capacity with a high specific heat and is commonly used in macro scale rocket engines.

Hydrogen peroxide offers a good heat capacity. However, its stability and behavior at the high heat fluxes and pressures seen in the micro rocket engine is a major issue. Further tests will be required to determine the suitability of hydrogen peroxide as a coolant.

We have presented in this section an evaluation of the heat capacity of each propellant. However, we cannot decide on the suitability of a propellant as a coolant without looking at the heat capacity of the combinations of propellants. Having a sufficient heat capacity means that the total heat capacity offered by both propellants matches the heat loads in the chamber and the nozzle. The heat loads depend on the temperature reached in the chamber due to the propellant combustion. Therefore, a combination of propellants with high specific heats can be unappropriate as coolant of the rocket if the temperature produced by their combustion in the chamber gives heat loads which exceed the heat capacity offered by those propellants. Several combinations of propellants have been studied [27] including an estimation of the final temperature of the propellants as a function of the heat load generated in the chamber and the nozzle.

2.3.4 Other criteria

Some of the propellants studied are commonly used and their properties are well-known, which is an advantage for the prediction of heat loads, cooling capacity, and fluid behavior in the passages and chamber of the engine. Uncertainty in the properties could be an issue for JP7, because its endothermic reaction is not well-documented, and for hydrogen peroxide, whose stability and behavior have not yet been tested at high heat fluxes and high pressures of interest here.

Compatibility with MEMS material is not an issue with hydrocarbons and ethanol. Nitrogen tetroxide is a strong oxidizer and reacts with silicon to form a growing layer of SiO_2. This oxide then acts as a barrier, protecting the silicon surface from further oxidation. Therefore nitrogen tetroxide should be compatible with silicon devices after passivation. A similar process occurs when hydrogen peroxide is in contact with silicon. Hydrogen peroxide is used in micro fabrication and shows good compatibility with silicon. However, as a strong oxidizer, compatibility of hydrogen peroxide with other materials used in micro fabrication can be an issue. The main compatibility issue concerns hydrazine. Hydrazine is often used as an etchant in micro fabrication processes. The etch rate of 100 microns an hour prohibits its use in the rocket unless protective coatings are added in the design.

Hydrocarbons, ethanol and hydrogen peroxide benefit from not being toxic.

2.3.5 Propellant summary

Figure 2-10 summarizes the pros and cons of the different potential candidates. The toxicity of hydrazine is considered a major disadvantage. Four candidates are considered the most promising: ethanol, JP7, JP10 with hydrogen peroxide as oxidizer.

2.4 Conclusions

This chapter summarized the propellant selection process for the liquid regeneratively cooled micro rocket engine and motivated the heat transfer experiments presented in the next chapters.

The characteristics and behavior of ethanol are well known from previous heat transfer experiments [24] [18] and tests in the gaseous micro rocket device. Relatively little is known about the other propellants and the work presented in this thesis aims at characterizing

Summary of Propellants Pros and Cons for Future Application in the Micro Rocket Engine

Criteria \ Propellants			Ethanol		Hydrazine		Hydrocarbons						N2O4		H2O2	
							JP7		Jp10							
			+	-	+	-	+	-	+	-	+	-	+	-	+	-
Perfo rman				Not very high Isp	Very high Isp		High Isp		High Isp		High Isp				High Id	
Suitability as coolant	Heat capacity		Not very high heat loads	Medium heat capacity	Very high heat capacity	High heat loads	Increased heat capacity (endothermic reaction)	High heat loads		High heat loads	High heat capacity	High heat loads			Not very high heat loads	Medium heat capacity
			Coolant capacity already demonstrated in micro rocket													
	Stability		Good stability already demonstrated at micro scale		*	May decompose	*	May be oscillations due to the reaction	*	*	*	*	*	*	*	*
			No deposits				May be less carbon deposits than regular hydrocarbons	May be carbon deposits	*	May be carbon deposits					*	May decompose
For design	Predictability		Well-known properties		Well-known properties		*	May be bad due to the additional reaction	*	*	Well-known properties					Not well-known properties at heat fluxes and pressures of rocket
		Supercritical properties already tested at micro scale						Complex composition								
	Reproducibility		Good (from previous experiments at micro scale)		*		*	May be bad due to the additional reaction	*	*					*	*
								Problem of reproducibility from one patch to another since complex composition	Less complex product, less of a problem from one patch to another							
Others	Compatibility		Very good			Film protection required for silicon compatibility	Very good		Very good		Oxide layer imply compatibility with silicon				*	May have compatibility issues
	Commonality	Toxicity	Non Toxic			Toxic	Non toxic		Non toxic				Toxic		Non Toxic	
		Easy supply		Easy supply, common propellant				Difficult supply (military fuel)		Difficult supply	Easy supply				Easy supply	
		Easy handling			Handling with care		Easy handling		Easy handling				Handling with care		Handling of a non toxic product	Handling with care
		Easy storage		Easy storage		Easy storage		Easy storage					Storage with care			Storage with care

Figure 2-10: Summary of the pros and cons of the different selected propellants. The darker color identifies the issues that will be addressed in the current thesis. * identifies issues still not addressed.

their cooling performance and their behavior. The heat transfer experiments will mainly focus on:

- the endothermic behavior of JP7 and its consequences on the stability, the properties and the behavior of JP7
- the behavior of JP10 in supercritical conditions and a comparison of JP7 and JP10 characteristics
- compatibility issues associated with the use of hydrogen peroxide in the micro rocket engine

Chapter 3

Description of the experiment

The heat transfer experiment has been designed to test fluids in horizontal micro channels under high heat fluxes and pressures. The heat transfer coefficient of the fluid is calculated from the measurement of the outside wall temperature. The stability of the fluid can also be studied. In this chapter, the principle of the heat transfer experiment is explained. The experimental apparatus and the reduction data method are presented. The limits of the assumptions and the experimental uncertainties are rapidly described.

3.1 Principle of the experiment

The propellant tested is run through a horizontal, electrically heated stainless steel micro tube, about 95 microns inside diameter and 300 microns outside diameter. A constant heat flux is applied to the fluid. The pressure across the tube, mass flow and heat flux are set. From the measurement of the outside wall temperature of the tube, the inside wall temperature, the bulk temperature and the heat transfer coefficient are estimated, therefore characterizing the heat capacity of the fluid. Long duration tests are done to study the stability of the fluid. The experiment was designed to be capable of conducting tests at very high pressures and heat fluxes in order to closely reproduce the conditions experienced by the coolant in the micro rocket engine.

3.2 Justification of heat transfer experiments

As discussed in previous chapters, the main issues are first to characterize the physical properties of the propellants tested (heat capacity, stability, behavior) and second to predict parameters needed for the design of the micro rocket engine.

The following section presents how the heat transfer experiments address the issues of propellant selection for the micro rocket engine.

3.2.1 Characterization of the propellant

- To study the heat capacity of the fluid, we are interested in studying both the heat transfer coefficient h and the enthalpy profile of the fluid H_{fluid} as a function of temperature T. The goal is to estimate their value and to study their evolution as a function of the fluid pressure (P), mass flow ($\dot{m}$), heat flux (q) and passage size (D). Some additional parameters that can help characterize the heat transfer properties of the fluid are the nondimensional Stanton number (St), the Nusselt number (Nu) and the Prandtl number (Pr).

Heat capacity	
Parameters studied	$h\,(P,T,q,\dot{m},D)$, $H_{fluid}\,(P,T,q,\dot{m},D)$
Related nondimensional parameters	St, Nu, Pr

- Oscillations occurring in the fluid are noticeable by oscillations of either the temperature or the pressure. They can also be noticed by the specific sound they produce in the tube, the type of noise being also a qualitative measure of the frequency of the oscillations.

Oscillations	
Parameters studied	$T(t)$ or $P(t)$

- Solid deposits are a concern if they clog the passages or if they cause hot spots on the wall by decreasing the heat transfer at the wall. If significant deposits occur in the tube, they will partially clog the passage and as a consequence the mass flow ($\dot{m}$) through the tube should decrease with time. Solid deposits may also reduce the heat

transfer to the wall and cause the temperature to significantly increase. Therefore the occurrence of deposits was studied by recording the temperature profile and the variation in mass flow at constant pressure drop across the tube.

Deposits	
Parameters studied	$\dot{m}$(t), $T(t)$

3.2.2 Prediction for the future design of the liquid regeneratively cooled rocket engine

- Reproducibility of the experiments is studied by comparing the temperature profile, heat transfer coefficient, St obtained for different tests at the same conditions of pressure, heat flux and mass flow.

Reproducibility	
Parameters studied	T, h
Related important parameter	St

- The design of the micro rocket engine requires a good knowledge of the characteristics and properties of the fluids. Viscosity (μ), density (ρ), conductivity (κ) and specific heat (Cp) must be estimated. The experiment is not designed to measure accurately the properties of the fluid tested. However, the design process relies on evaluations given by heat transfer correlations and the results of the heat transfer experiments offer the opportunity to validate the estimation of the properties and the suitability of those correlations.

Fluid properties	
Parameters studied	Nu, h

3.3 Experimental apparatus

3.3.1 Test section

The test section is a U shaped 304 stainless steel tube fabricated by MicroGroup, Inc as shown in Figure 3-1. A 10 mm long - 300 micron outer diameter - 95 micron inner diameter

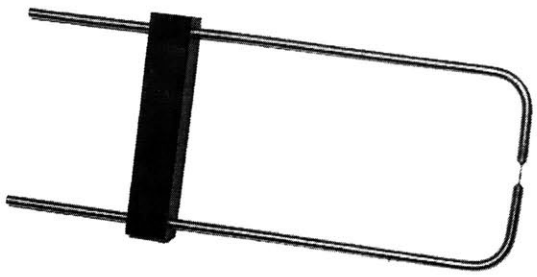

Figure 3-1: Micro test section used for the heat transfer experiments.

tube is silver soldered into a larger 1/16" tube. 3 mm of this micro tube is inside the larger tube on each side. Only the 4 mm in the center of the micro tube are visible and accessible for measurements. This allows the flow to develop in the micro tube before measurements are taken.

The micro tube being very fragile, a plastic piece was added to provide mechanical support to prevent the micro tube from being bent or broken in handling of the test section. Swagelok connections are used to easily connect a new test section to the rig. The test section has been found to resist high pressures up to 3,000 psi and temperatures up to 600°C. Above 600°C, the test section starts deforming, changing color and eventually fails.

In order to test the effect of the passage size on the heat transfer capacity of the fluid, one 190 micron inner diameter tube was also tested.

3.3.2 Test rig

The test rig is composed of two parts: the test apparatus located in the micro rocket test cell and the control system located in the control room. The first group includes all the hardware necessary for the test whereas the second is the data acquisition system. All controls are located in the control room so that experiments can be carried out without human intervention in the micro rocket test cell. Figure 3-2 shows a view of the control room.

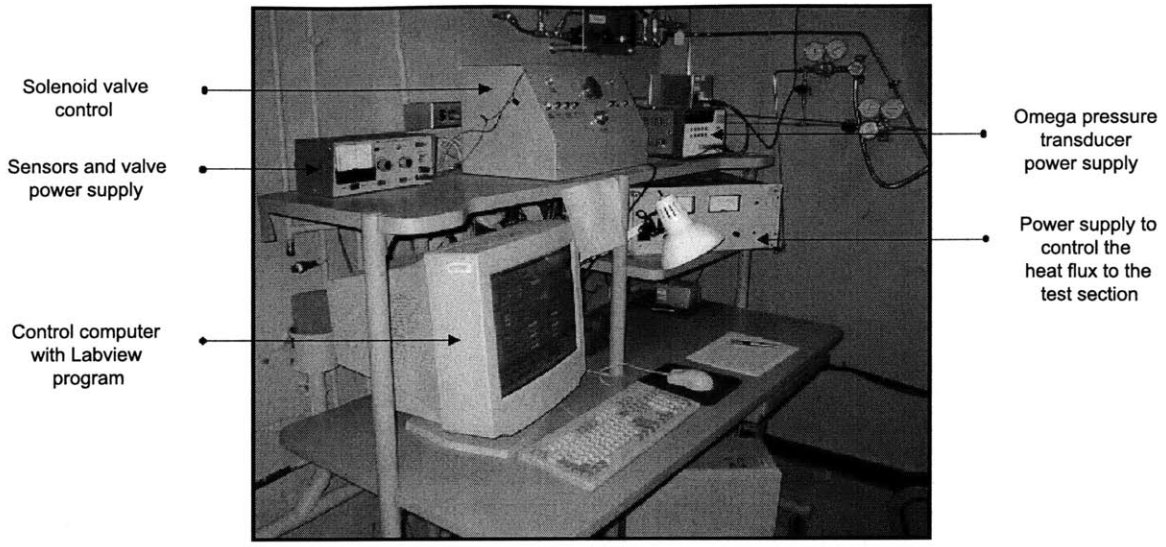

Figure 3-2: View of the control room.

3.3.2.1 Test apparatus

The test apparatus, shown in Figure 3-3, is located in the micro rocket test cell, which is designed to be safe for explosive experiments. The apparatus is designed to run a fluid through a micro test section and control heat flux, mass flow and pressure across the rig. The test rig is rated up to 6,000 psi. A schematic is shown in Figure 3-4.

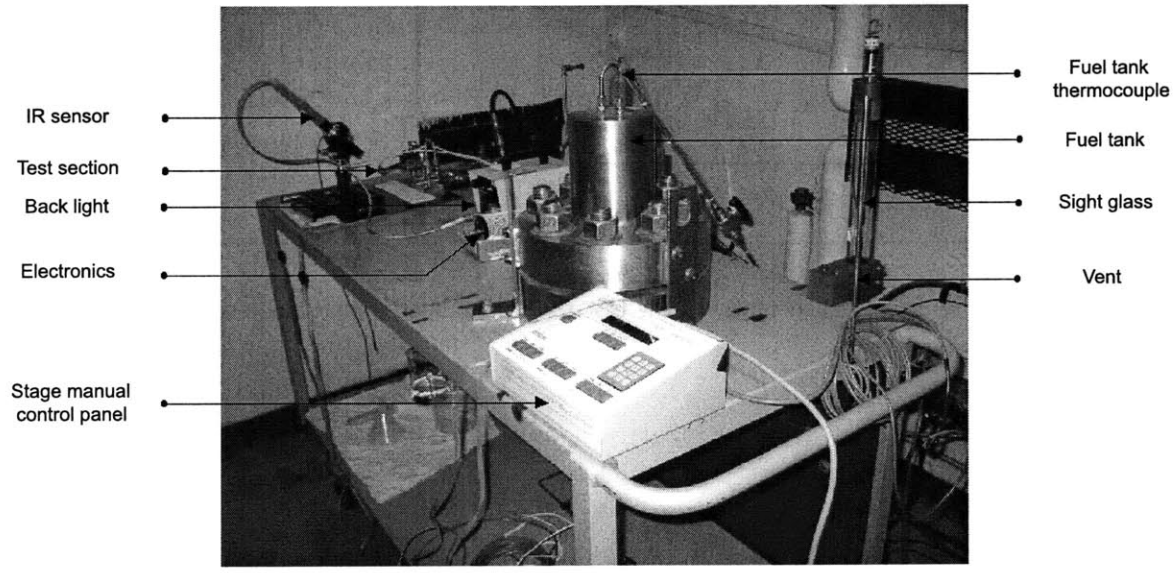

Figure 3-3: View of the test apparatus in the micro rocket test cell.

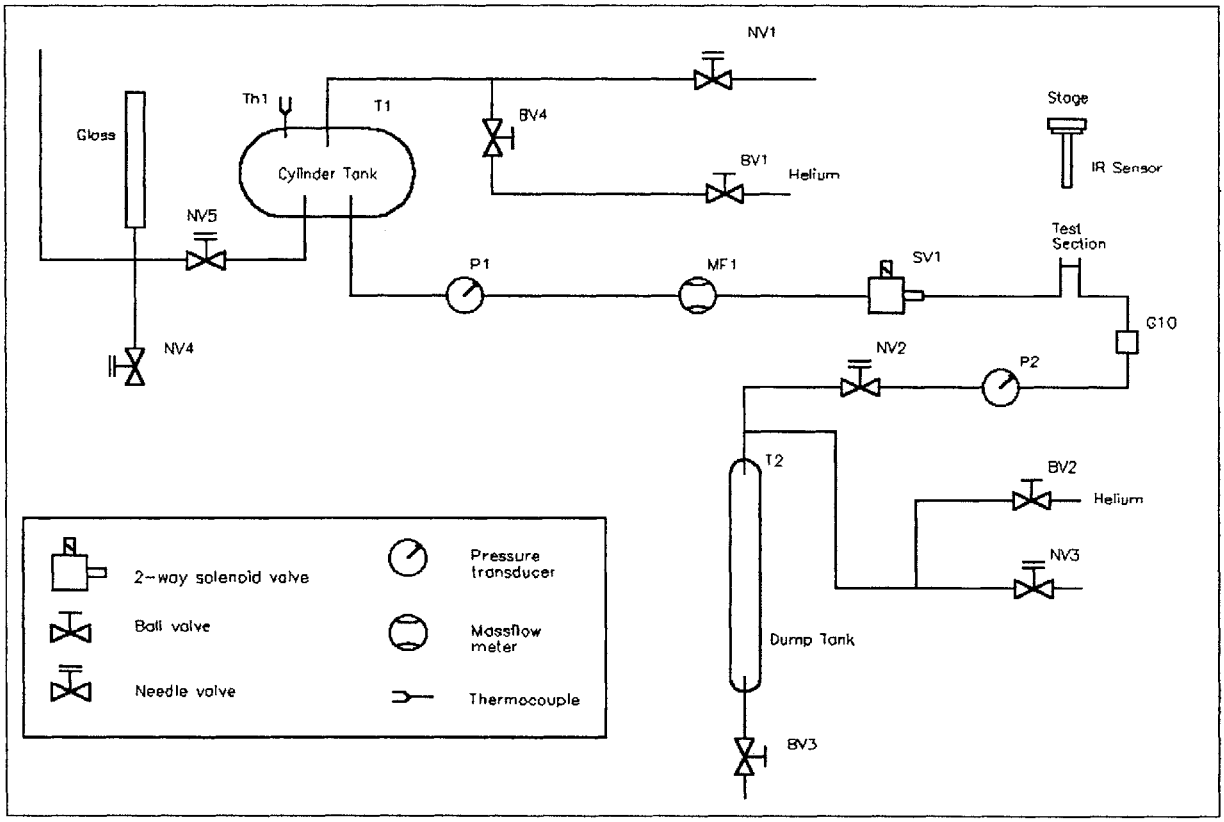

Figure 3-4: Schematic of the test rig for the heat transfer experiments.

Fluid circuit

The fluid is stored in the fuel tank, a stainless steel cylinder rated for 6,000 psi. The tank is filled via a sight glass downstream the tank. This system offers a way to check the level of fluid in the tank when the rig is depressurized. The fluid is injected in the sight glass with a plastic syringe, air being relieved via the vent line.
The flow through the rig is controlled via a solenoid valve situated between the fuel tank and the test section. The valve is remotely controlled from the control room. Once the valve is opened and the tank pressurized, the fluid runs through the piping, then through the test section before being collected in the dump tank downstream the rig. The mass flow is controlled by adjusting the pressure drop across the test section. A 2 micron filter upstream the test section prevents contaminants from reaching and clogging the test section.

Helium circuit

In order to control the mass flow going through the test section and the pressure at the mid point in the test section, both the fuel tank and the dump tank are pressurized. The fuel tank and the dump tank helium circuits are controlled separately by two regulators hooked up to a pressure 6,000 psi helium bottle.

Heating system

The test section is electrically heated via two copper electrodes which are attached prior and after the micro test tube on the U shaped 1/16" tube as shown in Figure 3-5. A voltage is applied across the electrodes by a Hewlett-Packard 1,000 W DC power supply, which can deliver high currents and low voltages. It was set to deliver constant current during experiments to reduce the variation of the heat flux when measurements were taken. The heat flux applied to the test section can be chosen and controlled. The system upstream the test section was chosen to be connected to the ground, therefore, the system downstream the test section must be insulated. A G10 fiberglass block is used as an insulator along the flow path after the test section. It is pressed between two steel plated to prevent it from delaminating at high pressures. Figure 3-6 illustrates the test section and the resistive

heating system. The temperature sensor is also shown on the schematic.

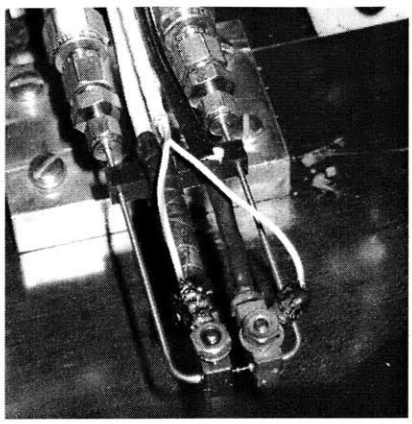

Figure 3-5: Electrodes attached to the micro test section.

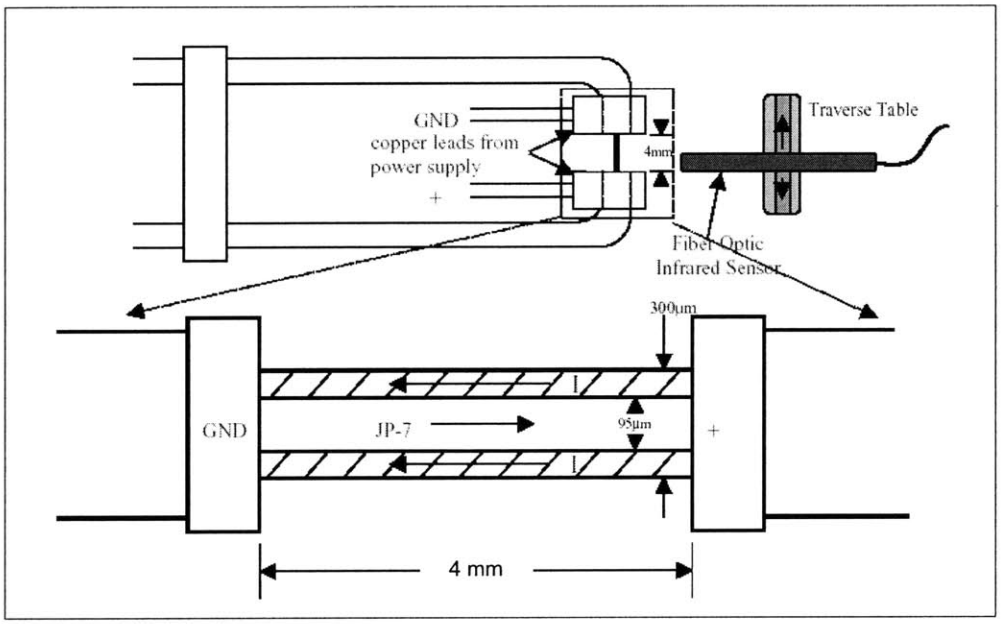

Figure 3-6: Schematic of the test section and the heating system.

3.3.2.2 Test section temperature measurement

In previous experiments carried out with water and ethanol [24] [18], 3 thermocouples were welded to the micro test section at the entrance, the mid point and the exit of the micro tube. The voltage applied across the tube caused some perturbations in the thermocouple reading. Therefore, an Omega Infrared Sensor has been used to remotely measure the outside wall temperature along the test section. The sensor aims at a 100 micron diameter spot. The

energy radiated from the spot is absorbed and integrated before being transmitted through a fiber optic chord to a spectrometer. The analog signal produced then goes into the data acquisition board. The temperature is calculated using a calibration relation. The sensor has a 5 ms response time and can measure temperatures from 330°C to 2,000°C.

The Omega Infrared Sensor has four components: the IR sensor, the electronics cylinder, the back light power supply box and the power supply. The IR sensor, a 15 cm long thin black cylinder, must be pointed towards the surface of which we want to measure the temperature. A fiber optic line connects this sensor to the electronics. The analog signal is generated inside the electronics. The back light is a way to precisely point the IR sensor at the surface to be measured. Before measuring the temperature, the IR sensor spot must be checked for aiming at the right surface. To make this process easier, the fiber optic can be removed from the electronics (while the sensor is turned off) and connected to the back light power supply. A light replaces the IR spot and identifies where the measurement is taken. The pointing of the IR sensor is a critical step and must be done very carefully. The temperature measurement, since it integrates over the entire spot, is very sensitive to the pointing of the sensor.

To calibrate it, the sensor was aimed at the weld of a stainless steel thermocouple. The thermocouple was heated with a propane flame up to 1,800°C. While the thermocouple was cooling down, the temperature reading from the thermocouple and the voltage reading from the IR sensor were recorded.

In order to measure the outside wall temperature along the entire micro tube, the IR sensor is mounted on a remotely controlled Oriel linear stage. The velocity of the stage, the size of the steps, the number of steps, the direction of motion can be controlled via a control board or a computer. Figure 3-7 shows the experimental set up with the temperature sensor.

3.3.2.3 Other measurements

The **temperature in the fuel tank** is measured with a K-thermocouple and is assumed to be the temperature of the fuel at the entrance of the tube.

A Kulite pressure transducer measures the **pressure at the exit of the fuel tank** prior to the test section (Pressure P_1). An Omega pressure transducer measures the **pressure at the entrance of the dump tank** downstream the test section (Pressure P_2). Pressure

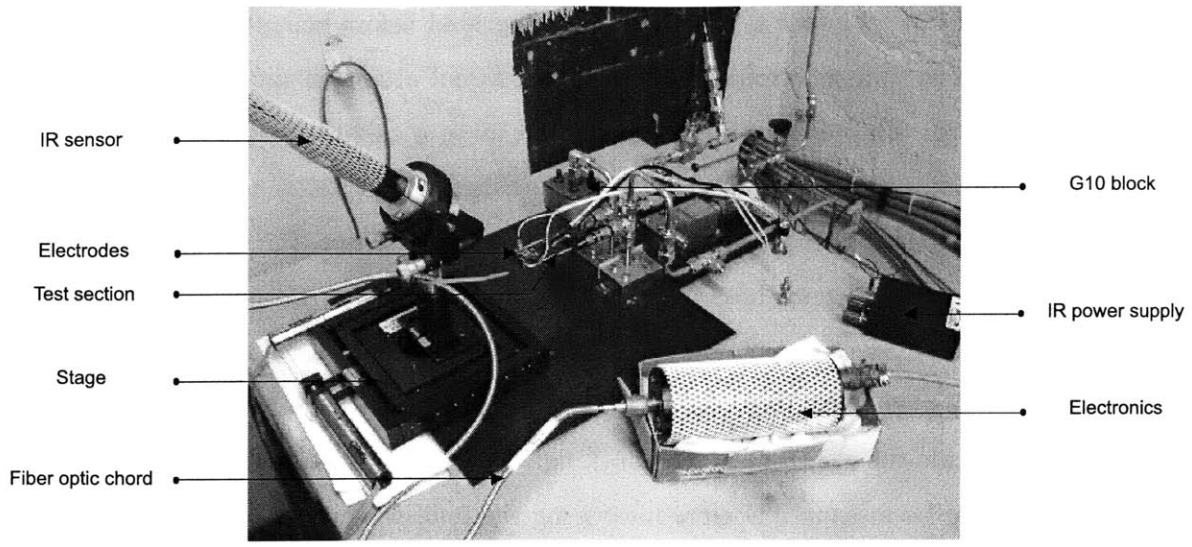

Figure 3-7: Experimental set up and temperature measurement using the IR sensor.

losses in the 1/4" piping are assumed to be small compared to the pressure losses across the test section. Therefore, P_1 is assumed to be the pressure at the entrance of the micro tube and P_2 the pressure at the exit of the micro tube. Pressure is not measured in the test section. A linear profile of pressure is assumed along the tube. The test pressure considered in the calculation for the reduction of the data is the average pressure:

$$\overline{P} = \frac{P_1 - P_2}{2} \tag{3.1}$$

Both pressure transducers have been calibrated using a pressure gauge. 5,000 psi pressure transducers are used.

The **mass flow** is measured using a high pressure factory-calibrated Micro Motion D6 mass flow meter.

Voltage and current are measured to determine the power delivered to the test section. Voltage is directly acquired from the voltage reading of the power supply. Current is measured using the voltage drop across a metal shunt of known resistance [18].

3.3.3 Data acquisition

The acquisition system uses a National Instruments acquisition board. All the sensors are wired to a separate channel, which acquires their output voltage and sends them to the computer used to control the experiment. A Labview program has been written to both control the experiment and display, organize and record the data.

3.3.3.1 Display of the data

The data are displayed on the screen, including pressures P_1 and P_2, mass flow, tank temperature, voltage and current. The heat flux, as the product of the current and the voltage, also appears. The temperature read by the IR sensor is both displayed as a numeric value and plotted as a function of time. The frequency at which the data are refreshed can be chosen. It usually was set at 2 Hz. Figure 3-8 shows a screen shot of the Labview interface.

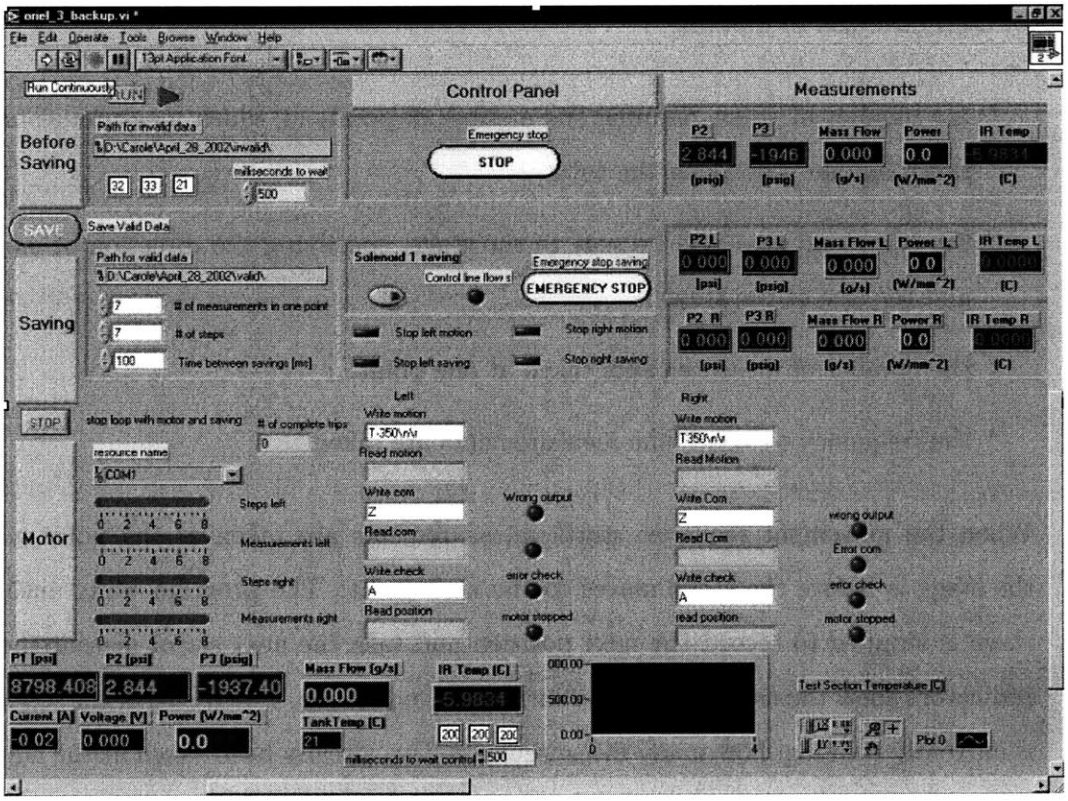

Figure 3-8: Screen shot of the Labview interface.

3.3.3.2 Control of the experiment

The Labview program allows control of the experiment from the control room.

Valve control The solenoid valve can be actuated from the Labview console and an indicator turns green when the fluid can flow. The run button must be switched on to have access to the control of the valve.

Stage control The program defines the sequence of the IR sensor scanning. Measurements can be taken at one point, or at different positions along the tube by moving the stage along the tube. Measurements are always taken while the stage is stopped. A set of measurements is taken at each stop of the stage.

There are two sets of commands: one for the left motion, one for the right motion. Commands can be different for each. The following parameters define the sequence for each direction of motion:

* the number of steps, defining the number of points at which measurements are taken on one pass along the tube
* the command that will be sent to the stage, specifying the direction of motion and the size of the steps
* the number of measurements taken at one point
* the frequency at which the measurements are taken

When the movement sequence starts, measurements are taken at the point where the stage is before the stage moves to the next point. The program waits until the stage is stopped to record the next position and take the next set of measurements. Indicators allow the user to know the current stage position, which step of the sequence is currently running, how many measurements have already been taken at the current position, the current state of the stage (moving, stopped or error) and the number of passes completed. Measurements at a single point are also possible by modifying the command sent to the stage.

3.3.3.3 Data handling and recording

From voltage to engineering data The calibration equations are coded in the program so that voltages from the sensors are converted into engineering data. Calibration coefficients can be modified in the subprograms.

Recording A run is divided in two different steps. When the program is started, the stage is stationary until the user pushes the save button. This allows the user to precisely set the conditions of the experiment and wait until the measurements are stabilized to take valid data. The stage then follows the defined sequence and measurements are taken. However, it was chosen to save all the data. Therefore, two text files are generated for each run, one contains the *invalid data* as the data recorded before the sequence is started, the other contains the *valid data* recorded during the sequence. The name and path of each output file can be specified on the Labview console. All the data are recorded as well as the time at which each measurement is taken. One line of the output file corresponds to one measurement, reporting the following data:

* the time at which the measurement is taken, in the following format: year, day of the year, hour, minute and second
* the useful data, in the following format: test section temperature, heat flux, mass flow, P_1, P_2, tank temperature
* the voltage readings: IR voltage, Kulite transducer voltage, Omega transducer voltage
* the position of the measurement

3.3.4 Experimental procedure

The main experimental steps are briefly presented in the following paragraph. The test rig is depressurized prior to the experiment and all valves are closed. The positions of the valves for each operation are listed in Figure 3-9.

1. Fuel tank level: The level of fuel in the tank is checked prior to the pressurization of the test rig.

2. Fuel tank fill: The fuel tank is filled if necessary prior to pressurization of the test rig.

Summary of the position of the valves for different operations

Operation \ Valve #	BV1	BV2	BV3	BV4	NV1	NV2	NV3	NV4	NV5	S 1
Fuel tank level check	■	■	■	■	○	■	■	■	○	■
Fuel tank refill	■	■	■	■	○	■	■	■	○	■
Tank pressurization	○	○	■	○	■	■	■	■	■	■
Before test	○	○	■	○	■	○	■	■	■	■
Run test	○	○	■	○	■	○	■	■	■	○
After test	○	○	■	○	■	○	■	■	■	■
Rig depressurization	■	■	■	■	○	○	○	■	■	■
Empty dump tank	■	■	○	■	■	■	○	■	■	■
Empty fuel tank	■	■	■	■	○	■	■	○	○	■
Empty rig	■	■	○	■	○	○	○	○	○	■

■ Valve closed
○ Valve open

Figure 3-9: Summary of the position of the valves for the different steps during the heat transfer experiments.

3. Test section set up: The swagelok connections are prepared on the new test section and the test section is mounted on the rig. The electrodes are attached to the test section. Then the IR sensor is aimed at the test section. The pointing is checked along the tube and the zero position of the stage is set at the beginning of the tube.

4. Stage preparation: The stage is reset to the zero position and turned online for remote control.

5. Controls online: In the control room, the chassis power, the main power button and the pressure transducers' power supplies are turned on. The sequence of the experiment is defined in the Labview console before the Labview program is run.

6. Pressurization: The helium bottle is opened and the regulators are both set to the desired pressures to give the desired mass flow and average pressure in the test section.

7. Measurements: Labview has started recording the data in the invalid output file as soon as the program starts. The solenoid valve is then opened to let the fluid flow through the test section. The Hewlett Packard power supply is turned on. Current and voltage are set to get the desired heat flux. Once the parameters seem stabilized,

the *Save* button can be pushed to start recording the data in the valid output file.

8. End experiment: Once the data are recorded, the Hewlett Packard power supply is turned off and the solenoid valve is switched off. By pushing the stop buttons in the Labview program, the data are saved and the program is terminated. The name files on the Labview console must be changed so that the data files are not overwritten. The Labview program may be run again to monitor the parameters while setting up the next experiment or depressurizing the test rig.

3.4 General data reduction

3.4.1 Measured parameters

From each experiment, we have access to:

- general experimental conditions: mass flow, pressure, pressure drop across the tube, voltage and current applied to the test section, temperature of the fluid in the fuel tank

- at each point of measurement: the measured outside wall temperature, the position of measurement along the tube and the time at which the measurement was taken.

From these, we can derive the power delivered to the test section, the inside wall temperature, the bulk temperature, the heat transfer coefficient and, using the properties of the fluid, some useful dimensionless numbers as the Stanton number, the Reynolds number and the Nusselt number which will be useful in our analysis.

3.4.2 Power

The power Q delivered into the test section is simply a function of the current I and the voltage V applied.

$$Q = I\,V \tag{3.2}$$

where Q is power expressed in Watts, I the current in Amps and V the voltage in Volts. It was assumed that the contact between the electrodes and the test section was good enough so that electrical losses are negligible.

3.4.3 Bulk temperature

The bulk temperature at a position X along the tube is defined as the temperature that the fluid would have if the temperatures were uniform in the cross section at that position.
The bulk enthalpy at the fractional distance x of the tube is deduced from an energy balance between the entrance and the cross section of the tube at that point. Longitudinal conduction along the tube is assumed to be negligible compared to convection transfer and radial conduction. Moreover, we assume that there is no heat loss towards the 1/16" tube. Therefore, we assume in the calculation that all the power produced by the electrical heating is absorbed by the fluid and used to increase its enthalpy.

$$\dot{m}\,(H_b(x) - H_b(0)) = Q\,x \tag{3.3}$$

$$H_b(x) = H_b(0) + \frac{Q\,x}{\dot{m}} \tag{3.4}$$

where H_b represents the bulk enthalpy, Q the power in Watts, x the fractional distance defined as the ratio between the position and the total length of the tube and $\dot{m}$ the mass flow in kg/s. Since the temperature of the fluid at the entrance of the tube is assumed to be the fuel tank temperature, the enthalpy at the entrance of the tube is found from an enthalpy diagram as the enthalpy corresponding to the fuel tank temperature at the pressure considered.
The bulk temperature $T_b(x)$ along the tube can be deduced from the bulk enthalpy using an enthalpy diagram showing the enthalpy as a function of temperature at the pressure considered.

3.4.4 Inside wall temperature

The inside wall temperature is calculated from the measured outside wall temperature using the energy dissipated by the electric field. The electric field and therefore the current flowing through the tube are assumed constant.
Let's take the control volume shown in grey in Figure 3-10. we consider the volume delimited by the outside surface, the surface at a distance r from the center axis and the cross sections at point X and $X + dX$. In the steady state problem, all the heat dissipated by the electric field in this volume is conducted radially towards the center since we assume no longitudinal conduction. Therefore the energy conducted radially through the surface at a distance r

from the center axis must equal the energy dissipated by the electric field in the control volume. The energy conducted is given by the expression:

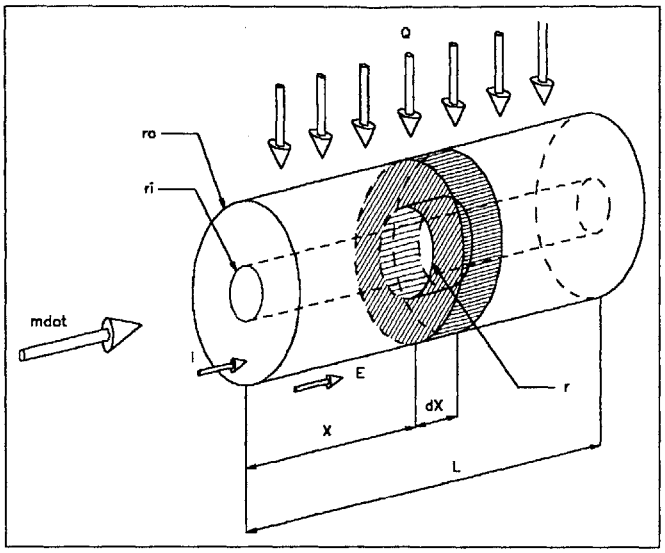

Figure 3-10: Schematic of the micro test section.

$$q_{conduction} = 2\pi r\, \kappa_{ss} \left.\frac{dT}{dr}\right|_r dX \tag{3.5}$$

where $q_{conduction}$ represents the energy conducted, r the radial distance from the center axis, κ_{ss} the electric conductivity of 304 stainless steel, T the temperature distribution and dX a small distance along the axis.

The energy dissipated by the electric field is given by:

$$q_{dissipated} = dX \int_r^{r_o} \frac{\sigma E^2}{2} 2\pi r\, dr \tag{3.6}$$

where $q_{dissipated}$ is the energy dissipated by the electric field, dX is a small distance along the axis, r is the radial distance from the center axis, r_o is the tube outer radius, E the electric field and σ is the dielectric constant of the 304 stainless steel which is assumed constant in this model.

Therefore, we get the following equation:

$$r\kappa_{ss} \left.\frac{dT}{dr}\right|_r = \int_r^{r_o} \sigma E^2 r\, dr \tag{3.7}$$

The conductivity of stainless steel increases with temperature. A linear profile is assumed for this calculation:

$$\kappa_{ss} = 0.0152\,T + 14.2444 \tag{3.8}$$

where κ_{ss} is the conductivity of stainless steel in W/mK and T the temperature expressed in °C.

From equations 3.7 and 3.8, we get:

$$r\,(0.0152\,T + 14.2444)\,\frac{dT}{dr}\bigg|_r = \int_r^{r_o} \sigma E^2 r\,dr \tag{3.9}$$

Since E and σ are assumed constant, the variables can be separated and the equation integrated to get:

$$\frac{0.0152}{2}\,T^2 + 14.2444\,T = \frac{\sigma E^2}{2}\left(r_o^2\,lnr - \frac{r^2}{2}\right) + A \tag{3.10}$$

where A is a constant determined by the following boundary conditions:

$$for \quad r = r_o, \quad T = T_o \tag{3.11}$$

$$for \quad r = r_i, \quad T = T_i \tag{3.12}$$

$$\tag{3.13}$$

where the subscript o refers to outside wall conditions and i to inside wall conditions.

The final expression for the inside wall temperature can be expressed from equation 3.10 where A has been replaced by its expression as a function of T_i and T_o:

$$T_i = -937.13 + 65.79\,\sqrt{202.90 + 0.0304\,B} \tag{3.14}$$

with

$$B = -\frac{Q}{2\pi l}\left[\frac{ln\frac{r_o}{r_i}}{1-(\frac{r_i}{r_o})^2} - \frac{1}{2}\right] + 0.0076\,T_o^2 + 14.2444\,T_o \tag{3.15}$$

where Q is the power in Watts, l is the micro tube length in m, r_o is the tube outside diameter in m, r_i is the tube inside diameter in m and T_o is the outside wall temperature in °C.

3.4.5 Heat transfer coefficient

The heat transfer coefficient is expressed from the difference between the inside wall temperature and the bulk temperature:

$$h = \frac{Q}{A_i\,(T_i - T_b)} \tag{3.16}$$

where Q represents the power delivered to the test section in Watts, A_i the inside wall surface in m^2, T_i the inside wall temperature in °C (see equations 3.14 and 3.15) and T_b the bulk temperature in °C.

3.4.6 Non dimensional number: St

The Stanton number is a useful non dimensional number for heat transfer studies. It offers a way to eliminate some biases introduced by the Reynolds number and the fluid flow. St is directly related to the inside wall and bulk enthalpies. The Stanton number is defined as:

$$St = \frac{Q}{\rho u A_i \, Cp \, (T_i - T_b)} \tag{3.17}$$

where St represents the Stanton number, Q the power delivered to the test section in Watts, ρ the fluid density in kg/m^3, u the fluid velocity in $m.s^{-1}$, A_i the inside wall surface in m^2, Cp the fluid specific heat in J/kg.K, T_i the inside wall temperature in °C and T_b the bulk temperature in °C.

From

$$\dot{m} = \rho u A_e \tag{3.18}$$

where A_e refers to the cross section area of the tube, we can express the Stanton number as:

$$St = \frac{Q \, A_e}{\dot{m} A_i \, Cp \, (T_i - T_b)} \tag{3.19}$$

The characteristics of supercritical fluids are very sensitive to the temperature and can vary significantly across a small range of temperatures. Therefore, the specific heat at the inside wall temperature and at the bulk temperature are in most cases significantly different. Therefore, to avoid the issue of selecting at which temperature the specific heat is taken to express the Stanton number, we will calculate St directly from the enthalpy values:

$$St = \frac{Q \, A_e}{\dot{m} A_i \, (H_i - H_b)} \tag{3.20}$$

where H_i represents the fluid enthalpy at the inside wall temperature in J/kg and H_b the fluid enthalpy at the bulk temperature in J/kg.

The structure of the reduction data programs is presented in Appendix B.

3.5 Different experimental procedures

Two different types of experiments have been carried out:

- **Measurements at constant heat flux along the tube**: This corresponds to most of the experiments done. Pressure, mass flow and heat flux are fixed during the

experiment. The stage is commanded to run back and forth three times along the tube. In most of the experiments, measurements are taken at 8 points along the tube, separated by 350 microns each. At each stop of the stage, measurements are taken every 100 ms with a total of 7 measurements in each point on each pass of the stage. The redundancy in the measurements offers a way to check for the reproducibility of the measurements. In the analysis, an average value of all the measurements taken at one point is considered.

- **Stability measurements**: Stability was studied by monitoring the evolution of the mass flow during experiments that lasted more than 10 minutes. Pressure and heat flux are hold constant, while the outside wall temperature and the mass flow are recorded in one point.

3.6 Experimental issues and errors

Some experimental limitations inherent to the design of the experiment are presented. Moreover, different sources of errors can be identified. A distinction can be made between the consequences of uncertainties inherent to the experiment and the issue of the validity of some model assumptions. This section refers to general issues applicable for every fluid tested. Specific issues linked to the tests or the models developed for a particular fluid will be addressed in the chapter dedicated to this fluid. A more detailed uncertainty analysis is presented in Appendix C.

3.6.1 Experimental limitations

The main limitations on the conditions tested come from the resistance of the test section. The test section can withstand high pressures but cannot withstand very high temperatures. Therefore, mass flow and heat flux must consequently be adapted to keep the temperature below 600°C for long tests with possible short periods where the temperature goes up to 800°C.

The temperature sensor imposes a low level limitation on the measurement of the temperature. The temperature sensor cannot measure temperatures below 330°C. The temperature along the tube may drop below this limit and not be recorded during the test. Conditions must be adapted so that temperature is kept above 330°C.

Finally, pressure is regulated to stay constant in the fuel tank and the dump tank. Therefore, pressure oscillations within the fluid cannot be observed in this experiment.

3.6.2 Experimental uncertainties

3.6.2.1 Test Section

The tube diameters can range from 35 microns to 100 microns as specified by MicroGroup, Inc. Since the characteristics of the tubes are not constant, reproducibility of the experiments from one tube to another and comparison between experiments done on different tubes may be an issue. Moreover, the uncertainty on the tube diameter causes errors in the calculation of the inside wall temperature which depends on the radii of the tube and in the calculation of the Stanton number which depends on the inside and cross section areas. However, this could be accounted for in the data by estimating the tube dimensions from the mass flow and the pressure drop across the test section.

Moreover, tubes are very fragile and any constraint can cause the tube to deform, bend or even break. Many constraints can be put on the tube while attaching the test section to the test rig or while attaching the electrodes. Once the tube is heated, it softens and may deform because of these constraints. This can have two consequences. First, the IR sensor may not be perfectly aimed at the tube once the tube has deformed and the temperature measurement may be inaccurate. Second, there may be some hot points where the tube is bent, causing the temperature at these points to increase artificially. The temperature profile measured may therefore not be representative of the physical and chemical phenomena. The shape of the tube and the aim point of the IR sensor were checked after each test to valid the measurements.

3.6.2.2 Temperature sensor

Aiming the IR sensor at the tube is a critical and delicate operation. The temperature reading is very sensitive to the aim point. First, taking a good measurement requires the spot to only cover the heated tube. Since the tube is deforming while heated, the IR sensor pointing was done prior to the experiment when the tube was cold and then readjusted after a first short heating. It was then checked regularly. Second, the temperature reading depends lightly on the orientation of the sensor with respect to the tube surface. It has

been therefore decided that the IR sensor would not be moved in between experiments so that this error would be limited.

Temperatures cannot be measured below 330°C. Therefore, the temperature measurement around this limit is more noisy. A variation of approximately 30°C at 350°C is noticed (8.7 % variation). At higher temperatures, the temperature measurements variations are within 3%.

3.6.2.3 Experimental errors

The position on the tube where the measurement is taken is an important parameter in the analysis. The position is measured by the stage on its course with a precision of 0.1 micron. However, the reference position is the zero position of the stage which is set at the entrance of the tube. There is no easy way to mark the entrance of the tube to make sure the zero point is always set at the same relative position with respect to the tube. The zero position was set as the position where the spot of the back light was at the start of the braise cone of the micro tube on the 1/16" tube.

Conditions are quite difficult to reproduce exactly from one tube to another because of the temperature sensor set up, the tube characteristics changing from tube to tube and the stage zero position set up.

3.6.3 Validity of model assumptions

The main assumption of the model is that all the heat generated by the electric field is absorbed by the fluid, increasing the bulk temperature of the fluid. No heat losses are assumed. Losses can occur from radiation, from free convection via the outside surface of the tube and from conduction axially inside the tube thickness.

Radiation losses were estimated [24] to be approximately 20 kW/m^2 (0.002 W/mm^2) which would be equivalent to 0.075 W for the test section considered. This is negligible compared to the heat fluxes imposed during the experiments which range from 30 W to 150 W. Free convection should not be a problem either. For an outside surface temperature of 1,000 K and an ambient temperature of 288 K, free convection losses were estimated [24] to be approximately 0.067 W.

Longitudinal conduction is a major concern. The losses by conduction were estimated at 2 %. Longitudinal conduction along the tube reduces the amount of heat absorbed by the bulk fluid. If longitudinal conduction is not negligible, the bulk temperature and therefore the heat transfer coefficient could be overestimated.

Chapter 4

JP7 study

4.1 Introduction to JP7 jet fuel

JP7 stands for Jet Propellant 7 (code: MIL-T-38219). JP7 is a deoxygenated hydrocarbon fuel, complex mix of different hydrocarbon molecules. It was used as propellant for the SR 71, unofficially known as the *Blackbird*, which completed its first flight on December 22, 1964. The SR 71 is a long-range, advanced, strategic reconnaissance airplane that set a speed record flying up to 2,193.167 miles per hour in July 1976. JP7 was used for propulsion and cooling in the two Pratt & Whitney J-58 engines of the *Blackbird*. The temperatures reached in the airplane were high enough that thermal expansion of the structure was an issue. Fuel tanks were sealed only during flight when the structures were hot and leaked when the plane was on the ground at ambient temperature. This is one reason that led to the choice of JP7 as propellant for the *Blackbird*: JP7 has a low flash point. Moreover, the temperatures reached in the engines were very high and required efficient cooling. JP7 was used to cool the engines. JP7 has a higher heat capacity than regular hydrocarbon fuels because of an endothermic decomposition. This is one of the most important differentiations of JP7 compared to other hydrocarbons. In a certain range of temperatures, JP7 undergoes a reaction of decomposition, which absorbs heat and therefore increases significantly the heat capacity of the fuel. This chapter presents the current understanding we have of JP7 endothermic reaction in micro channels and its consequences on JP7 properties based on the heat transfer experiments that have been carried out. Conclusions about the suitability of JP7 as coolant of the micro rocket engine will be derived from the results.

4.2 Motivation for JP7 study

JP7 has been selected as a potential fuel in the liquid regeneratively cooled micro rocket engine for two main reasons. First, the enhanced heat capacity of JP7 is an opportunity to compensate for the relatively high heat loads experienced in the micro rocket engine. Second, as a deoxygenated fuel, JP7 forms fewer carbon deposits than other hydrocarbons; this reduces the risk of clogging the micro rocket engine passages or of creating an insulation layer on the wall, which would reduce the heat transfer to the wall. However, even if JP7 looks like a very promising candidate since it seems to offer resistance to coking and an enhanced heat capacity, there are important issues still to be studied before JP7 can be declared suitable as a coolant for the micro rocket engine.

4.2.1 JP7 stability: carbon deposit formation

4.2.1.1 Carbon deposits with hydrocarbon fuels

One of the main concerns with hydrocarbons is the formation of carbon deposits. Deposits are a particular concern in the micro rocket engine, first because it may clog the very small passages, and second, because a layer of carbon deposited on the surface of the passages may act as an insulation layer and therefore decrease the local heat transfer and cause a thermal failure in the device.

Two reactions occurring in hydrocarbon fuels can cause the formation of carbon deposits and two types of carbon deposits must be distinguished.

- **Thermal-oxidative deposition formation or *fouling*:** The thermal-oxidative deposits result from a reaction between the fuel and the dissolved oxygen in the fuel. They appear at low temperatures around 150°C. The formation of thermal-oxidative deposits can be reduced by using deoxygenated fuels or by adding additives in the fuel. Figure 4-1 illustrates the decrease in thermal-oxidative deposition for deoxygenated fuels. Surface carbon deposition obtained during tests in macro tubes is showed for various fuels. The outside wall temperature is shown in parallel. For a wall temperature between 150°C and 200°C (temperature range corresponding to thermal-oxidative deposits), a peak in carbon deposition is noticed for air saturated

fuels whereas no significant carbon deposition is seen for deoxygenated fuels.

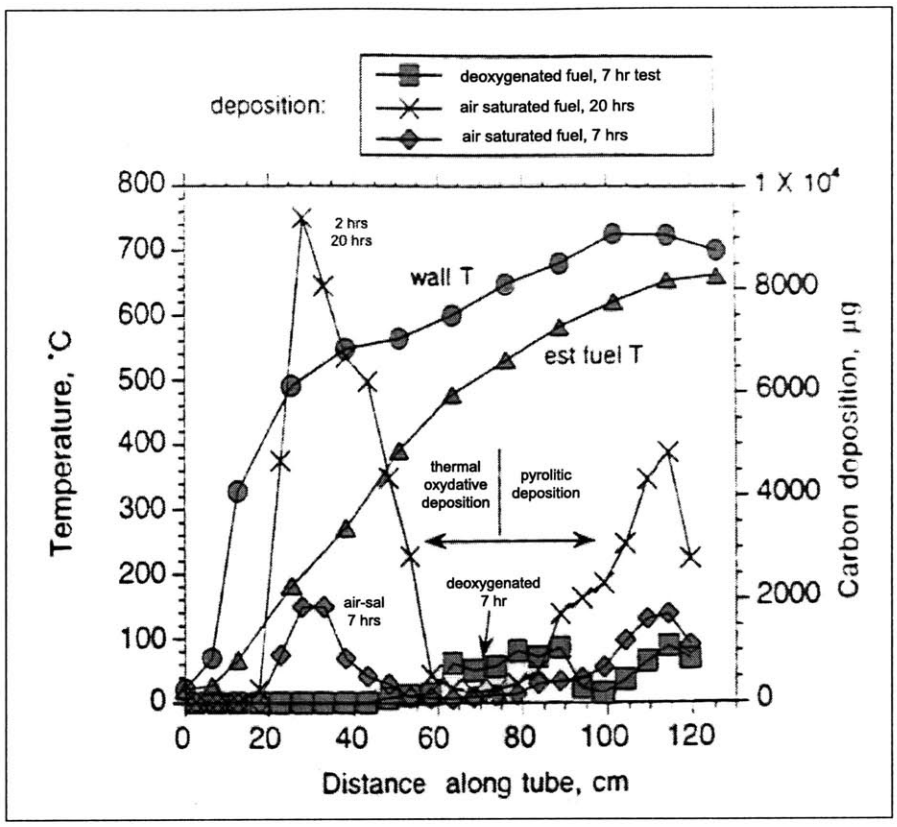

Figure 4-1: Typical surface deposition test results for tests at macro scale. Air saturated Jet A 3084, 33 mL.min^{-1}, 7 hrs, 69 atm [30].

- **Pyrolitic deposits or *coking*:** Pyrolitic deposits occur at higher temperatures around 500°C. The fuel experiences a reaction of decomposition and is said to *crack*. Carbon deposits are formed after the fuel has cracked. Therefore two factors contribute to the tendency of a fuel to form deposits: first, the tendency of the fuel to crack and second, the tendency to form deposits once it has cracked. Filamentous, amorphous and graphitic deposits may be formed depending on the reaction and the conditions. At a given mass flow, the amount of deposits formed is approximately increasing exponentially with temperature.

4.2.1.2 Carbon deposits with JP7

JP7 has a lower tendency to form both thermal-oxidative and pyrolitic carbon deposits than other hydrocarbon fuels as illustrated in Figure 4-2. Various fuels running through a

macro tube at a mass flow of 33 mL/min were heated to 650°C at a pressure of 69 atm. Surface deposition resulting from those tests is shown for each fuel. A distinction is made between oxidative and pyrolytic depositions, shown respectively in the left and right bars. JP7 produces very little carbon deposits.

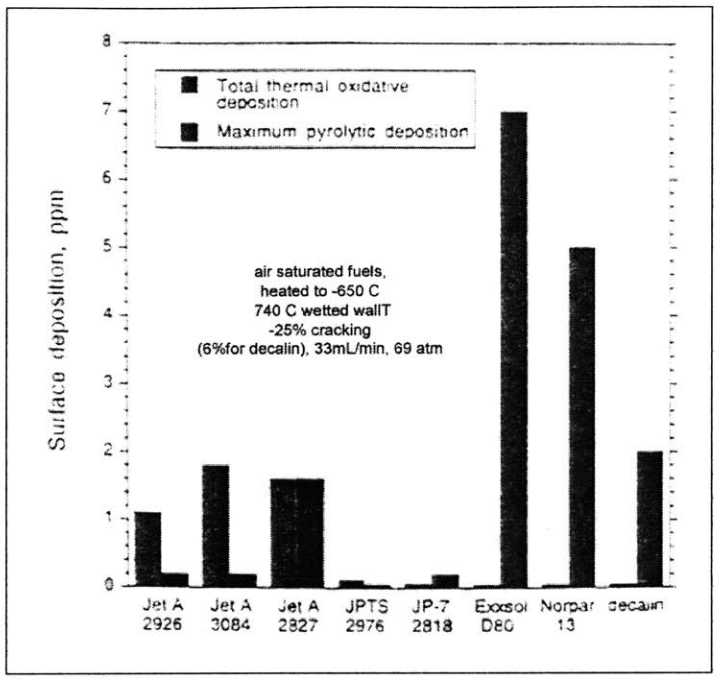

Figure 4-2: Cracking from several fuels in a flow reactor with a residence time of 1 to 2 seconds. For each fuel, the bar on the left represents the total thermal-oxidative deposition and the bar on the right the maximum pyrolitic deposition [30].

- Thermal-oxidative deposits are greatly decreased for JP7 as it is a deoxygenated fuel. Figure 4-3 presents the results of tests in which different fuels are run through a stainless steel macro tube at a constant mass flow of 12 mL/min. The amount of thermal oxidative surface deposition is plotted as a function of time for each fuel. JP7 and JPTS (Jet Propellant Thermally Stable) appear to produce very little thermal oxidative deposits compared to common Jet A fuels (JP8).

- JP7 does experience pyrolytic deposition. JP7 has a higher tendency to crack than other hydrocarbons at a given temperature. However, once cracking has occurred, JP7 has a lower tendency to form deposits. As a result, JP7 also forms less pyrolytic deposits than common hydrocarbon fuels as illustrated in Figure 4-2. As stated before, thermal oxidative deposition is limited for JP7 as a deoxygenated fuel. Pyrolytic

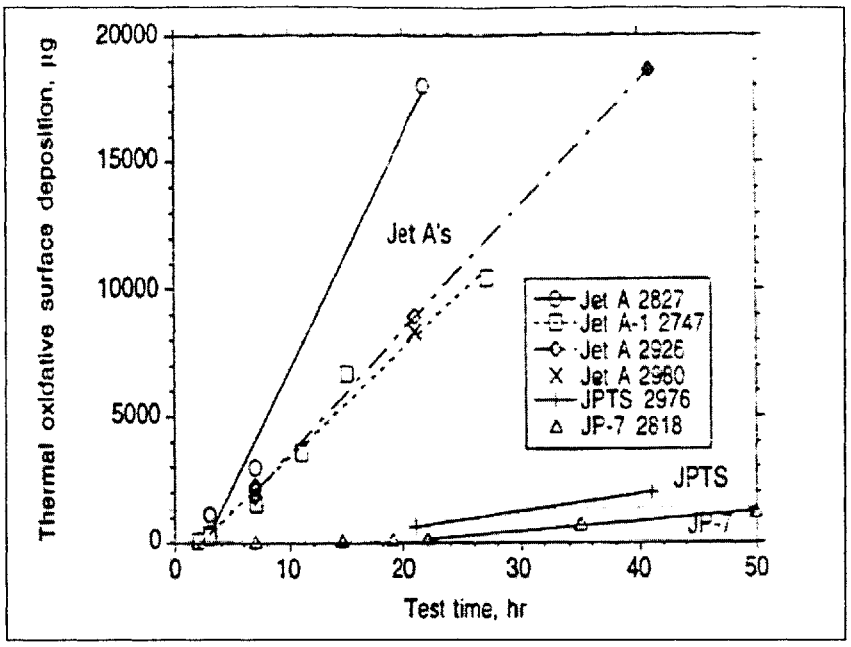

Figure 4-3: Surface deposition as a function of test time for 12 mL.min^{-1} tests [30].

deposition also appears to be significantly reduced in comparison to regular Jet A fuels [30].

All these tests have been carried out at macro scale in stainless steel tubes. These results do not necessarily predict the stability of JP7 in micro channels at much higher heat fluxes and pressures. However, they show promise for JP7 as a coolant in the micro rocket engine. Stability tests have been done with the heat transfer micro test sections and results are discussed in Section 4.4.

4.2.2 Enhancement in heat transfer with JP7

In the conditions experienced in the micro rocket engine, two phenomena will enhance the heat capacity of JP7. One is linked to the physical state of the fluid as JP7 will be supercritical. The other phenomenon is linked to a chemical modification of the fluid as the JP7 endothermically reacts.

4.2.2.1 Physical phenomenon: supercritical state

JP7 critical pressure is 17.7 atm (260 psi) and its critical temperature is 673.15 K (400°C). In the micro rocket engine, the coolant pressure reaches 300 atm and the estimated fuel exit

bulk temperature may be above 500°C. Therefore, as other fluids, JP7 will be supercritical in the cooling passages of the micro rocket engine. As presented in section 2.2, JP7, as a supercritical fluid, should benefit from an increased heat capacity due to a peak in its specific heat and an increase in the turbulence following a decrease in viscosity. Figure 4-4 presents the Cp profile of supercritical JP7 at a pressure of 265 psi as a function of temperature. The significant peak of the specific heat at the pseudo temperature is apparent. The profiles for other fluid properties are shown in Appendix A.

However, it must be noticed that pressures in the rocket are very high compared to the

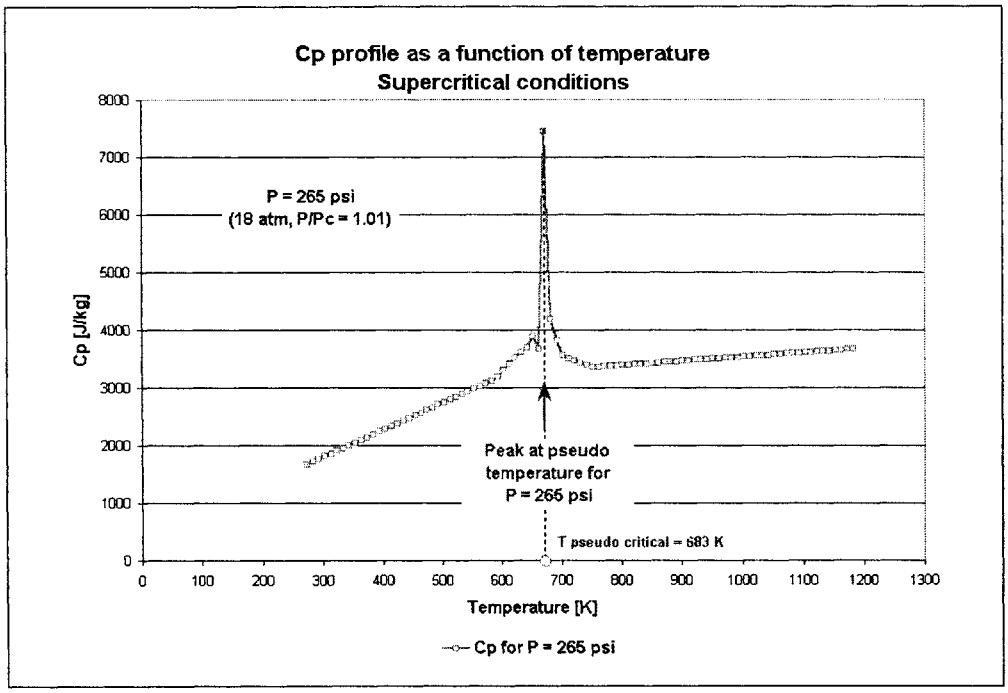

Figure 4-4: Specific heat profile as a function of temperature at P = 265 psi (18 atm, $\frac{P}{P_c} = 1.01$) [16].

critical conditions of JP7. Critical pressure ratios ($\frac{P}{P_c}$ where P represents the pressure and P_c the critical pressure) as high as 17 will be seen in the micro rocket engine. Supercritical properties have a strong dependence on pressure as explained in section 2.2. Therefore, the peak of specific heat will be so small at the pressures experienced in the engine that this effect will not have a significant impact on the heat capacity of JP7. The peak of Cp is already almost non detectable at a pressure of 70 atm [16] as seen in Figure 4-5, which shows the specific heat profile as a function of temperature for a pressure near critical (265 psi,

18 atm, $\frac{P}{P_c} = 1.01$) and a high pressure (1,000 psi, 68 atm, $\frac{P}{P_c} = 3.8$). Viscosity will decrease smoothly and therefore a temperature as high as 700°C may be necessary to reach a gas like viscosity.

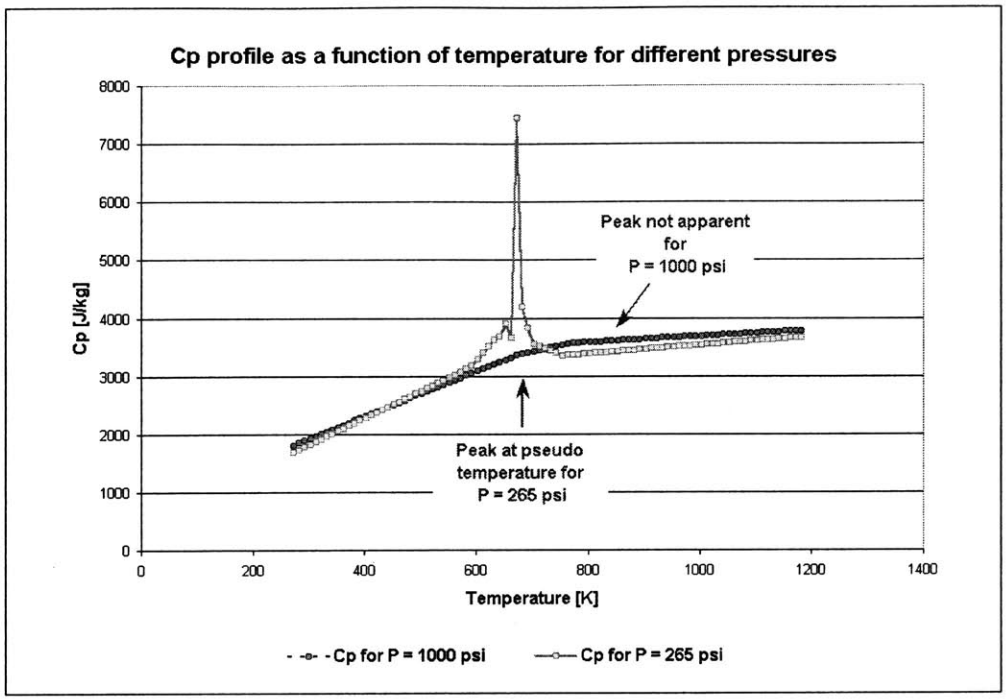

Figure 4-5: Specific heat profile as a function of temperature for two pressures: P = 265 psi (18 atm, $\frac{P}{P_c} = 1.01$) and P = 1,000 psi (68 atm, $\frac{P}{P_c} = 3.8$) [16].

4.2.2.2 Chemical phenomenon: endothermic decomposition

JP7 undergoes a chemical reaction in which heavy hydrocarbons decompose into lighter hydrocarbons (C1 - C4 hydrocarbons), mainly hydrogen and methane. The higher the temperature, the more conversion towards hydrogen and methane is noticed. Both gaseous and liquid products are obtained. This reaction occurs in a certain temperature range and is highly endothermic. Experiments carried out in macro scale tubes at a pressure of 1,000 psi show that the reaction would occur between 1,000°F (537°C) and 1,200°F (648°C) in those conditions [4] with an approximate endothermy of 1,400,000 J/kg. Figure 4-6 illustrates the enhancement in fuel heat capacity produced by the endothermic reaction. The enthalpy profile of the fluid is modeled as a function of temperature for a pressure of 1,000 psi. The model assumes a reaction occurring between 1,000°F and 1,200°F, an endothermy of 1,400,000 J/kg, a 50 % conversion and a certain final composition. This model does not

account for supercritical properties of the fluid. For more details about the model, refer to section 4.3.6.2.

The reaction can be characterized by four parameters:

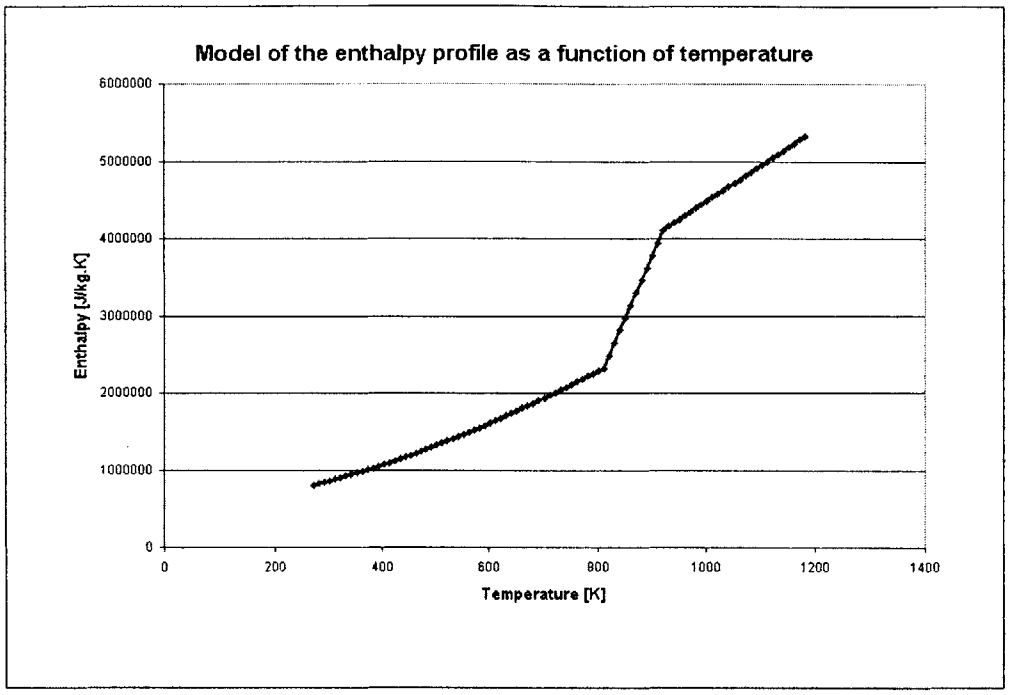

Figure 4-6: Model of the fluid enthalpy taking into account the endothermic reaction. The reaction is assumed to occur between 550°C and 650°C and to give an endothermy of 1,395,588 J/kg.

- **Temperature range within which the reaction occurs**: The reaction is temperature dependent: it only occurs within a range of temperatures. This range is more likely to be a function of other conditions as pressure, heat flux or even the size of the passage. Very little is known about when the reaction starts and ends, especially in micro channels.

- **Degree of conversion of the fluid**: The degree of conversion characterizes the proportion of heavy hydrocarbons that have decomposed into C1 to C4 hydrocarbons within the fuel. This is an indicator of the degree of reaction and strongly influences the total heat absorbed by the reaction: the more fluid reacts the more heat is taken and the higher the final heat capacity of the fluid is. The degree of conversion is also important to estimate the composition of the fuel after the reaction is completed. The

conversion is believed to be a function of the conditions of the fluid as pressure, mass flow, heat flux, etc.

- **Endothermy of the reaction**: The amount of heat absorbed by the reaction is a major parameter for the estimation of the heat capacity of JP7. The higher the conversion, the higher the final endothermy reached.

- **Evolution of the composition of the products of the reaction**: The gas and liquid reaction products are C1 to C4 hydrocarbons. There are mainly eight light hydrocarbons produced. As the reaction proceeds, the composition of the products varies. Moreover, a recomposition of the fuels is seen in the liquid products. The composition of the fuel after decomposition is important to model the heat capacity of the fluid after the reaction has occurred or to predict the behavior of the fluid in the injectors and the chamber.

If the onset temperature for the reaction at micro scale is close to what is seen at macro scale, we can expect reactions to occur near the wall where the temperature is the highest in our tests. The fluid near the wall will react as well as the bulk fluid conducted to the wall by turbulences. The more turbulence in the fluid, the more non reacted bulk fluid would get to the wall and we would expect the conversion to increase with turbulence.

JP7 reaction is endothermic and therefore very promising for an application in the micro rocket engine. However, very little is known about the main parameters characterizing it and prediction of JP7 properties and behavior will certainly be an issue.

4.2.2.3 Relative importance of these phenomena

Supercritical conditions and endothermic reaction of the fuel will be concurrent in the micro rocket engine. The behavior and the properties of JP7 are expected to depend on both of those phenomena.

In the micro rocket engine, the pressures are so high that the supercritical enhancement of heat capacity should not be seen much. Even if the characteristics of the endothermic reaction are not known at such high pressures, the endothermic enhancement is expected to be the predominant phenomenon. Supercritical conditions still influence the stability

and the properties of the fluid as well as the reproducibility of the behavior of JP7. In particular, the decreased viscosity due to supercritical conditions contributes to increase the turbulence. Because of the increased turbulence, bulk fluid may reach the wall where the temperature is maximum and where the reaction is expected to occur. Therefore, more fluid will decompose providing a better cooling.

In the experiments presented in this work, experimental conditions have been chosen first to cover a large range of pressures from subcritical to supercritical conditions and high critical pressure ratios, and second to cover a large range of temperatures to capture both conditions in which decomposition does and does not occur. In some test conditions, pressure is therefore close to critical and the supercritical enhancement cannot be neglected without further study of the endothermic reaction.

However macro scale data seem to suggest that the enhancement of heat capacity provided by the endothermic reaction far exceeds the enhancement provided by the supercritical conditions even around the critical pressure where the effect of supercritical conditions is maximum. Figure 4-7 presents a model of JP7 enthalpy profile based on experimental data from tests in macro scale tubes. The effects of supercritical conditions and of the endothermic reaction are combined to visualize their relative importance. For the supercritical effect, the specific heat around critical pressure has been chosen (P=265 psi) [16] since it corresponds to the highest supercritical heat capacity enhancement. For the effect of the endothermic reaction, we used the only available data from tests at macro scale at 1,000 psi [4]. Even if the data do not correspond to the same conditions, it appears clearly that at macro scale the enhancement from the endothermic reaction is many orders of magnitude higher than the effect of supercritical conditions. Therefore, it would be expected that the endothermic would be predominant when both phenomena are occurring.

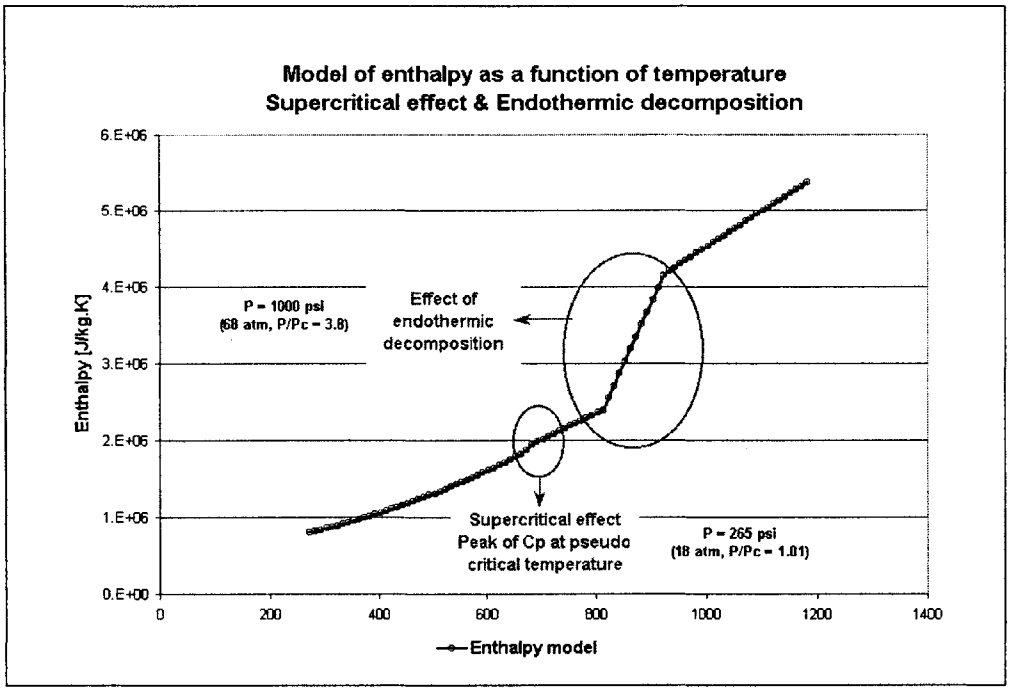

Figure 4-7: Comparison of the effects of both phenomena. The enthalpy profile of JP7 is shown as a function of temperature. The supercritical effect is calculated from the specific heat of JP7 at P=265 psi ($\frac{P}{P_c}$=1.01). The effect of the endothermic reaction is estimated from experimental data at macro scale at P=1,000 psi.

4.3 Heat transfer experimental study

4.3.1 Description of the experiments

4.3.1.1 Summary of the experiments

A total of 65 experiments have been conducted with JP7 under different conditions. Experimental conditions for JP7 tests were chosen within the following test matrix:

- pressures ranging from 165 psi ($\frac{P}{P_c} = 0.64$) to 1,500 psi ($\frac{P}{P_c}$=5.77); mainly five pressure levels were tested: subcritical pressures (between 180 psi and 200 psi), critical pressures around 260 psi, and three high pressures (400 psi, 600 psi and 1,500 psi)
- mass flows ranging from 0.03 g/s to 0.304 g/s
- heat fluxes ranging from 20 W/mm^2 to 120 W/mm^2

Subcritical and supercritical conditions have been tested. Inside wall temperatures between 200°C and 650°C have been reached to capture a large temperature range for the possible onset of decomposition. Tests at high heat fluxes, high pressures and high mass flows have been conducted to test conditions as close as possible to rocket engine conditions, within the limits of the experimental apparatus and the thermal resistance of the micro test section. Some conditions are close to conditions chosen in previous experiments with water and ethanol [18] in order to compare the performance and the behavior of JP7 and ethanol.

4.3.1.2 Reduction data method

The reduction of JP7 data has followed the general scheme presented in Section 3.4. Decomposition was not accounted for in the reduction of the data since very little was known to model it. Data on JP7 properties were available only for two pressures 500 psi and 1,000 psi [16]. These pressures are much higher than the critical pressure of JP7 and therefore do not show the sharp behavior characteristic of the fluid properties around the critical pressure. These properties were not suitable to reduce data near critical. Since n-dodecane properties are often used as a substitute for JP7 properties, we chose to use the properties of n-dodecane [16], for which much more data are available, to reduce JP7 data at pressures around critical. The properties used for the calculations are presented in Appendix ??.

4.3.2 General overview of the results

4.3.2.1 Temperature profile

If there is no heat capacity enhancement in the fluid, the temperature is expected to increase rapidly along the tube. During supercritical experiments conducted with water and ethanol [24] [18], the temperature was seen to increase along the tube but after a sharp increase, the fluid reached the pseudo critical temperature on the inside wall of the tube and the enhanced cooling due to the supercritical effect caused the temperature to increase more slowly. Ethanol and water tests obtained temperature profiles similar to the dashed curve shown in Figure 4-8.

For JP7 different scenarios are possible [5]. We could expect temperature profiles similar to those obtained with water and ethanol supercritical behavior. However, the temperature could stabilize or even decrease along the tube due to the increase cooling provided by the decomposition reaction if the heat capacity enhancement is high enough. The different possible profiles are illustrated in Figure 4-8. The temperature can stabilize and then, depending on the level of enhancement provided by the endothermic reaction, can increase again, stay stabilized or even start decreasing. Experiments done by Dang and Chen [5] indicate that the enhancement in heat capacity is high enough to cause the temperature to decrease at the end of the test section in some test conditions. In most of the experiments carried out with JP7, the same trend has been noticed where a bell temperature profile is seen along the tube.

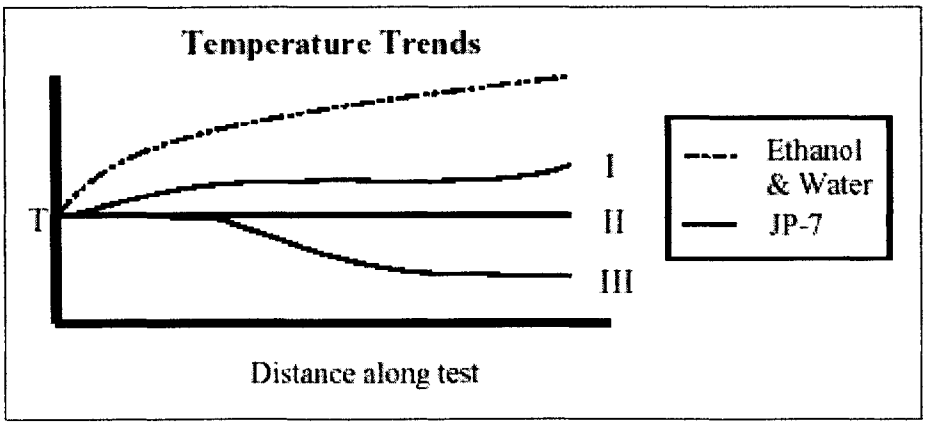

Figure 4-8: Possible temperature profiles along the test section in JP7 experiments [5].

4.3.2.2 Heat transfer coefficient

The heat transfer coefficient is expected to decrease as the thermal entry length develops and then to stabilize if there is no heat capacity enhancement. In supercritical experiments done with water and ethanol [24] [18], supercritical effects cause the heat transfer coefficient to increase significantly when the pseudo critical temperature is reached at the inside wall. This increase is not seen at high pressures (critical ratio above 2) and high heat fluxes with supercritical ethanol and water since high pressures and high heat fluxes tend to annihilate the pseudo critical Cp peak. In tests with JP7, the heat transfer coefficient is seen to significantly increase at the end of the tube providing a large improvement in cooling at all pressures.

4.3.2.3 Stanton number

The Stanton number is studied to better understand the origin of the enhancement. The Stanton number is calculated from the difference between the wall and the bulk enthalpies. If the enthalpy profile captures the behavior of the fluid and if there is no additional source of heat capacity enhancement, the Stanton number will decrease at the entrance of the tube because of the entrance effects before stabilizing when the flow is fully developed. It must be noted that the increase in turbulence due to supercritical conditions will cause an enhanced flow circulation and an increased cooling. This effect is not taken into account in the enthalpy profile and may cause the Stanton number to slightly increase.

In previous experiments carried out with supercritical water and ethanol [24], the Stanton number increased as the wall temperature reached the pseudo critical temperature. The enhanced cooling due to the supercritical effect caused the inside wall temperature to drop. As the difference between the inside wall and the bulk temperatures decreased, the Stanton number increased.

In the experiments carried out with JP7, the Stanton number starts to decrease at the entrance of the tube, then stabilizes and starts to significantly increase at the end of the tube. Since the supercritical effect is accounted for in the enthalpy profile, this seems to indicate that the origin of this enhancement, seen in the Stanton number profile, could be the endothermy of the reaction of decomposition. The enhancement has bee seen at all pressures subcritical, critical and supercritical at very high critical pressure ratios. The

supercritical effect should not be apparent at very high pressures or at subcritical pressures. This confirms that the increased cooling capacity is due to the endothermic reaction.

The effect of the endothermic reaction on the cooling capacity of JP7 has been identified and confirmed. It seems to provide a large enhancement in the heat transfer coefficient. More details on the quantitative results of the experiments are presented in the next sections.

4.3.3 Summary of the experiments

4.3.3.1 Temperature profiles

Two different profiles have been recorded during the tests:

- The temperature increases rapidly at the entrance of the tube, then starts stabilizing to a peak value before decreasing significantly and eventually stabilizing again. The decrease in temperature can be as high as 1/3 of the peak temperature in about 700 microns. This is the most common profile obtained during the experiments. 41 tests out of 65 show this profile (63 %). Figure 4-9 shows an example of such a profile. The test was done at a subcritical pressure (187 psi) for a mass flow of 0.044 g/s and a heat flux of 23 W/mm^2.

- In other cases, the temperature profile is smooth and there is no sharp peak. The measured outside wall temperature stays almost constant along the tube as shown in Figure 4-10 or decreases slowly from the entrance. Significant drops can still be achieved.

During similar experiments in macro tubes, different temperature profiles were recorded even in the same test conditions [15] as it is seen in the present experiments at micro scale.

4.3.3.2 Heat transfer enhancement

In JP7 experiments, the heat transfer coefficient significantly increases along the tube, with increases as high as 1.2×10^6 W/K.m^2. Heat transfer coefficients as high as 1.62×10^6 W/K have been reached for high heat fluxes (96 W/mm^2). The increase is seen in subcritical and supercritical conditions, at very high pressures (critical pressure ratio of 5) and at very high heat fluxes. Therefore, supercritical effects alone seem not to explain the behavior of

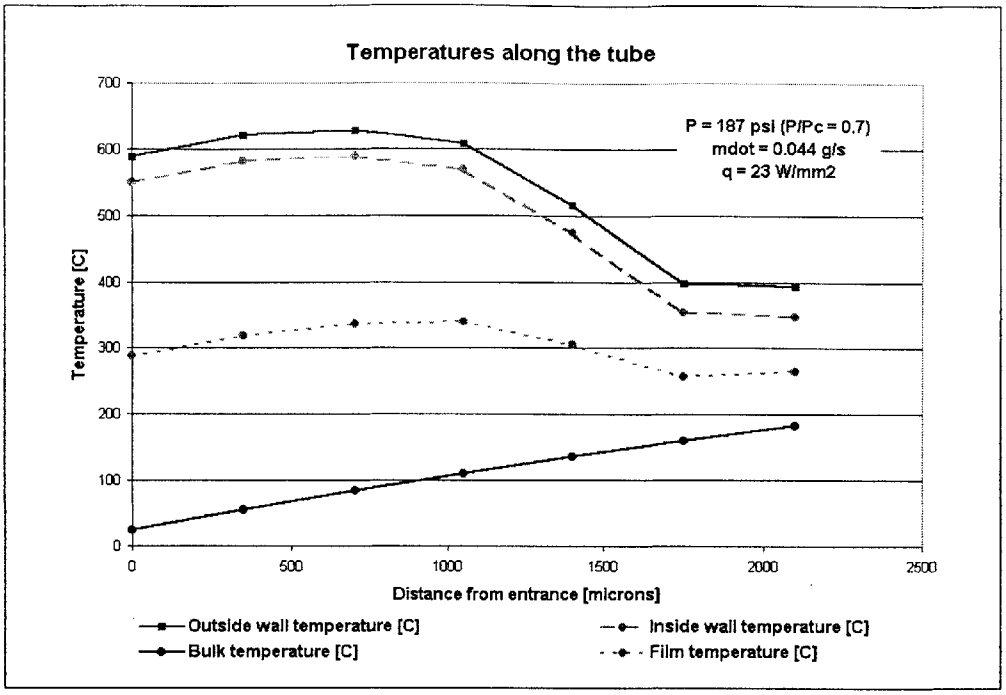

Figure 4-9: Outside wall temperature, inside wall temperature, bulk temperature and film temperature ($T_{film} = (T_i - T_{bulk})/2$) as a function of the distance from the entrance of the tube. The outside wall temperature shows a peak in the middle of the tube before decreasing significantly.

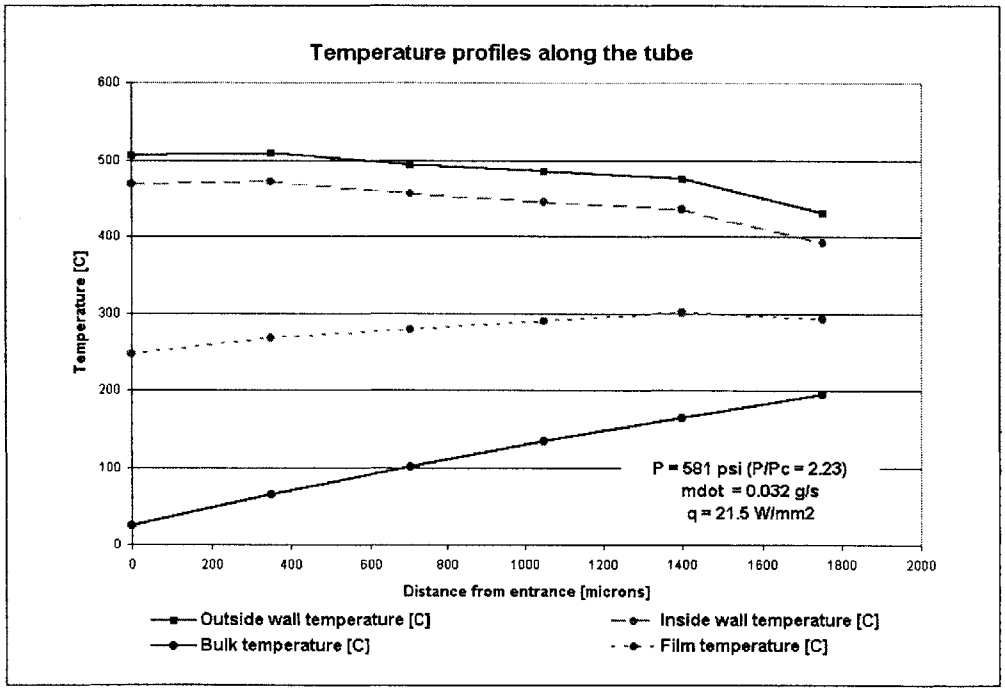

Figure 4-10: Outside wall temperature, inside wall temperature, bulk temperature and film temperature ($T_{film} = (T_i - T_{bulk})/2$) as a function of the distance from the entrance of the tube. The outside wall temperature shows a flat profile along the tube.

the fluid. The endothermy of the reaction of decomposition of JP7 has been verified.

In parallel to the temperature profiles observed during the tests, two different types of heat transfer coefficient profiles have been recorded.

- Figure 4-11 shows the profile of the heat transfer coefficient calculated along the tube corresponding to the temperature profile shown in Figure 4-9. The heat transfer coefficient starts decreasing slightly at the entrance of the tube because of the heating of the fluid. We start to see an enhancement in the fuel heat capacity contributing to an increase in the heat transfer coefficient. This increase compensates the decrease due to the heating of the fluid, resulting in the stabilization of the heat transfer coefficient. The enhancement then becomes more and more efficient and the heat transfer coefficient starts increasing. Eventually, at the end of the tube the rate of increase of the heat transfer coefficient decreases and the heat transfer coefficient reaches a plateau.

  The heat transfer coefficient profile is directly related to the profile of the inside wall temperature. As the heat transfer coefficient stabilizes and slowly increases the inside wall temperature stabilizes. The significant enhancement in heat transfer coefficient implies a much more efficient cooling of the tube and the decrease of the inside wall temperature.

- Other tests have shown a smooth heat transfer coefficient profile. The heat transfer coefficient starts increasing slowly directly from the entrance of the tube and no sharp increase is seen. Figure 4-12 shows the heat transfer coefficient profile corresponding to the smooth temperature profile shown in Figure 4-10. The enhancement of the cooling properties of the fluid manages to keep the temperature constant at the wall.

4.3.3.3 Stanton number

A maximum increase of 0.026 has been calculated at critical pressure. Increases as high as 0.005 have been observed at all pressures. Except in 4 tests, an increase of at least 20 % of the Stanton number has been seen. The floor value at which the Stanton stabilizes is usually

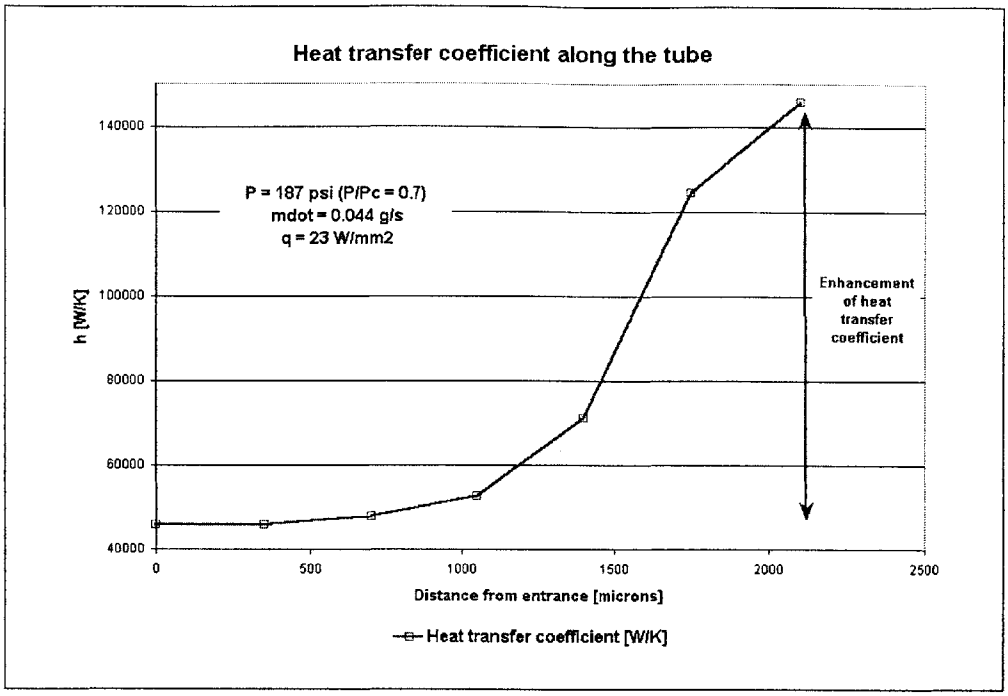

Figure 4-11: Calculated heat transfer coefficient corresponding to the temperature profile shown in Figure 4-9. The test conditions are P = 187 psi ($\frac{P}{P_c} = 0.7$), $\dot{m} = 0.044$'g/s and q = 23 W/mm^2.

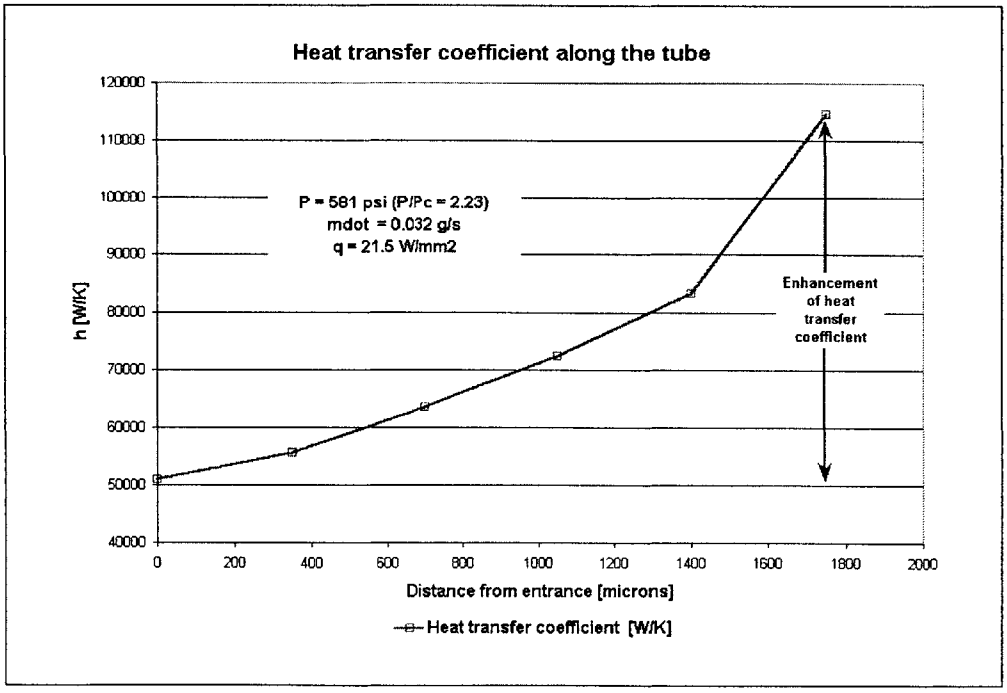

Figure 4-12: Calculated heat transfer coefficient corresponding to the temperature profile shown in Figure 4-10. The test conditions are P = 581 psi ($\frac{P}{P_c} = 2.23$), $\dot{m} = 0.032$ g/s and q = 21.5 W/mm^2.

calculated between 0.002 and 0.003. Figure 4-13 shows the Stanton number calculated along the tube for a test at P = 1,523 psi ($\frac{P}{P_c} = 5$), with a mass flow $\dot{m} = 0.23$ g/s and a heat flux q = 72 W/mm^2.

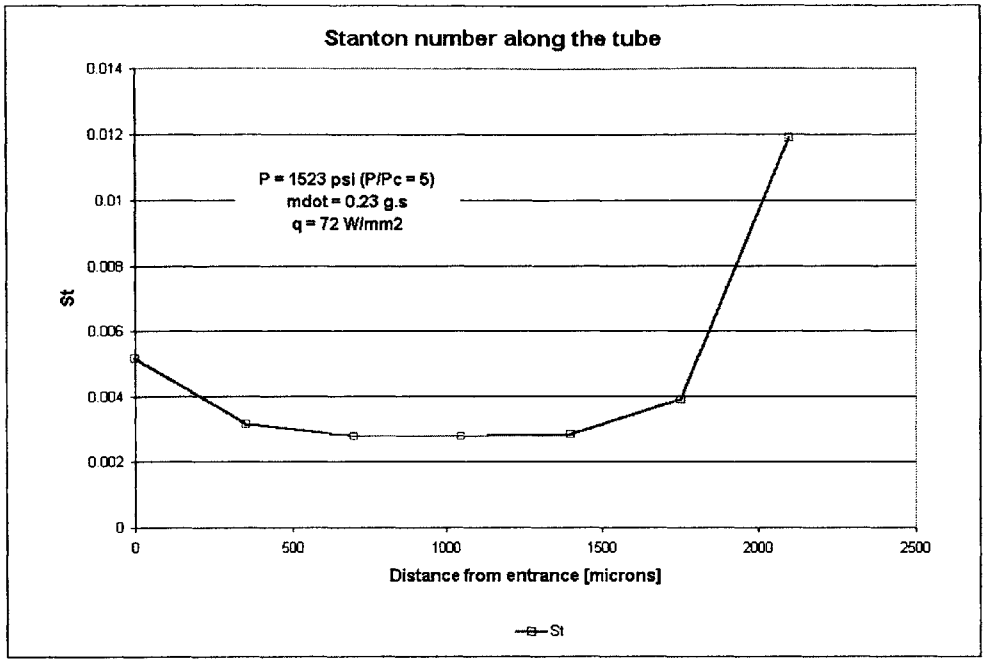

Figure 4-13: Stanton number along the tube for a test at 1,523 psi ($\frac{P}{P_c} = 5$), a mass flow of 0.23 g/s and a heat flux of 72 W/mm^2.

4.3.4 Conditions of appearance of the different profiles and comparison of the enhancements offered

4.3.4.1 Sharp profile

As seen in tests with other fluids, the wall temperature starts increasing because of the heat flux imposed. The inside wall temperature increases and reaches the range of temperature in which the endothermic reaction occurs. Because of the reaction, more heat is absorbed by the fluid and the cooling is more efficient. The temperature starts stabilizing.

The fluid keeps decomposing. The cooling is then so efficient that the temperature drops. The temperature starts decreasing because the heat capacity of the fluid increases greatly. Two phenomena could explain this improvement. A first explanation is that the conversion rate of the fluid increases therefore absorbing more heat, there is more decomposition of the fluid. A second explanation could be that the reaction and the products relieved increase

the turbulence in the tube and therefore facilitate the recirculation of the fluid. The bulk fluid, which has not reacted yet, assuming that the bulk temperature is still below the reaction onset temperature, reaches the wall and starts reacting, improving the overall cooling.

Different reasons can explain the floor reached at the end of the tube. The temperature could reach a floor because the inside wall temperature has decreased and starts approaching the low temperature limit at which the reaction stops. As the temperature drops, it is expected that the equilibrium will be shifted towards a slow down of the decomposition reaction since it is an endothermic reaction. Therefore, as less fluid decomposes, the heat capacity of the fluid decreases and the temperature starts stabilizing.

If the low temperature limit was reached and no decomposition was occurring anymore in the fluid, the temperature would be expected to start increasing again because the heat load applied to the fluid would not be compensated by the decomposition endothermy anymore. The test section was not long enough to allow us to derive any conclusion about the evolution of the temperature after the floor. No increase in temperature was recorded after the temperature drop. Possibly, the temperature could increase enough to reenter the range within which the decomposition occurs.

In some cases, the temperature profiles recorded do not show the first phase where the temperature increases and the temperature starts decreasing from the entrance of the tube. This may be due to the fact that the inside wall temperature reached at the first point of measurement was already within the temperature range in which the reaction occurs. We may also consider the possibility of instrument pointing error which would mean that the first point of measurement was taken downstream the entrance of the tube.

4.3.4.2 Temperature at which the temperature starts dropping

The temperature at which the temperature starts decreasing is not the temperature at which the reaction starts. The reaction starts at a lower temperature since it contributes to the prior stabilization of the temperature. A better indicator of the lower temperature delimiting the range of temperature within which the reaction occurs may be the temperature at which the temperature stabilizes after the temperature drop. Unfortunately, this

floor is rarely seen in the results of our experiments.

However, the temperature at which the temperature starts decreasing marks the point where the enhancement becomes significantly more efficient. The following paragraph presents some trends of the inside wall drop temperature.

The inside wall drop temperature does not strongly depend on pressure as seen in Figure 4-14 which shows the inside wall drop temperature as a function of the critical pressure ratio. At each pressure tested, drop onset temperatures range from 200°C to 700°C.

The drop temperature tends to increase with the heat flux and to decrease with the mass flow. Figure 4-15 shows the inside wall drop temperature as a function of the difference

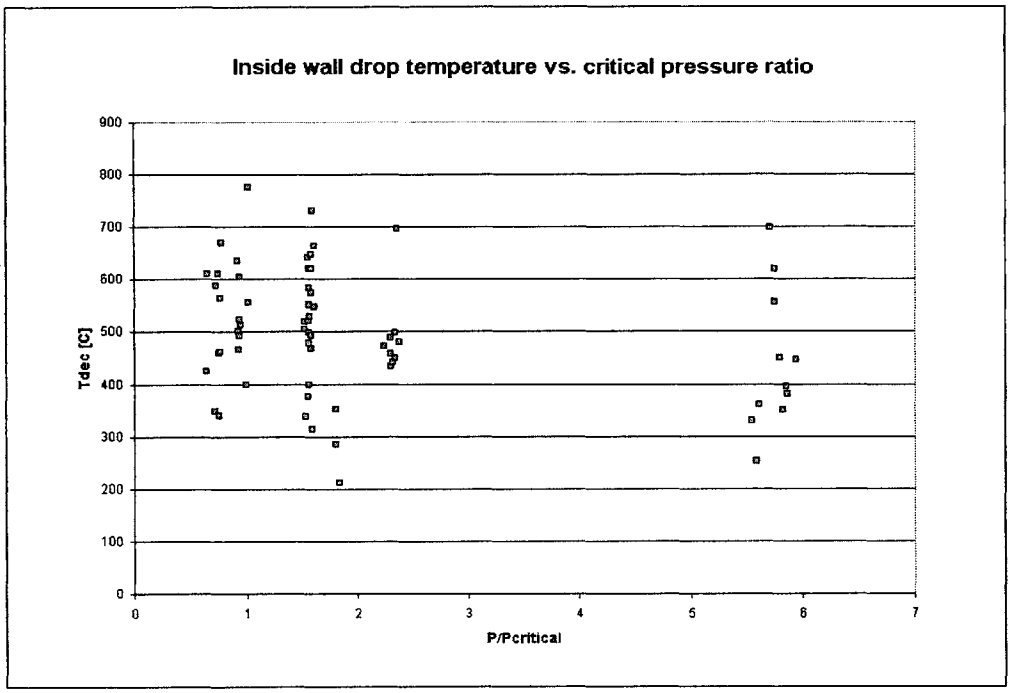

Figure 4-14: Inside wall drop temperature vs. the critical pressure ratio.

between the inside wall temperature and the bulk temperature at the point of the drop of the wall temperature. Each plot corresponds to a different mass flow range (0.04-0.05 g/s, 0.05-0.06 g/s, 0.23-0.26 g/s). The drop temperature increases as the temperature difference between the inside wall and the bulk fluid increases. At higher mass flows, the drop in temperature appears at a lower temperature and for a smaller temperature difference between the inside wall and the bulk fluid.

More specific trends are seen at high heat fluxes. Figure 4-16 shows the inside wall temper-

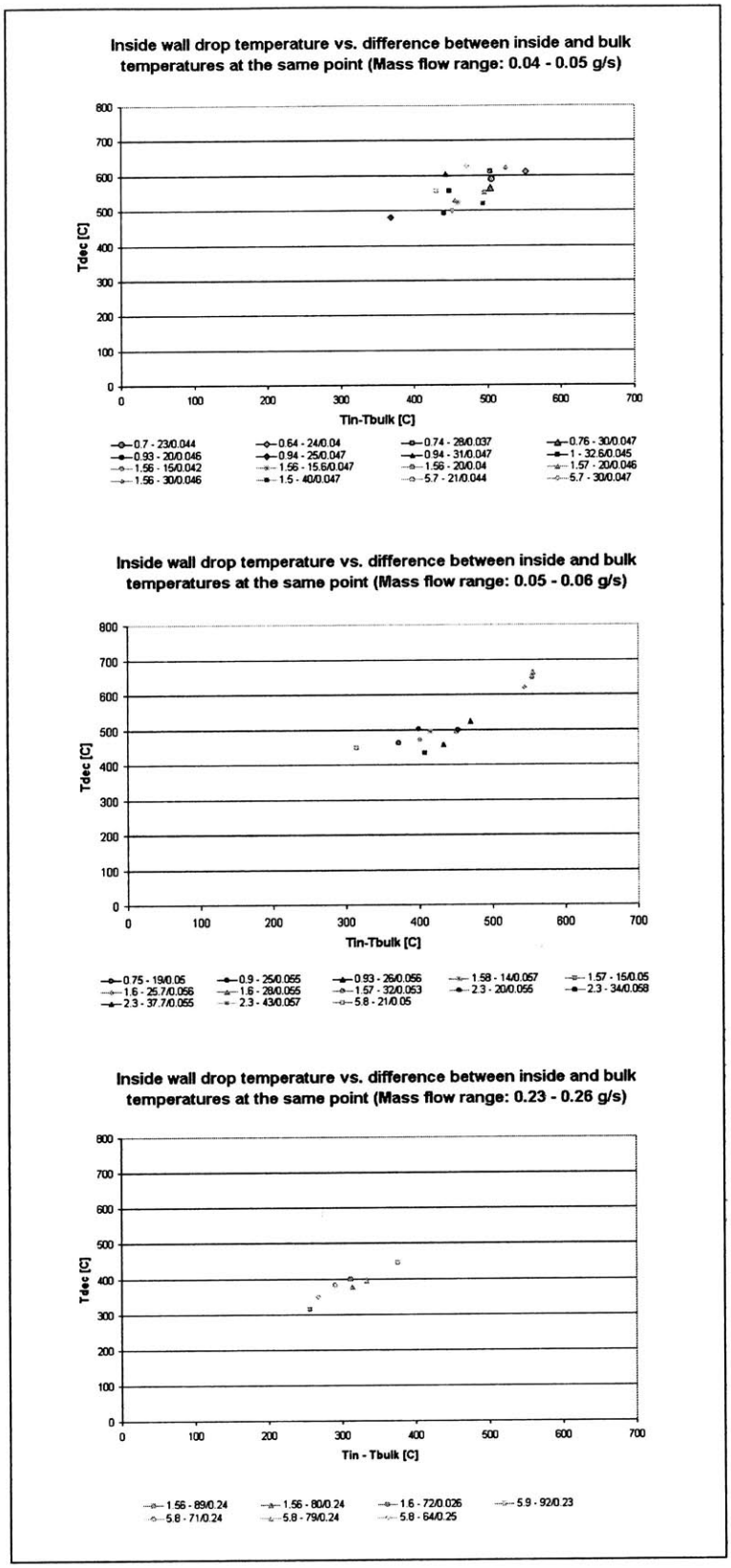

Figure 4-15: Inside wall drop temperature vs. the difference between the inside and the bulk temperatures at the same point for different mass flow ranges.

ature versus the temperature difference between the inside wall and the bulk fluid along the tube for some of the high heat flux tests. At the beginning of the test section, the inside wall temperature increases faster than the bulk temperature. The inside wall temperature then reaches its peak value and starts decreasing. The inside wall drop temperature is the end point on the right for each curve. As the heat flux increases, the drop temperature increases as stated before. It can also be noticed that the drop in temperature appears sooner in the tube and the inside wall temperature difference between the entrance and the drop point decreases as the heat flux is increased. Tests at higher pressures show a higher inside wall drop temperature.

In order to understand which phenomenon determines the temperature profile obtained during experiments, we analyzed the onset conditions of each of these profiles and the enhancement they provided.

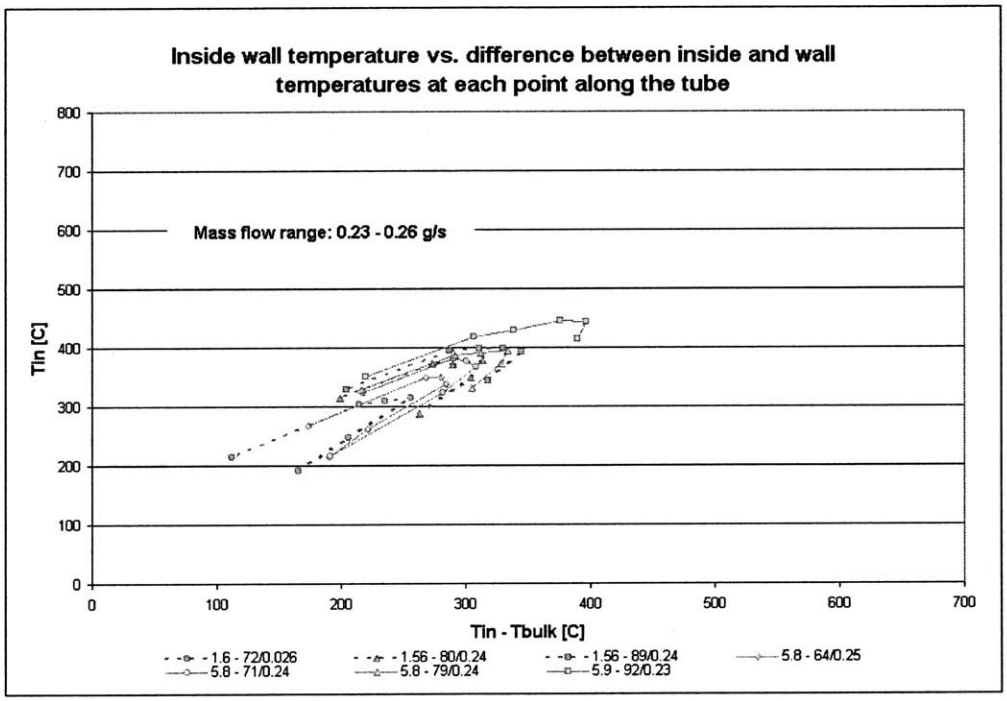

Figure 4-16: Inside wall temperature vs. the difference between the inside and the bulk temperatures at each point along the tube for mass flows between 0.23 and 0.26 g/s.

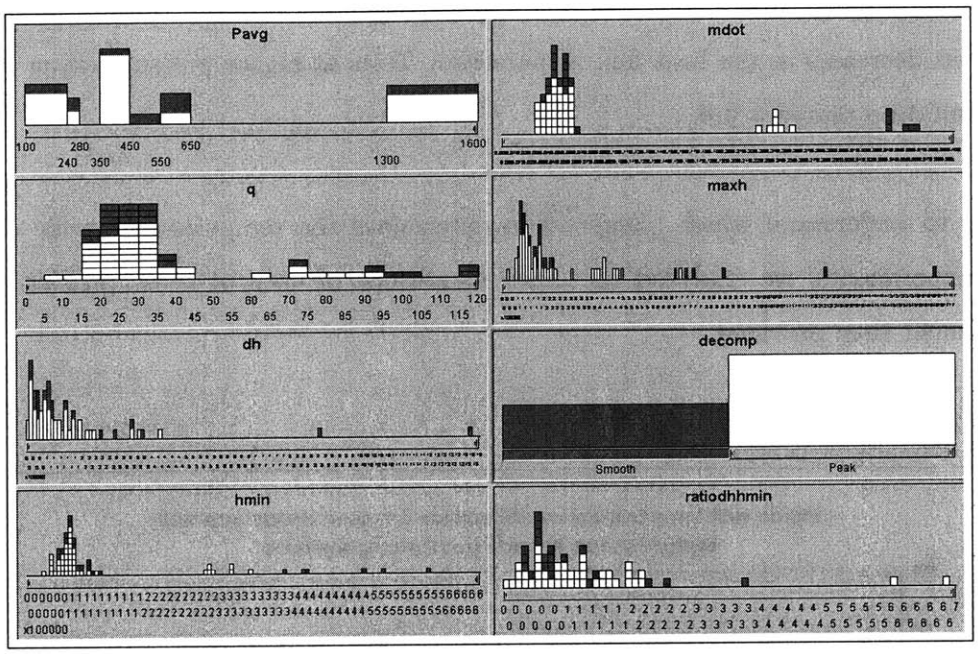

Figure 4-17: Summary of all the characteristics of the tests in which a smooth temperature profile was recorded. The three first plots show the conditions of the tests: pressure, mass flow and heat flux are shown. The five following graphs show the results of the tests: the maximum heat transfer coefficient recorded, the increase in heat transfer coefficient at the end of the tube, the type of profile noticed (either a smooth profile or a profile where the temperature shows a sharp peak value), the minimum heat transfer coefficient recorded along the tube and the ratio of the increase in the heat transfer coefficient and its minimum value. Each case is a test. The 65 tests appear on the graph. The dark cases are the tests which showed a smooth profile.

4.3.4.3 Onset conditions for sharp or smooth temperature profiles

Figure 4-17 gives a summary of the conditions in which the two profiles have been seen. The program Attribute Explorer has been used to visualize the conditions and results of the 65 tests. This tool allows visualization of different variables at the same time on different plots. In this figure, the tests conditions are shown in the three first graphs (pressure, mass flow and heat flux are shown) whereas the results of the tests are shown in the five other graphs (the maximum heat transfer coefficient, the increase in the heat transfer coefficient, the type of temperature profile seen, the minimum heat transfer coefficient and the ratio of the increment and the minimum value of the heat transfer coefficient are shown). The program allows highlighting of all the variables corresponding to one test. One test is selected by choosing one case on any plot, the corresponding variables on the other plots are highlighted. The program is an interesting tool to visualize which tests correspond to a particular constraint. For example, all the tests done at high pressures can be selected. The program will highlight the corresponding mass flows, heat fluxes and the corresponding results seen in the tests. This tool can greatly facilitate the identification of trends or dependencies in the experimental results and will be used in other sections of this thesis.
In the Figure 4-17, the dark cases correspond to tests in which a smooth profile is seen whereas the white cases correspond to tests in which the temperature shows a sharp peak. There is no real trend in the conditions in which a smooth profile is seen. It appears at all the different pressures tested. Only smooth profiles are seen at very high heat fluxes above 100 W/mm^2. However sharp profiles are seen at high heat fluxes between 80 W/mm^2 and 90 W/mm^2 and smooth profiles are seen at low heat fluxes as well. Smooth profiles are seen at the highest mass flows around 0.3 g/s. However, sharp profiles are seen at mass flows as high as 0.25 g/s and smooth profiles can be seen at low mass flows. Therefore, we found no clear set of conditions for which the smooth or the sharp profiles were obtained. Two tests carried out in similar conditions of pressure, mass flow and heat flux can give two different profiles. Two tests carried out in similar conditions (pressure around 400 psi ($\frac{P}{P_c} = 1.55$), mass flow around 0.058 g/s and heat flux about 28 W/mm^2) have been chosen as an illustration. Figure 4-18 shows the outside wall and the inside wall temperature obtained for each test. In one test, the temperature presents a sharp peak and a significant temperature drop at the end of the tube. In the second test, the temperature stays almost constant

along the tube. The temperature at the end point of the tube is the same for both tests. The conditions in terms of pressure, heat flux and mass flow, do not seem to determine the temperature profile. Other parameters should be considered as the roughness of the surface

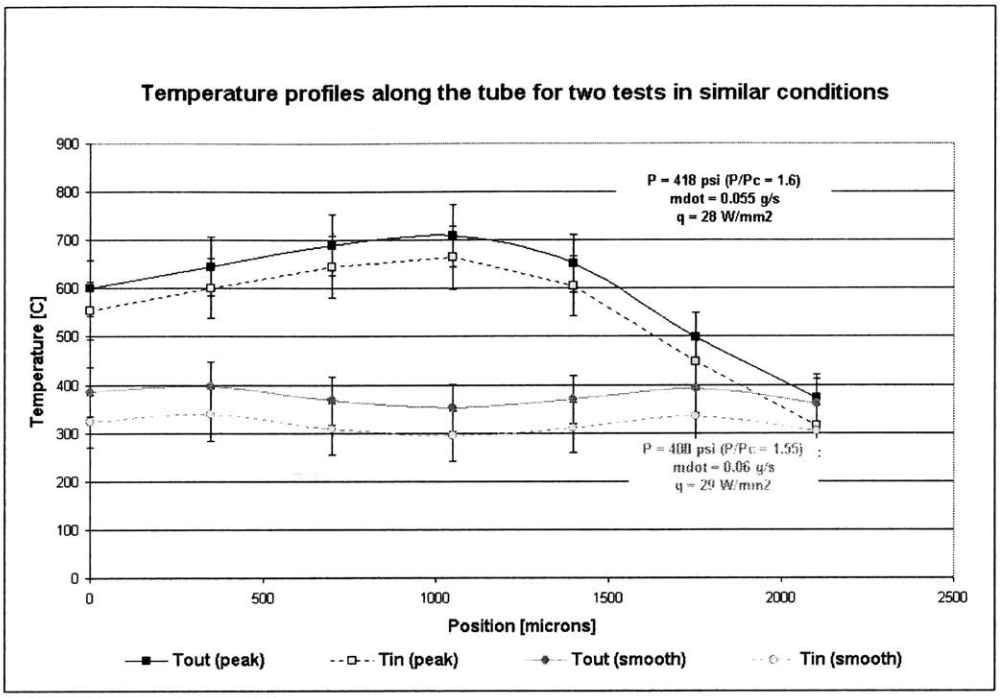

Figure 4-18: Temperature profiles for two tests carried out in similar conditions: P = 400 psi ($\frac{P}{P_c} = 1.55$), $\dot{m} = 0.058$ g/s and q = 28 W/mm^2. The outside wall and the inside wall temperatures are shown for both tests with experimental error bars.

of the tube or some instabilities developing in the tube. No clear condition has been found to determine the temperature profile in tests at macro scale [15].

4.3.4.4 Comparison of heat capacity enhancement reached for both profiles

Figure 4-17 presents the enhancement offered by JP7 for the different profiles. Four parameters are shown: the minimum and the maximum values reached by the heat transfer coefficient along the tube, the increase in the heat transfer coefficient and its value when non dimensionalized by the minimum heat transfer coefficient. Great enhancement is seen with both profiles. The highest values of the maximum and the minimum heat transfer coefficient are obtained with smooth profiles. This is due to the fact that these tests correspond to the highest heat fluxes. The non dimensional increase in the heat transfer coefficient obtained with each profile cover the whole range of values.

However, better cooling seem to be obtained with smooth profiles where lower outside wall temperatures are measured for the same test conditions. Figure 4-19 shows the heat transfer coefficients corresponding to the temperature profiles shown in Figure 4-18. One profile shows a smooth increase in the heat transfer coefficient with a sharper increase at the end of the tube, whereas in the other, the heat transfer coefficient stays at a floor value before a sharp increase at the end of the tube. It can be noticed that the final heat transfer coefficient reached at the end point of the tube is about the same for both profiles with a small advantage for the smooth profile. However, since the heat transfer coefficient is higher all along the tube in the smooth profile, the cooling is better with the smooth profile, which gives a lower wall temperature.

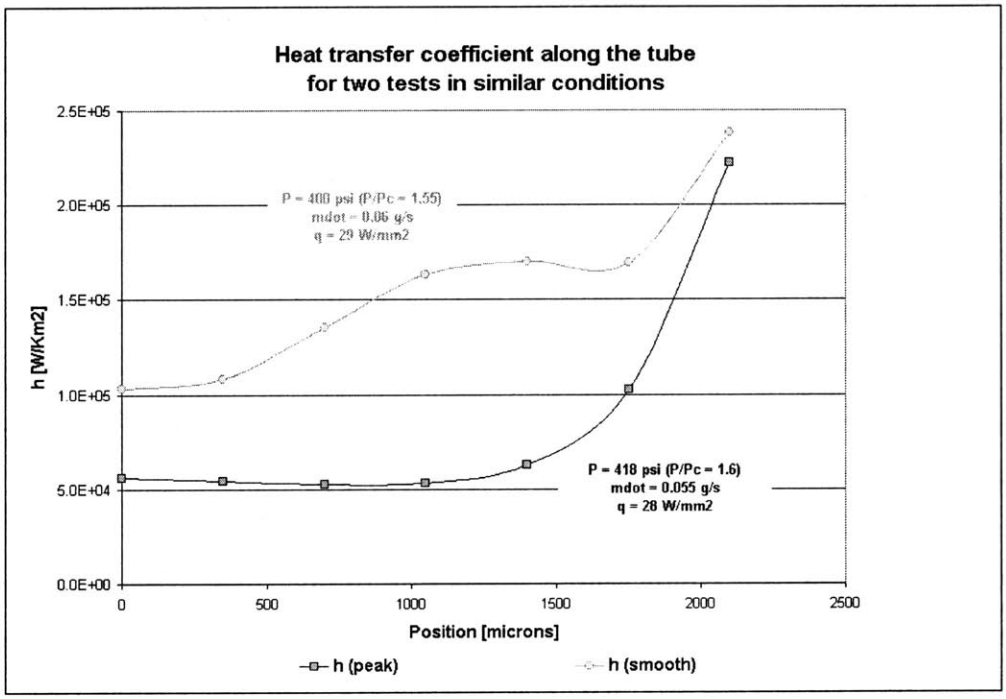

Figure 4-19: Heat transfer coefficient profiles for two tests carried out in similar conditions: P = 400 psi ($\frac{P}{P_c} = 1.55$), $\dot{m} = 0.058$ g/s and q = 28 W/mm^2.

4.3.5 Dependence of the heat capacity of JP7 on experimental conditions

4.3.5.1 Study of the heat transfer coefficient

4.3.5.1.1 High heat transfer coefficients Figure 4-20 illustrates the conditions in which the 20 % highest heat transfer coefficients are seen. The highest heat transfer coefficients (maximum and minimum values along the tube) are obtained for high heat fluxes.

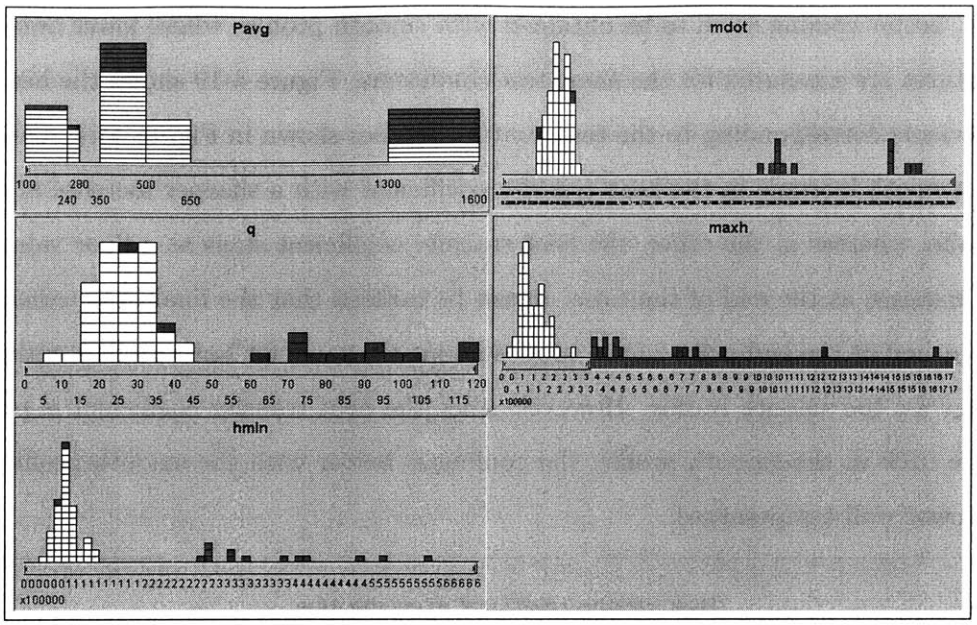

Figure 4-20: Summary of the attributes of the 65 tests carried out with JP7. The dark cases correspond to the tests which offer the 20 % highest heat transfer coefficients along the tube. The end point is assumed to be at 1,750 microns from the entrance.

The heat transfer coefficients obtained during tests at very high heat fluxes from 60 W/mm^2 to 120 W/mm^2 are shown in Figure 4-21. Tests are done at two mass flows (0.24 g/s and 0.35 g/s) and for two pressures ($\frac{P}{P_c}$ = 1.5 and $\frac{P}{P_c}$ = 5). Heat transfer coefficients are calculated between 3.43×10^5 W/Km^2 and 1.62×10^6 W/Km^2.

4.3.5.1.2 Heat transfer coefficient as a function of heat flux Figure 4-22 presents the heat transfer coefficients obtained at 1,750 microns from the entrance of the tube for the different tests carried out at a mass flow of 0.055 g/s. The heat transfer coefficient is seen to increase as a function of the heat flux applied to the tube. However, it may be noticed that the heat transfer coefficient values obtained may be biased by the thermal entry length in the tube. The thermal entry length is estimated at approximately 10 times the tube diameter, which gives an estimated thermal length of 950 microns for the tubes used in these experiments. Therefore, results at the end point should not be influenced by the entrance region. However, even if the thermal entry length is said not to be dependent on the heat flux applied, experiments done with water and ethanol [18] have reported that, in micro tubes, longer entry lengths were seen as the heat flux was increased. For heat fluxes around 100 W/mm^2, the entry length extended past the midpoint and sometimes reached

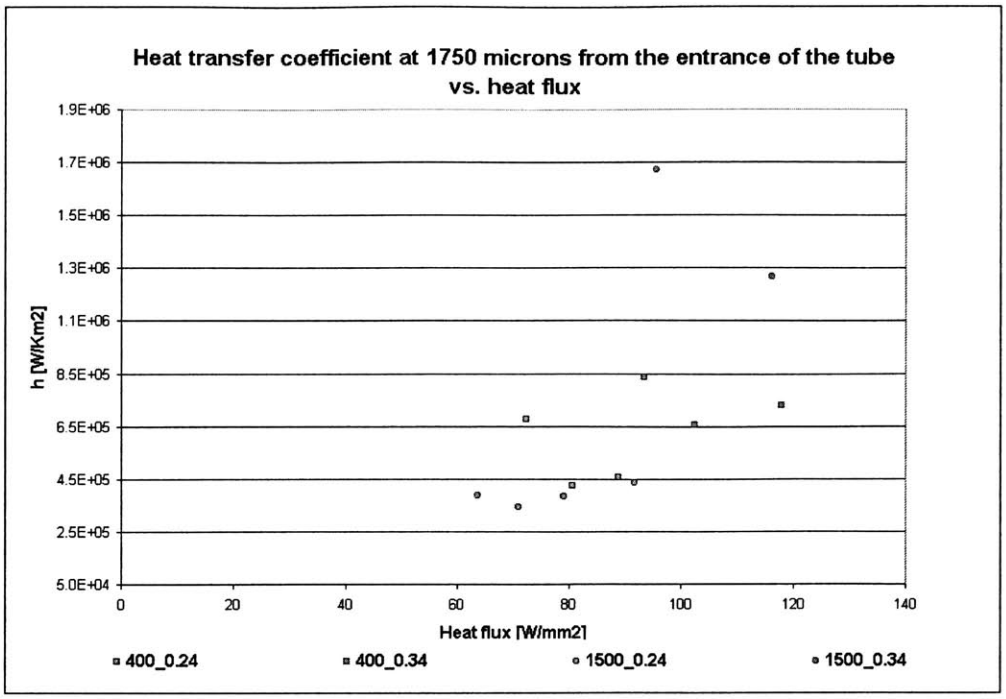

Figure 4-21: Heat transfer coefficient as a function of heat flux for different pressures at high heat fluxes. The series labels correspond to *pressure_mass flow* for the test.

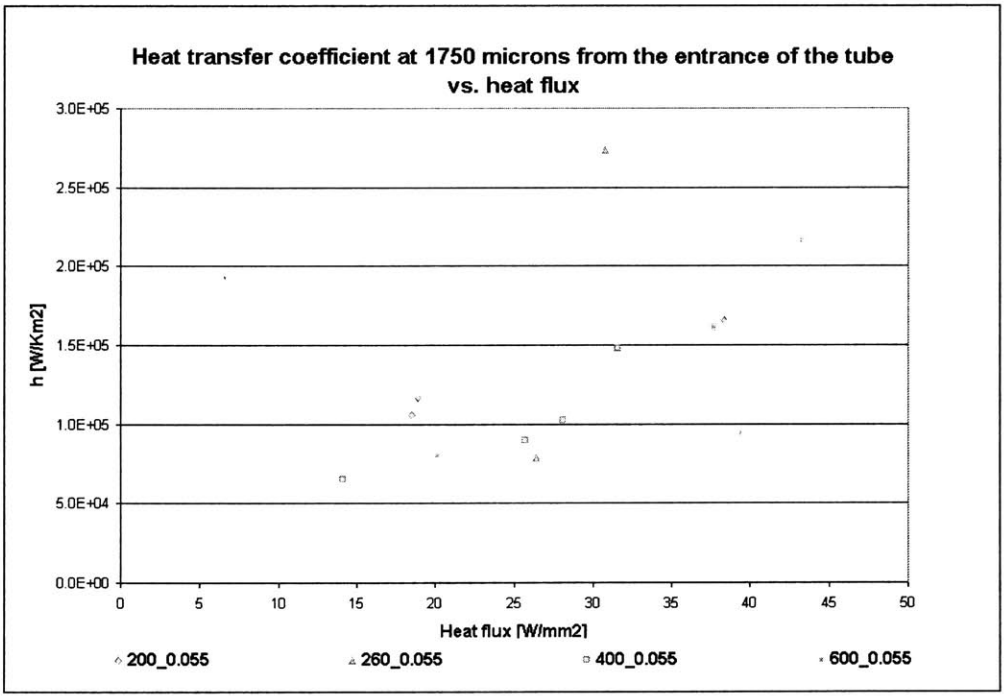

Figure 4-22: Heat transfer coefficient at 1,750 microns from the entrance as a function of heat flux for different pressures and a mass flow of 0.055 g/s.

the end point of the tube. Therefore, at high heat fluxes the heat transfer coefficient may be overestimated because of entrance effects.

The same trend is seen for the enhancement in heat transfer coefficient along the tube, which increases as the heat flux is increased. The enhancement in heat transfer is calculated as the difference in heat transfer coefficient between the minimum value measured along the tube and the value at 1,750 microns from the entrance. The minimum value of the heat transfer coefficient is reached at the point where the temperature starts to stabilize. Decomposition has already started at this point and therefore the minimum value of the heat transfer coefficient is not the value of the heat transfer coefficient before decomposition occurs. Moreover, the entrance effects also affect the results. However, the point where the decomposition effects become really significant corresponds to the point where the peak in heat transfer coefficient is seen. The minimum value corresponds to the value of the heat transfer coefficient before the decomposition effects are really significant. The increase in heat transfer coefficient as calculated can therefore be considered as a first approximation of the enhancement in heat transfer coefficient provided by the reaction. Figure 4-23 shows the increase in heat transfer coefficient for the tests carried out at a mass flow of 0.055 g/s shown in Figure 4-22. Again, entrance effects may affect the results.

Heat flux is expected to have an impact on both the supercritical phenomenon and the endothermic decomposition:

- Effect of the heat flux on supercritical effects: The supercritical effects are seen only if the heat flux is high enough so that the wall temperature reaches the pseudo critical temperature. However, at very high heat fluxes, the supercritical effects are expected to be reduced.

- Effect of the heat flux on the decomposition reaction: At high heat fluxes, the enhancement due to the decomposition of JP7 is expected to increase. As more heat is given to the fluid, the endothermic decomposition equilibrium is expected to shift towards more decomposition of the fluid, therefore increasing the fluid heat capacity.

No deterioration of the heat transfer coefficient has been seen at high heat fluxes in supercritical conditions.

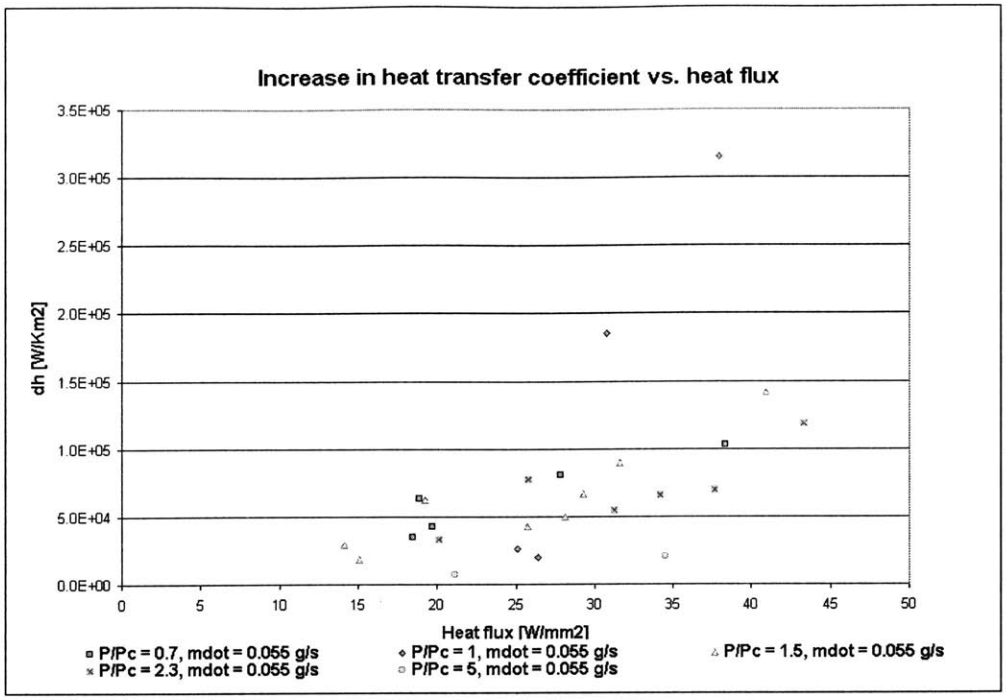

Figure 4-23: Increase in heat transfer coefficient along the tube as a function of heat flux for different pressures and a mass flow of 0.055 g/s.

4.3.5.1.3 Heat transfer coefficient as a function of pressure Effects of the supercritical conditions and of the reaction of decomposition are combined. At very high critical pressure ratios, the peak of Cp is much decreased so that the enhancement resulting from the supercritical effects can be assumed to be negligible compared to the endothermy of the decomposition reaction. The relative impact of the two phenomena can be studied by comparing the results obtained at different pressures.

Tests have been carried out at subcritical, critical and supercritical pressures. Figure 4-23 shows the increase in the heat transfer coefficient as a function of heat flux for different pressures at a mass flow of 0.055 g/s. It can be noticed that tests carried out around the critical pressure show a higher variation than at other pressures. Both high and low enhancements in the heat transfer coefficient are seen at critical pressure. This may be due to some instabilities occurring around the critical point. If the supercritical effects were predominant, enhancement in heat transfer coefficient would be expected to be negligible in subcritical tests, very high at critical and almost not apparent at very high critical pressure ratios. Increases in the heat transfer coefficient are seen both at subcritical and high critical pressure ratios. Therefore, the assumption that the endothermic reaction is the predomi-

nant phenomena in the enhancement of JP7 heat capacity seems to be verified.
The enhancement in the heat transfer coefficient slightly decreases as pressure increases as seen in Figure 4-23 for the tests at a mass flow of 0.055 g/s. As pressure increases, it is expected that the reaction equilibrium will be modified to react by decreasing the number of moles and therefore to be shifted towards less decomposition of the fluid. However, as the decrease is small, the experimental errors may not give much confidence in this evolution. Pressure does not seem to be a major parameter.

4.3.5.1.4 Non dimensional increase in heat transfer coefficient The increase in the heat transfer coefficient gives an estimation of the absolute value of the enhancement in heat transfer coefficient offered by the decomposition reaction. The minimum level from which the increase is calculated strongly varies from one test to another. The increase was non dimensionalized by studying the ratio of the increase in heat transfer coefficient to the minimum value of the heat transfer coefficient. Figure 4-24 presents the non dimensional increases in the heat transfer coefficient as a function of pressure. Subcritical results are very variable; increases in heat transfer coefficient from 14 % to 700 % are reached. Increases as high as 1.5 times the minimum heat transfer coefficient are obtained at all pressures. At high pressures ($\frac{P}{P_c} = 5$), the results depend on the mass flow. Three groups, which correspond to different mass flows, are identified by circles in Figure 4-24. The higher the mass flow is, the higher the non dimensional increase is. The same mass flow dependence is not seen at 400 psi. The circle at 400 psi identifies the results at the highest mass flow of 0.36 g/s. These results do not correspond to the highest non dimensional increases. Other groups appear for the tests at 400 psi and 600 psi. No common parameters were identified to characterize these similar results. They do not correspond to tests done on the same tube. No dependence on heat flux, inside wall temperature or bulk temperature was found to explain those results.

4.3.5.1.5 Mass flow effect The study of the heat transfer coefficient is strongly affected by the mass flow and the Reynolds number. Figure 4-25 shows the minimum value of the heat transfer coefficient along the tube as a function of pressure. Different groups appear, corresponding to different ranges of mass flows. The higher the mass flow, the higher the heat transfer coefficient. To study the endothermy of the reaction, it was therefore decided

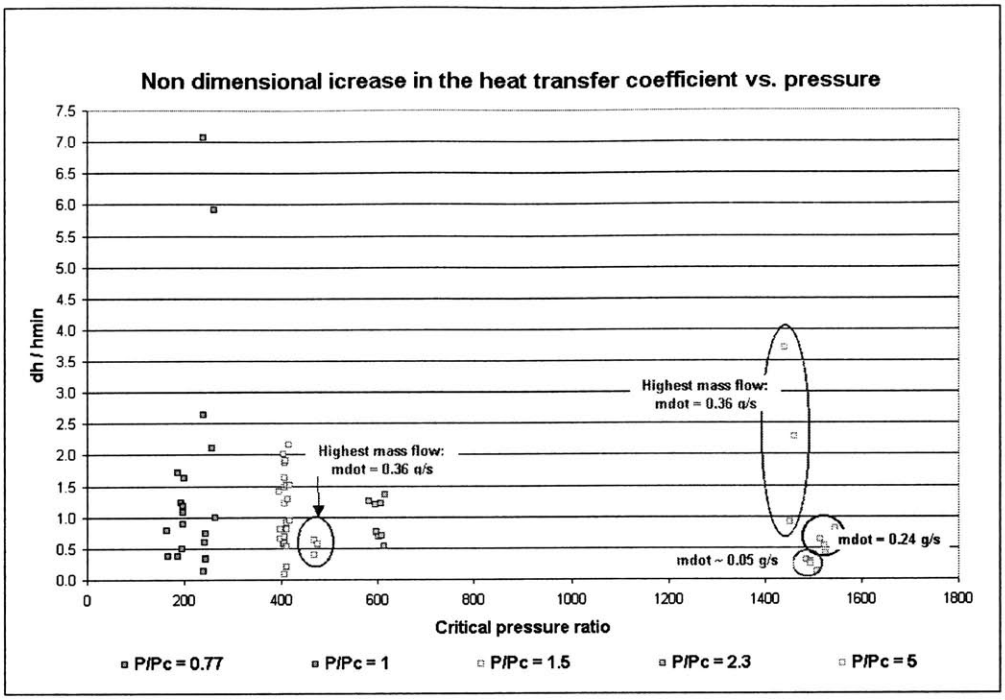

Figure 4-24: Non dimensional increase in the heat transfer coefficient as a function of pressure.

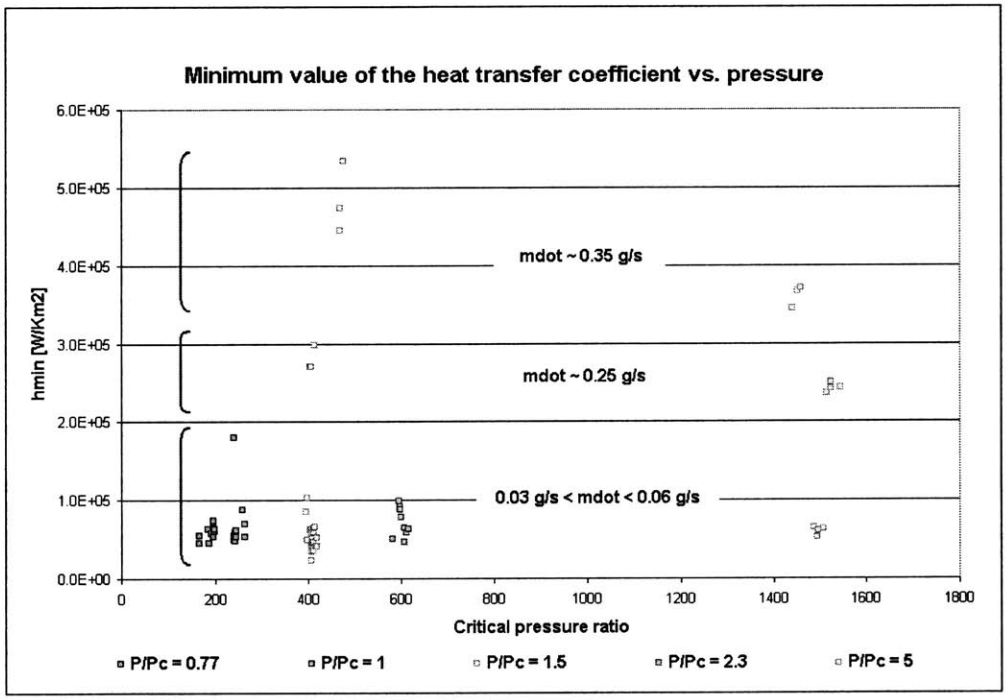

Figure 4-25: Minimum heat transfer coefficient along the tube as a function of pressure.

to use the non dimensional Stanton number which allows to eliminate the bias due to the Reynolds number.

4.3.5.2 Stanton number Study

4.3.5.2.1 Mass flow effect minimized The study of the Stanton number allows suppression of the effect of the Reynolds number. Figure 4-26 shows the minimum value of the

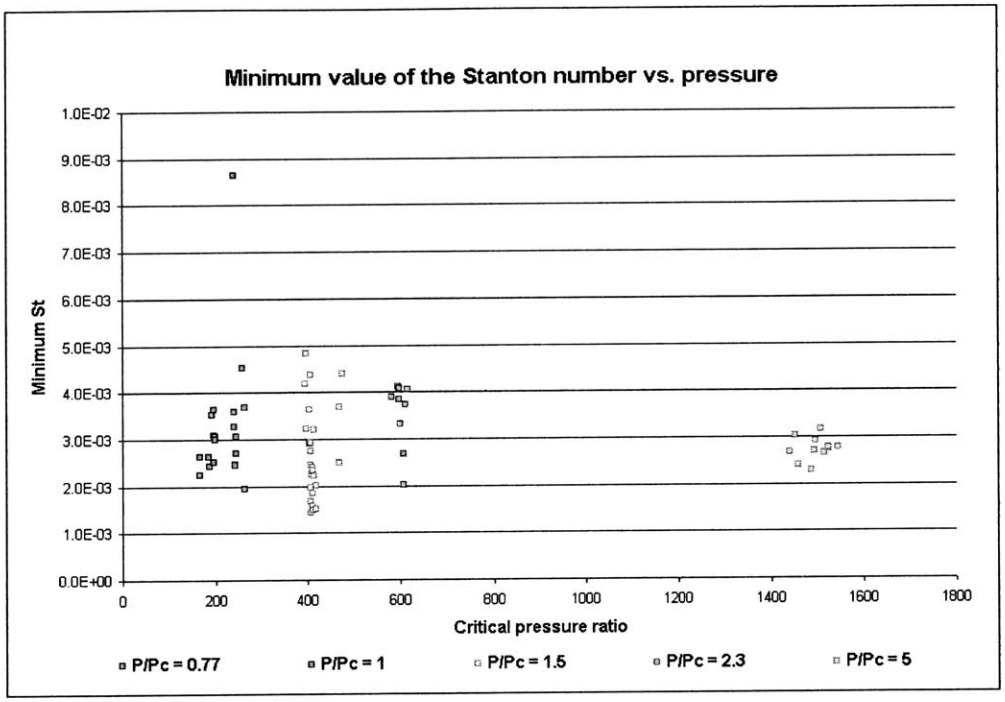

Figure 4-26: Minimum Stanton number along the tube as a function of pressure.

Stanton number as a function of pressure. The strong effect of the mass flow on the heat transfer coefficient, which was clear in Figure 4-25, does not appear in the Stanton number.

4.3.5.2.2 Stanton dependence on experimental conditions The Stanton number should start to increase at the point where the decomposition starts to become significant. As for the heat transfer coefficient, the floor value of the Stanton number is assumed to be a first estimation of the value of the Stanton number before decomposition becomes significant. The floor value is only a rough estimation of the Stanton number with no enhancement phenomena. First, decomposition has already started causing the Stanton number to stabilize. Second, the point at which the Stanton number starts to rise is usually still in the entrance region. Therefore the floor value chosen to evaluate the effect of decomposition

is overestimated. The effect of the enhancement is estimated from the difference between the maximum value (the end point is set at 1,750 microns from the entrance) and the floor value of the Stanton number. Since the supercritical effect is accounted for in the enthalpy, the enhancement in the Stanton number is assumed to correspond to the endothermy due to the reaction of decomposition.

The increase in the Stanton number is plotted as a function of heat flux for different mass flows and pressures in Figure 4-27. The enhancement in the Stanton number seems to increase as the heat flux is increased as seen with the points on the left of the plot. However, at high heat fluxes, the increase in Stanton number is lower and no clear trend appears as the heat flux is increased. Fewer tests have been done at very high heat fluxes and trends may not be so apparent. Moreover, the highest heat fluxes have only been tested at very high mass flows.

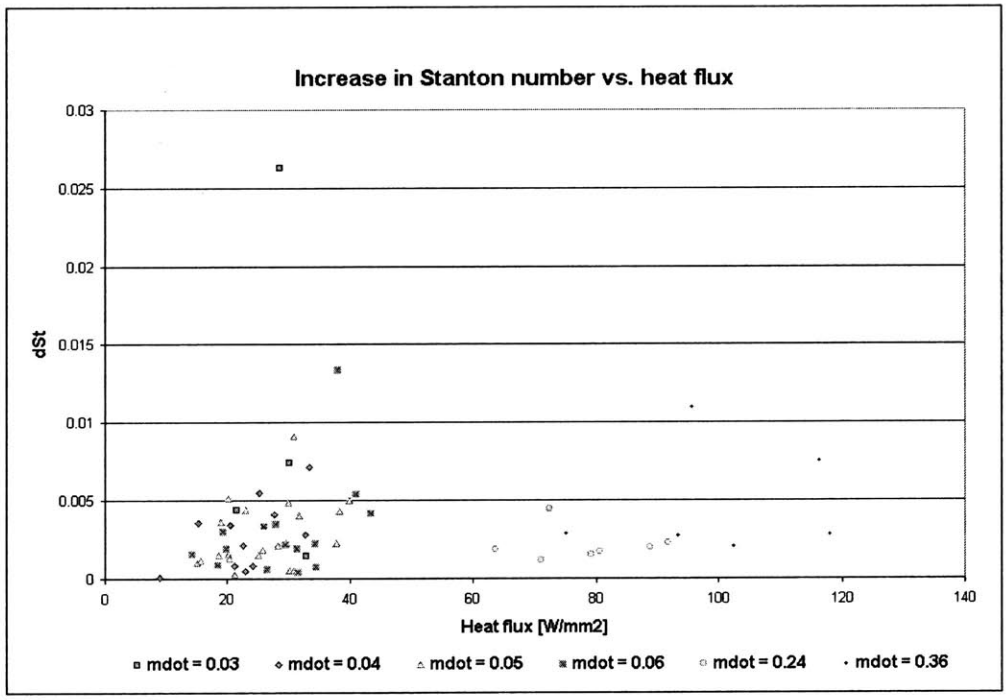

Figure 4-27: Increase in Stanton number as a function of heat flux for different mass flows.

The same trend appears with the minimum value of the Stanton number shown in Figure 4-28. The minimum value of the Stanton number even decreases as the heat flux is increased for a mass flow of 0.34 g/s. No trend related to the pressure seems to explain this decrease. As the heat flux is increased, the entry length increases and therefore the Stanton number

should stabilize at a higher value. One possible reason could have been that the decomposition effects were seen later in the tube so that the Stanton number decreases further at high heat fluxes. However, this is not the case, the higher the heat flux, the sooner the increase in Stanton number is seen.

Since decomposition is linked to the temperature, the increase in Stanton number has been

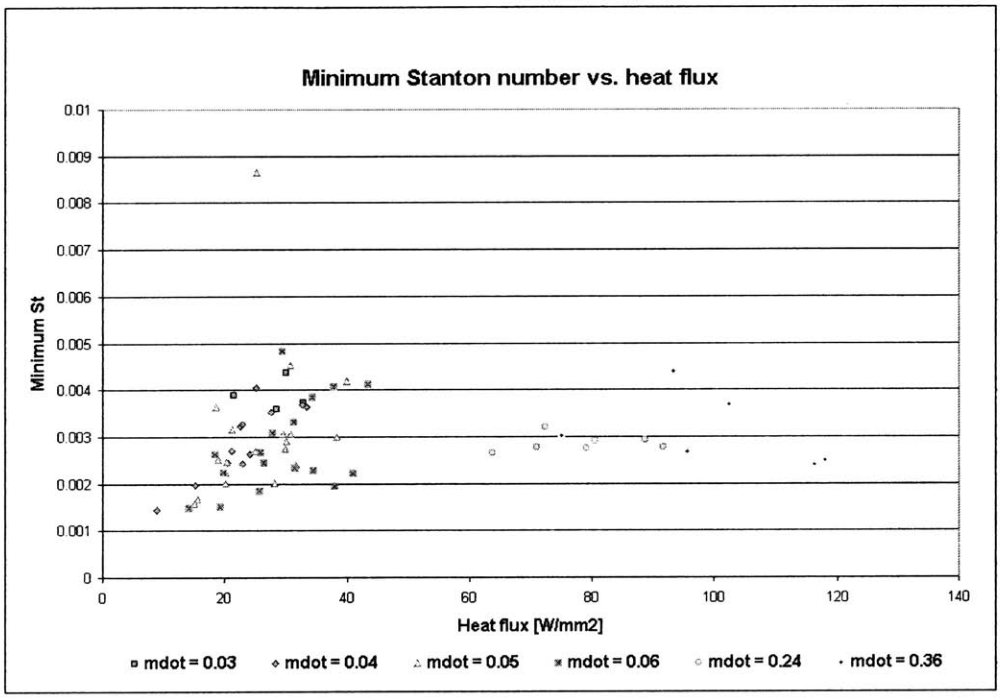

Figure 4-28: Minimum value of the Stanton number as a function of heat flux for different mass flows.

plotted against the maximum inside wall temperature reached in the tube. Figure 4-29 illustrates that as the inside wall temperature increases, the enhancement in the Stanton number increases. As pressure increases, the enhancement seems to be reduced as shown in Figure 4-30. In this figure, the increase in the Stanton number is plotted as a function of pressure. For mass flows around 0.05 g/s, the increase in the Stanton number is reduced at higher pressures.

Figure 4-30 also underlines the effect of the mass flow still apparent at high pressures. At P = 1,500 psi, three groups are apparent corresponding to the three levels of mass flows. The higher the mass flow is, the higher the increase in the Stanton number is. This trend is not apparent at 400 psi, for which similar mass flows have been tested.

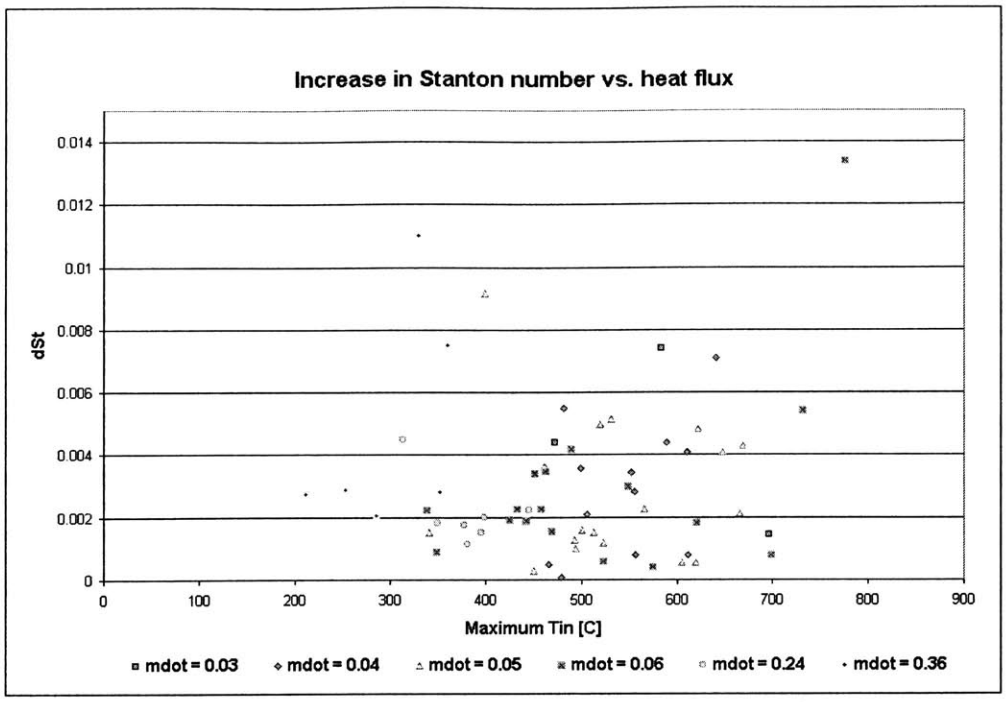

Figure 4-29: Increase in the Stanton number as a function of the maximum inside wall temperature reached along the tube.

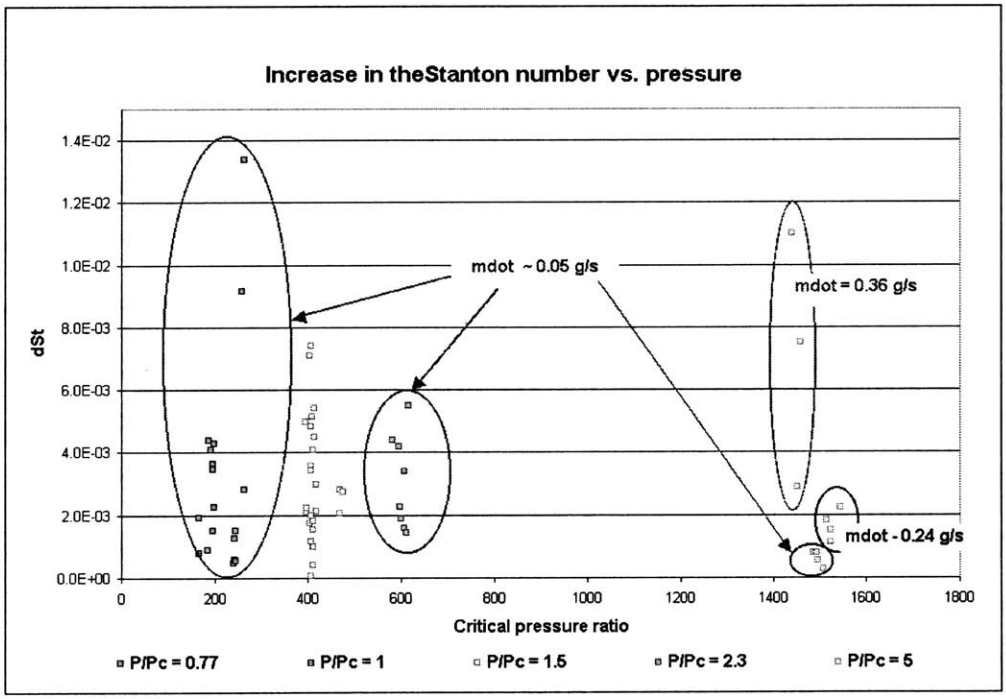

Figure 4-30: Increase in the Stanton number as a function of pressure.

4.3.5.3 Conclusions

Both the heat transfer coefficient and the Stanton number have been studied to characterize the heat capacity of JP7. The heat transfer coefficient is of great interest since it is the parameter used to design the micro rocket engine cooling passages. The increase in the heat transfer coefficient characterizes the enhancement offered by both the supercritical conditions and the reaction of decomposition of JP7. The Stanton number is studied first to get rid of the bias introduced by the Reynolds number in the heat transfer coefficient; and second, because as the supercritical effect is accounted for in the enthalpy profile used in the calculations, the Stanton number increase is only due to the effect of the reaction of decomposition. The increase in the Stanton number offers a way to characterize the endothermy and the enhancement in heat capacity due to the reaction of decomposition.

The enhancement offered by the endothermic reaction of JP7 has been verified and very high heat transfer coefficients have been reached at high heat fluxes. The analysis of the data shows a trend towards an increased endothermy at higher heat fluxes and a decreased endothermy at higher pressures. However, no clear trends have been identified to allow a good prediction of the enhancement at different pressures and heat fluxes. The analysis of the endothermy is difficult because of different parameters:

- Even if the supercritical effects are thought to be negligible compared to the endothermic reaction, the combination of the two phenomena increases the complexity of the analysis of the results.
- Mass flow and heat fluxes are linked and the combination of both effects is unclear. There is a discrepancy between tests at mass flows around 0.05 g/s and tests at very high mass flows (0.24 g/s). There may be another parameter governing the evolution of the endothermy that would link those results.
- The IR sensor does not allow measurements below 328°C and the tube cannot withstand temperature above 600°C. Additional data at low heat fluxes and high mass flows or high heat fluxes and low mass flows could have been helpful.

4.3.6 Analysis of JP7 endothermic reaction

In this section, a first model of the effect of the endothermic reaction is presented.

4.3.6.1 Background information: macro scale data

Very few data are available on JP7 endothermic reaction. Some studies have been carried out at the Air Force Research Laboratory. Some data available at macro scale estimate the endothermy of the reaction around 1,395,600 J/kg at 1,000 psi for a 50 % conversion of the fluid [4]. The reaction is said to occur between 550°C and 650°C.

4.3.6.2 Model developed

4.3.6.2.1 Enthalpy increase The reaction can be characterized by four parameters:

- the conversion of the fluid
- the temperature range within which the reaction occurs
- the endothermy of the reaction
- the composition of the fluid after the reaction occurred

The reaction is endothermic. Therefore, as the fluid reacts, its heat capacity is increased. This can be considered as an increase in the enthalpy of the fluid as it reacts. Therefore, the model was constructed by adding the endothermy of the reaction to JP7 enthalpy from regular supercritical data.
The following assumptions were taken:

- The reaction only occurs within a specific temperature range.
- The endothermy is assumed to be gained linearly within the temperature range.
- Only part of the fluid hydrocarbons convert to lighter hydrocarbons and the reaction is characterized by a conversion factor. This conversion factor affects the total endothermy offered by the reaction and the final composition of the fluid after the reaction has stopped.

The enthalpy profile of the fluid is then calculated as a function of temperature. The temperature is assumed to increase from a temperature below the reaction onset temperature to a temperature above the reaction temperature range.
The model has the following inputs:

- JP7 specific heat profile without decomposition, which depends on the conditions chosen for the fluid
- a baseline endothermy of the reaction for a baseline conversion factor
- the conversion factor of the fluid, which may depend on the conditions chosen for the fluid
- the initial composition of the fluid
- a baseline final fluid composition for a baseline conversion factor

The model is derived as follow:

1. JP7 enthalpy profile without taking into account the decomposition is derived from the specific heat profile. In case of supercritical conditions, the supercritical effect is taken into account in the specific heat profile. It represents the enthalpy the fluid would have if no decomposition occurred. This enthalpy profile corresponds to the enthalpy used in the data reduction process for JP7 tests.

2. The heat capacity enhancement is calculated from the endothermy of the fluid reduced to the fluid conversion obtained in the specific conditions chosen. The baseline endothermy is multiplied by the ratio of the conversion factor and the baseline conversion factor to get the enhancement in heat capacity.

3. This heat capacity enhancement is added to the enthalpy profile obtained in step one. A linear profile is assumed between the onset reaction temperature and the temperature at which the reaction stops.

4. The enthalpy profile after the reaction has occurred has to be modified to take into account that the composition of the fluid is no longer the same. The final composition of the fluid is calculated from the initial composition, the conversion factor and the baseline assumptions.

$$[X]_f = [X]_i + \varepsilon\left([X]_i^b - [X]_f^b\right)\frac{conversion}{conversion^b} \tag{4.1}$$

where X refers to one of the fluid component, $[X]$ is the concentration in X in the fluid and $conversion$ corresponds to the conversion factor. The subscripts i, f and b

refer respectively to the fluid before the reaction occurred, the fluid after the reaction occurred and the baseline assumptions. $\varepsilon = 1$ if X reacts during the reaction and $\varepsilon = -1$ if X is a product of the reaction. The specific heat of the final fluid is calculated from the specific heat of each component in the specific conditions chosen and the final composition of the fluid.

An example of the enthalpy profile obtained is shown in Figure 4-31. The assumptions for this model are summarized in Table 4.1. The enthalpy with no decomposition has been calculated from JP7 supercritical properties.

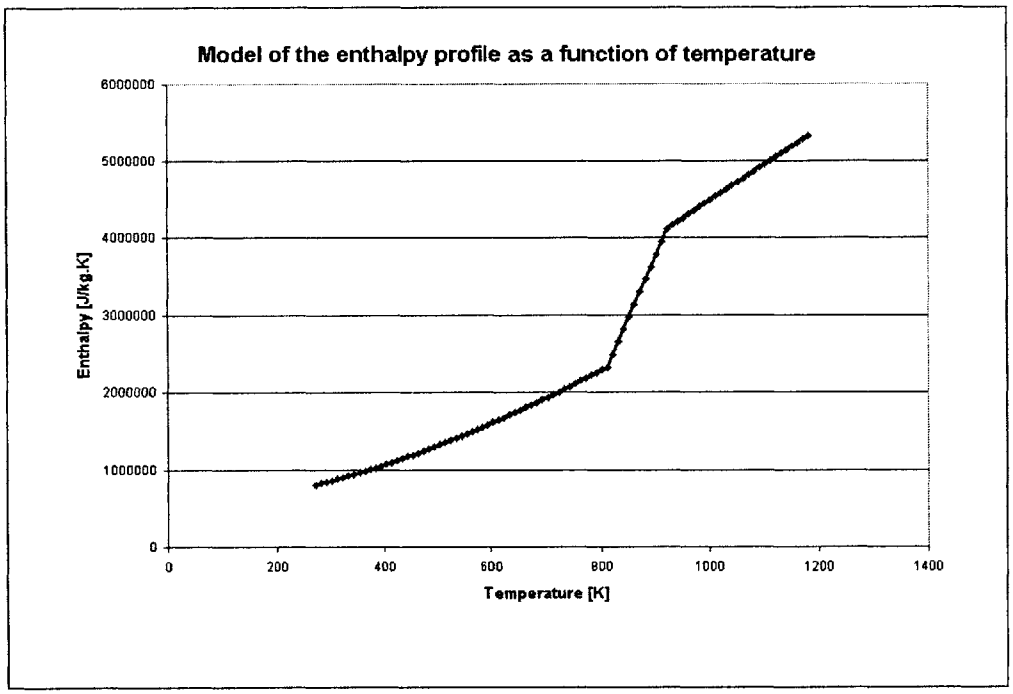

Figure 4-31: Model of JP7 enthalpy profile taking into account the endothermic decomposition. The model uses the assumptions presented in Table 4.1.

4.3.6.2.2 Hysteresis In the tests carried out, the temperature increases at the entrance, stabilizes and then decreases at the end of the tube. The previous model gives the enthalpy profile as the temperature is increasing. As the temperature decreases, the same profile cannot be used since the enthalpy does not decrease in the range of temperature where the reaction occurred. Therefore, a different enthalpy profile is derived for decreasing temperatures.

The temperature decreases because the effects of the reaction are significant. The enthalpy

Enthalpy Model Assumptions

Reaction temperature range	Reaction onset temperature	450°C
	Reaction stop temperature	550°C
Endothermy	Baseline endothermy	1,395,600 J/kg
	Baseline conversion factor	50%
Initial composition	H_2	3.0%
	CH_4	18.0%
	C_2H_4	16.0%
	C_2H_6	19.5%
	C_3H_6	17.5%
	C_3H_8	15.0%
	C_4H_8	7.0%
	C_4H_10	4.0%
Baseline final composition	H_2	4.0%
	CH_4	28.0%
	C_2H_4	15.0%
	C_2H_6	18.5%
	C_3H_6	16.5%
	C_3H_8	11.0%
	C_4H_8	4.0%
	C_4H_10	3.0%
	Baseline conversion factor	50%
Specific conditions	Pressure	1000 psi
	Conversion factor	50%

Table 4.1: Assumptions for the enthalpy model

profile must take into account the on-going decomposition. The following model is adopted:

- As the temperature increases along the tube, the previous enthalpy profile is used to estimate the enthalpy of the fluid. An endothermy and a temperature range for the reaction are chosen.

- As the temperature starts to decrease, the enthalpy is assumed to still increase linearly until the reaction onset temperature is reached. The profile has been chosen symmetric to the enthalpy profile as the temperature increases and the reaction occurs. The increase in enthalpy due to the reaction is assumed to be limited by the endothermy chosen for the profile used as the temperature increases. A certain conversion of the fluid can be reached providing a certain available endothermy. As the temperature decreases, the conversion of the fluid should be smaller than if higher temperatures were reached. Therefore, it was assumed that the maximum endothermy reached was the endothermy chosen for the increasing temperatures. The enthalpy of the fluid as the temperature decreases back to the onset reaction temperature is assumed to be the minimum between the enthalpy given by the symmetric profile and the enthalpy reached at the end reaction temperature in the increasing temperature enthalpy profile.

- As the temperature decreases below the reaction onset temperature, the reaction is assumed to stop. The enthalpy profile is then calculated from the final composition of the fluid and the specific heat of the different components. The specific heat of the fluid is calculated as the specific heat of the mix of its components weighted by their respective concentration.

Figure 4-32 illustrates the model used for a maximum endothermy of 2,895,588 J/kg, a reaction occurring between 530°C and 641°C and a 50 % conversion. Under these assumptions, the maximum endothermy limits the enthalpy of the fluid.
Figure 4-33 shows an example of a set of assumptions for which the symmetric enthalpy profile is used for the decreasing temperatures because the maximum endothermy does not limit the enthalpy profile.

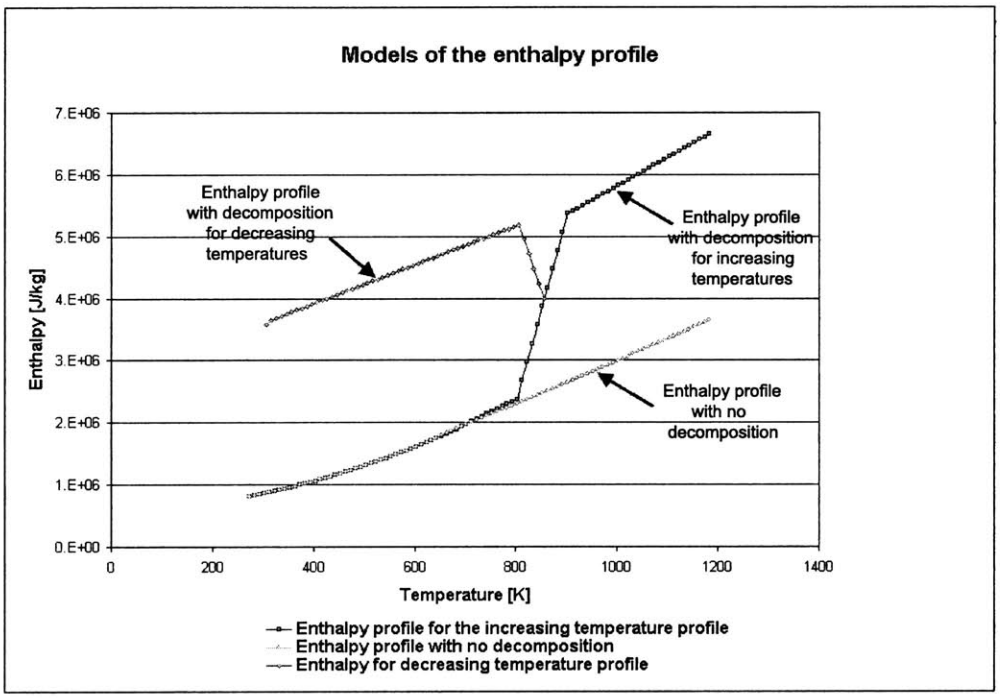

Figure 4-32: Model of the enthalpy profiles. The enthalpy profiles without decomposition and with decomposition respectively for increasing and decreasing temperatures are shown. The following assumptions were used to model the reaction: a maximum endothermy of 2,895,588 J/kg, an onset temperature of 530°C, an end reaction temperature of 641°C and a conversion of 50 %.

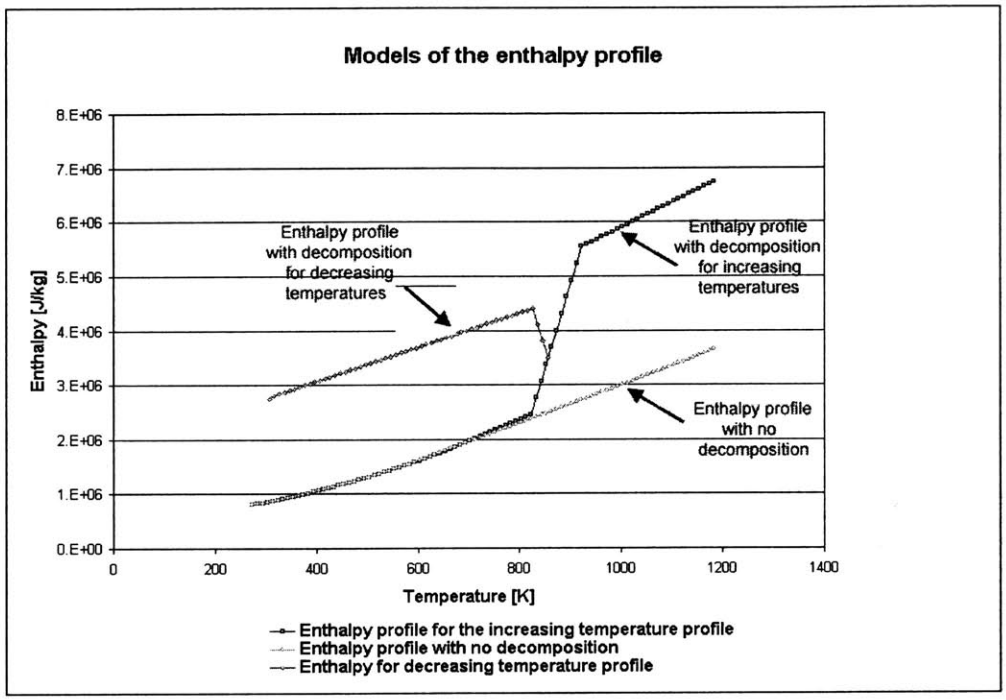

Figure 4-33: Model of the enthalpy profiles. The enthalpy profiles without decomposition and with decomposition respectively for increasing and decreasing temperatures are shown. The following assumptions were used to model the reaction: a maximum endothermy of 3,000,000 J/kg, an onset temperature of 550°C, an end reaction temperature of 661°C and a conversion of 50 %.

4.3.6.2.3 Comparison of the model with the data The Stanton number was recalculated from the experimental data using the enthalpy model developed in the previous paragraph. Since the reaction is expected to start at temperatures above the maximum bulk temperature reached, the bulk temperature has not been recalculated. Different calculations have been done varying the onset temperature and the maximum endothermy obtained. The final composition used in all the calculations has not been modified and is the same as the one shown in Table 4.1 since no data were available. As the composition is held constant, the conversion factor only impacts the endothermy seen. Therefore, it has been chosen to hold the conversion factor constant at 50 % and to modify the maximum endothermy. Only the onset reaction temperature is varied. The reaction is assumed to occur in a temperature range of 100°C as seen in macro scale tests.

Figure 4-34 compares the Stanton number obtained with the enthalpy model with the Stanton number obtained without taking into account the decomposition for a test at a pressure of 400 psi, a mass flow of 0.033 g/s and a heat flux of 30 W/mm^2. As explained in sec-

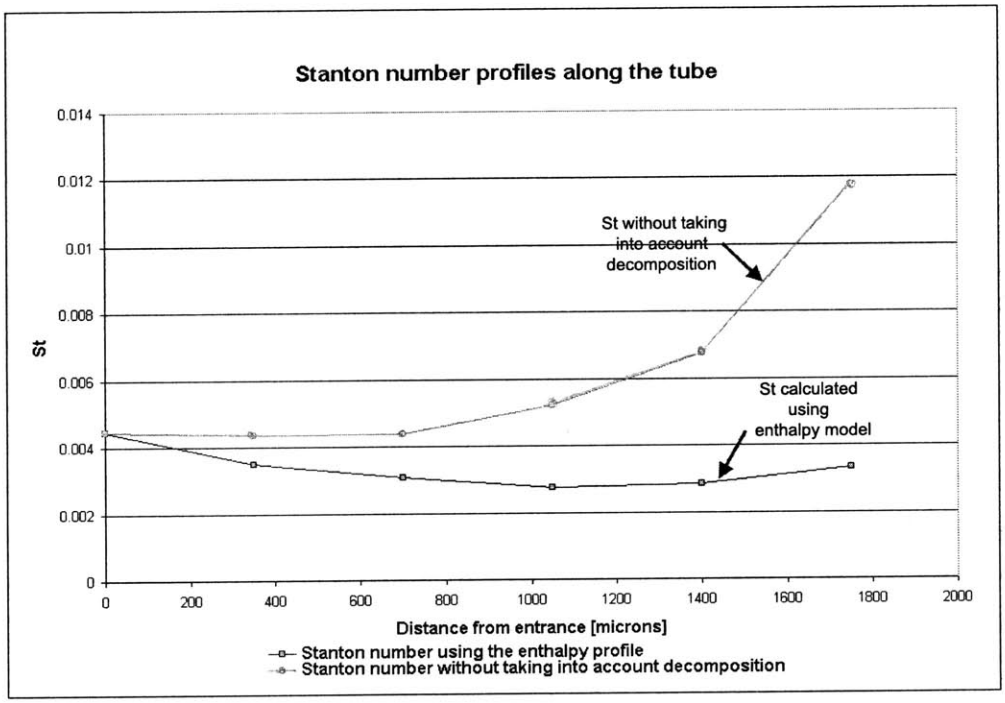

Figure 4-34: Stanton number profiles along the tube. The Stanton numbers calculated without taking into account the decomposition and from the enthalpy model are represented. For this calculation, a reaction onset temperature of 530°C and a maximum endothermy of 1,395,588 J/kg are assumed.

tion 4.3.5.2, if the effect of the decomposition is not accounted for, the Stanton number increases significantly at the end of the tube as shown on Figure 4-34. However, as the flow develops in the tube, the Stanton number is expected to decrease slowly before stabilizing to a floor value. The increase in the Stanton number is believed to be due to the reaction. By introducing the decomposition endothermy with the enthalpy model, the Stanton number has been significantly flattened as seen with the flat profile in Figure 4-34. The value of the Stanton number at the end of the tube is decreased from 0.012 to 0.003 (decrease of 75 %). However, the Stanton number is still increasing slowly at the end of the tube.
The inside wall and bulk enthalpies calculated with the entahlpy model for the same test

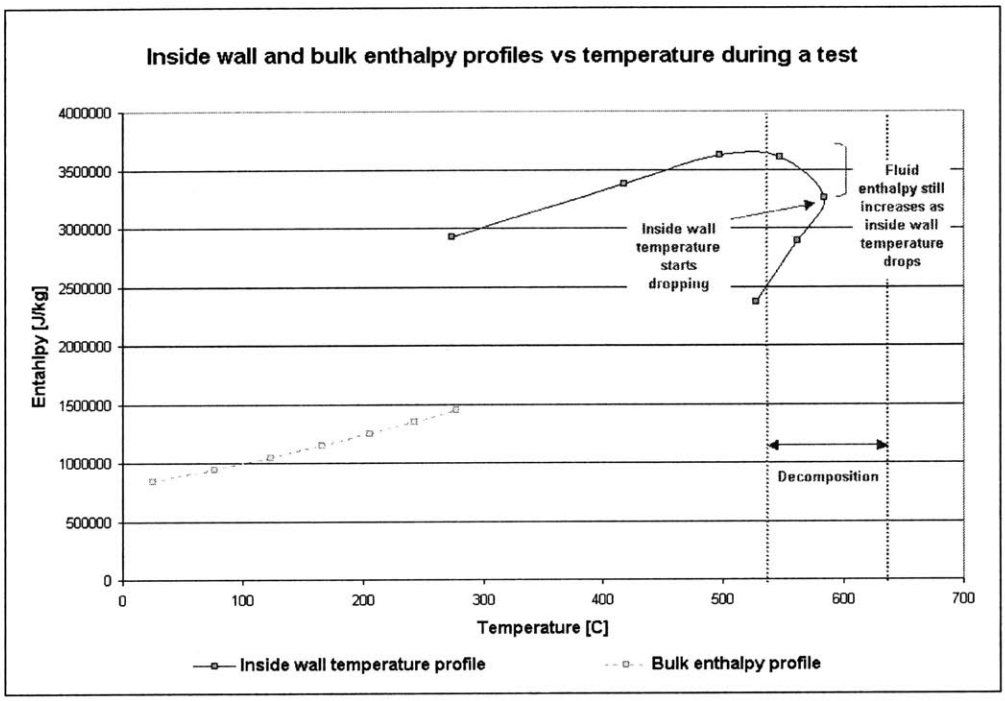

Figure 4-35: Inside wall and bulk enthalpies calculated from experimental data using the enthalpy model. The test was carried out at a pressure of 400 psi, a mass flow of 0.033 g/s and a heat flux of 30 W/mm^2. The calculation was done assuming for the model a reaction onset temperature of 530°C and an endothermy of 1,395,588 J/kg.

are shown in Figure 4-35.

4.3.6.2.4 Model fidelity JP7 enthalpy profile without taking into account decomposition is the most well-known parameter in the model. JP7 supercritical characteristics have been taken from [16]. The other parameters describing the reaction are guessed from few data obtained at macro scale and in conditions of pressure and mass flows different from

the conditions tested in the experiments presented in this work. It is very probable that the temperature range in which the reaction occurs, the endothermy and the conversion of the fluid are much dependent on the experimental conditions: pressure, mass flow, temperature and the size of the passages may be important factors. The conversion factor may depend also on turbulence. As turbulence increases, the bulk fluid is brought to the wall where the temperature is high enough for the fluid to decompose, therefore causing the conversion to increase. The composition of the products is one of the main unknowns.

Linear profiles were adopted for simplicity but may not be a good representation of the reaction mechanism.

The experimental results seem to show that most of the conversion of the fluid happens after the temperature starts dropping. If the model does take into account that the decomposition still occurs at the inside wall surface, it does not provide a greater enhancement as the temperature drops than when it increases. At best the same enhancement is provided (for a symmetric profile). The Stanton number profiles obtained with the enthalpy model still increase at the end of the tube and therefore illustrate that the model does not entirely capture what happens as the temperature drops and underestimates the enhancement provided by the reaction after the peak in temperature.

4.3.6.3 Sensitivity to the decomposition onset temperature and the reaction endothermy

4.3.6.3.1 Sensitivity to the temperature range where the reaction occurs The Stanton number has been calculated for a test at a pressure of 400 psi, a mass flow of 0.033 g/s and a heat flux of 30 W/mm^2 for different reaction onset temperatures ranging from 400°C to 600°C. The results are presented in Figure 4-36. The Stanton number without taking into account the decomposition is shown for comparison.

The Stanton number profile depends on the relative position of the onset temperature with respect to the inside wall temperature. The inside wall temperature calculated along the tube for the test considered in this study is shown in Table 4.2. As long as the inside wall temperature is below the reaction onset temperature, the Stanton number is not modified by the model since the enthalpy profiles are identical before the start of the reaction. For the points at which the inside wall temperature is above the reaction onset temperature, the Stanton number calculated from the model is lower. The endothermy of the reaction

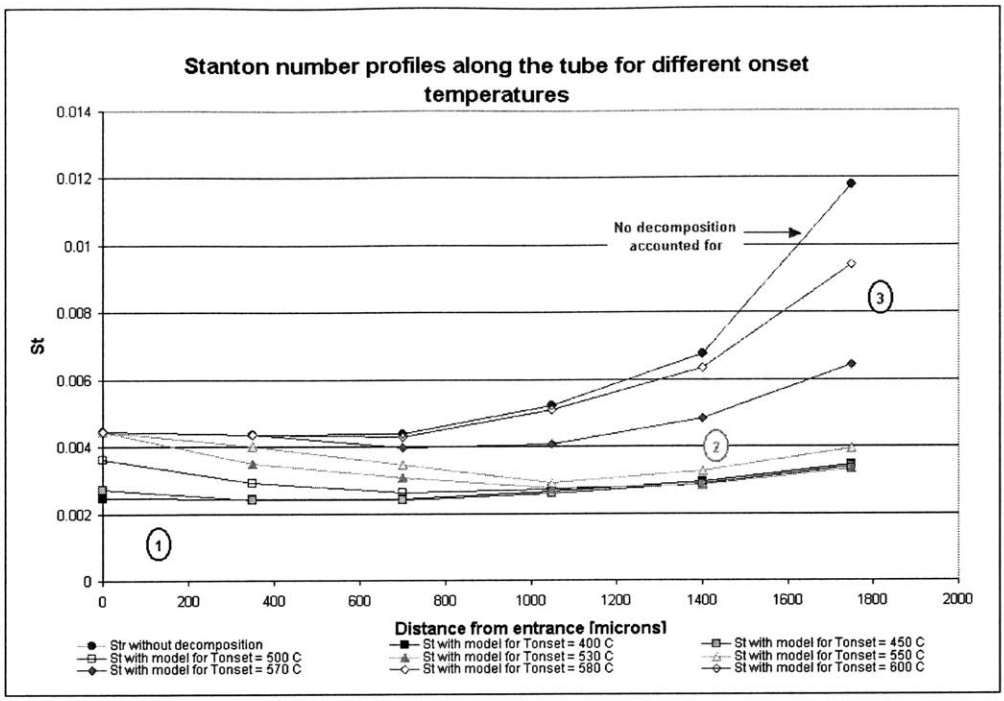

Figure 4-36: Stanton number profiles along the tube for reaction onset temperatures ranging from 400°C to 600°C. An endothermy of 1,395,588 J/kg is assumed in all the calculations. The Stanton profile obtained without accounting for the decomposition is showed as a comparison.

increases the enthalpy of the fluid at the inside wall. Therefore, the difference between the enthalpy of the fluid at the inside wall and the bulk fluid increases, causing the Stanton number to decrease.

Three trends can be seen:

1. If the onset temperature is below the inside wall temperature calculated at the first point, the model gives a flat Stanton number but far below the floor value obtained without the modeled enthalpy. As the onset temperature is increased, the Stanton number increases at the first points until the onset temperature reaches the inside wall temperature at the first point of measurement. Since the onset temperature is below the inside wall temperature at the first point, the fluid is assumed to already decompose at the entrance of the tube. The wall enthalpy is therefore higher since decomposition occurs and the Stanton number decreases as the difference between the inside wall and bulk enthalpy is bigger. As the onset temperature is increased, less endothermy is assumed at the entrance of the tube: the inside wall enthalpy decreases causing the Stanton number to increase.

Position [microns]	Inside wall temperature [°C]
0	528
350	561
700	583
1050	547
1400	497
1,750	417

Table 4.2: Inside wall temperature along the tube for a test at a pressure of 400 psi, a mass flow of 0.033 g/s and a heat flux of 30 W/mm^2.

2. The same process happens with the inside wall temperature at the second point of measurement. The Stanton number at the first point is the same with or without taking into account the decomposition. The Stanton number along the second half of the tube does not change significantly whereas the Stanton number at the second and third points increases slowly.

3. When the reaction onset temperature approaches the inside wall temperature at which the temperature starts dropping, the Stanton number profile on the second half of the tube varies rapidly, increasing towards the profile with no decomposition.

The reaction onset temperature has to be below the temperature at which the temperature starts to decrease. The temperature at which the decomposition stops is thought to be above the temperature at which the temperature starts to drop since the drop is caused by the decomposition endothermy.

4.3.6.3.2 Sensitivity to the endothermy of the reaction The study of the evolution of the Stanton profile as the endothermy was varied has been done on the same experimental test as the reaction onset temperature sensitivity analysis. The reaction onset temperature has been set to 530°C. The endothermy has been tested from 0 J/kg to 6,000,000 J/kg. The results are shown in Figure 4-37. At the highest endothermies, the Stanton number profile is decreasing at the entrance of the tube and stabilizes to a floor value. The higher the endothermy is, the lower the floor value is. For a large range of endothermies, from 6,000,000 J/kg to 2,000,000 J/kg, a flat Stanton profile is obtained. Floor values vary from 0.001 to 0.0025. As the endothermy decreases below 2,000,000 J/kg, the Stanton number

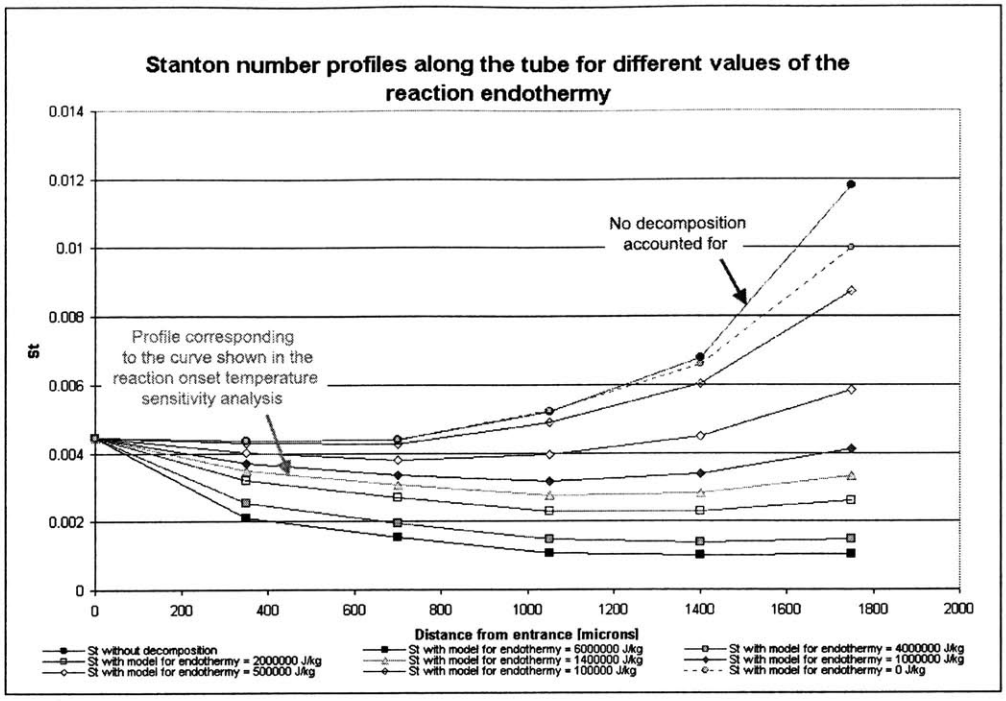

Figure 4-37: Stanton number profiles along the tube for a maximum reaction endothermy ranging from 0 J/kg to 6,000,000 J/kg. A reaction onset temperature of 530°C is assumed. The Stanton number profile obtained without accounting for the decomposition is showed as a comparison.

profile starts to curve starting from the end point. The lower the endothermy is, the more curved the Stanton profile is. For a 0 J/kg endothermy, the discrepancy between the Stanton profiles obtained with or without taking into account decomposition is due to the difference of enthalpy due to the difference in the fluid composition.

4.3.6.4 Study of the Stanton profile

4.3.6.4.1 Principle The Stanton number is expected to stabilize after the flow has developed, the increase in the Stanton number at the end of the tube being assumed to be only due to the decomposition effect. This was used to characterize the decomposition reaction. The characteristics of the reaction (reaction onset temperature and maximum endothermy) have been modified in order to minimize the increase in the Stanton number at the end of the tube and flatten the Stanton profile to the expected profile.

Reaction onset temperature and maximum endothermy were modified to minimize the error defined as the non dimensional sum, from the point at which the temperature starts to drop to the end of the tube, of the square of the difference between the Stanton number

at the point and the minimum Stanton number reached along the tube. The sum was non dimensionalized by dividing by the square of the minimum Stanton number and the number of points considered in the sum.

4.3.6.4.2 Main issues The major issue with this approach is that there is no baseline profile for the Stanton number. Some assumptions give a completely flat Stanton number, and therefore a minimal error, but at a very low floor value. This type of profile was shown in Figure 4-36 with very low reaction onset temperatures. There is no indication on what the floor value should be. The sensitivity analysis shows that a very large range of endothermies gives acceptable Stanton number profiles for different floor values. For the tests in which the Stanton number with no modification of the enthalpy was decreasing at the entrance of the tube, it was assumed that the reaction had not started. Therefore the Stanton number at the first point of measurement was constrained to be the same as the one calculated without the enthalpy model.
The optimization is very dependent on initial conditions which may bias the results.

4.3.6.4.3 Results An example of the Stanton number profile obtained by varying the endothermy and the reaction onset temperature is shown in Figure 4-38. An onset temperature of 365°C and a maximum endothermy of 1,395,588 J/kg are found to give a flat Stanton number profile. This result seems to imply that the integration of the endothermy in the enthalpy of the fluid manages to capture the enhancement seen in the heat transfer tests.

4.3.6.4.4 Conclusions A model of JP7 enthalpy has been derived to take into account the reaction of decomposition. The effect of the reaction has been accounted for by adding the endothermy of the reaction to the enthalpy of the fluid. The Stanton number obtained with the modeled enthalpy shows a flat profile, which would be expected for a developed flow. This results seem promising and imply that the model captures some of the effects of the decomposition of JP7. However, the model first depends on rough assumptions on the onset temperature and the endothermy of the reaction, which are not known, and second does not account for the fact that the enhancement offered by the reaction is higher after the drop in temperature.

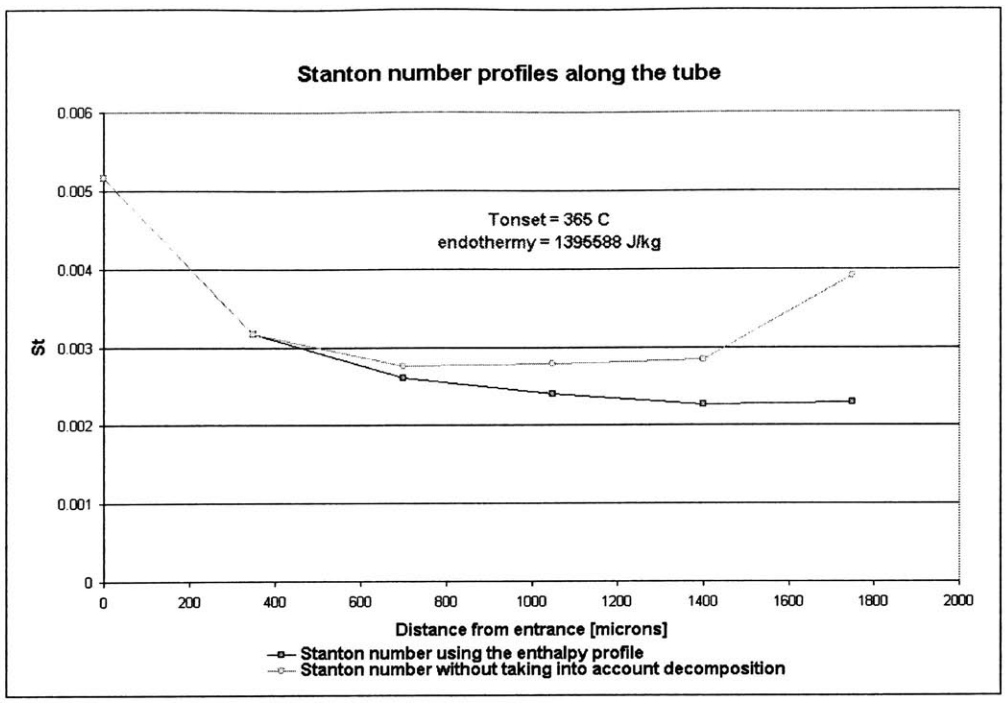

Figure 4-38: Stanton number profiles along the tube. The model assumes a reaction onset temperature of 365°C and a maximum endothermy of 1,395,588 J/kg.

4.4 Stability

The stability of the fluid has been studied by measuring the outside wall temperature in one point for 10 minutes in the same conditions of pressure, mass flow and heat flux. Both the occurrence of instabilities and the formation of deposits were studied. A total of 7 stability tests have been carried out at a pressure of 400 psi, heat fluxes ranging from 15 W/mm^2 to 35 W/mm^2 and mass flows from 0.04 g/s to 0.65 g/s.

4.4.1 Oscillations of the temperature

No temperature oscillations have been noticed at any time during the stability tests. The temperature is stable and only varies within 10°C. Oscillations reported at macro scale had an amplitude of 100°C. Figure 4-39 shows 5 minutes recorded during a stability test conducted at a pressure of 400 psi, a mass flow of 0.04 g/s and a heat flux of 30 W/mm^2. Figure 4-40 shows the temperature measured at 350 microns during a 10-minute stability test at a pressure of 400 psi, a mass flow of 0.055 g/s and a heat flux of 30 W/mm^2.

Some high frequency noises have been heard during the tests. Their frequency was varying

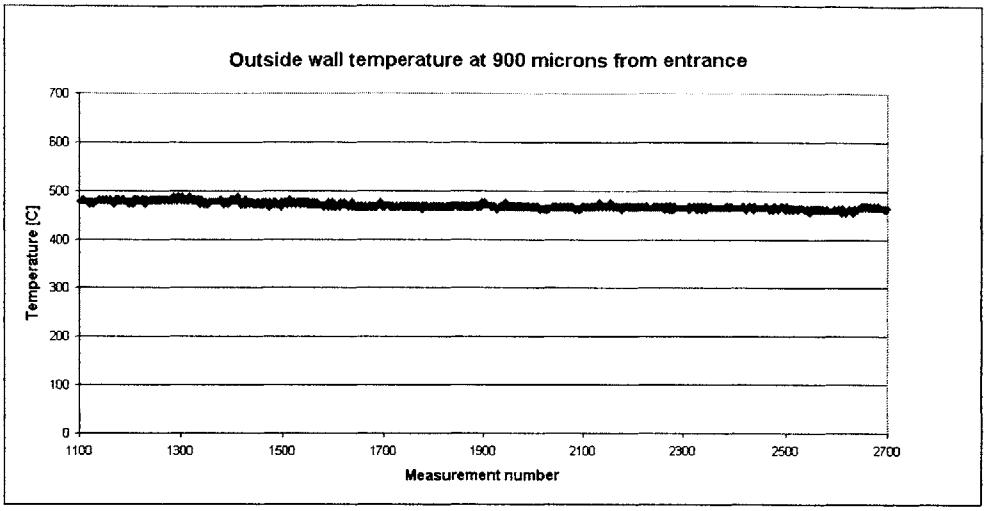

Figure 4-39: Outside wall temperature measured at 900 microns from the tube entrance. The plot shows 5 minutes recorded during a stability test conducted at a pressure of 400 psi, a mass flow of 0.04 g/s and a heat flux of 30 W/mm^2.

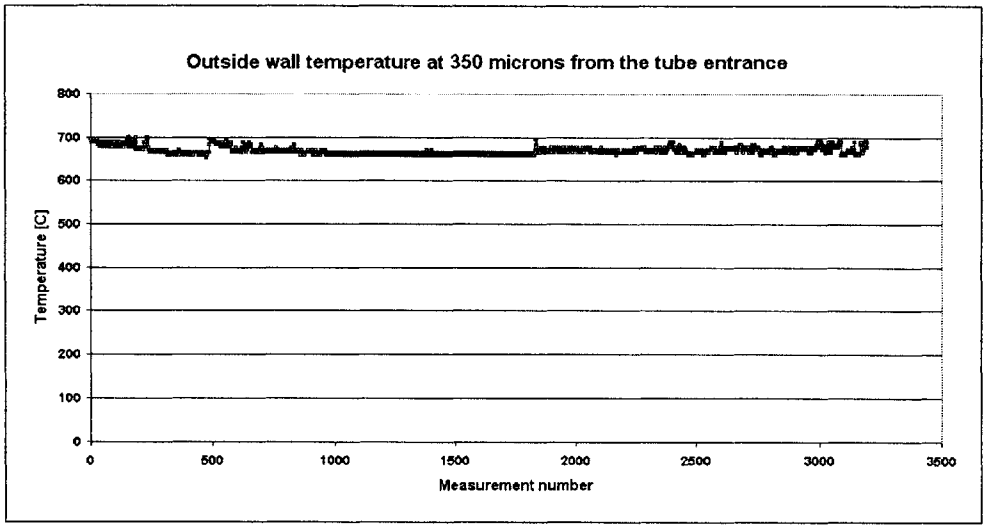

Figure 4-40: Outside wall temperature measured at 350 microns from the tube entrance. The plot shows 10 minutes recorded during a stability test conducted at a pressure of 400 psi, a mass flow of 0.055 g/s and a heat flux of 30 W/mm^2.

and sometimes pulsating. Similar noises have been reported in tests done with JP7 in macro tubes and corresponded to oscillations within the fluid. Since the diameter of the test section is very small and no temperature oscillations were seen within the test section, it is assumed that these noises may have been produced by oscillations occurring in the larger pipes which connect to the test section.

4.4.2 Deposits

4.4.2.1 Stability experiments

JP7 cracking in the test section may form deposits that may partially or totally clog the test section. If deposits are formed, they will reduce the cross section of the test section causing the mass flow to decrease. The formation of deposits was studied by looking at the evolution of the mass flow during stability tests. No decrease in the mass flow is seen

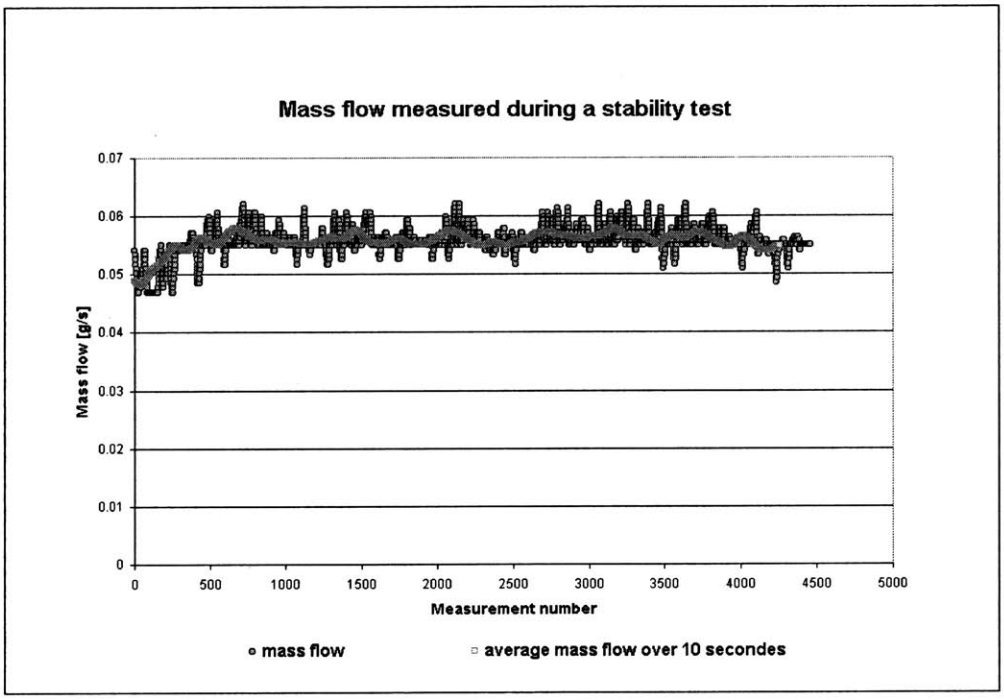

Figure 4-41: Mass flow measurement at 1,050 microns from the entrance of the tube during a 10-minute stability test carried out at a pressure of 400 psi, a mass flow of 0.056 g/s and a heat flux of 17 W/mm^2.

during the 10-minute tests. Figure 4-41 shows the mass flow measured during a test at a pressure of 400 psi, a mass flow of 0.055 g/s and a heat flux of 17 W/mm^2. The mass flow increases at the beginning of the test as the tube heats up. During the test, the mass flow

varies between 0.055 g/s and 0.06 g/s because of the sensitivity of the mass flow meter. The average mass flow over one second shows no decrease over the test.

Moreover, in tests done at macro scale, the temperature was seen to increase rapidly at the end of the tube because of deposits which created an insulation layer and limited the cooling of the wall. The temperature was constant in the stability tests carried out at micro scale and no such rapid increase in temperature was seen. This confirms that there was no evidence of deposit formation during the tests carried out with JP7 in micro test sections.

4.4.3 Hot points

During some tests, the tube heats to red in some places. The red spots appear, move along the tube and eventually disappear. They can be seen on the temperature measurements as shown in Figure 4-42 and Figure 4-43, which show the outside wall temperature as a function of time during two stability tests. The hot spot seen in Figure 4-42 shows an increase of 70°C in temperature, corresponding to a 20 % increase. These hot spots may

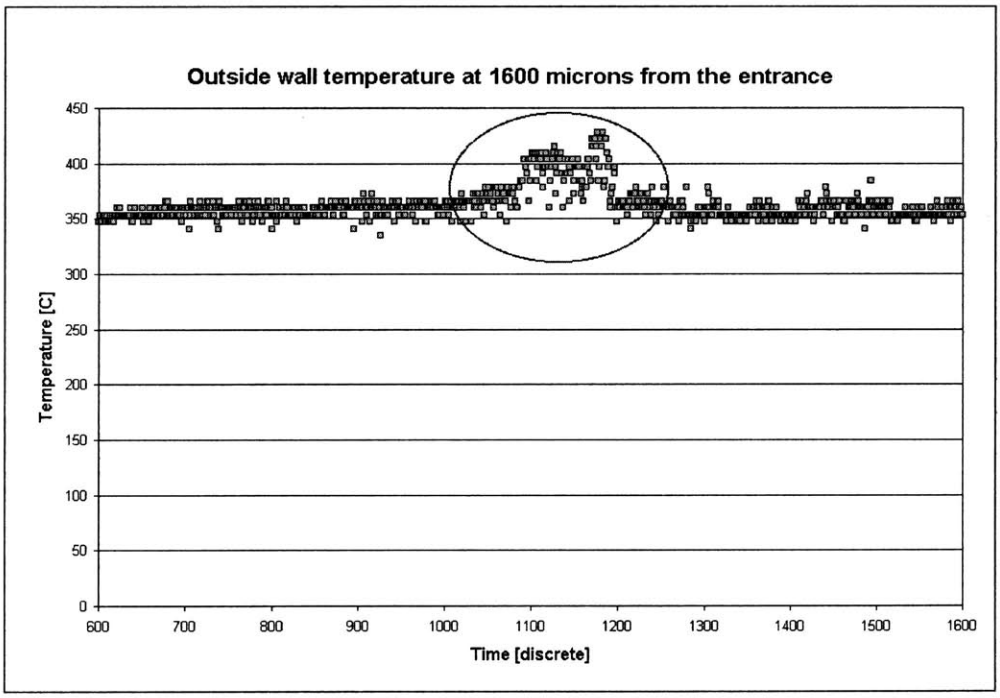

Figure 4-42: Outside wall temperature measured at 350 microns from the tube entrance. The plot shows 10 minutes recorded during a stability test conducted at a pressure of 400 psi, a mass flow of 0.055 g/s and a heat flux of 30 W/mm^2.

be due to some particles in the fluid that could be some deposits from the cracking of JP7.

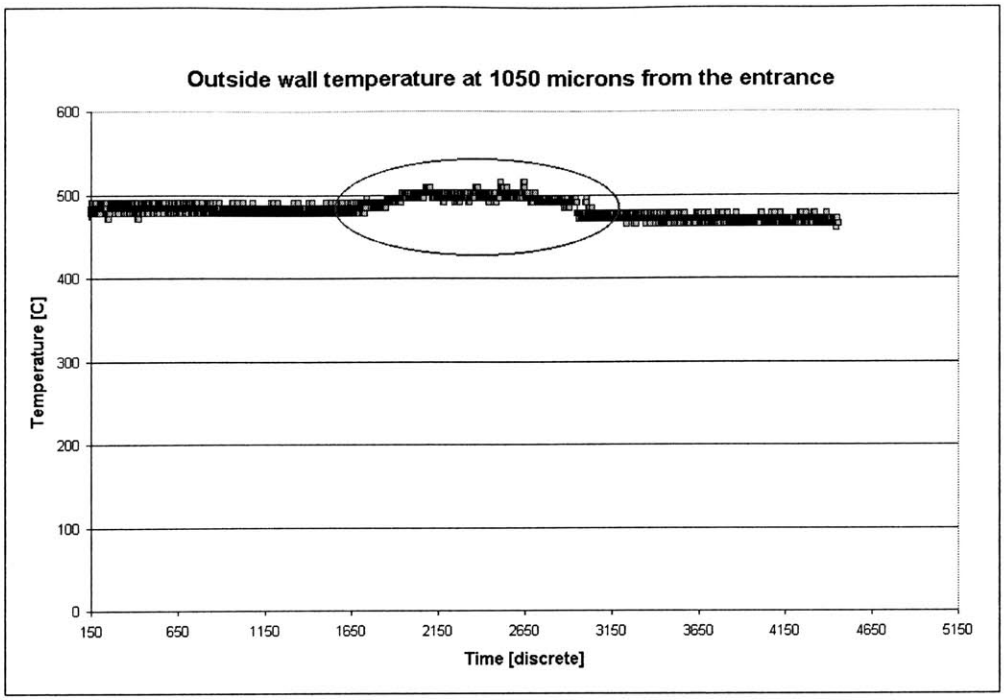

Figure 4-43: Outside wall temperature measured at 1050 microns from the tube entrance. The plot shows 10 minutes recorded during a stability test conducted at a pressure of 400 psi, a mass flow of 0.055 g/s and a heat flux of 17 W/mm^2.

This could be a problem in the micro rocket engine passages since a hot spot could cause a single point failure.

4.5 Reproducibility issue

Different sources can cause the experimental results not to be reproducible.

1. For tests done on the same tube: The pointing of the IR sensor is redone at the start of each test and therefore the temperature sensor is not similarly pointed. The temperature profile can be different depending on the number of previous experiments done on the tube. The tube may have been damaged, bent because of previous experiments or deposits formed on the surface during previous experiments can alter the temperature profile (even if stability tests have shown no evidence of deposits).

2. For tests done on separate tubes: Tubes can have significantly different lengths and diameters (between 35 microns to 100 microns as specified by MicroGroup, Inc). This could be normalized out using the mass flow $\dot{m}$ and the pressure drop across the tube

to evaluate the tube diameter and length. The data could be corrected for the effect of the variability in the tube dimensions. The pointing of the IR sensor is different from one tube to another. To minimize this issue, the IR sensor was not moved in between tests. The zero position of the motor for the first measurement is variable. It was chosen to always position the first measurement at the start of the braise of the micro tube to the 1/16" tube for more consistency between tests done on different tubes.

3. Some differences may occur because of a different behavior of the fluid. For example the roughness of the tube may have an impact on turbulence or on the decomposition of JP7. In studies of supercritical JP7 in macro tubes, tests carried out under the same conditions could show either instabilities or a stable flow [15].

Tests were carried out to study the reproducibility of the results between different experiments. Tests in specific conditions were carried out five times on two different tubes. Results from tests carried out on the same tube are close and show little variability. However, results from tests done in the same conditions but on different tubes can be much different and show different temperature profiles.

Figure 4-44 presents the outside wall temperature measured in different tests carried out in similar conditions at a pressure around 400 psi, a mass flow between 0.055 g/s and 0.06 g/s and a heat flux around 30 W/mm^2. Tests done on the same tube give almost the same temperature profiles, as seen with the two tests done on tube A. Tests done on different tubes can either be very similar, as seen with Tube A and B, or give different profiles, as shown with Tube A and C.

It is to be noticed that for Tubes A and C, the temperature profiles are different, either sharp or smooth. However, if the temperature profile is the same in two tests carried out in different tubes, the values of the measured temperatures are very similar. This may imply that the experimental causes of non reproducibility are not predominant and that the formation of deposits is limited.

4.6 Conclusions

The experiments carried out with JP7 have confirmed the enhancement in heat capacity offered by JP7. The increase in the heat transfer coefficient resulting from the endothermic

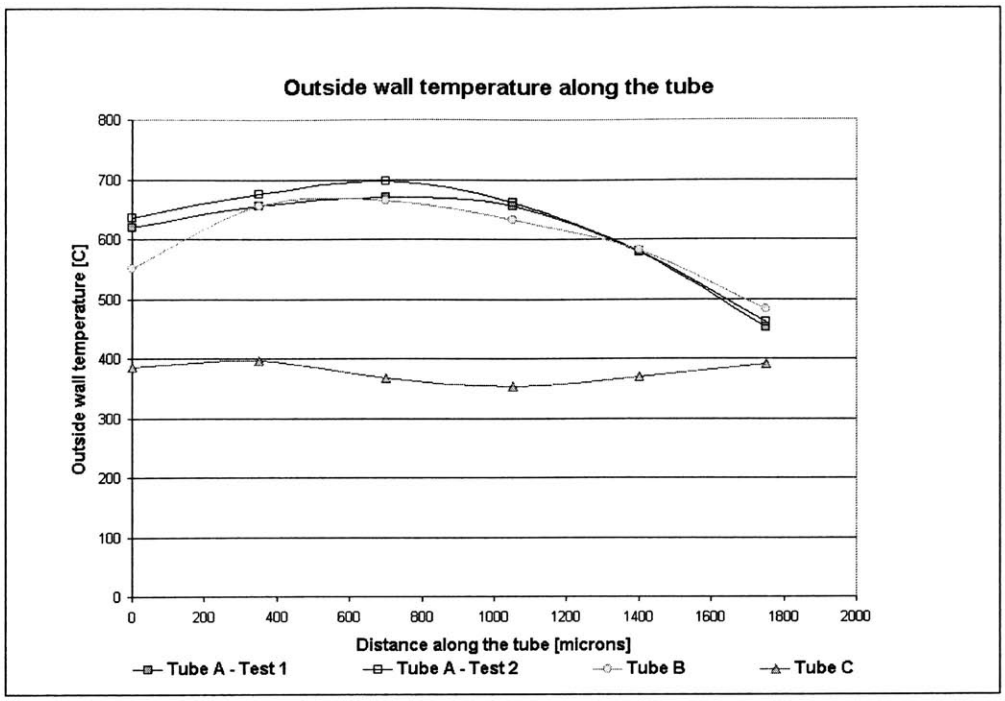

Figure 4-44: Outside wall temperature along the tube for different tests carried out approximately in the same conditions: a pressure around 400 psi, a mass flow between 0.055 g/s and 0.006 g/s and a heat flux around 30 W/mm^2.

reaction has been verified. Heat transfer coefficients as high as 1.62×10^6 W/K have been calculated at high heat fluxes.

Two different behaviors have been seen:

- The temperature starts increasing at the entrance of the tube, showing a sharp peak before decreasing.
- The temperature profile is smooth. The measured temperature stays constant or decreases slowly along the tube.

No trend has been identified to determine the conditions that produce a smooth or a sharp temperature profile.

The enhancement in heat transfer capacity of the fluid seems to be increased at high heat fluxes and decreased at high pressures. Prediction of the endothermy offered by the reaction of decomposition of JP7 appears to be difficult and no clear trend has been found.

The model developed shows that if the endothermy of the reaction is taken into account in the enthalpy of the fluid, a flat Stanton number can be obtained, as would be expected.

This may imply that if the endothermy of the reaction is characterized, the heat capacity of the fluid can be predicted.

JP7 seems to offer good stability. No major deposit formation has been noticed within 10 minutes. No oscillations are noticed during the tests. However, some hot spots have occurred during some tests and may be a concern in the micro rocket engine.

Good reproducibility was obtained with tests carried out on the same tube which provides more confidence in the results and the heat transfer coefficients. However, different fluid behaviors may occur in the same conditions in different tubes.

Chapter 5

JP10 study

5.1 Introduction to JP10 jet fuel

JP10 (MIL-P-87107) has been developed essentially for use in aircraft-launched missiles. On the contrary of JP7, which is a mix of various hydrocarbons and additives, JP10 is principally a single component molecule, a high-density naphtene $C_{10}H_{16}$ called exo-tetrahydrodicyclopentadiene. Developed as a missile fuel, JP10 provides a high volumetric energy content. The minimum volumetric heat content is estimated at 39,434 MJ/m^3, which is almost a 13 % increase compared to the volumetric heat content of Jet A or JP8 fuel [12]. JP10 also offers a clean burning and good low-temperature performance. JP10 is one of the three JP9 missile fuel components. Figure 5-1 shows an illustration of JP10 molecule.

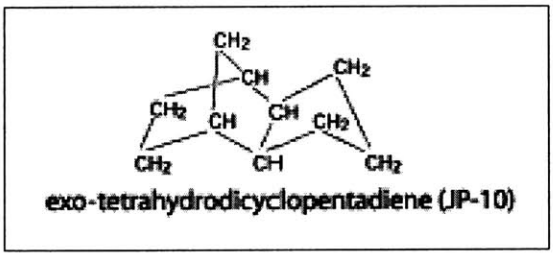

Figure 5-1: Molecule of JP10 ($C_{10}H_{16}$ or exo-tetrahydrodicyclopentadiene)[12]

5.2 Motivation for JP10 study

5.2.1 Possible endothermic reaction

JP10 is categorized as an endothermic fuel. JP10 does experience cracking and this reaction may provide a significant endothermy. This decomposition could offer an enhancement of the heat capacity of the fluid and therefore make JP10 a good candidate for use as a coolant in the micro rocket engine. No information has been found on the decomposition of JP10 therefore no data can give an estimate of the endothermy of this reaction. The heat transfer tests done with JP10 in micro channels aim at characterizing the heat capacity of JP10 and at trying to capture whether JP10 cracking reaction provides or not an enhancement in heat capacity.

5.2.2 Simple molecule

One of the advantages of JP10 over JP7 is its simplicity. JP10 is a single molecule and therefore it is expected to be easier to predict its behavior. Moreover, the reproducibility between one batch and another is less an issue for JP10 than for JP7 since there is no mixture nor additional additives.

5.2.3 Main issue associated with JP10

As for JP7, instabilities and carbon deposits may be undesirable consequences of the decomposition. JP10 is not a deoxygenated hydrocarbon and may form a lot more deposits than JP7. Carbon deposits seem to be the major concern for the use of JP10 in the micro rocket engine.

5.3 Heat transfer experimental study

5.3.1 Description of the experiments

5.3.1.1 Summary of the experiments

A total of 19 satisfying experiments have been carried out with JP10. The experimental conditions have been chosen within the following matrix:

* pressures ranging from 360 psi to 3,120 psi; the pressures were chosen so that similar critical pressure ratios were tested as with JP7. Mainly five pressure levels were tested: subcritical pressures (between 360 psi and 460 psi, $\frac{P}{P_c}$ 0.74), critical pressures around 540 psi and three high pressures 840 psi ($\frac{P}{P_c} = 1.54$), 1,500 psi ($\frac{P}{P_c} = 2.77$) and 3,120 psi ($\frac{P}{P_c} = 5.77$)

* mass flows ranging from 0.06 g/s to 0.77 g/s

* heat fluxes ranging from 18 W/mm^2 to 113 W/mm^2

The sets of conditions have been chosen to compare the results with the tests carried out with JP7. Some high mass flows and high heat fluxes have been tested to give some estimation of the heat transfer coefficients in conditions as close as possible to the micro rocket engine conditions. Tests at pressures above 1,500 psi were not possible because of a leak in the G10 block. Only one test has been carried out at a pressure of 3,120 psi ($\frac{P}{P_c} = 5.86$).

5.3.1.2 Reduction data method

The general data reduction method presented in Section 3.4 has been used. Specific characteristics for JP10 have not been found in supercritical conditions. Therefore, the characteristics of n-dodecane have been used with a correction for the critical pressure. JP10 critical pressure (541 psi) is twice that of n-dodecane. n-dodecane data have been chosen to match the critical pressure ratio. For example, n-dodecane properties at a pressure of 200 psi are used for tests with JP10 at 400 psi ($\frac{P}{P_c} = 0.75$). No precise data have been found about JP10 critical temperature so no correction has been taken into account for the critical temperature. Table 5.1 presents the properties that have been used for the reduction of JP10 data for each pressure tested.

5.3.2 General features

In most of the tests, the temperature starts to slowly decrease at the end of the tube after an initial increase. A significant enhancement in the heat transfer coefficient is seen at the end of the tube up to an increase of 120 %.

As for JP7, the Stanton number is studied to understand the origin of the enhancement. The enthalpy profile used for the calculations takes into account the supercritical effects. If no additional effect was seen, the Stanton number profile should decrease to reach a floor

$\frac{P}{P_c}$	JP7	JP10	n-dodecane properties for JP10 data
0.75	200 psi	400 psi	220 psi
1	260 psi	540 psi	294 psi
1.55	400 psi	841 psi	500 psi
2.5	600 psi	1500 psi	500 psi
5.77	1500 psi	3120 psi	1,000 psi

Table 5.1: Correspondence between JP7 and JP10 pressures for the same critical pressure ratios. Summary of the properties used for the reduction of JP10 data

value as the flow has thermally developed. The Stanton profile in most of the tests still show an increase at the end of the tube. This seems to suggest that an additional source of enhancement contributes to the increase in the heat transfer coefficient. The fact that this enhancement occurs at subcritical, critical and supercritical pressures seems to confirm that another phenomenon than the supercritical effect provides an enhancement in heat transfer coefficient. The endothermy of the cracking of JP10 could be the source of the enhancement identified by the increase in the Stanton number. Increases in the Stanton number have not been seen in all tests.

However, it must be noted that the properties used for the calculations with JP10 are not precise data on JP10. There might be significant differences in particular due to a shift in the pseudo critical temperature. This may cause the supercritical effect not to be accounted for completely and could explain some of the increase in the Stanton number.

5.3.3 Summary of the results

5.3.3.1 Temperature profile

Different temperature profiles have been seen during the various tests carried out with JP10. In all the tests, the temperature increases rapidly at the entrance of the tube during the first 350 microns or 700 microns.

In some experiments, the temperature profile obtained is very similar in shape to that obtained with JP7. The temperature increases at the entrance of the tube before stabilizing and decreasing sharply at the end of the tube. This bell shape profile is illustrated in

Figure 5-2 which shows the temperature profile obtained for a test at a pressure of 410 psi ($\frac{P}{P_c} = 0.76$), a mass flow of 0.06 g/s and a heat flux of 18 W/mm^2. The temperature stabilizes after 700 microns then starts decreasing slowly to 1,750 microns where the decrease in temperature is more significant. The decrease in temperature at the end of the tube indicates that there is a source of enhancement of the cooling offered by JP10. The decrease in temperature can be as high as 30 % of the maximum temperature reached along the tube. This decrease in temperature indicates that there is an enhancement in the heat capacity of the fluid that could be due to the cracking of JP10. The temperature increases at the entrance of the tube as the flow thermally develops. At some point, the enhanced heat capacity of the fluid (either due to JP10 cracking, supercritical effects or a combination of both) makes the cooling more efficient: the temperature stabilizes. The enhancement is more efficient as we get further along the tube and is sufficient to make the temperature decrease, slowly first and then more rapidly. The change in slope at the end of the tube suggests that at this point, the enhancement gets significantly more efficient.

In most of the tests, the temperature profile does not show a sharp decrease. The tem-

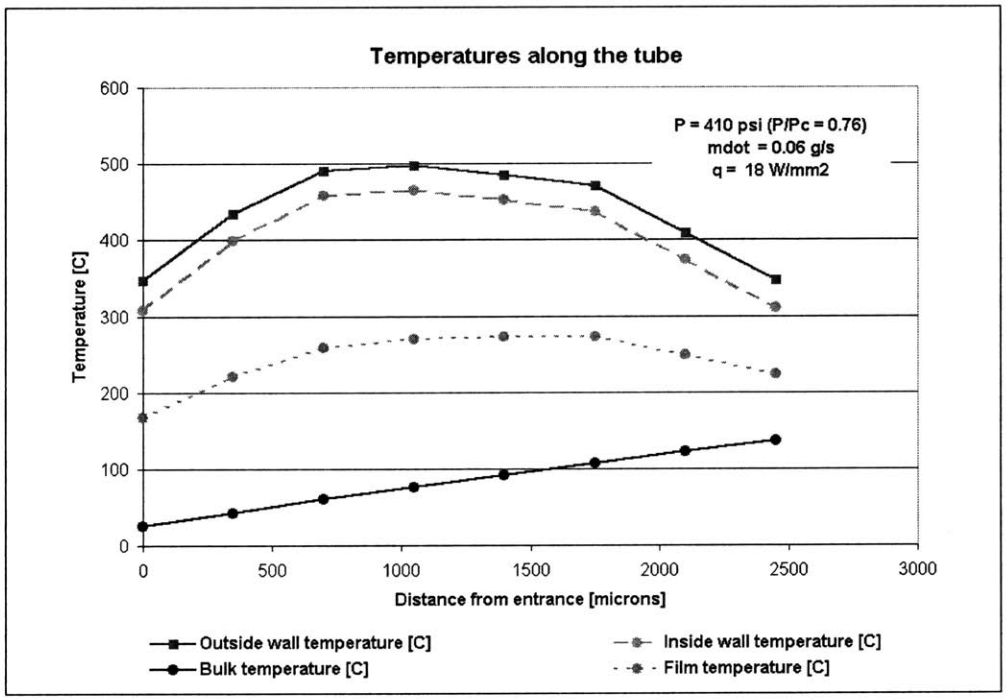

Figure 5-2: Temperature along the tube for a test with JP10 at a pressure of 410 psi ($\frac{P}{P_c} = 0.74$), a mass flow of 0.06 g/s and a heat flux of 18 W/mm^2.

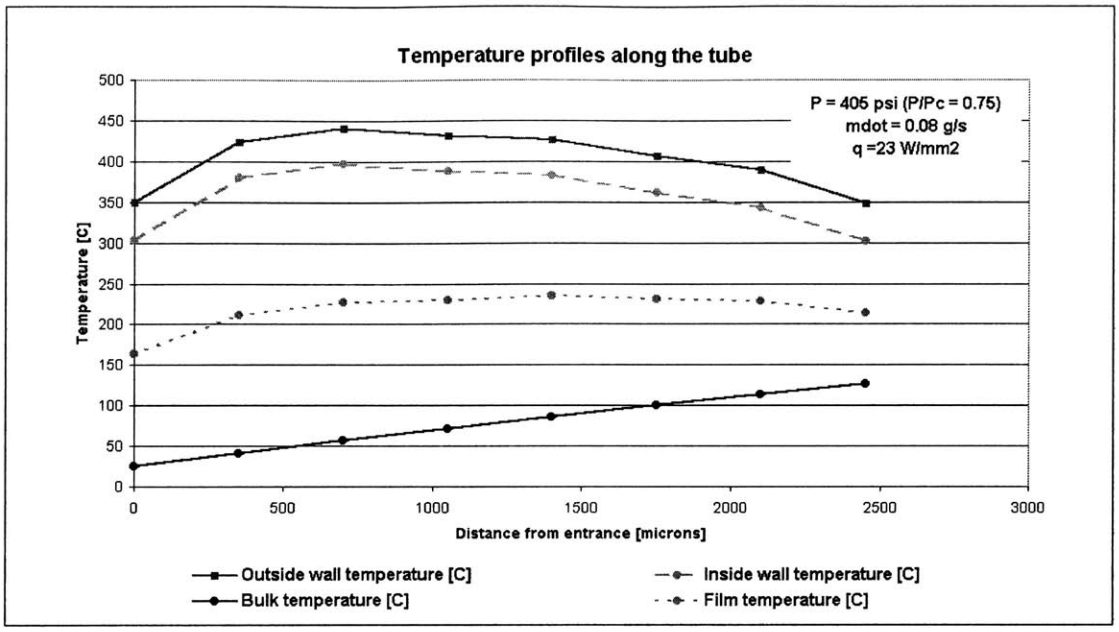

Figure 5-3: Temperature profiles for a test with JP10 at a pressure P = 405 psi ($\frac{P}{P_c} = 0.75$), a mass flow $\dot{m} = 0.08$ g/s and a heat flux q = 23 W/mm^2.

perature stabilizes before slowly decreasing as shown in Figure 5-3 for a test at a pressure P = 405 psi ($\frac{P}{P_c} = 0.75$), a mass flow of 0.08 g/s and a heat flux of 23 W/mm^2. In some tests, the temperature profile even stays flat after the increase at the entrance of the tube as shown in Figure 5-4 for a test at a pressure P = 849 psi ($\frac{P}{P_c} = 1.57$), a mass flow of 0.07 g/s and a heat flux of 26.6 W/mm^2. This may imply that there is no decrease in the temperature or that the decrease happens after the last point of measurement.

In only one test, the temperature has not decreased along the tube. In this test, the temperature has been measured only up to 1,750 microns from the tube entrance. After this point the IR sensor got misaligned. The temperature profile recorded during this test at a high pressure P = 3,173 psi ($\frac{P}{P_c} = 5.86$), a mass flow $\dot{m} = 0.05$ g/s and a heat flux q = 30 W/mm^2 is shown in Figure 5-5. The temperature increases rapidly at the entrance of the tube as in all the tests carried out. There is a sharp change in slope at 350 microns from the entrance. The temperature flattens before increasing again with a smaller slope.

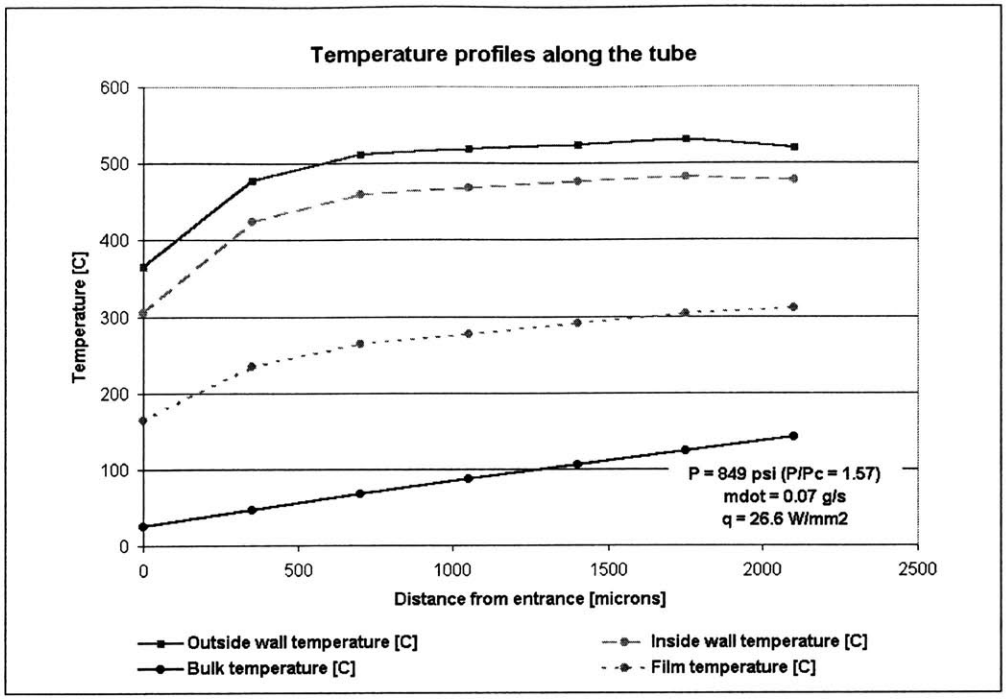

Figure 5-4: Temperature profiles along the tube for a test with JP10 at a pressure P = 849 psi ($\frac{P}{P_c} = 1.57$), a mass flow $\dot{m} = 0.07$ g/s and a heat flux q = 26.6 W/mm^2.

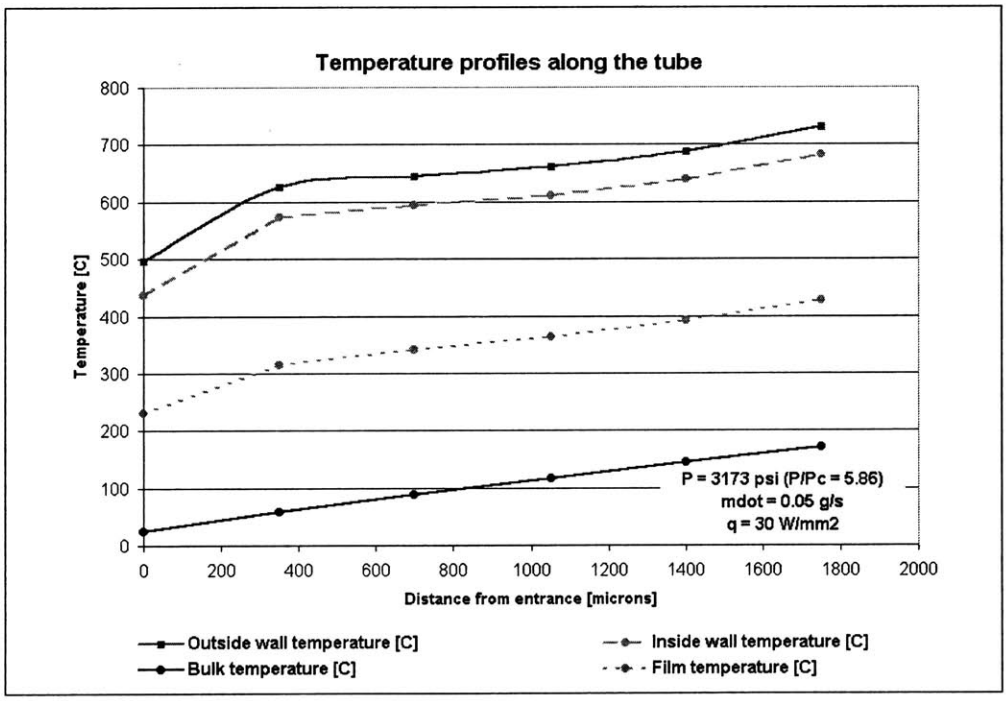

Figure 5-5: Temperature profiles along the tube for a test carried out with JP10 at a pressure P = 3,173 psi ($\frac{P}{P_c} = 5.86$), a mass flow $\dot{m} = 0.05$ g/s and a heat flux q = 30 W/mm^2.

5.3.3.2 Heat transfer coefficient

The heat transfer coefficient decreases at the entrance of the tube for all tests before stabilizing and increasing at the end of the tube in all tests except the test at a pressure of 3,120 psi. Heat transfer coefficients as high as 4.4×10^5 W/K have been reached. The minimum values of the heat transfer coefficient varies between 40,000 W/K and 70,000 W/K. Increases in heat transfer coefficient as high as 1.7×10^5 W/K have been calculated at 1,750 microns from the entrance. As for tests carried out with JP7, the increase in heat transfer coefficient is calculated as the difference between the heat transfer coefficient at 1,750 microns from the entrance and the minimum value of the heat transfer coefficient along the tube.

The heat transfer coefficient profile corresponding to the sharp temperature profile is also very similar to the heat transfer coefficient profile seen with JP7 tests. The heat transfer coefficient starts to decrease at the entrance of the tube due to the heating of the fluid and the entrance region. The heat transfer coefficient then stabilizes before sharply increasing at the end of the tube. Figure 5-6 presents the heat transfer coefficient calculated along the tube for the same test shown in Figure 5-2. Similarly to what happens with JP7, as the temperature increases at the entrance of the tube, an enhancement of the cooling provided by JP10 is noticed which is characterized by a higher heat transfer coefficient. The increase in the heat transfer coefficient first compensates for the decrease due to the heating in the entrance region. As the enhancement becomes more efficient, the heat transfer coefficient starts to increase.

The heat transfer coefficient profile for the smooth decreasing temperature profile shown in Figure 5-3 is shown in Figure 5-7. The heat transfer coefficient slowly increases after the initial decrease at the entrance of the tube. The final enhancements in the heat transfer coefficient can be comparable as the enhancements seen with a sharp profile.

In the case of tests that show a flat temperature profile, the heat transfer coefficient profiles can be much different. In some cases, the heat transfer coefficient increases slowly along the tube, most often when the test is carried out at a high heat flux. In other cases, the heat transfer coefficient stays constant after the initial decrease at the entrance of the tube

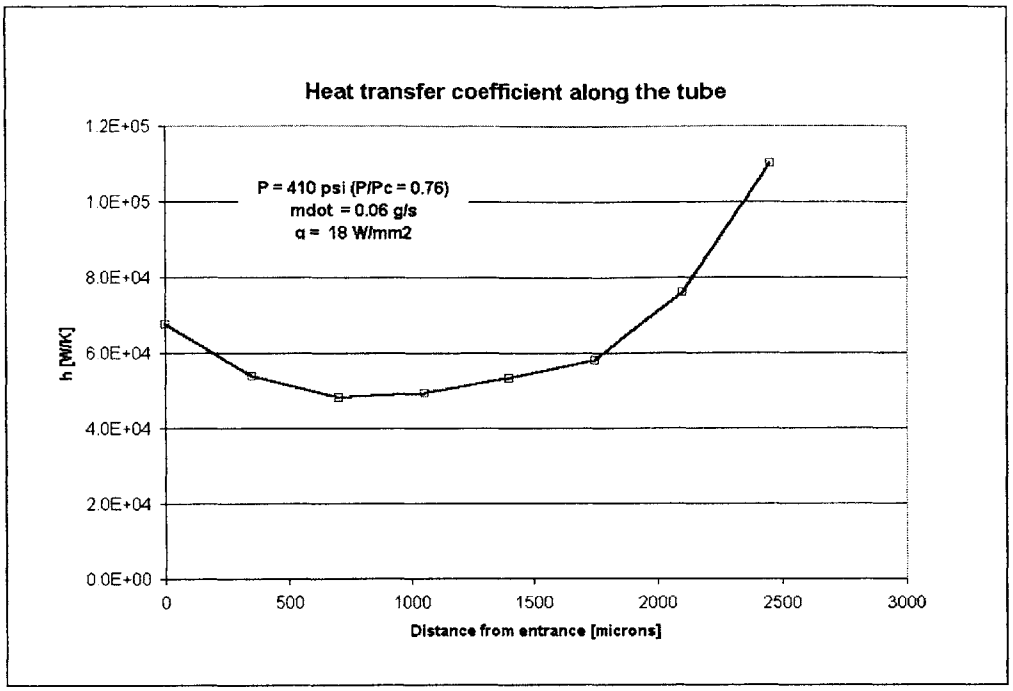

Figure 5-6: Heat transfer coefficient profile along the tube for a test with JP10 at a pressure of 410 psi ($\frac{P}{P_c} = 0.74$), a mass flow of 0.06 g/s and a heat flux of 18 W/mm^2.

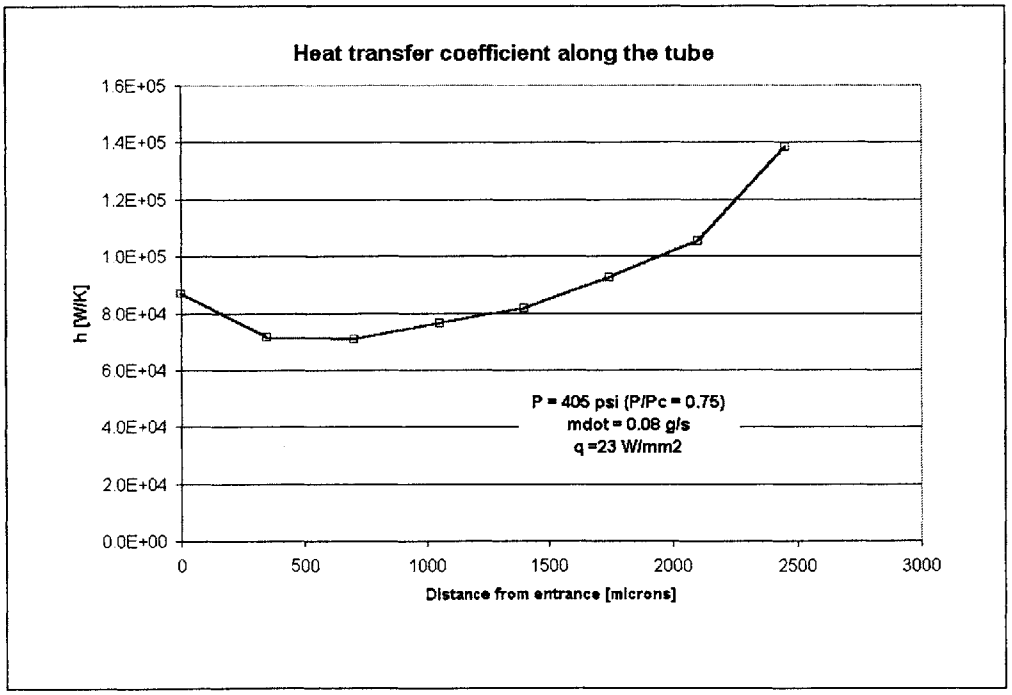

Figure 5-7: Heat transfer coefficient profile for a test with JP10 at a pressure P = 405 psi ($\frac{P}{P_c} = 0.75$), a mass flow $\dot{m} = 0.08$ g/s and a heat flux q = 23 W/mm^2.

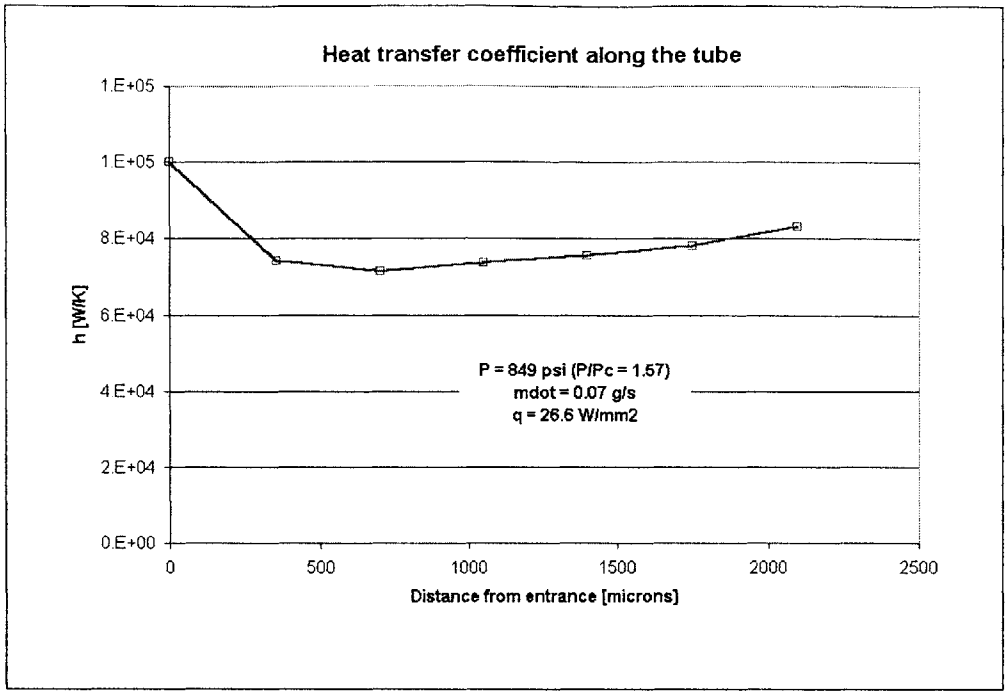

Figure 5-8: Heat transfer coefficient profile along the tube for a test with JP10 at a pressure P = 849 psi ($\frac{P}{P_c} = 1.57$), a mass flow $\dot{m} = 0.07$ g/s and a heat flux q = 26.6 W/mm^2.

and no enhancement is seen as shown in Figure 5-8.

For the test at a pressure of 3,120 psi for which the temperature was increasing along the tube, the heat transfer coefficient stays constant along the tube and even starts to slowly decrease at the last point of measurement. Figure 5-9 shows the heat transfer coefficient profile for this test.

The shape of the temperature profile does not seem to be directly linked to the amplitude of the enhancement in the heat transfer coefficient, similarly to JP7. Some tests presented no enhancement of the heat transfer coefficient. No criteria could be found to determine for which conditions the enhancement occurred.

5.3.3.3 Stanton number profile

The non dimensional Stanton number shows comparable profiles as the heat transfer coefficient. The Stanton number starts to decrease at the entrance of the tube, as the fluid thermally develops, before stabilizing. The Stanton number starts to increase at the end

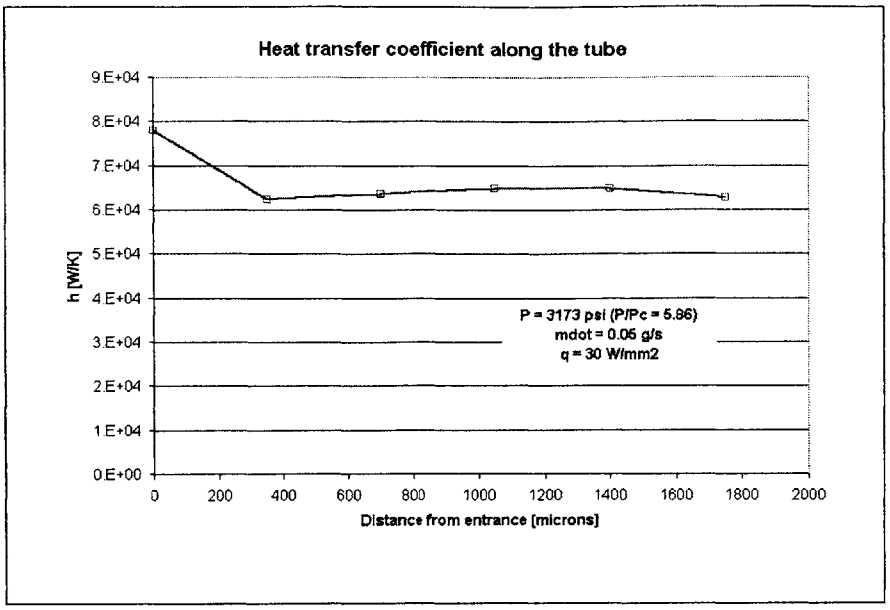

Figure 5-9: Heat transfer coefficient profile along the tube for a test carried out with JP10 at a pressure P = 3,173 psi ($\frac{P}{P_c}$ = 5.86), a mass flow $\dot{m}$ = 0.05 g/s and a heat flux q = 30 W/mm^2.

of the tube in the tests showing an enhancement in heat capacity of the fluid. Common values of the minimum Stanton number lay between 0.0015 and 0.0025. A maximum increase in the Stanton number of 0.0017 has been noted. The shape of the Stanton number profile is similar to the shape of the heat transfer coefficient profile. The Stanton number is presented for the four different types of profiles respectively in Figure 5-10, Figure 5-11, Figure 5-12 and Figure 5-13 as a function of the distance from the entrance of the tube. In some experiments no enhancement in heat capacity is seen, as for the tests illustrated in Figure 5-12 and Figure 5-13. No clear dependence on experimental conditions has been found to determine when the enhancement was occurring.

5.3.4 Dependence of JP10 cooling capacity on experimental conditions

5.3.4.1 Heat transfer coefficient

5.3.4.1.1 Heat transfer coefficient and heat flux The highest heat transfer coefficients are obtained with high heat fluxes. The heat transfer coefficient calculated at the end point (chosen at 1,750 microns from the entrance) is plotted as a function of the heat flux for the different tests in Figure 5-14. Different mass flows are identified by different symbols. There is a clear trend towards a higher heat transfer coefficient for a higher heat

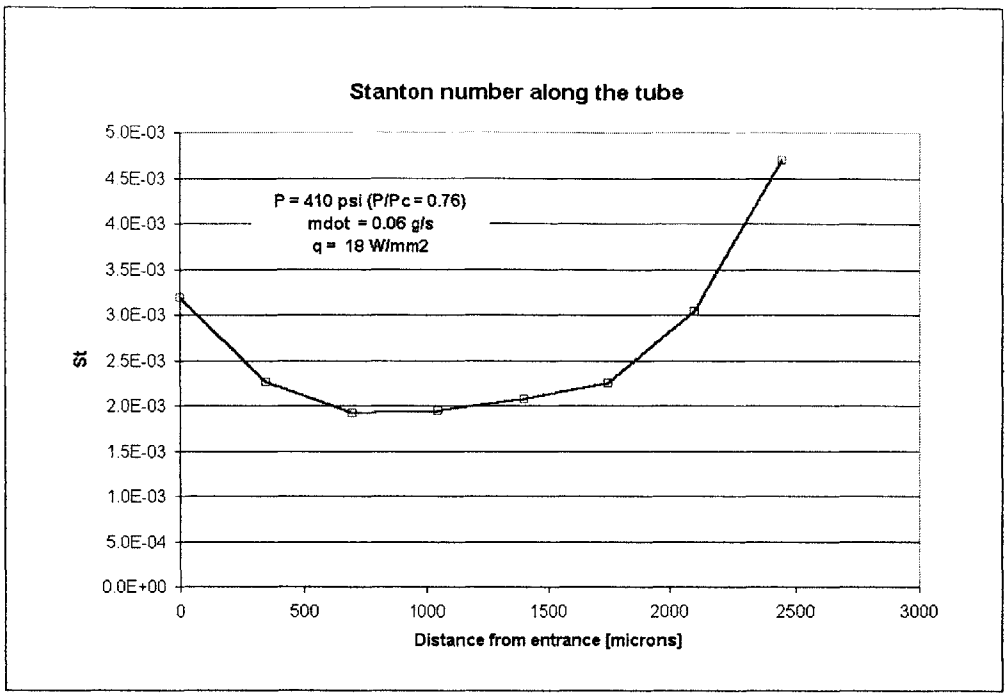

Figure 5-10: Stanton number profile along the tube for a test with JP10 at a pressure of 410 psi ($\frac{P}{P_c} = 0.74$), a mass flow of 0.06 g/s and a heat flux of 18 W/mm^2.

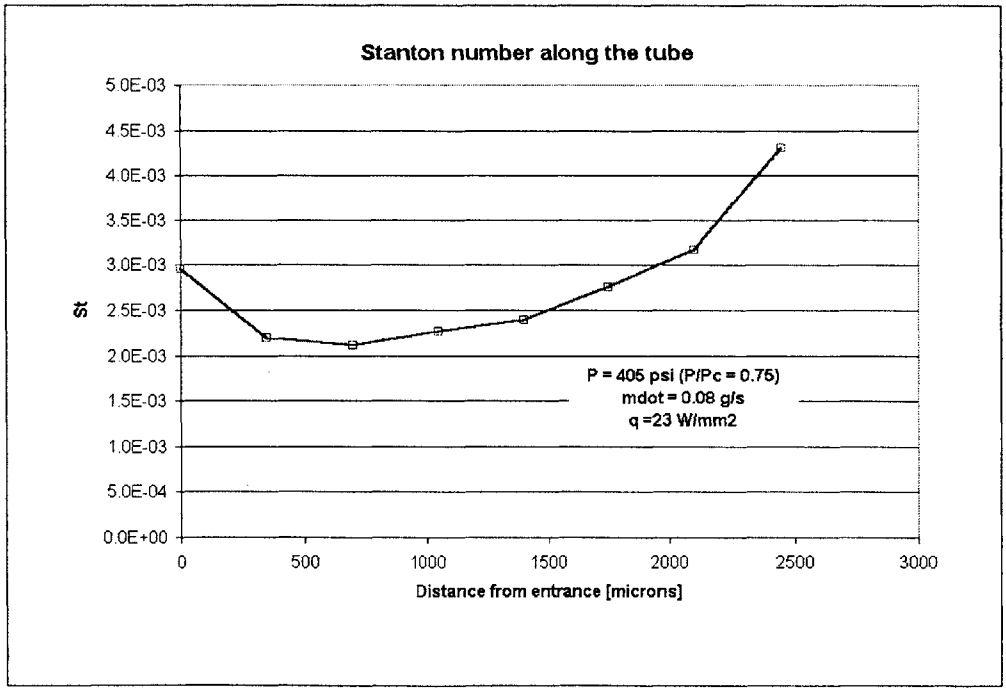

Figure 5-11: Stanton number profile for a test with JP10 at a pressure P = 405 psi ($\frac{P}{P_c} = 0.75$), a mass flow $\dot{m}$ = 0.08 g/s and a heat flux q = 23 W/mm^2.

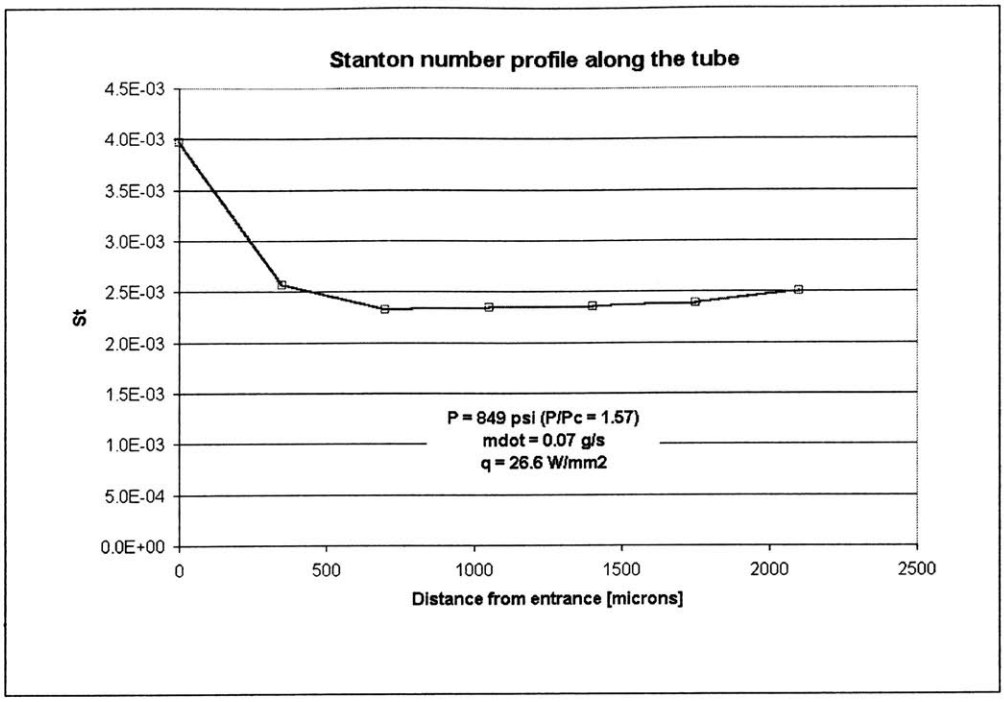

Figure 5-12: Stanton number profile along the tube for a test with JP10 at a pressure P = 849 psi ($\frac{P}{P_c} = 1.57$), a mass flow $\dot{m} = 0.07$ g/s and a heat flux q = 26.6 W/mm^2.

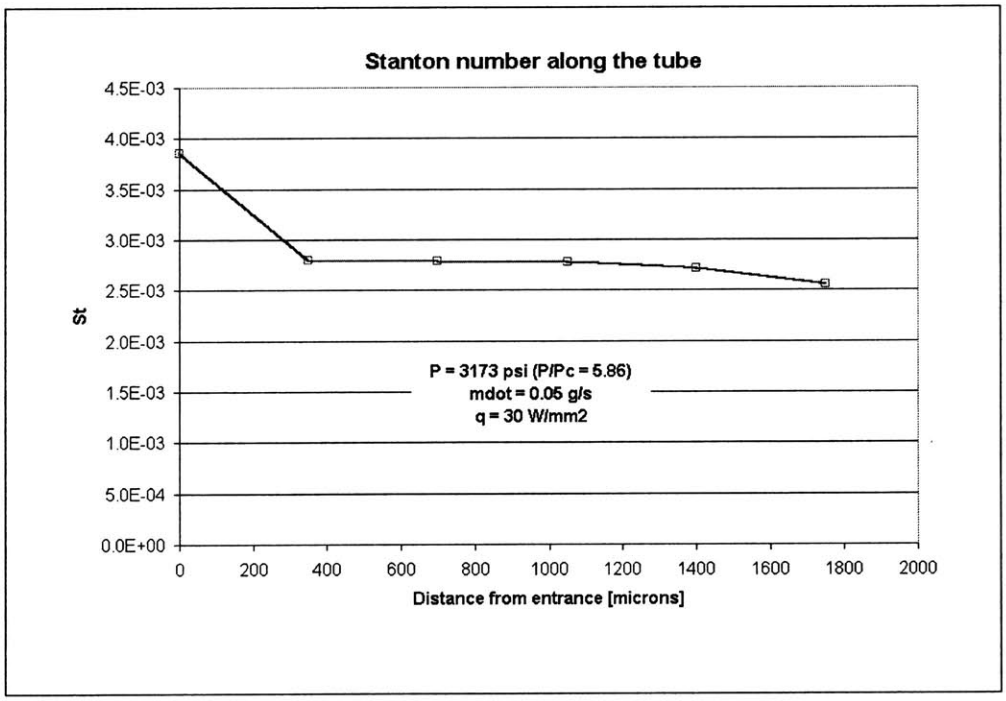

Figure 5-13: Stanton number profile along the tube for a test carried out with JP10 at a pressure P = 3,173 psi ($\frac{P}{P_c} = 5.86$), a mass flow $\dot{m} = 0.05$ g/s and a heat flux q = 30 W/mm^2.

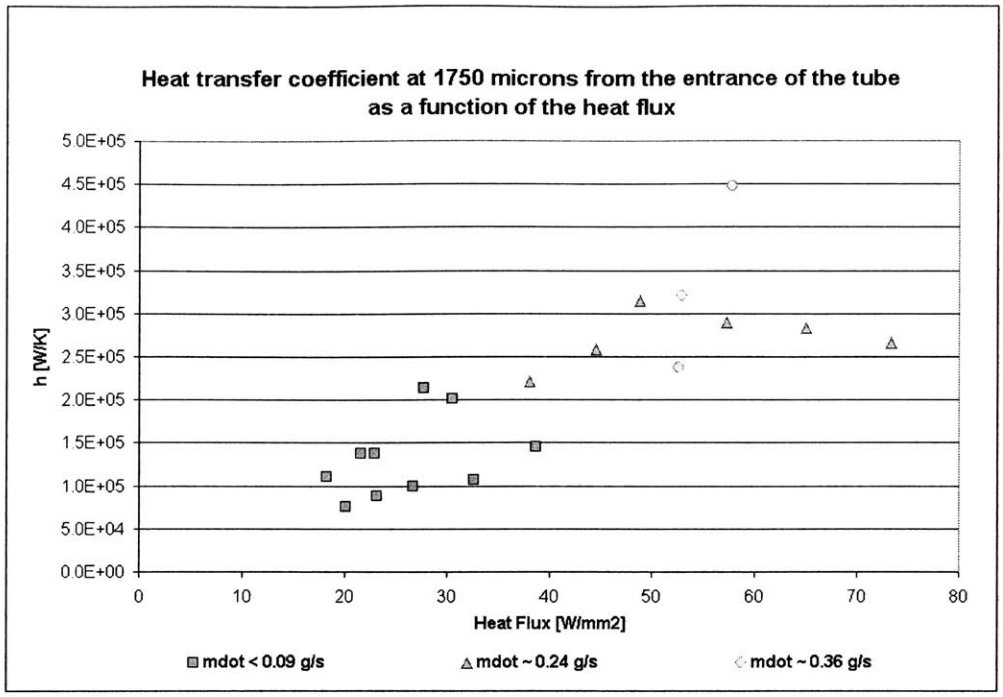

Figure 5-14: Heat transfer coefficient at 1,750 microns from the entrance of the tube as a function of heat flux.

flux except for the tests at a mass flow of 0.24 g/s, which will be discussed in the next section. As the heat flux increases, the same trend is noticed for the minimum value of the heat transfer coefficient shown in Figure 5-15 and the enhancement in the heat transfer coefficient shown in Figure 5-16.

5.3.4.1.2 Deterioration of the heat transfer coefficient at high heat fluxes In the tests carried out at a mass flow of 0.24 g/s, the heat transfer coefficient calculated at 1,750 microns from the entrance increases before stabilizing as the heat flux is increased above a critical heat flux. The critical heat flux is noted between 55 W/mm^2 and 60 W/mm^2. At this critical heat flux, there is a sharp change in the slope of increase of the minimum value of the heat transfer coefficient. There is no clear trend as far as the enhancement in the heat transfer coefficient is concerned. The enhancement in heat transfer coefficient seems to stay almost constant at high heat fluxes but the variability of the data and the lack of points of measurements prevent from drawing any conclusion.

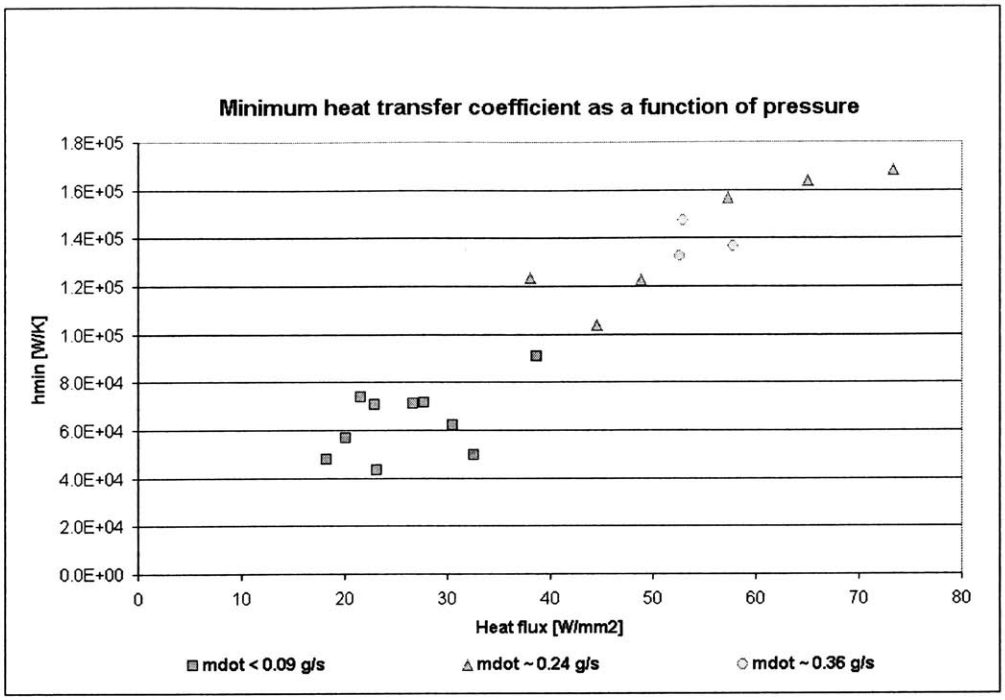

Figure 5-15: Minimum heat transfer coefficient along the tube as a function of heat flux.

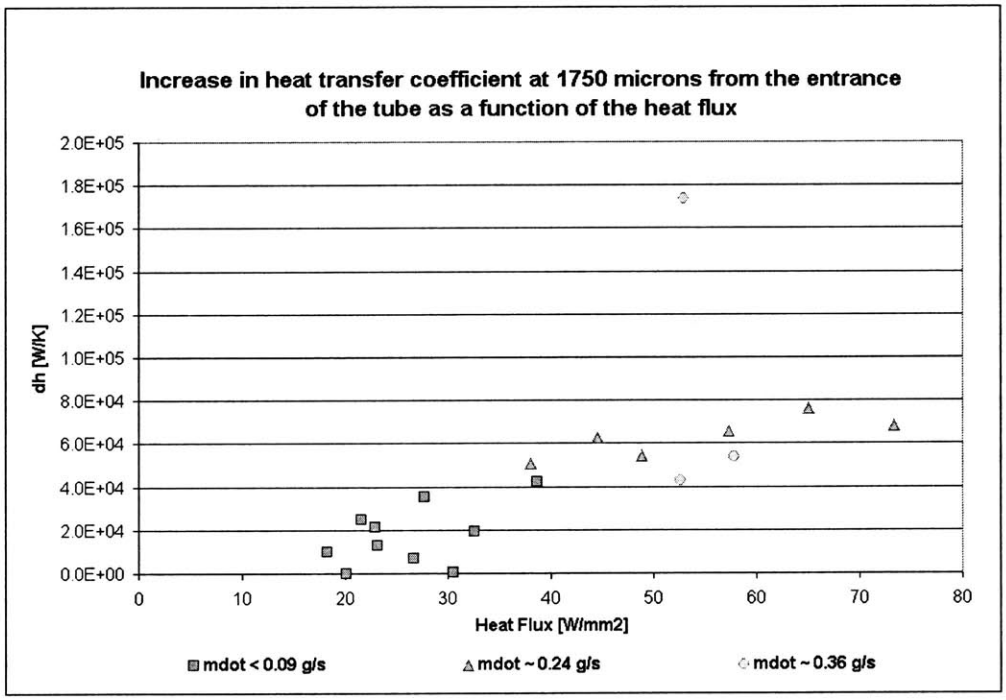

Figure 5-16: Increase in heat transfer coefficient along the tube as a function of heat flux. The increase in the heat transfer coefficient is defined as the difference between the maximum and the minimum heat transfer coefficients calculated up to 1750 microns from the entrance of the tube.

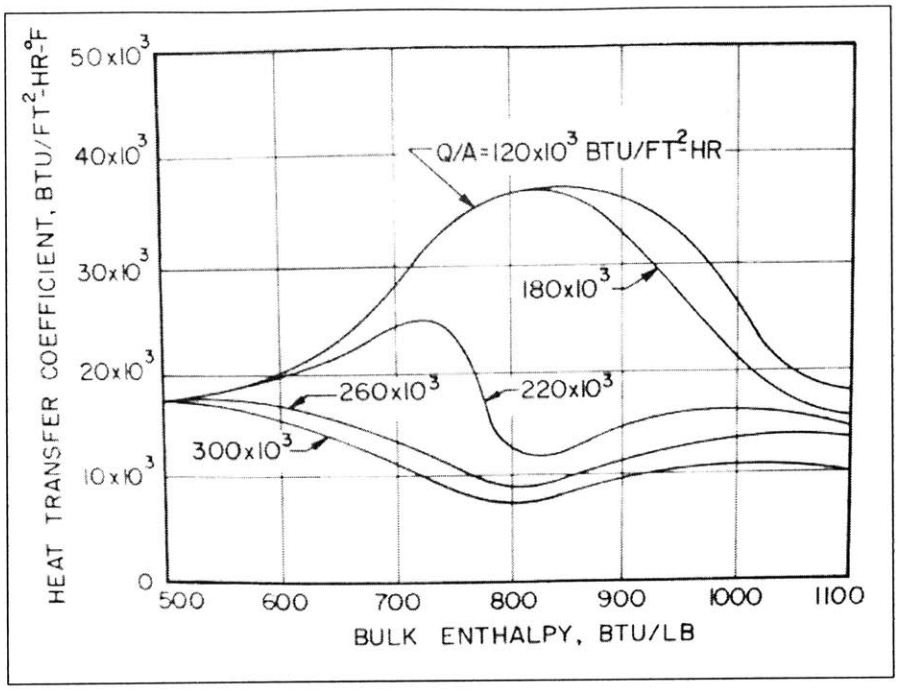

Figure 5-17: Deterioration of the heat transfer coefficient at high heat fluxes with supercritical fluids [7].

Deterioration in the heat transfer coefficient has been noticed in supercritical fluids when the bulk temperature is below the critical temperature and the heat flux applied to the fluid is above a critical heat flux [7]. Figure 5-17 illustrates the deterioration of the heat transfer coefficient as the heat flux is increased. At a heat flux below the critical heat flux, the heat transfer coefficient increases because of the supercritical effect. As the heat flux is increased, the enhancement decreases before disappearing completely at heat fluxes far above the critical heat flux. A decrease in the heat transfer coefficient can even be seen. An empirical relation to determine the critical heat flux for supercritical water has been derived [24]:

$$q_c = 0.20\, G^{1.2} \tag{5.1}$$

where q_c represents the critical heat flux and G the mass velocity (defined as the ratio of the mass flow and the cross section area). For a mass flow of 0.24 g/s, the critical heat flux is estimated at 54.5 W/mm^2. This is close to the heat flux for which the change in slope is seen. However, it must be noticed that the deterioration in the heat transfer coefficient has not been seen at the lowest mass flows (0.06 g/s) even if the theoretical critical heat flux estimated with equation 5.1 has been exceeded. The formula has been derived from tests

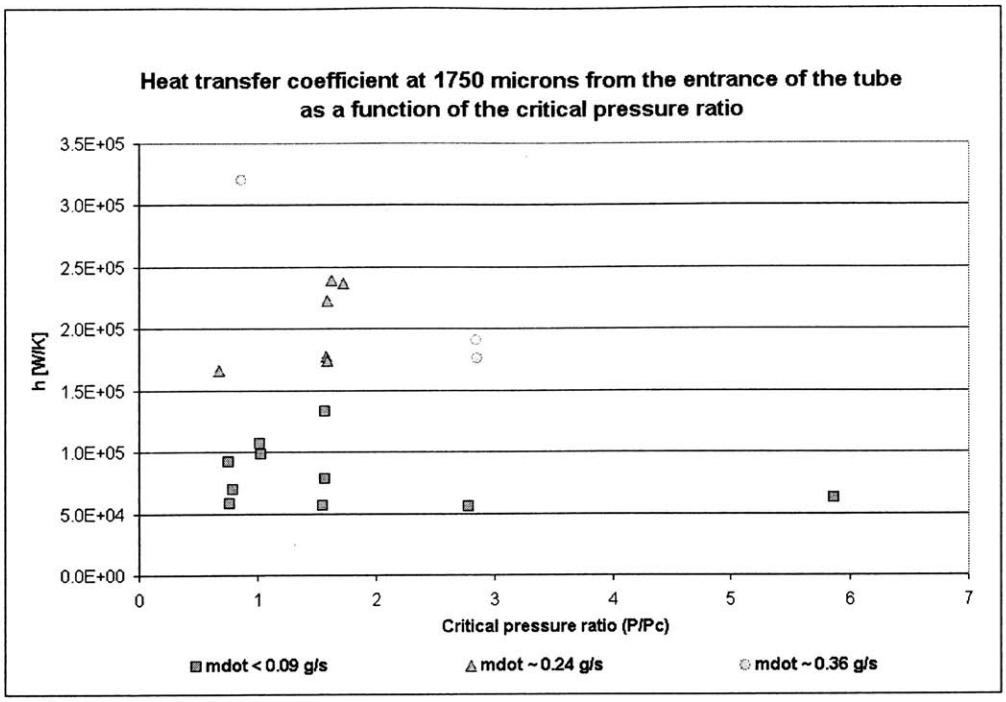

Figure 5-18: Heat transfer coefficient at 1,750 microns from the entrance of the tube as a function of the critical pressure ratio.

with supercritical water in vertical tubes and for conditions in which the bulk temperature reached the critical temperature so the formula may not be adapted to the current tests.

5.3.4.1.3 Heat transfer coefficient and pressure Pressure does not seem to be a major parameter over the pressures tested. High enhancements are seen both at subcritical, critical and supercritical pressures. This seems to imply that the supercritical phenomenon does not manage to completely explain the cooling enhancement obtained during the tests. It must be noted that it could also be due to the fact that the unprecise properties used in the reduction of the data are not capturing all the supercritical effect. The heat transfer coefficient at 1,750 microns from the entrance is shown as a function of the critical pressure ratio in Figure 5-18 and the increase in the heat transfer coefficient along the tube as a function of the critical pressure ratio is shown in Figure 5-19.

5.3.4.1.4 Heat transfer coefficient and mass flow As seen in Figure 5-19 and Figure 5-18, the heat transfer coefficient and the increase in the heat transfer coefficient both increase as the mass flow is increased. There is a clear separation of the experimental points as the mass flow is varied. As for JP7, the Stanton number was studied to get rid of the

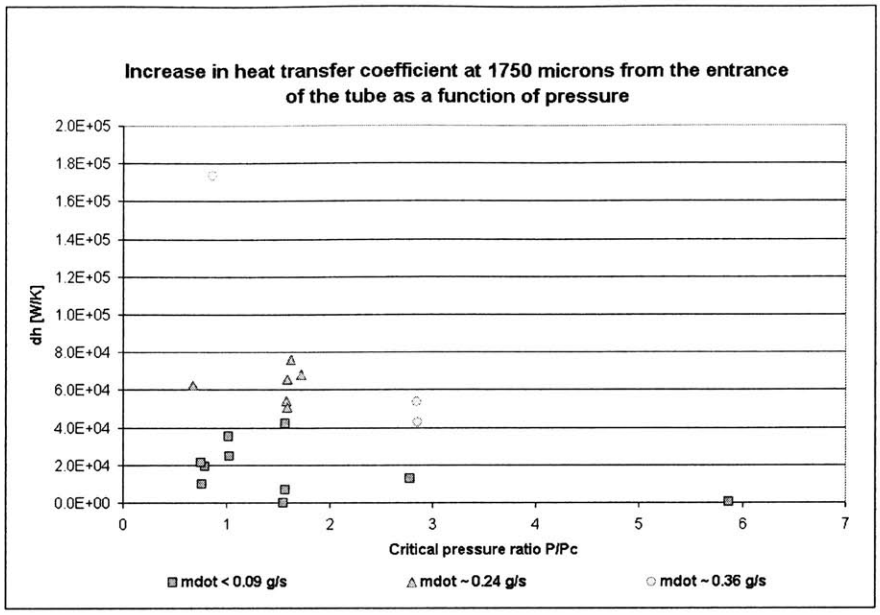

Figure 5-19: Increase in the heat transfer coefficient along the tube as a function of the critical pressure ratio.

bias introduced in the heat transfer coefficient by the Reynolds number.

5.3.4.2 Stanton number

The dependence on the mass flow is not apparent anymore with the Stanton number as seen in Figure 5-20, which presents the increase in the Stanton number as a function of the critical pressure ratio. Different mass flows are identified by different symbols.
The enhancement in the Stanton number (defined as the difference between the maximum and minimum values obtained along the tube up to 1,750 microns from the entrance) increases as the heat flux is increased. Figure 5-21 shows the increase in the Stanton number as a function of the heat flux. Tests at a mass flow of 0.24 g/s show an almost constant enhancement in the Stanton number even for heat fluxes increasing from 40 W/mm^2 to 75 W/mm^2.

5.3.5 Conclusions

The enhancement in heat transfer offered by JP10 has been highlighted. Increases in the heat transfer coefficient and the Stanton number have been obtained both in subcritical, critical and supercritical conditions, implying that the supercritical effect may not be the

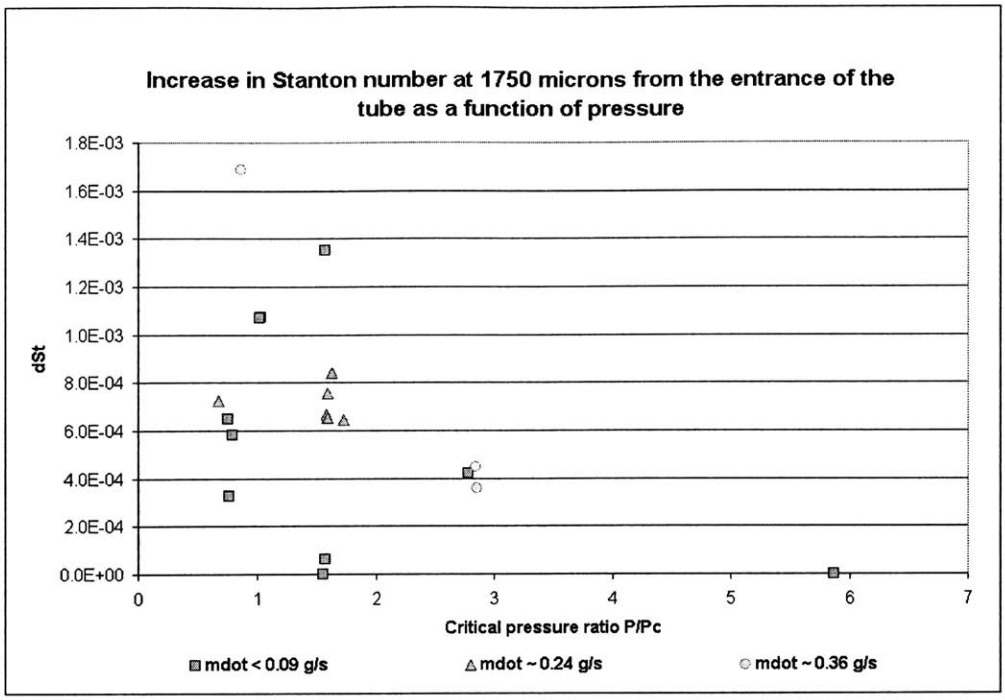

Figure 5-20: Increase in the Stanton number along the tube as a function of the critical pressure ratio.

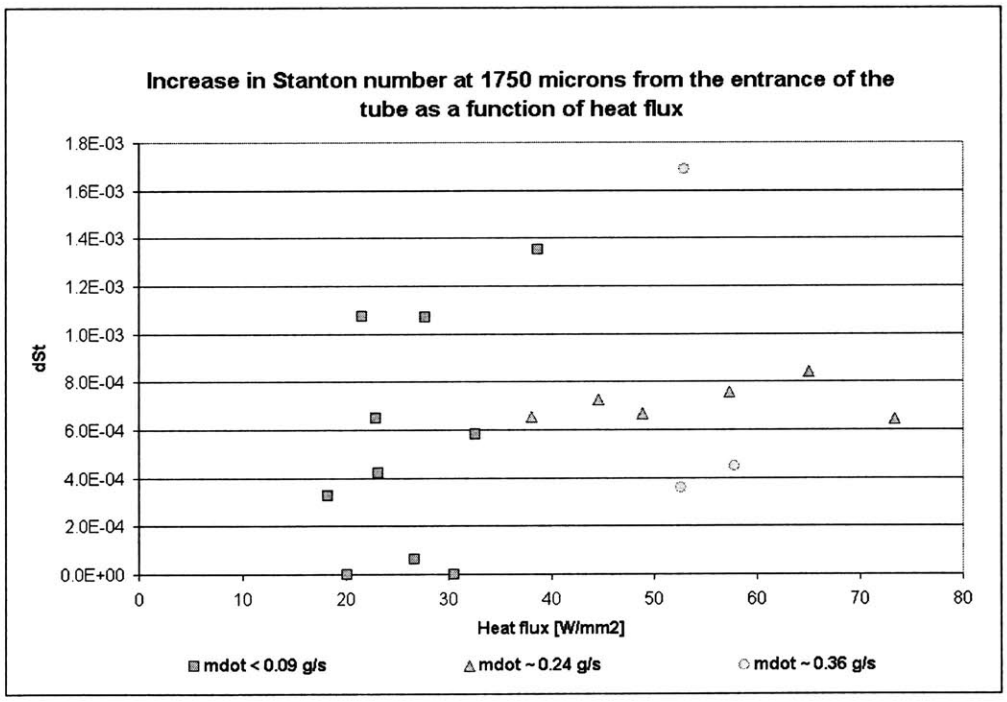

Figure 5-21: Increase in the Stanton number along the tube as a function of heat flux.

only source of enhancement. Different profiles of temperature have been obtained but no clear relation with experimental data (pressure, heat flux, mass flow, wall or bulk temperatures) could be derived. The enhancement in cooling capacity is not seen in every test. No relation has been found to predict when the enhancement is occurring. The enhancement offered by JP10 appears to be smaller than that of JP7 in the same experimental conditions. It must be noted that calculations for JP10 tests have been done with approximate data on JP10 properties. There is no estimations of the accuracy of those data. This uncertainty may impact the calculation of the bulk temperature and therefore the heat transfer calculation. The main effect will be on the estimation of the Stanton number which uses the inside wall and bulk enthalpies. The pseudo critical temperature is a main unknown that may have a strong effect on the results since it positions the peak in specific heat. This could be responsible for part of the increase in the Stanton number at the end of the tube.

5.4 Stability

Four 10-minute stability tests have been carried out with JP10 at a critical pressure ratio of 1.55, a mass flow of 0.07 g/s and a heat flux of 30 W/mm^2, following the same protocol as for those with JP7. The measurements were done at 1,400 microns from the entrance since it was a point at which the temperature was expected to be among the highest. Carbon deposits are more likely to deposit at the point of maximum temperature. Figure 5-22 shows the outside wall temperature measured during one of the stability test.

Oscillations No temperature oscillations have been recorded during the 10-minute stability tests. The temperature was stable and variations were within 20°C.

Deposits No significant decrease in the mass flow has been seen during the 10-minute stability tests. The same tube was run for a total of 40 minutes (four 10-minute stability tests). No rapid increase in temperature or decrease in mass flow can suggest deposits have formed in the tube.

Temperature profiles During the stability tests, no sharp hot points were seen. However, some variations in the temperature have been recorded. Figure 5-23 shows an increased temperature for 5 minutes in the middle of a stability test. The increase is not as high as

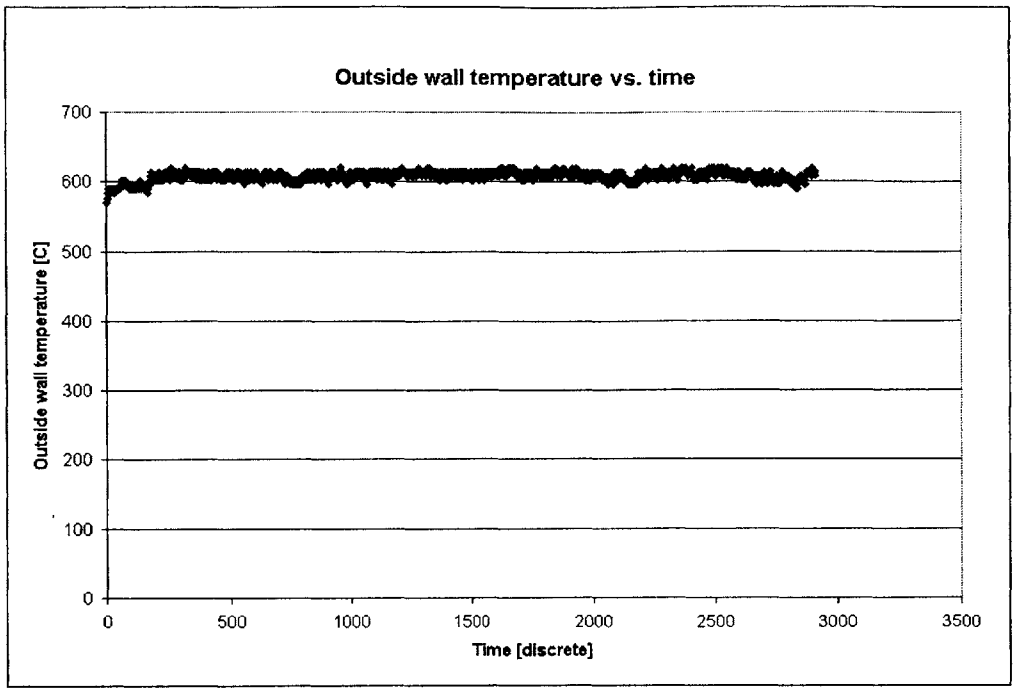

Figure 5-22: Outside wall temperature measured at 1,400 microns from the entrance during a stability test carried out at a critical pressure ratio $\frac{P}{P_c} = 1.55$, a mass flow $\dot{m} = 0.07$ g/s and a heat flux q = 30 W/mm^2.

with JP7 tests and stay within 50°C. In the tests illustrated by Figure 5-24, some instabilities in the temperature appear, which contribute to a 50°C increase in temperature. The temperature then suddenly drops to stabilize again at a 100°C lower temperature. A misalignment of the IR sensor cannot explain this drop in temperature since the pointing of the IR sensor was checked after the test.

5.4.1 Comparison with JP7 experiments

Tests have been carried out with JP7 and JP10 for the same mass flows, heat fluxes and critical pressure ratios. For both hydrocarbon fuels, the temperature measured along the tube increases at the entrance of the tube before stabilizing and decreasing at the end of the tube. Therefore, for both fuels, a significant cooling enhancement is obtained. This enhancement is seen both at subcritical, critical and supercritical pressures which seem to indicate that this enhancement is not only due to the supercritical conditions. JP7 was known to endothermically decompose providing a significant endothermy. It may be possible that JP10 is also undergoing an endothermic decomposition.

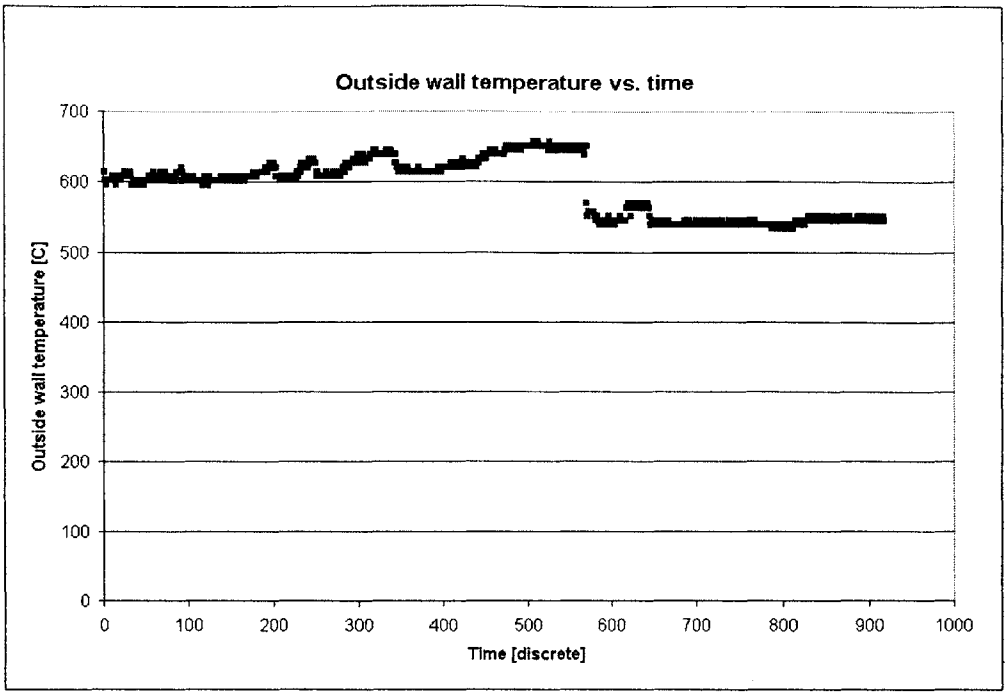

Figure 5-23: Outside wall temperature measured at 1400 microns from the entrance during a stability test carried out at a critical pressure ratio $\frac{P}{P_c} = 1.55$, a mass flow $\dot{m} = 0.07$ g/s and a heat flux q = 30 W/mm^2.

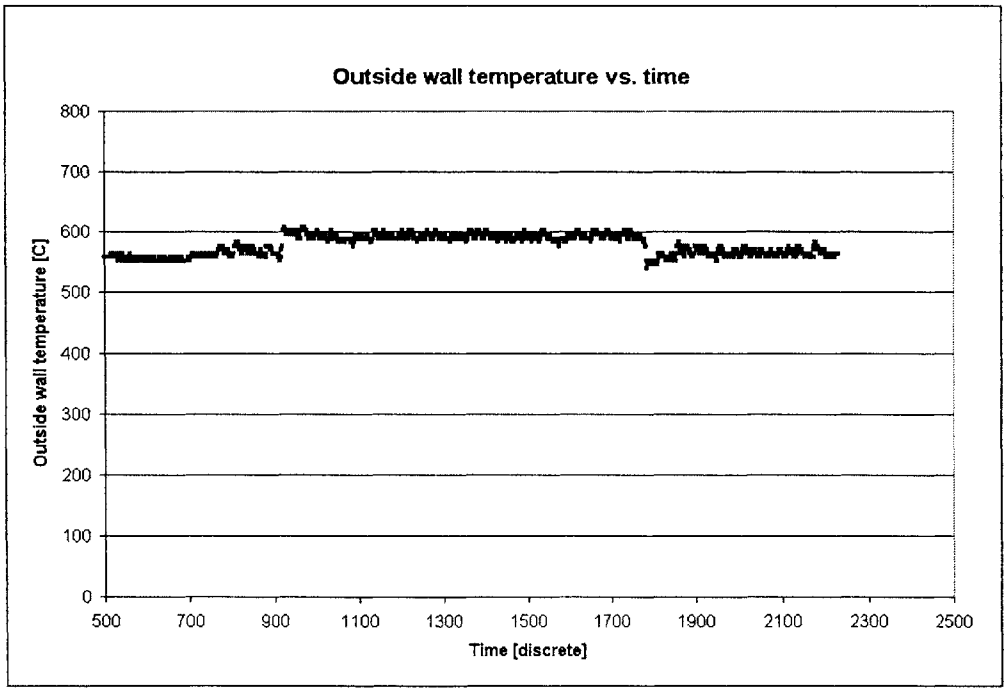

Figure 5-24: Outside wall temperature measured at 1,400 microns from the entrance during a stability test carried out at a critical pressure ratio $\frac{P}{P_c} = 1.55$, a mass flow $\dot{m} = 0.07$ g/s and a heat flux q = 30 W/mm^2.

However, the enhancement seen with JP7 is sharper than with JP10. The temperature slowly decreases in most of the tests carried out with JP10, even staying stable in some cases, whereas with JP7, in half of the tests, the temperature was decreasing rapidly. Moreover, the enhancement seen with JP7 is more significant than that seen with JP10. The temperatures reached with JP10 are higher in the same experimental conditions. The heat transfer coefficients are higher with JP7 for the same experimental conditions. Figure 5-25 shows the heat transfer coefficients obtained at 1,750 microns from the entrance of the tube for different tests carried out with JP7 and JP10. The first graphic shows the low heat fluxes from 0 W/mm^2 to 35 W/mm^2 whereas the second shows a wider range of heat fluxes. The enhancement in heat transfer coefficient for tests carried out with JP7 and JP10 is presented in Figure 5-26. A more detailed comparison can be seen in Figure 5-27 in which the results of tests carried out with JP7 and JP10 are showed for three different set of conditions. The enhancement obtained with JP7 is much more significant. Both JP7 and JP10 show good stability. No oscillations or significant effects of carbon deposition have been seen during 10-minute tests.

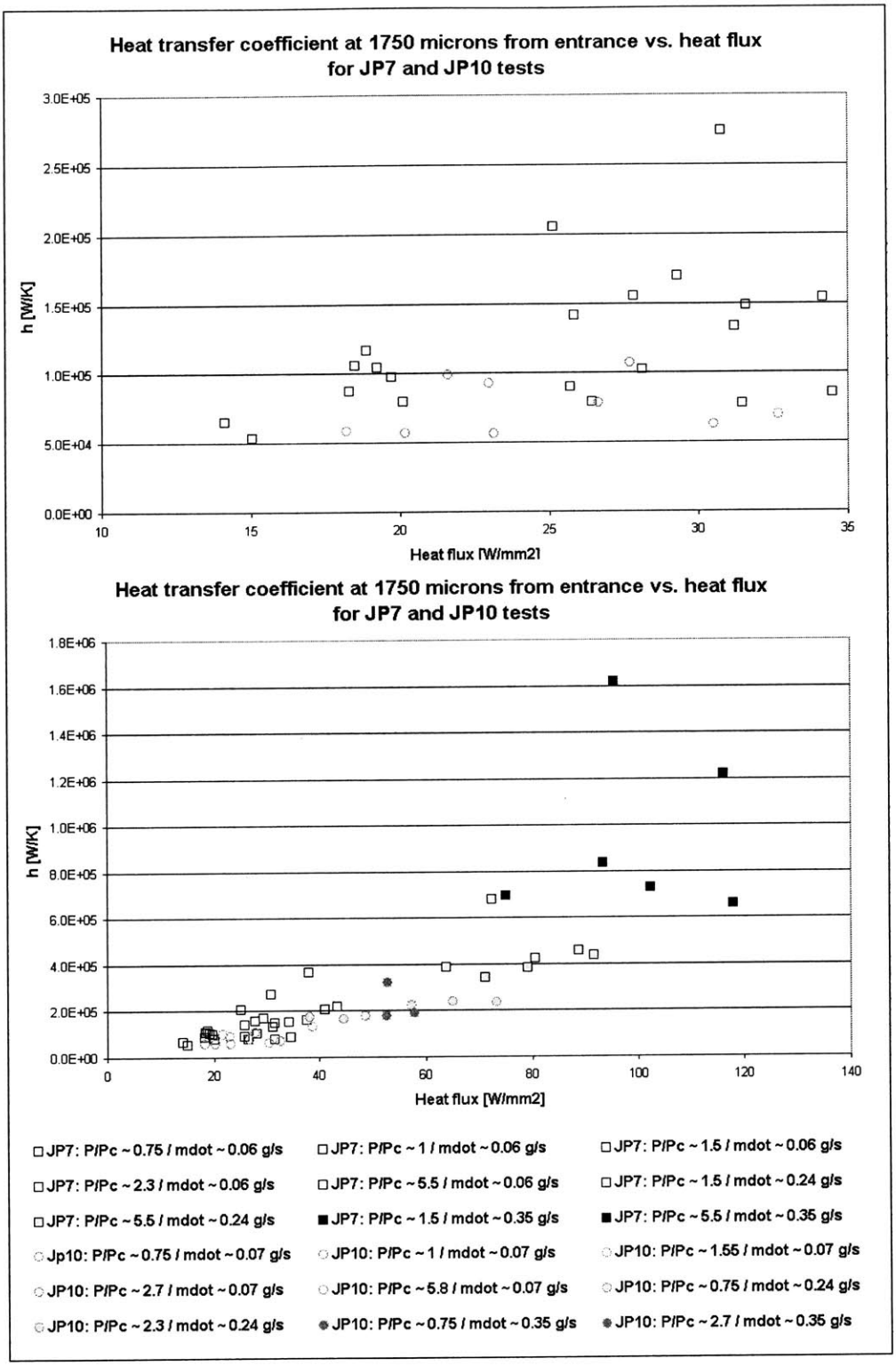

Figure 5-25: Heat transfer coefficients at 1,750 microns from the entrance as a function of heat flux for JP7 and JP10 tests.

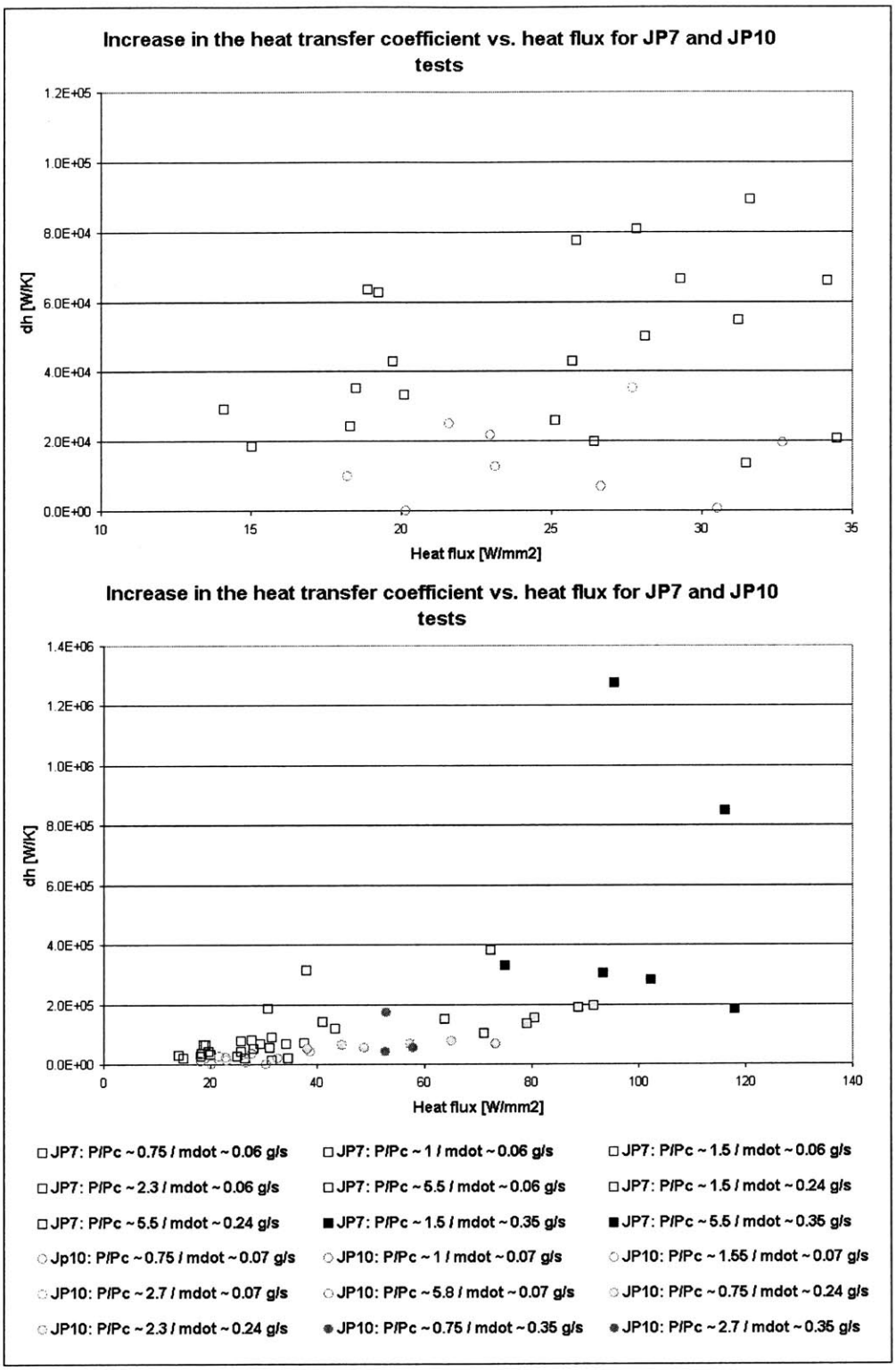

Figure 5-26: Increase in the heat transfer coefficient along the tube as a function of heat flux.

Propellant	Parameter	mdot = 0.24 g/s q = 73 W/mm2	mdot = 0.065 g/s q = 38 W/mm2	mdot = 0.065 g/s q = 20 W/mm2
JP7	*h min [W/K]*	241984< <297456	53227 < < 91696	41460
	h at 1750 microns [W/K]	343192< <678344	161775 < < 368535	104127
	dh [W/K]	101207< <380888	70078 < < 315307	62667
	St min	0.00276 < <0.0032	0.00195 < < 0.00408	0.00151
	St at 1750 microns	0.00392 < <0.0077	0.00226 < < 0.01339	0.004509
	dSt	0.00115< <0.00449	0.030 < < 0.1602	0.00299
JP10	*h min [W/K]*	97576	91118	48096
	h at 1750 microns [W/K]	236676	133356	58019
	dh [W/K]	68372	42237	9923
	St min	0.00182	0.003454	0.00192
	St at 1750 microns	0.002467	0.00481	0.00225
	dSt	0.000647	0.00135	0.00033
Difference [% of JP10 value]	*h min*	1.48< <2.04	(-)0.41	(-)0.14
	h at 1750 microns	0.45< <1.87	0.21	0.79
	dh	0.48< <4.57	0.66	5.3
	St min	0.52< <16.58	(-)0.44	(-)0.21
	St at 1750 microns	0.59 < <2.12	(-)0.53	1
	dSt	0.78< <5.94	21.22	8

Figure 5-27: Comparison of the results obtained with JP7 and JP10 for 3 experimental conditions.

Chapter 6

Hydrogen Peroxide

6.1 Presentation of Hydrogen Peroxide

Hydrogen peroxide (H_2O_2), discovered by Thenard in 1818 [6], is a clear liquid slightly more viscous than water. At low concentrations, it is used in common applications such as a bleaching agent. At high concentrations, between 70 % and 98 % (the rest being water), hydrogen peroxide is used as oxidizer in rocket applications. It is known as the military MIL-H-16005. It can be used both as a monopropellant or as an oxidizer in a bipropellant system. Hydrogen peroxide was first used as a monopropellant at a concentration of 80 % in the Helmuth Walter & Heinkel He 52 aircraft first flown in 1937 [6]. It was first used as a bipropellant in the Walter 109-509 engine which used 30 % hydrazine as fuel and 80 % hydrogen peroxide as oxidizer.

Hydrogen peroxide is more stable as the concentration increases. It is non explosive, non inflammable, non toxic and insensitive to detonation by shock or impact.

Even if it is non toxic, it can cause irritation when in contact with the skin or the eyes.

Hydrogen peroxide is stable at high concentrations as long as it is not contaminated. Hydrogen peroxide decomposes into oxygen and steam. If hydrogen peroxide is contaminated, it starts decomposing at a higher rate liberating a great amount of energy. It produces explosive mixtures with most organics. Fire will be caused by any contact of hydrogen peroxide with a combustible. As the temperature increases, the rate of decomposition increases. If heated at high temperatures in a confined area, the vapor phase may undergo a very rapid decomposition and can cause an explosion if put in contact with a flame or fire.

Density of 98% Hydrogen Peroxide

Temperature [° C]	*Density [kg/m^3]*
0	1,459.4
25	1,430.9
50	1,402.4
96	1,347*

*extrapolated value

Table 6.1: Density of 98 % hydrogen peroxide at different temperatures [29].

6.2 Hydrogen peroxide characteristics

Heat transfer tests will be done with 98 % hydrogen peroxide to try to estimate its heat capacity and its stability in conditions close to those experienced in the micro rocket engine. Some properties of 98 % hydrogen peroxide such as the density, the viscosity, the specific heat or the thermal conductivity, need to be known in order to reduce the experimental data and estimate the heat transfer coefficient. Data at 1 atm and ambient temperature are available from a FMC Chemicals Technical bulletin [29]. However, very few data are available at very high pressures and temperatures and no data have been found in super-critical conditions. This section summarizes some properties of 98 % hydrogen peroxide at 1 atm and ambient temperature [29].

6.2.1 Density

The density at different temperatures is shown in Table 6.1.

6.2.2 Viscosity

The viscosity from 0°C to 50°C is shown in Table 6.2. For temperatures ranging from 100°C to 300°C, the following formula is recommended for the estimation of the viscosity of 98 % hydrogen peroxide (precision ± 2%):

$$\mu = 134 + 0.35(T - 100) - 13.3 \tag{6.1}$$

where μ is the viscosity in micropoises and T the temperature in °C [29].

Viscosity of 98 % hydrogen peroxide

Temperature [° C]	*Viscosity [centipoises]*
0	1.51
25	1.156
50	0.815

Table 6.2: Viscosity of 98 % hydrogen peroxide at different temperatures [29].

Thermal conductivity of 98 % hydrogen peroxide

Temperature [° C]	*Thermal conductivity [Btu.ft/(hr.ft^2.F)*
0	0.321
25	0.339

Table 6.3: Thermal conductivity of 98 % hydrogen peroxide at 0°C and 25°C and ambient pressure [29].

6.2.3 Thermal conductivity

The thermal conductivity of 98 % hydrogen peroxide at 0°C and 25°C is shown in Table 6.3.

6.2.4 Surface tension

Hydrogen peroxide has a surface tension of about 80.2 Dynes/Cm at 20°C.

6.2.5 Critical point

The critical conditions of 100 % hydrogen peroxide are P_c = 214 atm (3,140 psi) and T_c = 457°C (730 K). Therefore, the hydrogen peroxide will be around critical conditions in the passages of the rocket engine at the difference with JP7, JP10 or ethanol which will be at very high critical pressure ratios. Supercritical effects will be significant and H_2O_2 properties will be very sensitive to temperature since pressure will be around critical.

6.2.6 Thermal properties

The specific heat or the enthalpy profile of hydrogen peroxide is required in the reduction of the results of hydrogen peroxide heat transfer tests to calculate the bulk temperature and therefore the heat transfer coefficient. Some data available at 1 atm are presented in

this section.

The mean specific heat of liquid 98 % hydrogen peroxide solution between 0°C and 27°C is 0.6322 cal/(C.g of solution). The heat capacity and the enthalpy of 100 % hydrogen peroxide vapor is presented in Figure 6-1.

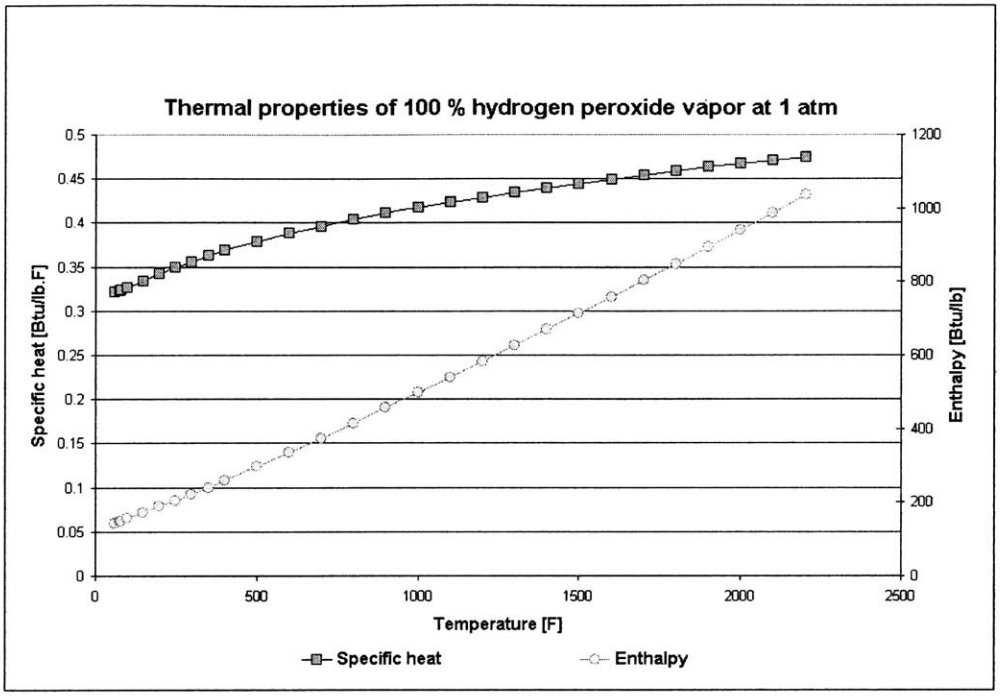

Figure 6-1: Specific heat and enthalpy of 100 % hydrogen peroxide vapor for different temperatures at 1 atm [29].

6.2.7 Decomposition reaction

The hydrogen peroxide decomposes into oxygen and steam as seen in the following balance equation:

$$H_2O_2 \,.\, 0.0526\, H_2O(liq) \quad = \quad 1.0526\, H_2O(liq) \quad + \quad \frac{1}{2}\, O_2(gas) \tag{6.2}$$

The typical rate of decomposition is approximately of 1 % per year. The rate of decomposition increases with temperature and pressure. The heat of decomposition at 1 atm and 25°C is 1,213.7 Btu/lb of solution.

6.3 Hydrogen peroxide handling

98 % hydrogen peroxide is non toxic but can cause some irritations when in contact with the skin or the eyes. It may ignite when in contact with any organics, leather, cotton, etc. Hair and clothes must be protected. Safety goggles, a facial mask, a complete clothing made of Dacron, Dynel or Orlon, gloves and rubber shoes are required when handling 98 % hydrogen peroxide [1]. Most care must be put into not contaminating the hydrogen peroxide with any organics, dust, carbon, etc.
In case of emergency, deionized water must be used to rinse and dilute the hydrogen peroxide. Hydrogen peroxide is not dangerous at low concentrations.

6.4 Hydrogen peroxide compatibility

6.4.1 Compatibility issues

Hydrogen peroxide at a high concentration (98 %) is a strong oxidizer and presents some compatibility issues. The effect of hydrogen peroxide to the material and the effect of the material to the hydrogen peroxide are both to be considered.

- 98 % hydrogen peroxide is a strong oxidizer and may cause some damage to the material. Before using a material with high concentrated hydrogen peroxide, it must be passivated with low concentration hydrogen peroxide (usually 30 %). Hydrogen peroxide reacts with the material to form a protective layer which will prevent high concentrated hydrogen peroxide to come in contact with the material.
- Hydrogen peroxide is more stable at high concentrations than at low concentrations. However, when in contact with a non compatible material, the decomposition will accelerate and eventually liberate a great amount of energy. If placed in a confined area, this may cause an explosion.

6.4.1.1 Common materials compatibility [3]

The best materials to contain hydrogen peroxide are aluminum, 316 or 304 stainless steel and glass. Materials not to be used are copper, graphite and most of the metals (iron, gold, nickel, silver) except for zirconium. The compatibility of a material is ranged on a scale from 1 to 4. A class 1 material can be used for long term storage. A class 4 material should

not be in contact with hydrogen peroxide at high concentrations. Compatibility of some materials are very sensitive and depends on the way they are fabricated. Materials from different suppliers can have different compatibility classes sometimes from a class 1 to a class 4 material. Therefore, it is recommended to tests the compatibility of the materials which are going to be used [1].

6.4.1.2 Tanks and long term storage [3]

Best materials for long term storage are aluminum, glass and 304 stainless steel. Tanks must be vented so that the products of the decomposition can escape and monitored in pressure and temperature. A rapid increase in temperature indicates a rapid decomposition of the hydrogen peroxide. As the temperature increases, the rate of decomposition will increase. Therefore, in case of a rapid increase in temperature or pressure, the hydrogen peroxide must be neutralized immediately with deionized water.

6.4.2 Compatibility tests for MEMS material

MEMS devices use mainly silicon. Hydrogen peroxide is used in some cleaning steps in micro fabrication and is compatible with silicon at ambient conditions. Hydrogen peroxide reacts with silicon to form a protective layer of oxide SiO_2. However, high temperature oxygen and steam are used in micro fabrication to grow oxide layers. Therefore as the decomposition reaction of hydrogen peroxide produces oxygen and steam, compatibility of hydrogen peroxide at high temperatures will have to be tested.

Tests have been carried out to verify the compatibility of 98 % hydrogen peroxide with different materials used in MEMS device as the micro rocket engine, the turbopump and the electric motor.
The experimental protocol was the following:

- The die is cleaned with deionized water prior to the experiment.
- The die is placed in a glass Petri dish with 30 % hydrogen peroxide for passivation. In regular tests, the 30 % hydrogen peroxide bath lasted for 1 hour.
- The die is then rinsed in deionized water before being introduced in a glass Petri dish with 98 % hydrogen peroxide.

Pictures of the die and some of its features have been taken before the 30 % hydrogen peroxide bath, between the two baths and after being introduced in 98 % hydrogen peroxide. A summary of the tested materials and the results of the tests is shown in Figure 6-2.

Summary of compatibility tests with MEMS materials							
	Piece tested	*Number of tests*	*Time in 30% H2O2*	*Behavior in 30% H2O2*	*Time in 98% H2O2*	*Behavior in 98% H2O2*	*Compatibility at ambient temperature*
Dies	Piece of silicon wafer	3	30 minutes	no reaction	up to one month	no reaction	Perfect
	Pyrex (turbopump)	1	30 minutes	no reaction	up to one week	no reaction	Perfect
	Layer of turbopump	2	1 hour	no reaction	up to one month	small bubbles when first in contact, no reaction after one minute, features intact	Perfect
	Bearing die	2	1 hour	no reaction	up to one month	small bubbles when first in contact, no reaction after a few minutes, features intact	Perfect
	Stator layer of the electric motor	2	1 hour	Large amount of bubbles when first in contact, emission of gases concentrated in the central zone, still bubbles after 1 hour	30 minutes	Large reaction and emission of bubbles, die taken out as the emission was not diminishing	Need long passivation, not a perfect compatibility
	Stator layer of the electric motor	2	48 hours	Large amount of bubbles when first in contact, emission of gases concentrated in the central zone, no bubbles after 48 hours	up to one week	small bubbles when first in contact, no reaction after 30 minutes	
Packaging	Glass beads (micro rocket)	2	30 minutes	no reaction	up to one week	small bubbles when first in contact, no reaction after a few minutes	Perfect
	Kovar tubes	2	30 minutes	no reaction	up to one week	no reaction, surface intact, attach of the glass bead to the Kovar tube still holds	Perfect

Figure 6-2: Compatibility of 98 % hydrogen peroxide with MEMS materials. Summary of compatibility experiments.

6.4.2.1 Dies

Most of the dies tested showed a perfect compatibility with 98 % hydrogen peroxide. Some small emissions of bubbles is seen when the sample is introduced in 30 % hydrogen peroxide. After passivation, no reaction is seen in 98 % hydrogen peroxide for most of the samples. Some vapor is seen on the cap of the Petri dish for tests in 98 % hydrogen peroxide, which shows that H_2O_2 is decomposing, but no rapid decomposition has been seen except for the stator layer of the electric motor.

Both the effects of hydrogen peroxide on the surface and on precise features have been studied. Pictures and observations show that no damage has been seen on the surface of

the dies. No change in the shape of the precise features (turbine blades, holes, etc.) has been seen.

The stator of the electric motor is the only tested die which showed a strong reaction to hydrogen peroxide both at a concentration of 30 % and 98 %. The firsts dies tested caused a strong reaction when introduced in 30 % hydrogen peroxide. The hydrogen peroxide was decomposing fast creating a lot of bubbles and steam. The reaction occurred only on the two inner rings and the external part which correspond to the features made of platinum on a thin layer of titanium. Figure 6-3 gives a description of the stator layer of the electric motor and indicates the regions where the reaction occurred. A better cleaning of the die did not improve the compatibility. Therefore, there seem to be some compatibility issues between hydrogen peroxide and platinum. The die has been left for up to 2 days in the passivation bath in 30 % hydrogen peroxide. 2 days seemed enough to see the reaction stop in 30 % hydrogen peroxide. No major reaction was seen when the die was introduced in 98 % hydrogen peroxide after the 2-day passivation. Therefore, it seems that a longer passivation can solve the compatibility issue with platinum. However, a reaction occurs at the platinum surface and may alter the surface. This could be an issue for the operation of the electric motor. During passivation of silicon, hydrogen peroxide reacts with silicon to form the oxide SiO_2 which is inert to hydrogen peroxide and acts as a protective layer. Therefore, the part of the stator covered with SiO_2 will surely show perfect compatibility.

6.4.2.2 Packaging materials

The packaging of the rocket uses Kovar tubes to inject the propellants and coolant into the micro rocket chip and glass beads to seal the connection between the silicon surface and the Kovar tubes. Both materials have been tested for compatibility and both show perfect compatibility with 98 % hydrogen peroxide after passivation with 30 % hydrogen peroxide. A test has been done with a Kovar tube attached with a glass bead on a piece of silicon. No damage on the connection of the Kovar tube to the silicon or to the glass bead has been seen. However, the resistance of the glass bead seal has not been tested.

All those tests show that materials used in MEMS devices and packaging show good compatibility with 98 % hydrogen peroxide after passivation in a lower concentration solution

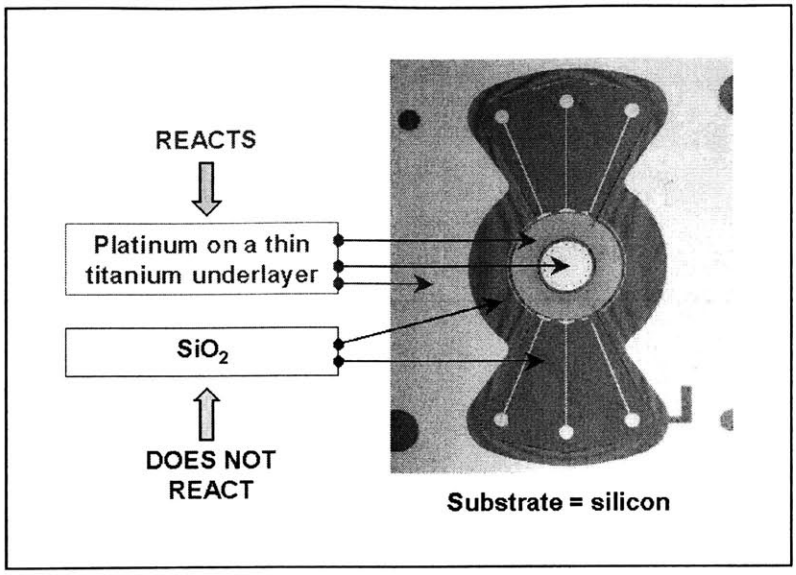

Figure 6-3: Stator layer of the electric motor with the different materials used in this layer.

at ambient temperature. However, no tests have been done to verify the compatibility at high temperatures.

6.4.3 Test rig preparation for tests with highly concentrated hydrogen peroxide

Materials and parts used in the test rig for heat transfer experiments with hydrogen peroxide must be checked for compatibility. The experimental set up described in Section 3.3.2 must be modified for safety. The schematic of the new test rig is shown in Figure 6-4.

6.4.3.1 Modifications of the test rig

If a problem occurs during the tests, 98 % hydrogen peroxide must be diluted with deionized water. Moreover, the pipes and valves must be flushed with deionized water after tests are done so that no hydrogen peroxide at high concentration stays in the test rig. Therefore, a deionized water circuit is added to the test rig. It allows to flush the whole test rig and then dump the water or diluted hydrogen peroxide in a tank called the H_2O dump tank on the schematic of the test rig.

The 98 % hydrogen peroxide left in the fluid tank at the end of the experiments can be dumped in the H_2O_2 dump tank prior to flushing the test rig with deionized water. This can be commanded from the control room.

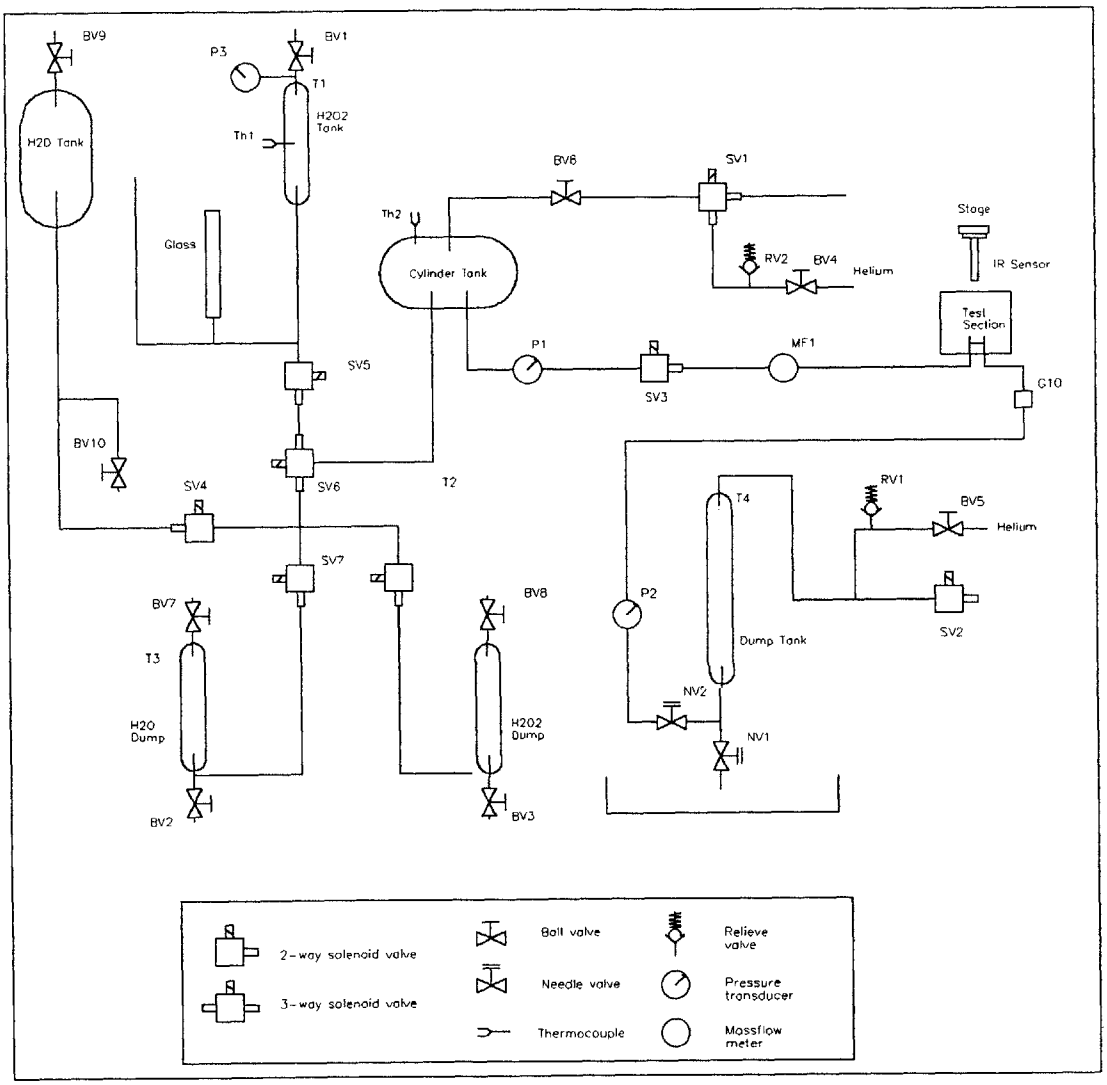

Figure 6-4: Schematic of the H_2O_2 rig.

The method to fill the fluid tank is modified so that it can be done remotely from the control room. An hydrogen peroxide tank is added. When the test rig is prepared for testing, the fluid tank can be filled from this tank by opening solenoid valves remotely controlled.
Relief valves are added on the helium circuit to maintain a constant pressure in the cylinder tank and the dump tank.
The test section is an issue as when the test section will break, hydrogen peroxide will be sprayed. A small electronic box is added around the test section. A hole allows the IR sensor to measure the outside temperature through the protective box. The IR sensor is therefore also protected.

6.4.3.2 Material compatibility

Materials have been carefully chosen and tested for compatibility.
The hydrogen tank is a 304 stainless steel tank rated up to 1,800 psi. The dump tanks (H_2O_2 dump tank, H_2O dump tank and dump tank) are all 316 stainless steel. The valves have been selected to be mainly stainless steel and all non stainless steel wetted parts have been tested for compatibility following the same protocol as the one presented in Section 6.4.2.
The electrodes are made of copper which is a class 4 material for compatibility with hydrogen peroxide at high concentration. However, this should not be an issue since the main reason for the non compatibility of hydrogen peroxide with copper is the rapid decomposition of hydrogen peroxide when in contact with copper (damage of the electrodes should not be an issue). The products will be relieved in a non confined area and little hydrogen peroxide will be available since the valves that connect to the tanks will be closed. The same applies to the electric wires of the voltage control loop for the power supply.

6.4.3.3 Passivation of the test rig

The test rig must be passivated prior to any contact with highly concentrated hydrogen peroxide. The passivation sequence must begin by cleaning the parts with 70 % nitric acid for 4 to 5 hours at room temperature. After rinsing with distilled water, the rig must first be filled with low concentration hydrogen peroxide (30 %). The rate of decomposition of the hydrogen peroxide must be carefully monitored. If no incompatibility is seen, the rig

can be filled with high concentration hydrogen peroxide. More details about the various passivation protocols for different parts can be found in Reference [3].

6.4.3.4 Operation of the test rig

The nominal operation steps are detailed in the following paragraph. The test rig is assumed to be non pressurized and all valves closed at the beginning of the experiments. The hydrogen peroxide tank is assumed to be filled.

1. Fill the cylinder tank.
2. Insert the test section, attach the electrodes.
3. Point the IR sensor and set the zero position of the stage to the entrance of the tube.
4. Make sure the pointing can be done through the protective box and install the protective box.
5. Pressurize the test rig. The relief valves must be set to the right pressure by adjusting the springs.
6. Check the IR sensor pointing right before testing.
7. Test: hydrogen peroxide flows through the test section. Set the heat flux to the required level and take measurements.
8. Stop the heating and stop the fluid flow through the test section.
9. Depressurize the test rig.
10. Back to step 2 for additional experiments
11. At the end of the experiments, empty the hydrogen peroxide remaining in the fluid tank into the H_2O_2 dump tank.
12. Flush the first half of the test rig with deionized water.
13. Open the solenoid valve which controls the flow to flush with deionized water the second half of the test rig.

In case of emergency during an experiment, the following procedure can be used:

1. Stop the heating and the flow of fluid.

2. Depressurize the test rig

3. Eventually empty the hydrogen peroxide remaining in the fluid tank.

4. Flush the test rig with deionized water. Extinguisher cannot be used nor any chemical products in case of fire. Deionized water must be used to extinguish a fire and dilute the hydrogen peroxide.

6.5 Conclusion

Materials used in the micro devices have shown good compatibility with highly concentrated hydrogen peroxide after passivation in 30 % hydrogen peroxide. Dies left in a passivation bath for 30 minutes to one hour seem to show no reaction with highly concentrated hydrogen peroxide. The stator layer must be left for 2 days so that a protective layer has been grown on the platinum surface. The passivation layer may modify the surface of the die which may be an issue for the operation of the electric motor.

The test rig must be modified for use with 98 % hydrogen peroxide: safety systems must be added and compatible materials must be used. A layout of the new test rig has been proposed and the new parts have been tested for compatibility with 98 % hydrogen peroxide. It must be noticed that all the compatibility tests done conclude about the compatibility at ambient pressure and temperature. Compatibility at high temperatures and pressures, such as those chosen for the heat transfer tests or for use in the micro rocket engine, may be different and additional tests may have to be conducted.

Chapter 7

Elements for the design of the liquid micro rocket engine

The tests carried out with ethanol, JP7 and JP10 aim at giving some background for the future design of the liquid micro rocket engine. This section presents a summary of the results found that could be used for the design of the engine. In a first section, a comparison of the cooling capacity of the three fuels tested is presented. In a second section, the validity of various heat transfer correlations is evaluated. Finally, some issues about the validity of the predictions given by the heat transfer experiments for the design of the micro rocket engine are investigated.

7.1 Cooling capacity of the fuels tested

The heat transfer coefficients obtained with ethanol, JP7 and JP10 during tests done under the same conditions are compared. For ethanol, the heat transfer calculated at the mid point of the tube is chosen. For JP7 and JP10, the heat transfer coefficient calculated at 1,750 microns from the entrance is considered.

At low critical pressure ratios, ethanol offers a better heat transfer coefficient than JP10 and comparable heat transfer coefficients as JP7 as shown in Figure 7-1. At higher critical pressure ratios, the effect of the supercritical enhancement is reduced whereas the effect of the endothermy is still significant. Heat transfer coefficients obtained with ethanol are much lower than those obtained for JP7. Heat transfer coefficients obtained with JP10 are lower than those obtained with ethanol. However, it must be noted that only one test has

Experimental conditions		P/Pc = 1.6 mdot = 0.075 g/s q = 27 W/mm2	P/Pc = 1.6 mdot = 0.063 g/s q = 19 W/mm2	P/Pc = 1.6 mdot = 0.057 g/s q = 14 W/mm2	P/Pc = 1.6 mdot = 0.057 g/s q = 31 W/mm2
Heat transfer coefficient [W/K]	JP7	-	99,403	61,873	141,728
	JP10	78,161	-	-	-
	Ethanol	140,000 (195,000 at end point)	50,000 (100,000 at end point)	60,000	140,000 (230,000 at end point)

Figure 7-1: Heat transfer coefficients for ethanol, JP7 and JP10 for different experimental conditions at a critical pressure ratio of 1.6.

been carried out at a high critical pressure ratio with JP10 because of the leak in the G10 block at pressures above 2,500 psi.

There are issues in comparing the measurements from experiments with different fuels. First the temperature measurement techniques were different for the ethanol tests for which thermocouples were welded on the tube. Secondly tests in the same conditions can give a wide range of heat transfer coefficients and reproducibility is an issue. Moreover, there is an uncertainty about the position of the mid point in ethanol tests. The heat transfer coefficients obtained with JP7 varies a lot depending on the position along the tube since there is a sharp increase at the end of the tube. The position at which the results should be compared is not clear. Heat transfer coefficients obtained after 1,750 microns are not showed in this comparison because the validity of the measurements after 1,750 microns was questionable. However, it must be noted that they can reach values above 2×10^6 W/K which are far above any heat transfer coefficient recorded during tests with ethanol.

To conclude, it seems that JP7 offers the highest heat transfer coefficients at high pressures.

7.2 Heat transfer correlations

7.2.1 Design of the rocket engine

In the design of the micro rocket engine, the hot side heat transfer coefficient which characterizes the convection at the chamber wall is evaluated from a heat transfer correlation

using the properties of the propellants and of the products of their combustion. The cold side heat transfer coefficient characterizes the convection at the coolant passage inside wall. The cold side heat transfer coefficient required to keep the silicon wall at 900 K is computed from the heat load and the conduction through the silicon wall. The actual cold side heat transfer coefficient is estimated with a heat transfer correlation. The coolant passage design is then adapted to match the actual and the required cold side heat transfer coefficients. The best heat transfer correlation to predict the behavior of the propellant in the cooling passages must be determined to help the design of the cooling passages.

The following nomenclature is used in the rest of this chapter:
Nu corresponds to the Nusselt number, Re to the Reynolds number, Pr to the Prandtl number, ρ to the density, μ to the viscosity, κ to the thermal conductivity, Cp to the specific heat, P to the pressure, Pc to the critical pressure, T to the temperature, Tpc to the pseudo critical temperature and H to the enthalpy. The subscripts w refers to the fluid properties at the inside wall and b to the properties of the bulk fluid. $\overline{c_p}$ is defined as:

$$\overline{c_p} = \frac{H_w - H_b}{T_w - T_b} \tag{7.1}$$

7.2.2 Ethanol tests

Among the various heat transfer correlations tested, the following has been seen to best match the results from the tests carried out with ethanol [23]:

$$Nu = 0.025\, Re^{0.8}\, Pr^{0.4} \tag{7.2}$$

7.2.3 Heat transfer correlations tested

The heat transfer coefficients predicted by different heat transfer correlations were compared to the experimental heat transfer coefficients obtained during tests with JP7 and JP10.
The following heat transfer correlations have been tested [23]:

Propane correlation This relation was derived for supercritical propane cooling of rocket thrust chambers:

$$Nu = 0.00568\, Re^{0.876}\, Pr^{0.4} \left(\frac{\rho}{\rho_w}\right)^{0.12} \left(\frac{\mu}{\mu_w}\right)^{-0.142} \left(\frac{\kappa}{\kappa_w}\right)^{0.828} \left(\frac{\overline{c_p}}{c_p}\right)^{-0.368} \left(\frac{P}{P_c}\right)^{0.254} \tag{7.3}$$

Hines correlation

$$Nu = 0.005\, Re^{0.95}\, Pr^{0.4} \tag{7.4}$$

Hendricks correlation

$$Nu = 0.021\, Re^{0.8}\, Pr^{0.4} \tag{7.5}$$

Nominal correlation This correlation has been chosen for the design of the gaseous micro rocket engine which uses ethanol as coolant. This correlation is called the Dittus-Boelter equation and is said to give a good prediction for supercritical JP7 [15].

$$Nu = 0.025\, Re^{0.8}\, Pr^{0.4} \tag{7.6}$$

Nominal corrected correlation This correlation called the Sieder-Tate equation has been shown to give good predictions with supercritical JP7 in macro tubes [15].

$$Nu = 0.027\, Re^{0.8}\, Pr^{0.333} \left(\frac{\mu}{\mu_w}\right)^{0.14} \tag{7.7}$$

K-P 2 correlation This correlation uses a friction factor defined as:

$$f = \frac{1}{(3.64\, ln(Re) - 3.28)^2} \tag{7.8}$$

and a Nusselt number for constant temperature properties defined as:

$$Nu_{c_p} = \frac{\frac{f}{2}\, Re\, Pr}{12.7\sqrt{\frac{f}{2}}\,(Pr^{\frac{2}{3}} - 1) + 1.07} \tag{7.9}$$

The Nusselt number is calculated as follow:

$$Nu = Nu_{c_p} \left(\frac{\rho_w}{\rho}\right)^{0.3} \left(\frac{\overline{c_p}}{c_p}\right)^n \tag{7.10}$$

where n is given by:

$$n = 0.4 \qquad if \quad T < T_w < T_{pc} \quad or \quad T_{pc} < T < T_w \tag{7.11}$$

$$n = 0.4 + 0.2\,(\frac{T_w}{T_{pc}} - 1) \qquad if \quad T < T_{pc} < T_w \tag{7.12}$$

$$n = 0.4 + 0.2\,(\frac{T_w}{T_{pc}} - 1)\,(1 - 5\,(\frac{T}{T_{pc}} - 1)) \qquad if \quad T_{pc} < T < 1.2\,T_{pc} \tag{7.13}$$

where T_{pc} represents the pseudo critical temperature.

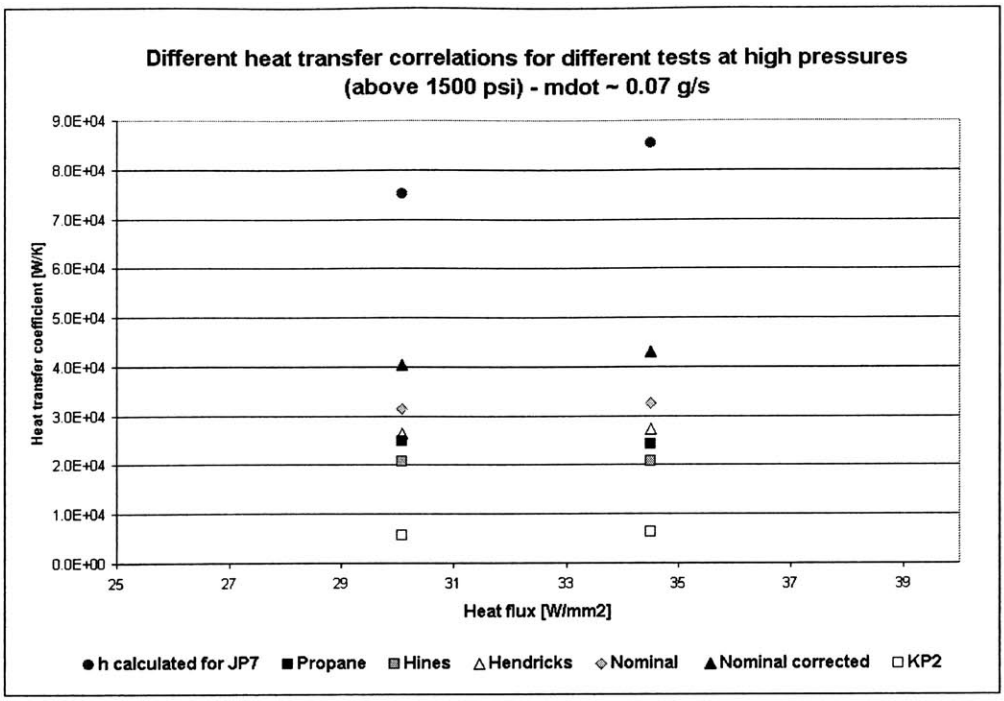

Figure 7-2: Heat transfer coefficients given by different heat transfer correlations are compared to the experimental heat transfer coefficients obtained during tests with JP7 at a mass flow of 0.07 g/s.

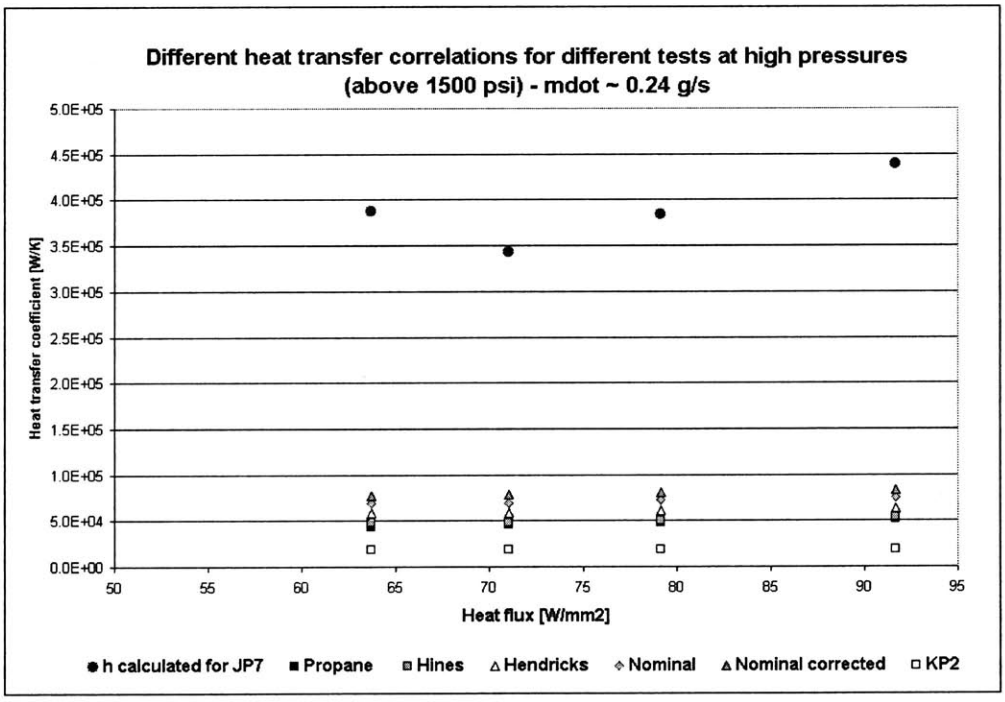

Figure 7-3: Heat transfer coefficients given by different heat transfer correlations are compared to the experimental heat transfer coefficients obtained during tests with JP7 at a mass flow of 0.24 g/s.

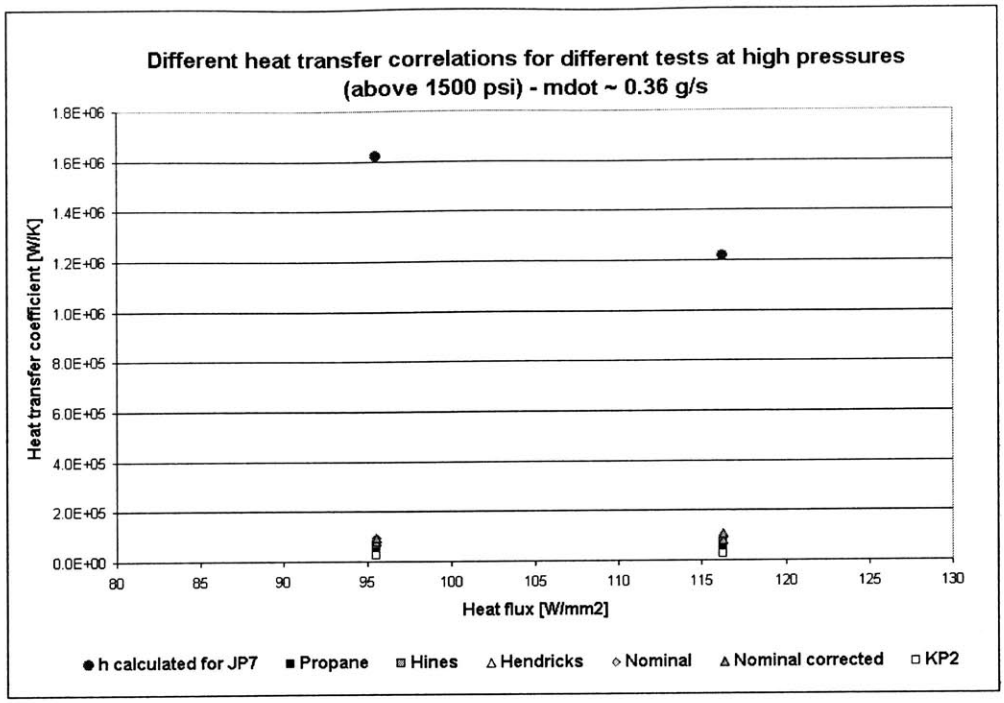

Figure 7-4: Heat transfer coefficients given by different heat transfer correlations are compared to the experimental heat transfer coefficients obtained during tests with JP7 at a mass flow of 0.36 g/s.

7.2.4 JP7 data

The results for tests with JP7 at 1,500 psi and different mass flows are shown in Figure 7-2, Figure 7-3 and Figure 7-4. The best estimation seems to be given by the Nominal corrected correlation. As the Reynolds number increases (for increased mass flows), the estimation from the correlation differs more from the experimental data.

In tests carried out with supercritical JP7 in macro tubes [15], the Nominal corrected correlation is reported to best match the experimental data at the beginning of the test while the Nominal correlation eventually best matches the experimental heat transfer coefficient later in the run. The same trend is not seen in the results from the experiments at micro scale as shown in Figure 7-5, which shows a comparison of the heat transfer coefficients predicted by these two heat transfer correlations with the experimental heat transfer coefficient obtained during a test with JP7. The heat transfer coefficient predicted by the Nominal corrected correlation even decreases at the end of the tube as the temperature decreases, whereas the experimental heat transfer coefficient increases due to the reaction of decomposition.

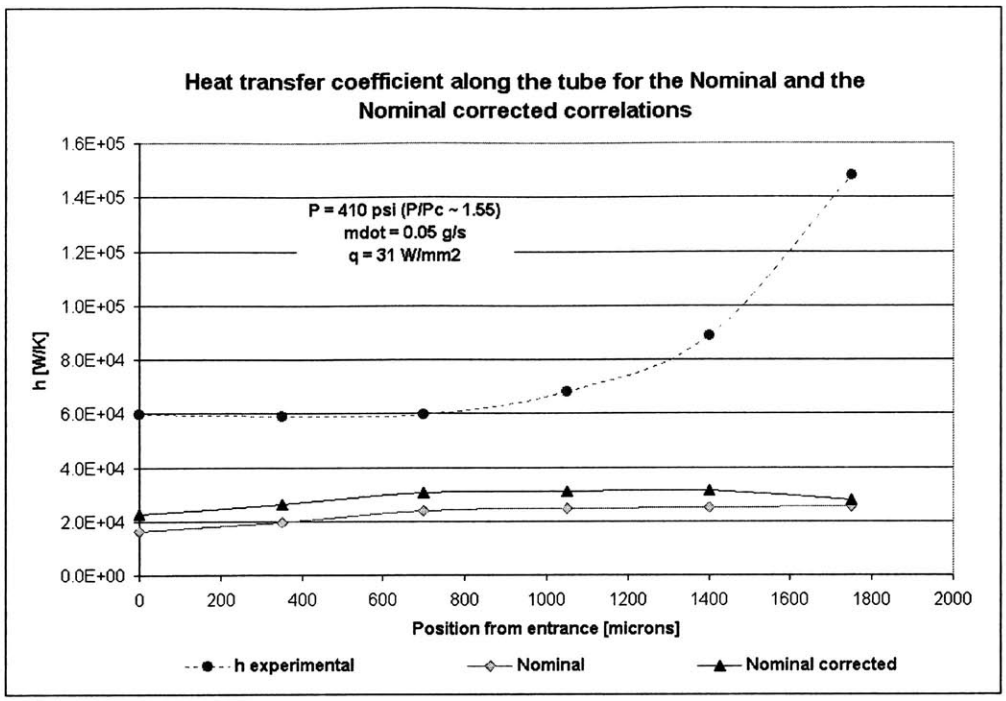

Figure 7-5: The heat transfer coefficients given by the Nominal and the Nominal corrected correlations are compared to the experimental heat transfer coefficients obtained during a test with JP7.

7.2.5 JP10 data

The results for tests with JP10 at pressures between 800 psi and 1,500 psi for different mass flows are shown in Figure 7-6, Figure 7-7, Figure 7-8 and Figure 7-9. The predictions given by the correlations seem to be closer for tests done with JP10 than for tests done with JP7. The Nominal corrected correlation seems to give the best predictions, as with JP7 data.

7.3 Extrapolation of the results of the heat transfer experiments for the micro rocket engine

The validity of the heat transfer tests carried out for the prediction of the behavior of the propellants in the micro rocket engine can be an issue. Tests have been carried out in micro channels at pressures and under heat fluxes as close as possible to the conditions experienced in the micro rocket engine. However, there are significant differences between the experimental conditions in the heat transfer experiments and in the micro rocket engine which may produce significant differences in the behavior of the fluids.

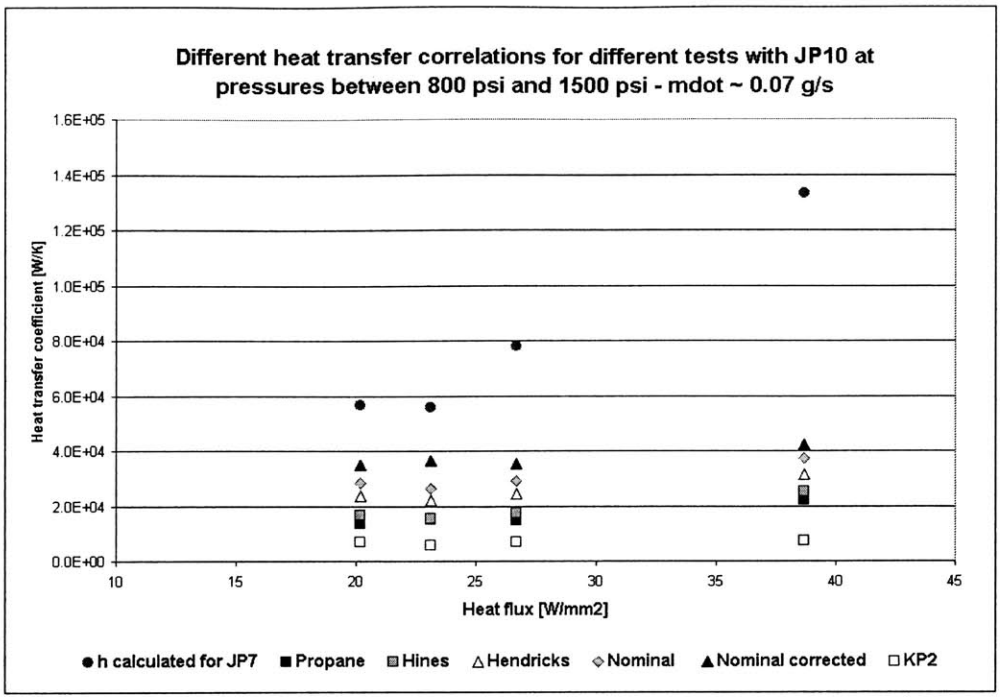

Figure 7-6: Heat transfer coefficients given by different heat transfer correlations are compared to the experimental heat transfer coefficients obtained during tests with JP10 at a mass flow of 0.07 g/s.

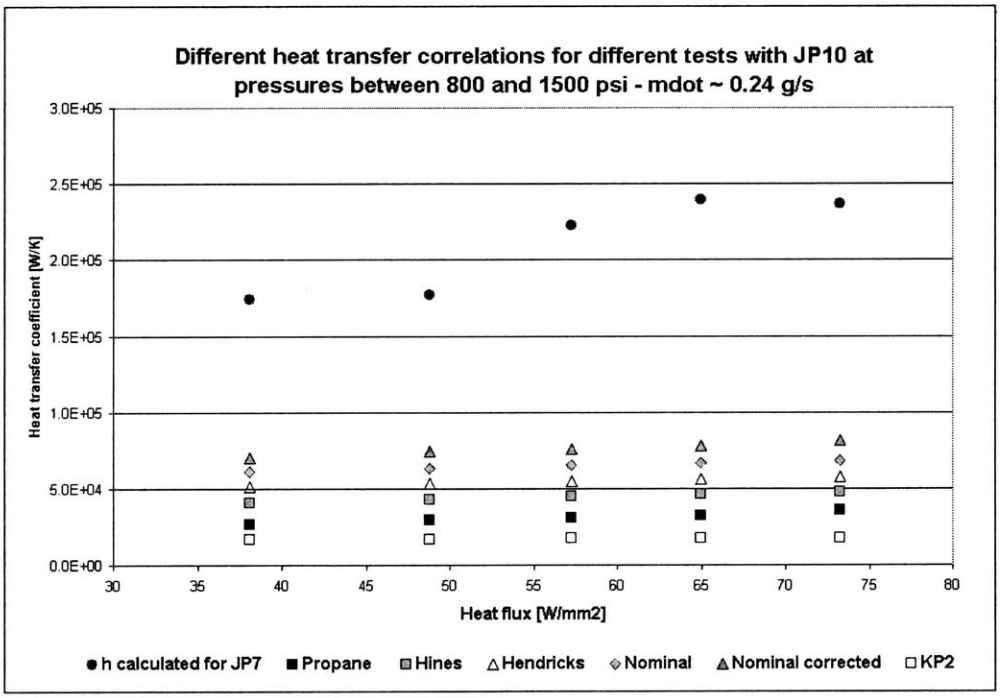

Figure 7-7: Heat transfer coefficients given by different heat transfer correlations are compared to the experimental heat transfer coefficients obtained during tests with JP10 at a mass flow of 0.24 g/s.

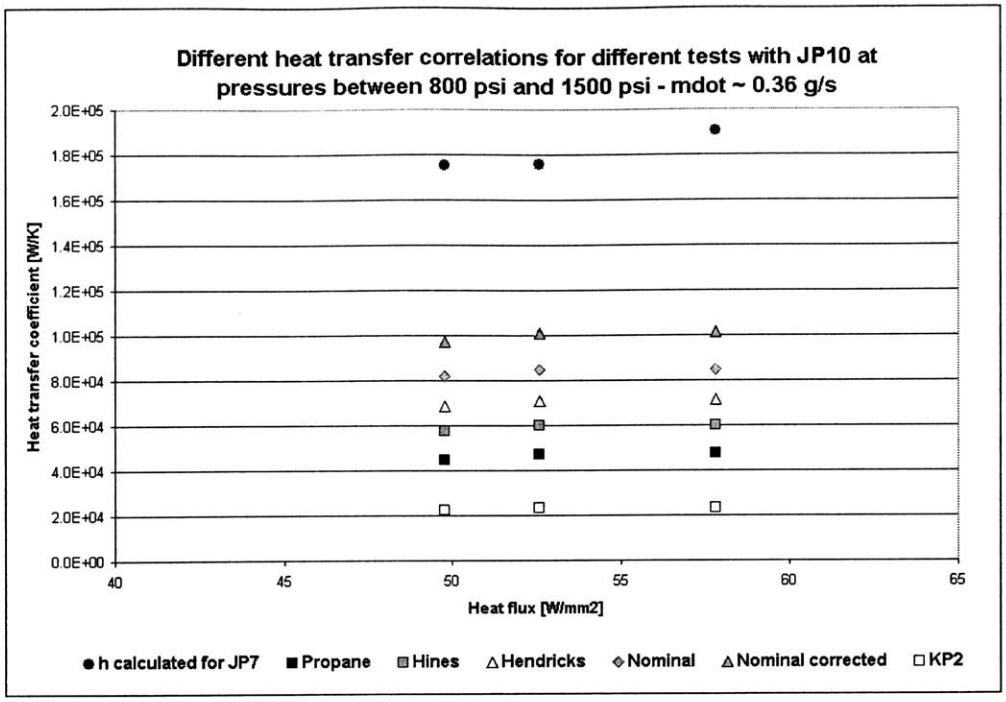

Figure 7-8: Heat transfer coefficients given by different heat transfer correlations are compared to the experimental heat transfer coefficients obtained during tests with JP10 at a mass flow of 0.36 g/s.

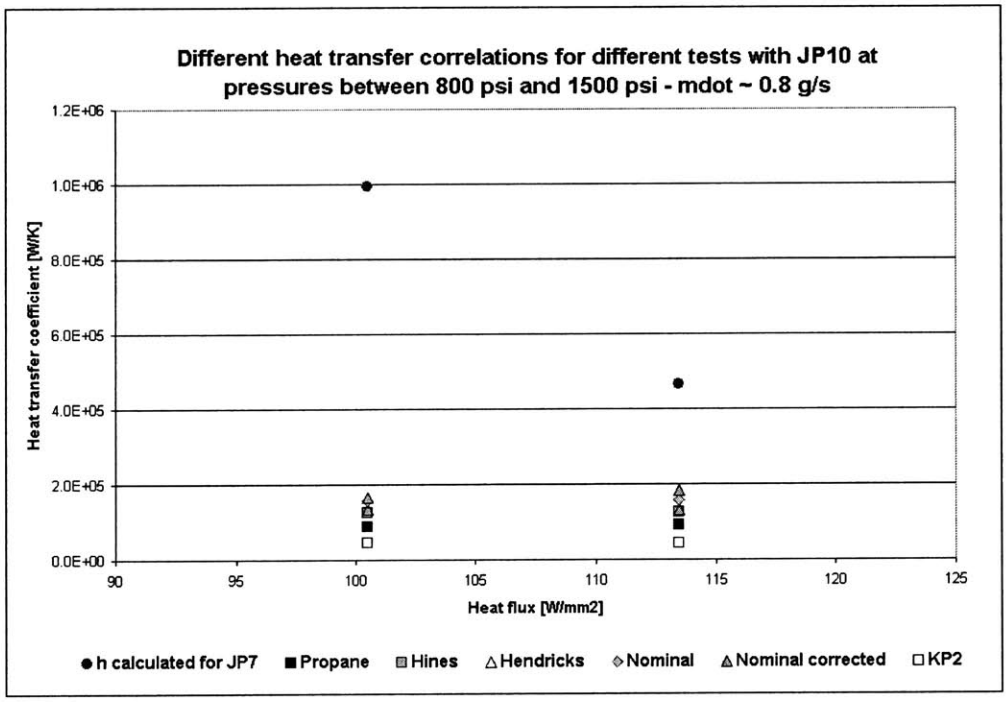

Figure 7-9: Heat transfer coefficients given by different heat transfer correlations are compared to the experimental heat transfer coefficients obtained during tests with JP10 at a mass flow of 0.8 g/s.

Most of the tests have been done on 95 micron inner diameter tubes. The effect of the diameter of the tube on the heat transfer properties should be studied. One test has been done with JP7 in a tube which has an inner diameter of 190 microns. No significant difference has been noticed but a more in depth study could be of interest.

The coolant mass flows in the engine can be as high as 5 g/s and the heat fluxes can reach 200 W/mm^2 at the throat. These conditions cannot be reproduced during the heat transfer experiments.

The main issue relates to the difference in materials. The heat transfer tests are done in stainless steel tubes whereas the device is made of silicon. This may have an impact on the heat transfer coefficient and in particular on the decomposition of JP7. Moreover, the amount of carbon deposits depend significantly on the material of the surface.

The heat transfer tests are carried out in horizontal tubes and buoyancy forces do not have a significant impact. In the micro rocket engine, passages may be vertical. A deterioration of the heat transfer coefficient has been noted in tests at macro scale in vertical tubes [15]. As the deterioration is reduced at high mass flows this should not be an issue for the micro rocket engine.

Those issues should be considered when evaluating the validity of the present results for the design of the cooling passages of the micro rocket engine.

Chapter 8

Conclusion

8.1 Summary

Selection of propellants for the liquid regeneratively cooled micro rocket engine

London's micro rocket engine uses gaseous propellants and a liquid coolant. The next step in the micro rocket engine program is to design a liquid regeneratively cooled micro rocket engine. The liquid propellants will cool the device before entering the chamber. They will experience high heat fluxes and pressures in the cooling passages and will be supercritical. The selection of the propellants must take into account both chamber performance and cooling properties of the fluids.

The heat capacity of the fluid is a major parameter so that the cooling passages can be designed to keep the silicon wall temperature below 900 K. The stability has also been identified as an important issue. Oscillations in the temperature and pressure could cause instabilities while operating the engine. Hydrocarbon fuels may form carbon deposits which may clog the passages or cause hot points. Other criteria such as the toxicity of the propellant and the ease of supply are considered. A brief evaluation of different potential propellants has been presented.

Heat transfer experiments

Heat transfer experiments in micro channels have been conducted with JP7 and JP10 to study the heat capacity of those fuels and their stability and behavior under high heat fluxes

and at high pressures. Tests at subcritical, critical and supercritical pressures have been conducted. Heat fluxes from 20 W/mm^2 to 120 W/mm^2 have been reached.

Heat capacity A great enhancement in the heat transfer coefficient has been identified in tests carried out with JP7 accompanied by a significant increase in the Stanton number. This enhancement has been noticed at subcritical, critical and supercritical pressures. It is believed that the high increase in heat transfer coefficients obtained during the tests illustrates the effect of the endothermic decomposition of JP7, in which heavy hydrocarbons convert into lighter hydrocarbons. Increases in heat transfer coefficients as high as 1.2×10^6 W/K.m^2 have been recorded. No relation has been found to quantify the enhancement depending on experimental conditions, the bulk temperature or the inside wall temperature reached. The heat transfer coefficient was seen to increase with heat flux and no deterioration of the heat transfer coefficient at high heat fluxes was noted. Pressure does not appear to have a major impact on the enhancement.

A model of JP7 enthalpy as the reaction of decomposition occurs is proposed. By varying the temperature at which the reaction begins and the amount of heat it consumes, the model has managed to predict an enthalpy profile for which the Stanton number slowly decreases at the entrance of the tube before stabilizing, as it would be expected for a thermally developed flow. This seems to imply that the model manages to capture part of the enhancement phenomenon. However, the model fails at capturing the fact that the enhancement is more significant at the end of the tube.

Experiments carried out with JP10 also show an increase in the heat transfer coefficient coupled with an increase in the Stanton number at the end of the tube. However, the increases are much smaller than those obtained with JP7. Tests with no enhancement are seen. Enhancements are seen at subcritical, critical and supercritical pressures. This seems to indicate that supercritical effects are not the only source of enhancement. However, no certain conclusion about the possible endothermy of the cracking of JP10 can be derived from these results. Since the properties used for the reduction of JP10 data are not precise, part of the enhancement seen in the Stanton number could be due to the supercritical effect that would not have been completely accounted for in the enthalpy profile. Higher heat transfer coefficients are seen with higher heat fluxes. For tests at a mass flow of 0.24 g/s, a change in the slope of increase of the heat transfer coefficient as a function of heat flux

is seen at a heat flux between 55 W/mm^2 and 60 W/mm^2. This heat flux is close to the critical heat flux given by a correlation derived for the onset of the heat transfer coefficient deterioration in supercritical water.
A comparison of the heat transfer coefficients obtained during heat transfer tests carried out with ethanol, JP7 and JP10 has been presented. JP10 offers the lowest heat transfer coefficients. Ethanol seems to offer better heat transfer coefficients than JP7 at low pressures whereas at high pressures, JP7 offers significantly higher heat transfer coefficients.

Stability Both JP7 and JP10 showed a good stability during the tests. No oscillations have been seen. There was no indication of the formation of deposits. In some tests carried out with JP7, the tube heated up red at some points corresponding to a short increase in temperature. An increase of 400°C has been recorded in one test.

Micro rocket engine design The heat transfer coefficients predicted by various heat transfer correlations have been compared to the experimental data obtained during the tests. The best estimations seem to be given by the Sieder-Tate correlation or the Dittus-Boelter correlation.

Hydrogen Peroxide

Compatibility issues associated with hydrogen peroxide have been investigated. Materials used in the MEMS devices have been checked for compatibility with 98 % hydrogen peroxide at ambient pressure and temperature. The experimental apparatus must be modified before conducting heat transfer tests with H_2O_2. Modifications to the current test rig to adapt it for safety and compatibility has been presented and all parts have been checked for compatibility. The passivation protocol and the operation of the new rig have been investigated.

8.2 Future work

The enthalpy model that has been derived for JP7 can be refined to better capture the effect of the decomposition. In particular, the results of the experiments seem to show that more endothermy is obtained at the end of the tube after the temperature has dropped and this could be implemented in the model.

One of the assumptions of the calculations is that the axial conduction along the tube is negligible compared to the radial conduction and convection at the inner surface of the tube. The bulk fluid is assumed to absorb all the heat from the applied current. However, in some experiments, the calculations from measurements at the far end of the tube were not valid. This could be due to an overestimation of the heat flux absorbed by the bulk fluid. New calculations taking into account the axial conduction along the tube would be of interest.

In the micro rocket engine, the mass flow and heat fluxes are fixed and the size of the cooling passages are adapted to give the required heat transfer coefficient. Only one test with JP7 has been done with a tube of bigger diameter and no major differences were seen in the heat transfer coefficient. The effect of the size of the passages on the heat transfer coefficient and on the stability of the fluid could be useful to investigate.

Hydrogen peroxide will be studied to determine its behavior and cooling properties at high pressures and temperatures. No data on hydrogen peroxide at 98 % are available at such pressures and temperatures. Tests should be carried out as soon as the test rig has been modified for safety and compatibility.

Finally, it would be interesting to test the propellants (JP7, JP10 and H_2O_2) in the gaseous engine. This would give an estimation of the validity of the predictions given by the heat transfer experiments.

Appendix A

Fluid properties used to reduce JP7 data

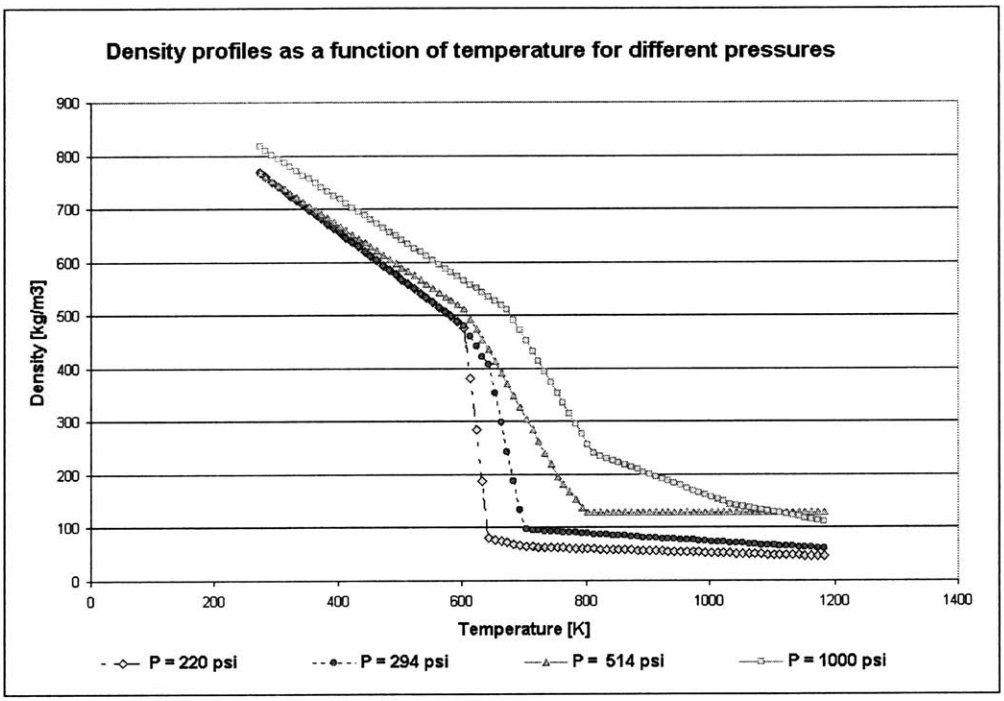

Figure A-1: Density profiles used in the reduction of JP7 data. Density is shown as a function of temperature for 4 different pressures. 220 psi, 294 psi are n-dodecane data. 514 psi and 1,000 psi are JP7 data.

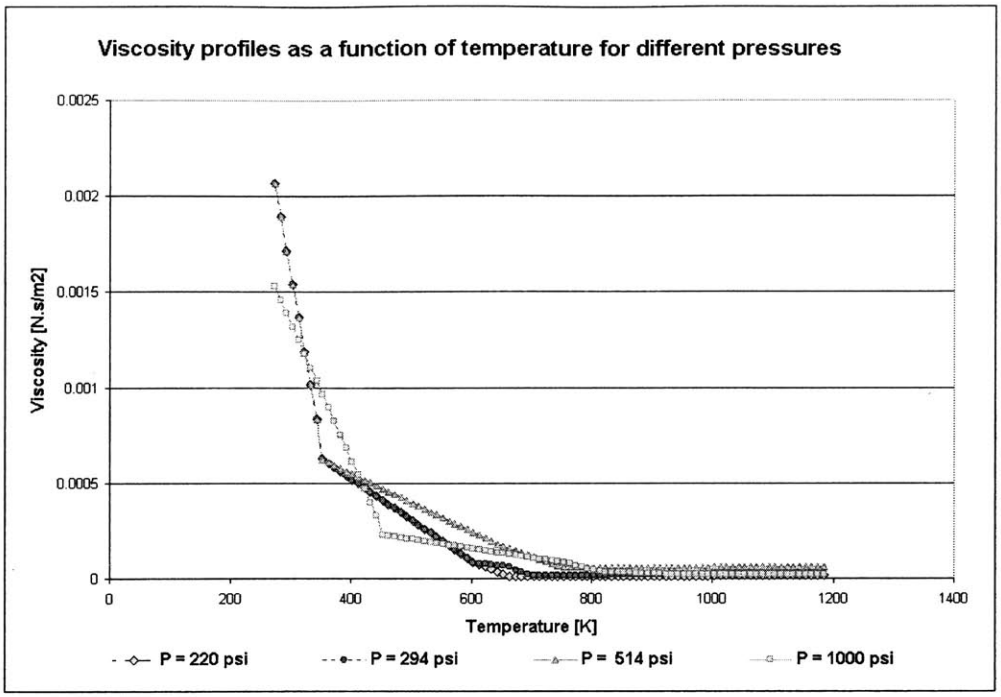

Figure A-2: Viscosity profiles used in the reduction of JP7 data. Viscosity is shown as a function of temperature for 4 different pressures. 220 psi, 294 psi are n-dodecane data. 514 psi and 1,000 psi are JP7 data.

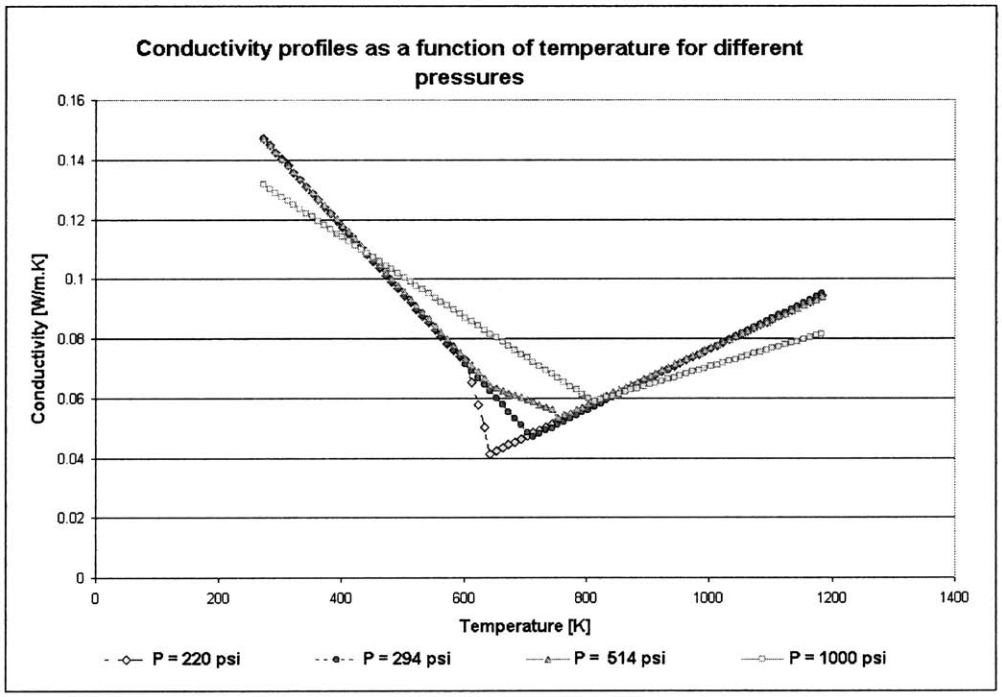

Figure A-3: Conductivity profiles used in the reduction of JP7 data. Conductivity is shown as a function of temperature for 4 different pressures. 220 psi, 294 psi are n-dodecane data. 514 psi and 1,000 psi are JP7 data.

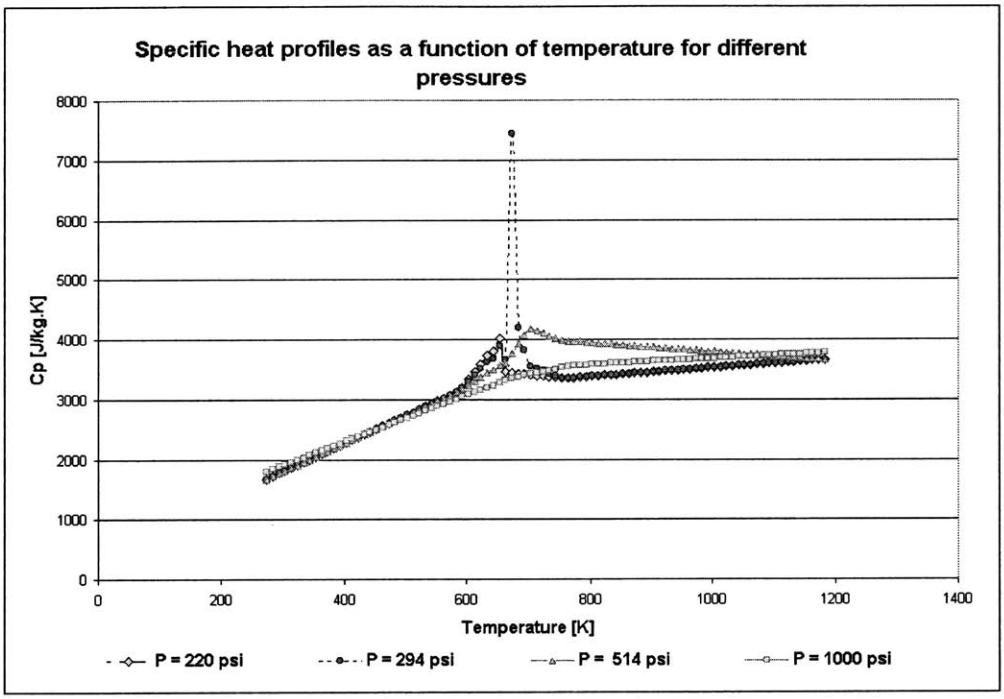

Figure A-4: Specific heat profiles used in the reduction of JP7 data. Cp is shown as a function of temperature for 4 different pressures. 220 psi, 294 psi are n-dodecane data. 514 psi and 1,000 psi are JP7 data.

Appendix B

Reduction data

The processus for the reduction of JP7 experimental data is summarized in Figure B-1.

The processus for the reduction of JP10 experimental data is summarized in Figure B-2.

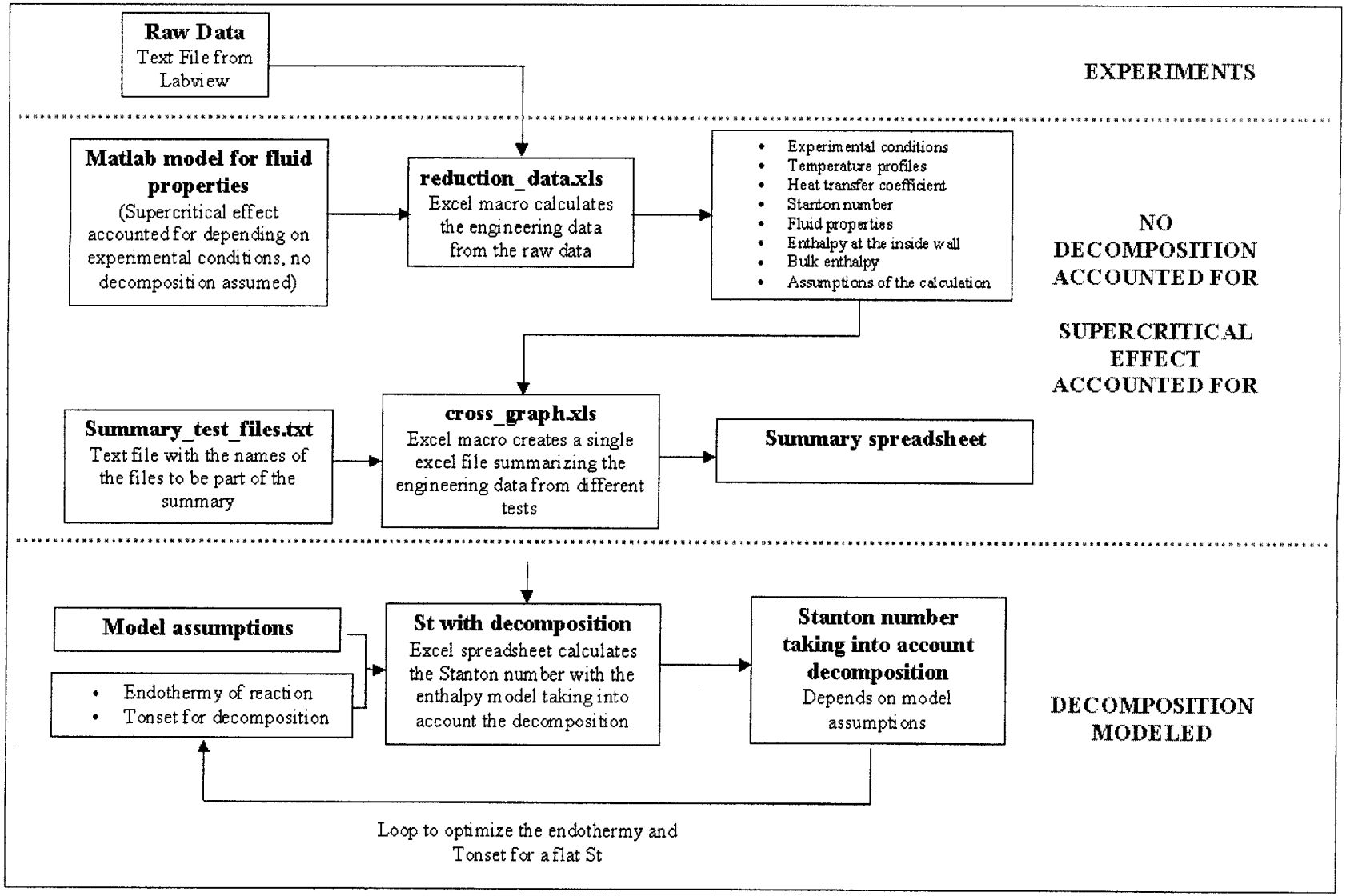

Figure B-1: Data reduction process for JP7 tests.

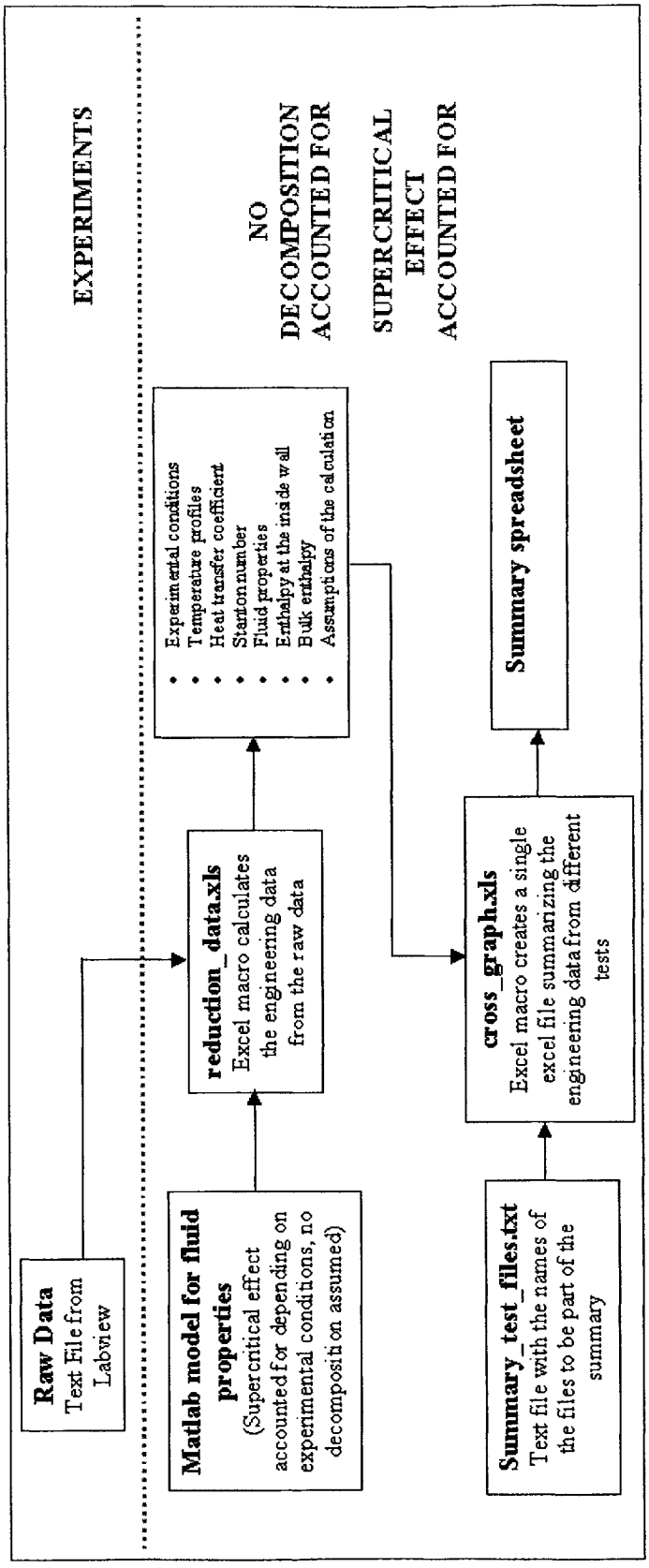

Figure B-2: Data reduction process for JP10 tests.

Appendix C

Uncertainty analysis

C.1 Introduction

This appendix presents a brief uncertainty analysis to estimate the confidence that can be given to the results presented. In a first section the experimental uncertainty associated with the independent measurements is presented. In a second section, these uncertainties are propagated to estimate the uncertainty on the derived quantities. The last section gives some comments about the effect of the uncertainty on the conclusions that have been derived.

If x is a variable, the following notation is adopted throughout this appendix:

- $\tilde{x}$ is the value of the variable indicated by the sensor
- dx is the uncertainty in the value of x
- S_x is the fractional uncertainty defined as the ratio of dx and $\tilde{x}$

C.2 Uncertainty associated with independent measurements

C.2.1 Pressure

Pressure is measured by two 5,000 psi pressure transducers which have been calibrated using a 6,000 psi pressure gauge. The calibration gauge has a stated accuracy of 0.25 %. This translated into a first uncertainty S_P^a on the scale factor derived from this calibration.

Uncertainty on the pressure measurements

Parameter	*Upstream P*	*Downstream P*
Scale factor β	1,354.7	1,887.6
Error on β due to gauge accuracy	0.30 %	0.30 %
S_P^a	0.003	0.003
Max difference between gauge P and linear correlation	10 %	7 %
S_P^b	0.1	0.07

Table C.1: Some uncertainties on the pressure transducers.

The calibration of the pressure transducer assumes a linear correlation between pressure and voltage. The characteristics of the pressure transducer is not always linear. This gives a second uncertainty S_P^b which has been estimated from the maximum difference between the pressure given by the gauge and the pressure given by the linear correlation.
In addition, there were variations in the pressure measurements. The variations were within ± 3.5 psi.
Therefore the total uncertainty was estimated at:

$$S_P = \pm S_P^a \pm S_P^b \pm \frac{3.5}{P} \tag{C.1}$$

where P is the measured pressure in psi, S_P^a and S_P^b are given for each pressure transducer in Table C.1.

C.2.2 Mass flow

The mass flow is measured using a factory-calibrated Micro Motion D6 mass flow meter. It has a stated accuracy of ±0.002. Variations in the readings of the mass flow meter were within ± 0.004 g/s. Therefore the uncertainty on the mass flow measurement was estimated at:

$$S_{\dot{m}} = \pm 0.002 \pm \frac{0.004}{\dot{m}} \tag{C.2}$$

where $\dot{m}$ is the measured mass flow in g/s. Uncertainties range from 1 % for $\dot{m} = 0.04$ g/s to 10 % for $\dot{m}$ 0.36 g/s.

C.2.3 Power delivered to the fluid

The heat flux is calculated as the product of the current and the voltage. There were variations for the current reading and the voltage reading. A maximum of ± 2.5 % variation in the heat flux has been recorded in the tests used for analysis.

The voltage is measured at the control loop on the power supply. There is a voltage drop along the wires of the control loop from the electrodes to the power supply. By measuring the difference between the voltage read at the power supply control loop and the voltage at the electrodes, the resistance R of the wires was estimated at 2.25×10^{-3} Ω. The uncertainty on the power was estimated at 2 % for heat fluxes below 40 W/mm^2, 1.5 % for heat fluxes between 40 W/mm^2 and 80 W/mm^2 and 1 % for heat fluxes above 80 W/mm^2. The current measurement is acquired as a voltage by measuring the voltage drop across a resitor of known resistance. There is an additional error in the current measurement due to the conversion of the current to a voltage at the resistor. This was not accounted for in the present uncertainty calculation.

It was assumed in the calculations that there was no heat losses and the power provided by the electric field was entirely absorbed by the fluid. However, there are losses by axial conduction along the tube, conduction into the 1/16" tube and losses at the contact between the electrodes and the tube. The losses due to axial conduction were estimated at 2 %. As the estimation of these losses was delicate, they were not taken into account in the uncertainty analysis. Losses due to radiation and free convection on the outer surface were negligible and therefore not accounted for in the uncertainty analysis (refer to Section 3.6.3). Therefore the uncertainty on the power delivered to the test section is estimated at:

$$S_Q{}^{electric} = \pm 0.025 + 0.02 \qquad for \quad q < 40\,W/mm^2 \tag{C.3}$$

$$S_Q{}^{electric} = \pm 0.025 + 0.015 \qquad for \quad 40\,W/mm^2 < q < 80\,W/mm^2 \tag{C.4}$$

$$S_Q{}^{electric} = \pm 0.025 + 0.01 \qquad for \quad q > 80\,W/mm^2 \tag{C.5}$$

C.2.4 Outside wall temperature

The IR sensor was calibrated using the temperature readings of a stainless steel thermocouple heated by a propane flame. The calibration was done several times and the shift in the scale factor was estimated around ± 0.005. The uncertainty due to the non linearity of

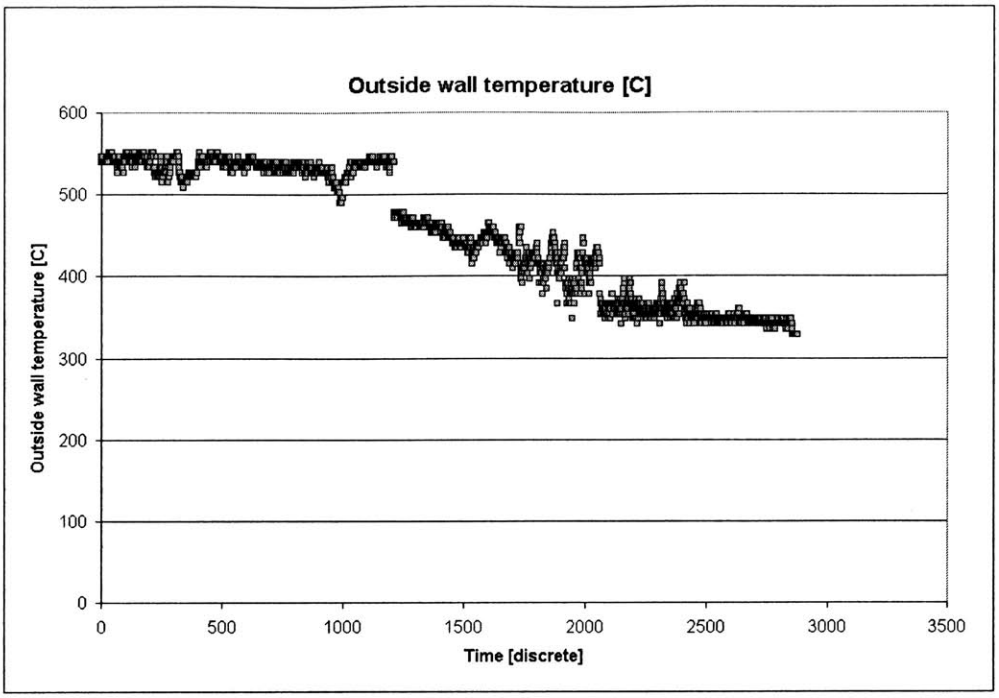

Figure C-1: Outside wall temperature vs. time during a stability test carried out with JP10. The IR sensor slowly gets misaligned with the tube.

the IR sensor characteristic $S_T^{linearity}$ has been estimated from the difference between the thermocouple temperature reading T_t and the temperature given by the linear calibration T_c as shown in the following relation:

$$S_T^{linearity} = Max\left(\frac{T_t - T_c}{T_c}\right) \tag{C.6}$$

An uncertainty of ± 1.5 % has been assumed for temperatures above 450°C and ± 5 % for temperatures below 450°C. Variations in the temperature reading of ± 15°C have been seen at temperatures below 450°C and ± 10°C at temperatures above 450°C. An uncertainty due to the drift of the aim point of the IR sensor has to be taken into account even it was checked after each measurement. The temperature sensor output is strongly sensitive to the pointing. Figure C-1 shows measurements taken during a stability test as the aim point of the IR sensor was slowly drifting. The additional uncertainty in the outside wall temperature due to the drift of the aim point of the IR sensor has been estimated from the difference between the temperature measured during a test at the same point during different passes. A maximum difference of ± 15°C has been seen. Uncertainties due to a change in the emissivity of the tube surface has not been taken into account. The total

uncertainty on the outside wall temperature measurement is:

$$S_P = \pm 0.005 \pm 0.05 \pm \frac{15}{T} \pm \frac{15}{T} \qquad for \quad T < 450\,^\circ C \tag{C.7}$$

$$S_P = \pm 0.005 \pm 0.05 \pm \frac{10}{T} \pm \frac{15}{T} \qquad for \quad T > 450\,^\circ C \tag{C.8}$$

where T is the temperature in °C.

C.2.5 Tube dimensions

The inner and outer diameters can vary from 35 microns to 100 microns as specified by Micro Group. However, test sections from the same serie have much closer characteristics. The cross section area has been estimated for 3 tubes from the measurements of the mass flow and the pressure drop across the tube. An uncertainty of ± 0.025 has been assumed for the inner diameter and the outer diameter. The uncertainty on the length of the heated part of the tube is difficult to estimate. An uncertainty of ± 0.01 has been chosen.

C.2.6 Position

The stage has an accuracy of ± 0.05 micron. The drift of the starting point of the stage has been estimated at ± 25 microns (taking into account the error in positioning the starting point and different shapes of the braze on different tubes). The total uncertainty for the position of measurement is:

$$S_X = \pm \frac{0.05}{X} \pm \frac{25}{X} \tag{C.9}$$

where X is the position of the measurement in microns. The uncertainty ranges from 1.4 % at the end point to 7.2 % at 350 microns from the entrance.

The uncertainty due to errors in the fluid properties is not taken into account.

C.3 Uncertainty associated with derived quantities [23] [25] [2]

The uncertainty of the derived quantities are propagated from the uncertainty of each of the independent measurements as follow [23].

Test conditions

Test	Mass flow $\dot{m}$ [g/s]	Heat flux q [W/mm^2]	Position [microns from entrance]
1	0.04	40	350
2	0.24	80	1,750
3	0.36	120	1,750

Table C.2: Tests conditions of the three tests chosen as examples for the uncertainty analysis.

Let's y be a quantity derived from $x_1, x_2, ..., x_n$.

$$y = f(x_1, x_2, ..., x_n) \tag{C.10}$$

The uncertainty dy is given by:

$$dy = \sum_{i=1}^{n} \left(\frac{\partial f}{\partial x_i} \Big|_{(\tilde{x_1}, \tilde{x_2}, ..., \tilde{x_n})} dx_i \right) \tag{C.11}$$

For each x_i, an influence coefficient C_{x_i} is defined as the non-dimensionalized partial derivative of y with respect to x_i:

$$C_{x_i} = \left| \frac{\partial f}{\partial x_i} \Big|_{(\tilde{x_1}, \tilde{x_2}, ..., \tilde{x_n})} \left(\frac{\tilde{x_i}}{\tilde{y}} \right) \right| \tag{C.12}$$

where $\tilde{y}$ corresponds to the value of y calculated from the $\tilde{x_i}$. C_{x_i} represents the percentage change in y due to one percentage change in x_i.
The fractional uncertainty is then calculated:

$$S_y = \pm \sqrt{\sum_{i=1}^{n} (C_{x_i} S_{x_i})^2} \tag{C.13}$$

When $C_{x_i} \neq 1$, the influence coefficient was evaluated using Excel by looking at the effect on the output of a slight change in the input. For each derived quantity, a table illustrates the uncertainty calculation for three measurements. The mass flow, the heat flux and the point of measurement for each of them are presented in Table C.2.

C.3.1 Inside tube area A_i

The inside tube area A_i is given by:

$$A_i = 2\pi r_i l \tag{C.14}$$

where r_i is the tube inner diameter and l the heated length of the tube. C_{r_i} and C_l are equal to 1. Therefore:

$$S_{A_i} = \sqrt{S_{r_i}^2 + S_l^2} \tag{C.15}$$

The uncertainty on S_{A_i} does not depend on the measurement.

Inside tube area A_i	
C_{ri}	1
C_l	1
S_{A_i}	1.6 %

C.3.2 Cross section area A_e

The uncertainty on S_{A_e} does not depend on the measurement.

Cross section tube area A_e	
C_{ro}	2.22
C_{ri}	0.22
S_{A_e}	2.8 %

C.3.3 Heat flux

	Heat flux q		
	1	2	3
C_Q	1	1	1
C_{A_i}	1	1	1
S_q	4.3 %	3.8 %	3.8 %

Fractional position x

Position [microns from entrance]	350	1,750
C_X	1	1
C_l	1	1
S_x	1.7 %	7.2 %

Inside wall temperature T_{in}

	1	2	3
C_Q	0.14	0.42	0.55
C_{To}	1.19	1.55	1.74
C_l	0.14	0.42	0.55
C_{r_o}	0.15	0.44	0.58
C_{r_i}	0.15	0.44	0.58
$S_{T_{in}}$	12 %	16 %	17 %

Bulk enthalpy H_b

	1	2	3
C_Q	0.11	0.04	0.04
C_x	0.11	0.04	0.04
$C_{\dot{m}}$	0.11	0.04	0.04
S_{H_b}	1.4 %	0.34 %	0.34 %

C.3.4 Fractional position

C.3.5 Inside wall temperature

C.3.6 Bulk enthalpy

C.3.7 Bulk temperature

The uncertainty on the bulk temperature has been interpolated from the uncertainty on the bulk enthalpy using the enthalpy table.

Bulk temperature T_b

S_{T_b}	8.4 %	3.7 %	3.6 %

C.3.8 Film temperature

Film temperature T_f			
	1	2	3
$C_{T_{in}}$	0.86	0.89	0.9
C_{T_b}	0.11	0.14	0.01
S_{T_f}	10 %	14 %	15 %

C.3.9 Heat transfer coefficient

Heat transfer coefficient h			
	1	2	3
$C_{T_{in}}$	1.19	1.13	1.12
C_{T_b}	0.2	0.14	0.12
C_Q	1	1	1
C_{A_i}	0.98	0.98	0.98
S_h	15 %	19 %	19 %

Uncertainties can reach 30 % for some of the tests.

C.3.10 Inside wall enthalpy

The uncertainty on the inside wall enthalpy has been interpolated fron the uncertainty on the inside wall temperature using the enthalpy table.

Inside wall enthalpy H_{in}			
	1	2	3
S_{H_i}	10 %	12 %	15 %

C.3.11 Stanton number

Uncertainties as high as 40 % have been reached. The influence coefficient indicates that the enthalpies have a large impact on the uncertainty on the Stanton number. The lack of precise data on the enthalpy profile of the fluids is expected to have a large impact on the

Stanton number St			
	1	2	3
C_Q	1	1	1
C_{A_i}	0.98	0.98	0.98
C_{A_e}	1	1	1
$C_{\dot{m}}$	0.99	0.99	0.99
$C_{H_{in}}$	1.75	2	1.9
C_{H_b}	0.77	1.08	0.9
S_{St}	21 %	26 %	28 %

results.

The uncertainties on the heat transfer coefficient and the Stanton number are large. Many uncertainties are still not taken into account in this calculation such as the uncertainty on the properties of the fluids which is expected to have a large impact.

Bibliography

[1] Personal communications with H. Steve Yuan, Business Development Manager, FMC Corporation, Hydrogen Peroxide Division.

[2] Error analysis. web site: http://science.widener.edu/svb/stats/error.html.

[3] Technical bulletin 104: Materials of construction for equipment in use with hydrogen peroxide. Technical Report 104, FMC Chemicals, Princeton, New Jersey, 1966.

[4] Personal communications with Professor Jack Kerrebrock, 2000.

[5] Lisa Dang Alan Y. Chen. Characterization of supercritical JP7's heat transfer and coking properties. AIAA Paper, 2001.

[6] Astronautix. H_2O_2/Kerosene. web site: http://www.friends-partners.org/mwade/props/h2oosene.htm.

[7] Peter Griffith Bharat S. Shiralkar. The deterioration in heat transfer to fluids at supercritical pressure and high heat fluxes. Technical Report Report No. 70332-51, Department of Mechanical Engineering, Engineering Projects Laboratory, Massachusetts Institute of Technology, Massachusetts, 1968.

[8] Michael Karpuk Brad Hitch. Enhancement of heat transfer and elimination of flow oscillations in supercritical fuels. Paper No. AIAA 98-3759.

[9] Michael Karpuk Brad Hitch. Experimental investigation of heat transfer and flow instabilities in supercritical fuels. Paper No. AIAA 97-3043. Presented at the 33rd AIAA/ASME/SAE/ASEE Joint Propulsion Conference.

[10] Brikowski and Norton. Fluid heat capacity at near critical conditions. web site: http://www.utdallas.edu/ brikowi/Publications/Geysers/GRC99_Talk/node14.html.

[11] CFD Research Corporation (CFDRC). Supercritical Fluid Technology at CFDRC. web site:
http://www.cfdrc.com/datab/Applications/Supercritical/supercritical.html.

[12] Chevron Products Corporation. Aviation fuels, chapter 4.

[13] Lisa Dang. Characterization of Supercritical JP7 Heat Transfer and Coking Properties. Student Research Project, Massachusetts Institute of Technology (MIT), 2000.

[14] Antoine Deux. Design of a silicon microfabricated rocket engine turbopump. Master of science, Massachusetts Institute of Technology, Department of Aeronautics and Astronautics, 2001.

[15] M.L. Meyer D.L. Linne. Evaluation of heat transfer and thermal stability of supercritical JP-7 fuel. AIAA paper 97-3041, 1997. 33rd AIAA/ASME/SAE/ASEE Joint Propulsion Conference and Exhibit, Seattle, WA.

[16] Tim Edwards. USAF Supercritical Hydrocarbon Fuels Interests. Paper No. AIAA 93-0807 Presented at the 31st Aerospace Sciences Meeting and Exhibit, 1993.

[17] A.H. Epstein et al. Micro-Heat Engines, Gas Turbines, and Rocket Engines: The MIT Microengine Project. Presented at the 28th AIAA Fluid Dynamics Conference and the 4th AIAA Shear Flow Control Conference, Snowmass Village, 1997. AIAA-97-1773.

[18] Adriane Faust. Forced convective heat transfer to supercritical water in micro rocket cooling passages. Master of science, Massachusetts Institute of Technology, Department of Aeronautics and Astronautics, 2000.

[19] K. Breuer K-S Chen F. Ehrich E. Esteve G. Gauba R. Ghodssi C. Groshenry S. Jacobson J. Lang C-C Lin A. Mehra J. Mur Miranda-S. Nagle D.J. Orr E. Piekos M. Schmidt G. Shirley S. Spearing C. Tan Y-S Tzeng I. Waitz A.H. Epstein S.D. Senturia G. Anathasuresh, A. Ayon. Power MEMS and microengines. Presented at IEEE Conference on Solid State Sensors and Actuators, Chicago, IL, 1994.

[20] Pillori G.L. *Material Safety Data Sheet (MSDS) for Anhydrous Hydrazine.* Fisher Scientific Chemical Division. 1997. Fair Lawn, NJ.

[21] Laurent Jamonet. Testing of a micro turbopump. Master of science, Massachusetts Institute of Technology, Department of Aeronautics and Astronautics, 2002.

[22] Lagtemperaturlaboratoriet Kylmalaboratorio. Typical phase diagram. web site: http://boojum.hut.fi/research/theory/typicalpt.html.

[23] Adam Pollock London. *Development and Test of a Microfabricated Bipropellant Rocket Engine.* PhD thesis, Massachusetts Institute of Technology. June 2000.

[24] J.B. Lopata. Systems analysis of a microfabricated storable bipropellant rocket engine. Master of science, Massachusetts Institute of Technology, Department of Aeronautics and Astronautics, 2000.

[25] Department of Chemical Engineering and Materials Science. Experimental errors and propagation of errors.
web site: http://www3.cemsumn.edu/courses/chen4402/ERROR.html.

[26] Sumita Pennathur. Micro-scale turbopump cavitation. Master of science, Massachusetts Institute of Technology, Department of Aeronautics and Astronautics, 2001.

[27] Chris Protz. Systems analysis of a microfabricated storable bipropellant rocket engine. Master of science, Massachusetts Institute of Technology, Department of Aeronautics and Astronautics, 2000.

[28] Jonathan Protz. *An assessment of the aerodynamic, thermodynamic, and manufacturing issues for the design, development, and microfabrication of a demonstration micro engine.* PhD thesis, Massachusetts Institute of Technology, Department of Aeronautics and Astronautics.

[29] Charles W. Raleigh. Technical bulletin 67: Hydrogen peroxide physical properties. Technical Report 67, FMC Chemicals, Princeton, New Jersey, 1969.

[30] Joseph V. Atria Tim Edwards. Thermal stability of high temperature fuels. ASME Paper 97-GT-143, 1997.